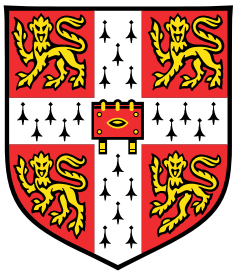

Development of Three-Dimensional Super-Resolution Imaging Using a Double-Helix Point Spread Function

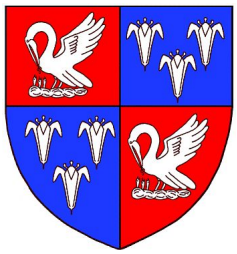

Alexander Roy Carr

Department of Chemistry
University of Cambridge

This dissertation is submitted for the degree of
Doctor of Philosophy

Corpus Christi College April 2018

Declaration

This dissertation summarises research carried out in the laboratory of Dr. Steven Lee at the Department of Chemistry, University of Cambridge, between October 2015 to April 2018. This dissertation is the result of my own work and includes nothing which is the outcome of work done in collaboration except as declared in the Preface and specified in the text. This dissertation has not been submitted in whole or in part for consideration for any other degree or qualification by this, or any other university. The length of this dissertation does not exceed the word limit of the Physics and Chemistry degree committee (60,000 words).

Alexander Roy Carr
April 2018

Acknowledgements

Dr Steven Lee, who has put his trust in me (and Lisa) to start his group, thank you for your support, enthusiasm and for giving me this opportunity. I hope you have enjoyed the experience as much as I have, or at least that you have learnt a lesson in hiring PhD students.

Prof David Klenerman and Prof Simon Davis, who have both had great input to my project as key collaborators and partial supervisors, thank you for the guidance and experience you have brought to my studies. Your advice has been invaluable and your passion for all aspects of science is inspiring.

Lisa-Maria, who is also part of the first generation of Lee Lab members, I really appreciate sharing this experience this with you. You've been there from the start to fill in the blanks (or rather, blank) in my chemistry knowledge. Thank you for everything.

To all the other members of the Lee and Klenerman groups, thank you for your help and company. I could not have wished for a better group. Specifically I would like to acknowledge: Aleks for his input in all things technical, Guida for being the big sister I never knew I wanted, Suman for his cooking lessons, James for shared footballing woes, Juan and Mathew for proofreading chapters as well as Anna, Ji-Eun, Rachel and Dimitri.

Although many collaborators have helped me along the way, I would like to specifically mention Mafalda, who was my source of all things T-cell related, and Sohaib, who has been trying to understand the DHPSF with me.

Finally, I would like to thank my parents, Jo and Tony, for always being there for me and, most importantly of all, for proofreading.

I couldn't have done it without you.

Thank you.

Abstract

Single-molecule localisation microscopy (SMLM), has allowed for optical microscopy to probe biological systems beyond the diffraction limit. The intrinsic 3D nature of biology has motivated the development of 3D-SMLM with novel techniques, including the double-helix point spread function (DHPSF). A bespoke microscope platform employing the DHPSF transformation was built, achieving $\sim$10 *nm* lateral and $\sim$20 *nm* axial localisation precision over a $\sim$4 μm axial depth.

Until recently, the DHPSF has been limited by spherical aberration present when imaging away from coverslip surfaces to the study of small volumes close to the coverslip. By matching the refractive index of the objective lens immersion liquid to that of the imaging media, this aberration can be minimised, facilitating large-volume imaging away from unphysiological flat surfaces. The work presented in this thesis illustrates the capabilities of the DHPSF for 3D-SMLM and single-particle tracking (SPT) in previously inaccessible areas of biological samples (*e.g.* in the nucleus and on the apical cell surface).

Application of the DHPSF for SPT in eukaryotic cells are presented; tracking the motion of T-cell membrane proteins on the apical surface and components of the chromosome remodelling complex in the nucleus of embryonic stem cells. For these applications, mean-squared displacement and jump distance diffusion analysis methodologies were extended into 3D and benchmarked against simulated datasets.

A variety imaging applications that are facilitated by the extended depth of focus of the DHPSF are presented, focusing on quantification of T-cell membrane protein reorganisation upon immunological activation. Finally, the clustering distribution of the T-cell receptor is investigated by Ripley's K analysis enabled by duel labelling of its position and the outer membrane in primary T cells.

Named Publications Relating to Thesis

- Three-Dimensional Super-Resolution in Eukaryotic Cells Using the Double-Helix Point Spread Function. **Alexander R. Carr**, Aleks Ponjavic, Srinjan Basu, James McColl, Ana Mafalda Santos, Simon Davis, Ernest D. Laue, David Klenerman and Steve F. Lee. Biophysical Journal, 2017.
- Maximizing the Field of View and Accuracy in 3D Single Molecule Localization Microscopy. Sohaib Abdul Rehman, **Alexander R. Carr**, Martin O. Lenz, Steven F. Lee and Kevin O'Holleran. Optics Express, 2018.
- Singlemolecule Light-Sheet Imaging of Suspended T Cells. Aleks ponjavic, James McColl, **Alexander R. Carr**, Ana Mafalda Santos, Klara Kulenkampff, Anna Lippert, Simon Davis, David Klenerman and Steven F. Lee. Biophysical Journal, 2018.
- A Cell-Topology Based Mechanism for Antigen Discrimination by T Cells. Ricardo A. Fernandes*, Kristina A. Ganzinger*, Justin Tzou, Peter Jonsson, Steven F Lee, Matthieu Palayret, Ana Mafalda Santos, **Alexander R. Carr**, Aleks Ponjavic, Veronica T. Chang, Charlotte Macleod, B. Christoffer Lagerholm, Alan E. Lindsay, Omer Dushek, Andreas Tilevik, Simon J. Davis, David Klenerman. (In submission at Nature Immunology)

Table of contents

List of figures

Abbreviations

List of Abbreviations and Acronyms

n_a Refractive index

(d)STORM (Direct) stochastic optical reconstruction microscopy

(f)PALM (Fluorescence) photoactivated localisation microscopy

(PA-)JF (Photoativatable-)JaneliaFluor

(S)SIM (Saturated) structured illumination microscopy

2D Two dimensional

3B Bayesian analysis of blinking and bleaching

3D Three dimensional

APC Antigen-presenting cell

BFP Back focal plane

CD28 Cluster of differentiation 28

CD45 Cluster of differentiation 45

CHD4 Chromodomain-helicase-DNA-binding protein 4

CSR Complete spatial randomness

DBSCAN Density-based spatial clustering of applications with noise

DHPSF Double-helix point spread function

EM Electron microscopy

EMCCD Electronmultiplying charged-coupled device

ES Embryonic stemcell

Fab Fragment antigen-binding region of an antibody

FACS Fluorescence-activated cell sorting

FOV Field of view

FRC Fourier ring correlation

FSC Fourier shell correlation

FWHM Full width at half maximum

HEK Human embryonic kidney

HILO Highly inclined and laminated optical sheet illumination

IgG Immunoglobulin G

iPALM Interferometric PALM

ITAM Immunoreceptor tyrosine-based activation motif

JD Jump distance

Lck Lymphocyte-specific protein tyrosine kinase

LED Light emitting diode

LS Least-squares criterion

MBD3 Methyl-CpG-binding domain protein 3

MFM Multifocus microscopy

MHC Major histocompatibility complex

MLE Maximum-likelihood estimation

MSD Mean-square displacement

MTA3 Metastasis-associated protein 3

NA Numerical aperture

NN Nearest neighbour

NuRD Nucleosome remodelling and deacetylase

OD Optical density

PA-PAINT Photoactivatable-PAINT

PAINT Points accumulation for imaging in nanoscale topology

PBS Phosphate-buffered saline

PLL Poly-L-lysine

PM Phase mask

Pre1 Proteasome core-particle subunit

PSD Post-synaptic density

PSF Point spread function

QE Quantum efficiency

qPAINT Quantitative PAINT

QWP quarter-wave plate

RESOLFT Reversible saturatable optical linear fluorescence transitions

RPN1 Proteasome regulatory-particle subunit

SA Spherical aberration

sCMOS Scientific complementary metal-oxide semiconductor

SMLM Single-molecule localisation microscopy

SNR Signal to noise ratio

SOFI Super-resolution optical fluctuation imaging

soSPIM Single-objective SPIM

SPI(M) Single-plane illumination (microscopy)

SPT Single-particle tracking

SR Super-resolution

SRRF Super-resolution radial fluctuations

STED Stimulated emission depletion microscopy

TCCD Two-colour coincidence detection

TCR T-cell receptor

TIRF Total internal reflection fluorescence illumination

TMR Tetramethylrhodamine

uPAINT Universal PAINT

VAEM Variable-angle epifluorescence microscopy

WGA Wheat germ agglutinin

Zap70 ζ-chain-associated protein 70

Chapter 1

Introduction to Super-Resolution Fluorescence Microscopy and 3D-Single-Molecule Localisation Microscopy

Continuing in the footsteps of Dr Steven Lee, who will take any opportunity to use this quote, Richard Feynman once said [1]:

> "It is very easy to answer many of these fundamental biological questions; you just look at the thing!"

In order to do exactly this, methods have been developed to image biological systems and processes with minimal artefacts and with nanoscale resolution. This chapter provides background and context for the microscopy approaches presented in this thesis. Optical microscopy and the diffraction limit are introduced with fluorescence microscopy highlighted due to its widespread adoption in biological studies. Methods developed to image beyond the diffraction limit are outlined with particular focus on single-molecule localisation microscopy (SMLM) methods. Multiple approaches extending SMLM into 3D are introduced with an emphasis on the double-helix point spread function (DHPSF). Finally, applications of SMLM to single particle tracking (SPT) and quantitative imaging are discussed. Specific technical challenges involved in building a DHPSF microscope and backgrounds to the biological problems investigated will be discussed in the individual results chapters.

1.1 Optical Microscopy and the Diffraction Limit

Optical microscopy employs visible light (≈400-800 nm in wavelength) passing through or emitted by a sample that is collected by a series of lenses to create an image of the sample of interest. The numerical aperture (NA) of an optical system is a measure of collecting power determined by the range of angles that a lens can accept light rays. The magnification of an optical microscope is primarily determined by the objective lens with high-NA objective lenses available typically up to 100x magnification. Regardless of how much the image is magnified, the diffraction limit prevents additional details from being seen below a certain distance. The diffraction limit was first described by Abbe in 1873 [2]. It states: all imaging systems are limited in their frequency space by a high-frequency cut-off corresponding to $\lambda/(2n_a)$ (where λ is the wavelength of collected light and NA is the numerical aperture of the objective lens). The physical manifestation of this is that a point source when viewed through any optical system will exhibit a diffraction pattern known as a point-spread function (PSF) (*i.e.* impulse response or optical transfer function). The final image produced by an optical system is a convolution of the sample's true structure and the PSF of the imaging system.

The origin of the PSF can be explained by considering the Fourier spectrum (the space of spatial frequencies) of an object in the focal plane of an imaging system and the transmission of the spectral components through the system. Lenses perform a spatial Fourier transform on the intensity distribution propagating from their focal plane, resulting in a spatial frequency distribution in their image plane [3]. An additional lens placed so that its focal plane coincides with the image plane of the first lens performs an inverse Fourier transform, forming an image of the object placed the focal plane of the first lens. In the simplest microscope system these lenses are the objective lens and the tube lens, respectively.

The Fourier transform of a point source is a uniform spatial frequency intensity over infinite space. In a simple microscope (figure 1.1a), this is the case for a point source in the focal plane of the objective lens (figure 1.1b&c). Due to the finite size of the apertures within the optical system (*e.g.* the finite widths of the lenses) this distribution is cropped so that is resembles a top-hat function (figure 1.1d). The inverse Fourier transform of a circular top-hat function (created by circular optics) is an Airy disk [3] (equation 1.1). The tube lens of the microscope performs an inverse Fourier transform on the cropped spatial frequency distribution, resulting in point source appearing as an Airy disk with width

inversely proportional to the widths of the top-hat function (figure 1.1e). This is the PSF of the microscope.

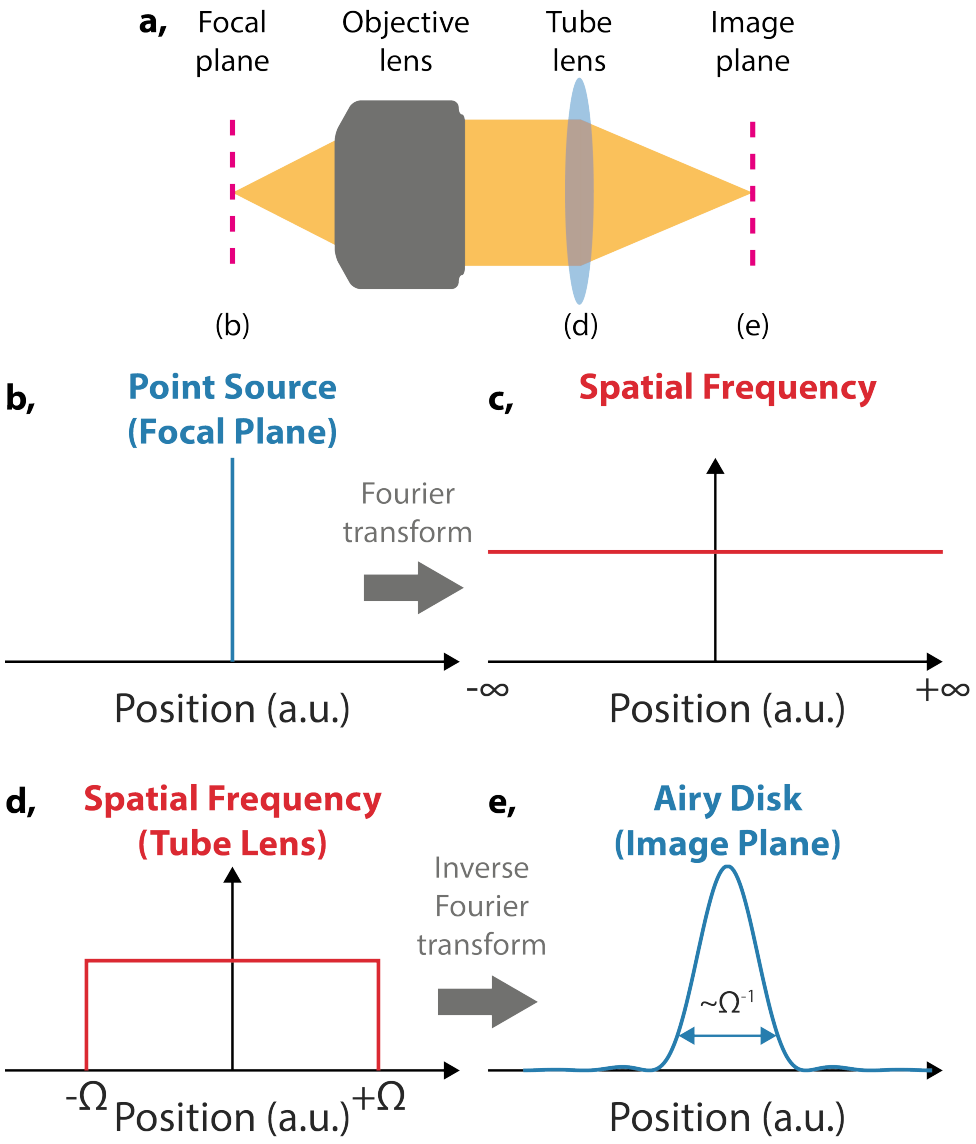

Fig. 1.1 The origin of the PSF described by Fourier Optics. Lenses perform a spatial Fourier transform on the intensity distribution in their focal plane. (a) A simple microscope system consisting of an objective lens and a tube lens. (b) Intensity distribution of a point source in the focal plane of a simple microscope. (c) Spatial Fourier transform of the intensity distribution of a point source: a uniform spatial frequency intensity over infinite space. (d) Intensity distribution at the tube lens: the Fourier transform of a point source is cropped by the lens aperture into a top-hat function. (e) Intensity distribution at the image plane: the inverse Fourier transform of a top-hat function results in a PSF defined by an Airy Disk.

$$PSF_{Airy}(x,y) = \frac{[J_1(\alpha\sqrt{(x-x_0)^2+(y-y_0)^2})]^2}{\pi(x-x_0)^2+\pi(y-y_0)^2} \tag{1.1}$$

Where (x_0, y_0) is the centre of the Airy disk, J_1 is the first-order Bessel function and α is a constant given by $\alpha = 2\pi NA/M\lambda$ where NA is the numerical aperture and M is the magnification of the imaging system and λ is the wavelength of light imaged.

An Airy disk can be readily approximated to a 2D Gaussian function (equation 1.2) [4] (figure 1.2), which is computationally easier to describe as it does not contain additional maxima at increasing width.

$$PSF_{Gaussian}(x,y) = \frac{1}{2\pi\sigma_x\sigma_y} e^{-\frac{(x-x_0)^2}{2\sigma_x^2}-\frac{(y-y_0)^2}{2\sigma_y^2}} \tag{1.2}$$

Where $\sigma_{x,y}$ is the standard deviation of the Gaussian function in x and y, given by [5].

$$\sigma_{x,y} = \frac{1.323\lambda}{2\pi n_a} \tag{1.3}$$

Equation 1.3 tells us that the width of the PSF of an optical system can be reduced by reducing the wavelength of light used to probe the sample. However, short-wavelength/high-energy electromagnetic radiation has a destructive effect on live samples, limiting its application in biological studies. The resolution of an imaging system can be defined in many ways, but is most commonly described by the Rayleigh criterion [6], which states that, in order to be resolved, two point sources must be separated by at least the distance between the centre of their Airy disk diffraction pattern to the first diffraction minima. This distance is approximately 250 nm for visible light. If two objects are closer than this distance their PSFs will overlap and they will not be resolved. Electron microscopy (EM) reduces this resolution limit with the shorter wavelength of electrons compared to photons in the visible range ($\approx$2 pm compared to 450-700 nm). However, EM requires fixation and heavy-metal staining of biological samples, limiting its application to fixed-cell imaging. Additionally, the ultra high vacuums used may have perturbation effects on the morphology of fragile biological samples, even after fixation.

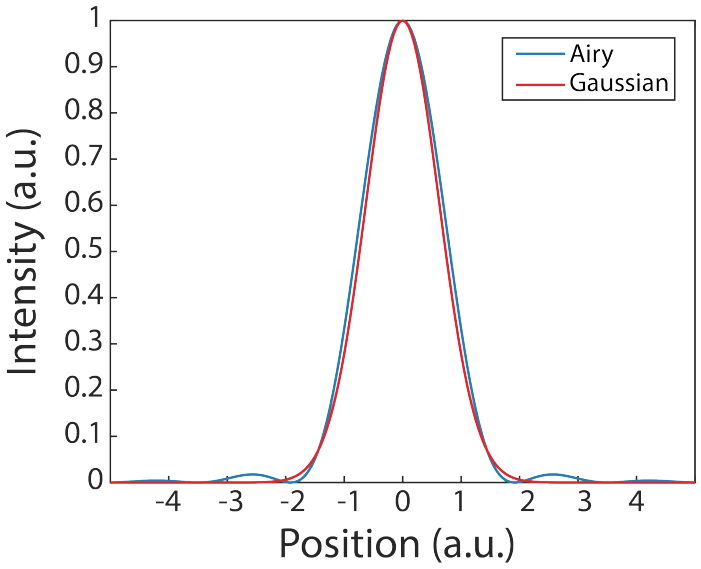

Fig. 1.2 Comparison of Airy Function to Gaussian function. The two curves were matched by equating the integrated area under the central maxima. The Gaussian function was plot with a standard deviation of one unit.

1.2 Fluorescence Microscopy

Fluorescence microscopy is a form of optical microscopy that exploits the phenomena of fluorescence in place of the absorption or reflection of light. Targets within the sample can be labelled with fluorescent probes. Once excited, the fluorescence emission of these probes is collected by an objective lens and projected to form an image in the image plane of the system, allowing for direct visualisation of specific biological components and processes with high contrast in live and fixed cells. These two factors (labelling specificity and compatibility with live-cell imaging) along with its relative ease of use have resulted in fluorescence microscopy becoming wide-spread in research.

The phenomena of fluorescence was first coined in 1852 by Stokes [7] and is described as: the emission of a photon of light when an electron of a molecule relaxes from an excited high-energy state to a lower-energy ground state with a temporal probability well-modelled by an exponential decay and a characteristic lifetime on the order of nanoseconds. In fluorescence microscopy the ground-state electrons of fluorescent probes are excited by absorption of incident photons of specific energy matching the energy gap between ground and excited states. The excited electron nonradiatively relaxes into a lower vibrational-energy excited state before it radiatively relaxes into the ground state, emitting a photon (figure 1.3). As a result, this photon has lower energy than the incident photon and thus has a longer wavelength

(*i.e.* a Stokes shift). This is the key phenomenon enabling fluorescence microscopy, as the fluorescence emission is spectrally separated from the excitation illumination it can be isolated by chromatic filters and imaged onto a detector [8]

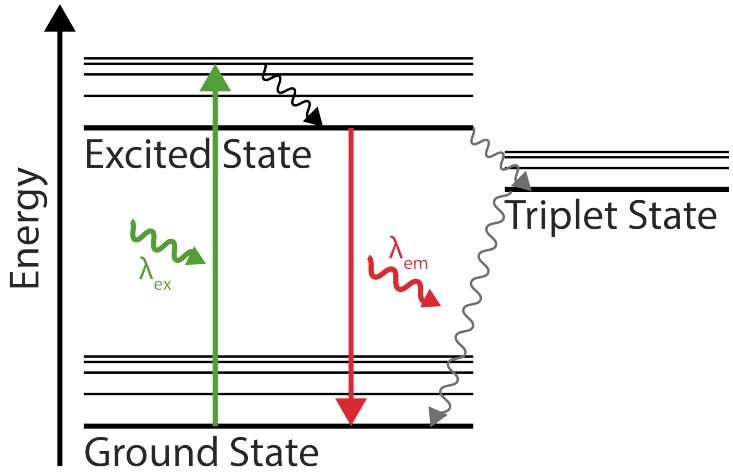

Fig. 1.3 Simplified Jablonski energy diagram of fluorescence absorption and emission. Incident light of wavelength λ_{ex} excites an electron from the ground state to a higher-energy excited state. Non-radiative relaxation occurs before the electron radiatively relaxes back to the ground state, emitting a photon of wavelength λ_{em} where $\lambda_{ex} < \lambda_{em}$. Additional relaxation pathways via a intersystem crossing to a triplet state are also possible.

Fluorescent probes exist in a range of forms including; quantum dots [9], nitrogen-vacancy point defects in nanodiamonds [10], organic dyes and fluorescent proteins. These last two are collectively reffered to as fluorophores. Fluorescent proteins are encoded by the target cell's genome or inserted via plasmids. This has the advantage that the genetic sequence can be introduced into a cell line, so that it is inherited and the fluorescent protein can be stably expressed by all subsequent cells. Organic dyes are fluorescent chemical compounds that are attached to the molecule of interest within the sample. Organic dyes generally emit more photons than fluorescent proteins and are more photo-stable [11] but require additional labelling to the target of interest prior to imaging. This is often achieved via immunostaining, in which an antibody is used to bind a specific antigen within the sample. This antibody is either labelled directly with an organic dye (primary antibody labelling) or is bound by secondary antibodies that are labelled with organic dyes (secondary antibody labelling). Antibodies are $\sim$10 nm [12], adding an additional spatial uncertainty when imaging. As such, primary antibody labelling is generally preferable for high-resolution applications. The specificity and affinity of antibodies varies between systems and their presence can alter function in live-cell experiments, limiting their application in some cases to fixed-cell imaging [13]. Another labelling approach for organic dyes achieves specificity

with bioconjugation systems such as HaloTag [14] or SNAP-Tag [15]. These systems, as well as fluorescent protein labelling, generally facilitate higher-resolution imaging than immunostaining methods due to their reduced size ($\sim$3-5 nm for HaloTag, SNAP-Tag and fluorescent proteins [16, 17]). Bioconjugation is readily compatible with live-cell imaging, providing the organic dye-HaloTag ligand can enter the cell for labelling to occur.

1.3 Super-Resolution Fluorescence Microscopy

While the resolution of conventional fluorescence microscopy is limited by diffraction to $\approx$250 nm, emerging methods known as 'super-resolution' (SR) techniques have been developed to image beyond this limit and improve the spatial resolution of fluorescence microscopy by orders of magnitude [18]. Routinely achieving sub 20 nm resolution, SR techniques have been demonstrated to achieve resolution below 10 nm in both non-biological [19] and biological samples [20]. Unlike other high-resolution imaging techniques, such as electron microscopy and X-ray crystallography, SR imaging can be minimally damaging to biological samples and offers nanoscale information and target-specific labelling in vivo.

SR methods can generally be classified into two classes: deterministic techniques and stochastic techniques. Stochastic SR methods are often referred to as single-molecule localisation microscopy (SMLM).

1.3.1 Deterministic 2D Super-Resolution Techniques

Although the work presented in this thesis does not contain any deterministic SR, an brief introduction is included for completeness. Deterministic SR techniques exploit nonlinear responses to excitation exhibited by fluorophores to reduce the size of the PSF of the imaging system or gain addition spatial information. The first implementation of such a technique was stimulated emission depletion microscopy (STED) [21, 22]. STED uses the phenomenon of stimulated emission, in which photons of a specific energy can interact with excited fluorophores causing their fluorescence to be emitted in the direction of the original photon, away from the objective lens of the microscope. The minimum of a donut-shaped depletion laser spot is aligned with the maximum of a diffraction-limited excitation spot resulting in a sub-diffraction effective excitation PSF (figure 1.4). By increasing the power of the depletion illumination the effective excitation PSF can be made arbitrarily small. The effective PSF is

scanned across the sample to create an intensity-based SR image containing the positions of the fluorophores. A key issue with STED is photodamage to live cell samples related to the use of high-power depletion illumination to confine to effective illumination PSF. Precise alignment of the confocal excitation stop and depletion spot is also required, increasing complexity, although STED microscopes are now commercially available. Unlike SMLM, STED is applicable to most fluorophores [23] as the process of stimulated emission affects all fluorophores.

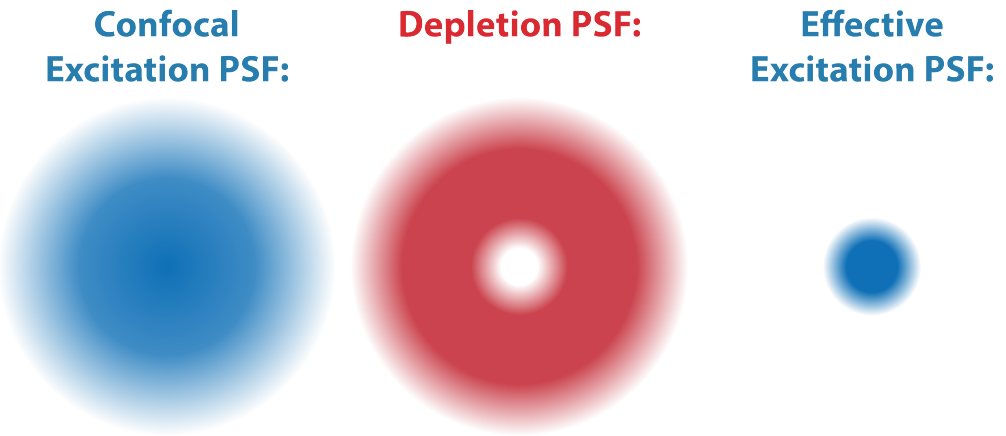

Fig. 1.4 The basic principles of STED illumination. A diffraction-limited confocal excitation PSF is aligned with a donut-shaped depletion PSF, creating a sub-diffraction-limited effective excitation PSF that is scanned across the sample.

A related scanning technique uses reversible saturatable optical linear fluorescence transitions (RESOLFT) [24]. Certain fluorophores, such as Dreiklang fluorescent protein and reversibly switchable enhanced green fluorescent protein (rsEGFP) [25], can be temporarily switched into a non-emissive ‘dark state’ when incident by photons of a certain wavelengths. Inhomogeneous illumination containing isolated zero-intensity regions is used to switch the majority of fluorophores to the dark state. Although the isolated zero-intensity regions display a diffraction-limited FWHM, the area that is below the intensity threshold required to ’switch off’ the fluorophores can be sub-diffraction limit in size. Fluorophores in these sub-intensity regions are not switched into the dark state and are thus emissive when incident by a separate excitation illumination. The zero-intensity points are then scanned across the sample to create an intensity-based SR image. In scanning illumination techniques the acquisition speed depends on the area that is being scanned. Video-rate SR images of small areas have been demonstrated by STED with 80 frames per second for diffusing fluorescent beads [26] and 28 frames per second for live-cell imaging [27].

Structured illumination microscopy (SIM) [28] provides an alternative method to gain sub-diffraction-limited information. In SIM, the sample is illuminated with known spatially structured excitation patterns. The resulting image is the product of the excitation pattern and the distribution of fluorophores within the sample, which contains moiré interference patterns. These moiré interference patterns contain additional high-resolution information about the sample that can be deconvolved to bypass the diffraction limit by a factor two. Three grid illumination patterns, each rotated by 60°, are used to image each sample in order to achieve isotropic lateral resolution of ≈100 nm. As SIM collects three wide-field images as opposed to scanning, it can theoretically operate at 1/3 the rate of conventional fluorescence microscopy and is typically capable of achieving ≈50 ms temporal resolution. Saturated Sim (SSIM) [29], similarly to STED, uses non-linear fluorophore saturation to limit the size of non-illuminated domains of the sample to further increase the resolution.

1.3.2 2D Single-Molecule Localisation Microscopy

In SMLM, the stochastic switching of certain fluorophores is exploited to gain sub-diffraction-limit information on the position of individual fluorophores within the sample. This approach was first demonstrated in 2006 by three independent groups with (fluorescence) photo-activated localisation microscopy ((f)PALM) [30, 31] and stochastic optical reconstruction microscopy (STORM) [32].

In SMLM, the detected PSF of a single emitter is considered as a probability function of its spatial position. Although the PSF is observed to be ≈500 nm in diameter, its centre position can be determined with greater precision, representing the statistically most likely position of the spatially isolated emitter. By fitting the intensity distribution of a PSF to a 2D Gaussian (equation 1.2) (or by find its centre of mass), the position of fluorophores within the sample can be localised with precision beyond the diffraction limit. In general, for individual PSFs to be localised they need to satisfy the Rayleigh criterion (although high-density localisation techniques such as DAOSTORM [33] have been shown to surpass this limitation at the cost of localisation precision). In most practical cases, if fluorophores within the sample are too dense and their PSFs overlap they cannot be localised. The key step in (f)PALM and STORM is separating the emission of overlapping fluorophores in time so that they no longer overlap in space. Another way to look at SMLM is sacrificing temporal information for spatial information. This is achieved in a variety of ways but the underlying concept involves modulating the emissive state of a subset of fluorophores, localising their isolated PSFs and then 'turning off' their fluorescence before repeating the process for a

new subset. Over time a SR map of the position of the fluorophores within the sample is produced (figure 1.5). The process that determines the emissive subset depends on the SMLM technique in question.

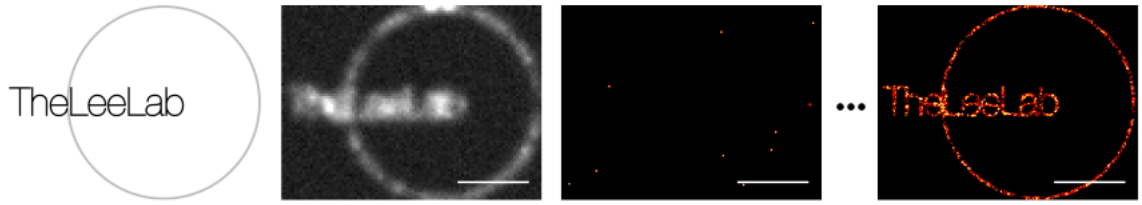

Fig. 1.5 Cartoon of the basic principles of SMLM. Far left: The Lee Lab logo is labelled with fluorescent probes. Centre-left: simulated diffraction-limited image observed when all fluorescent probes are simultaneously emitting. Centre-right: a subset of probes emitting so that their PSFs are separated and can be localised. Far right: after the localisation of numerous subsets, a super-resolved image is formed. High-resolution detail obscured in the diffraction-limited image can now be determined. Scale bars are 3 μm.

PALM and fPALM use photoactivatable fluorophores whose absorption and emission spectra are modified upon the absorption of a photon of specific wavelength. Initially non-emissive fluorophores are stochastically excited into an emissive state by illumination by an ultraviolet activation laser. The power of the activation illumination is tuned so that a small subset of the total fluorophores are emissive and their PSFs do no not overlap. PALM was initially demonstrated using the fluorescent protein Eos [30] and fPALM was demonstrated using photoactivatable green fluorescent protein (PA-GFP) [31]. Recent developments in fluorophore design have produced a range of photoactivatable fluorescent proteins and organic dyes that emit more photons and exhibit greater photo-stability [34].

STORM takes advantage of the non-emissive states exhibited by some fluorophores upon excitation illumination in specific buffer conditions. Initially emissive fluorophores are stochastically switched into a non-emissive state by the excitation laser. The fluorophores remain in the non-emissive state until they are returned to their emissive state, usually by illumination of a different colour. This was first demonstrated with a pair of Cy3 and Cy5 dyes in the presence of a primary thiol, that were shown to cycle hundreds of times before permanent photobleaching occurred [32]. The ability to localise each fluorophore multiple times increases the sampling density of the final image but can lead to counting artefacts when attempting to determine stoichiometry. Additional chemical modification methods have been developed to encourage desired effects in certain fluorophores such as increased

blinking of Cy5 fluorescent dye [35], reduce blinking of Cy5 [36] or photoactivatibility of Alexa Fluor 647 fluorescent dye [37].

Another method facilitating SMLM is points accumulation for imaging in nanoscale topology (PAINT) [38]. In PAINT, a reservoir of target-specific imaging probes (which can be a fluorophore itself, or a moiety with affinity for the target attached to a fluorophore [39]) is maintained in the imaging buffer of the sample. The imaging probe binds to the target of interest within the sample (either transiently or permanently). When unbound, fast-Brownian motion blurs the probe's emission so that it does not form a narrow PSF and it is not localised. When bound, the probe's emission forms a narrow PSF and its position can be localised. By controlling the concentration of imaging probe in the buffer, the density of PSFs can be tuned so that they no longer overlap.

PALM, STORM and PAINT methods of isolating the emission of single-molecules are discussed in further detail in chapter 2.

One of the first biological applications of SMLM techniques was PALM imaging the transmembrane protein CD63 tagged with the photoactivatable fluorescent protein Kaede in COS-7 cells (a monkey kidney-derived cell line) [30]. Since then many biological systems have been investigated by SMLM, with cytoskeletal networks making up some of the most commonly presented examples [40–42] due to their well-defined structure, diffraction-limited width and proximity to the coverslip surface. SMLM techniques have been pioneered in bacteria due to their small size, which generally fits within TIRF illumination volumes. This work has been concentrated on bacterial cell division and DNA replication [43]. The increased spatial resolution compared to traditional fluorescence microscopy has elucidated protein distributions within bacterial cells, such as the HU regulatory protein and chromosome segregation apparatus in *Caulobacter crescentus* [44, 45]. Other applications of SMLM include; determining the mechanism by which fluorescently-labelled Poliovirus particles enter live cells [46], imaging synapse morphology and the relative position of synaptic proteins within individual synapses in mouse brains [47], visualising the eightfold symmetry and central channel of the nuclear pore complex [48] and documenting the role of clathrin in spatially directing membrane invaginations during endocytosis [49]. The fluorophore Nile Red was demonstrated to transiently bind within lipid bilayers [50], enabling PAINT imaging of the plasma membrane in neuronal-like cells [51]. Additionally, 2D-SMLM (particularly PALM) has facilitated quantitative analysis in range of studies, including quantifying the clustering state of T-cell membrane proteins at the coverslip surface [52], the stoichiometry of the asialogycoprotein receptor complex in rat hepatic lectin [53] and G protein-coupled

receptors in HeLa cells [54] as well as revealing that CENP-A is deposited during G2 phase of the cell cycle in fission yeast [55].

Unlike excitation-scanning techniques, most SMLM techniques are compatible with wide-field excitation illumination although, in order to increase the signal-to-noise ratio (SNR), excitation confinement techniques are often employed. The most commonly implemented excitation confinement techniques are total internal reflection fluorescence illumination (TIRF) [56, 57], highly inclined and laminated optical sheet illumination (HILO) [58]/variable-angle epifluorescence microscopy (VAEM) [59] and single-plane illumination (SPI) [60, 61]. These techniques are discussed in detail in chapter 2.

1.3.3 SMLM-Facilitating Fluorophores

PSF isolation in PALM and STORM is primarily facilitated by the photomodulatable properties of certain fluorophores. The first examples of this were the fluorescent proteins PA-GFP [62], which was modified from wildtype GFP, and Kaede, which was isolated from Trachyphyllia geoffroyi coral. Two years later, Eos photoactivatable fluorescent protein was isolated from Lobophyllia hemprichii coral [63]. The absorption peak of Eos is primarily at 506 nm but is shifted to 571 nm upon ultraviolet illumination (photoconversion peak at 390 nm) due to a photo-induced break in the peptide backbone [64]. Wildtype Eos displays a higher quantum efficiency than other fluorescent proteins but exists in a tetrameric state in solution, which is undesirable for a fluorescent tag as this can lead to mislocalisation and destabilisation of the labelled protein. A number of variants of Eos have since been engineered to produce monomeric PALM probes. Monomeric-Eos2 (mEos2) [34] was first developed, maintaining the optical properties of Eos and displaying an activation efficiency (the fraction of fluorophores that can convert to the emissive state) of 0.6 [65]. However, it was later demonstrated that mEos2 still formed oligomers in solution, motivating the development of mEos3.2 [66]. mEos3.2 is monomeric in solution although its activation efficiency is reduced to 0.4 [65]. Both mEos2 and mEos3.2 exhibit short-lived fluorescence intermittency upon activation [67]. This is observed as ‘blinking’ of individual molecules in SMLM and can lead to over-counting artefacts in quantification studies. mEos3.2 is the PALM fluorophore of choice in this work as it facilitates high SNR imaging with minimal affect on the functionality of the target, that may arise due to aggregation, compared to other photoactivatable fluorescent proteins.

Photoactivatable organic dyes have also been developed, exhibiting greater quantum efficiency and photo-stability compared to photoactivatable fluorescent proteins. Caged rhodamine dyes that exhibit irreversible photoactivation under ultraviolet illumination, have been developed for a range of excitation wavelengths and display an activation efficiency of 60-90% [68]. Photoactivatable Janelia Fluor (PA-JF) dyes are a rhodamine derived range of fluorophores that initially adopt a closed, non-fluorescent conformation. Ultraviolet illumination of these dyes causes a photo-induced ring opening reaction to form a fluorescent rhodamine scaffold [69]. PA-JF fluorophores report an activation efficiency of up to 50% in solution, which can be increased depending on its environment, and display low fluorescence intermittency, with each fluorophore exhibiting a mean of 1.4 fluorescence events [69]. The activation efficiency of PA-JF549 and PA-JF646 is increased to ≈90% and 76% when bound to a HaloTag respectively [69], making these fluorophores ideal for counting applications providing they can be attached to a HaloTag.

Although STORM was initially achieved with a pair of organic dyes, direct STORM (dSTORM) [41] achieves photomodulation of conventional organic dyes by the presence of reducing agents in the imaging buffer. After a fluorophore is excited to a higher energy state from the ground state, rather than radiative relaxation, non-radiative intersystem crossing into a longer-lived triplet state can occur (see figure 1.3). In the presence of reducing agents electron transfer can then occur to create a stable radical anion that represents a nonfluorescent state. Upon reaction with oxygen or illumination by ultraviolet light the fluorophore can be returned to its emissive state as the electron is returned to the ground state [70]. STORM modulation can be achieved with a range of fluorophores, each requiring bespoke buffer conditions that should be optimised on an experimental basis for ideal imaging conditions.

PAINT imaging does not require photomodulatable fluorophores as the separation of PSFs is achieved by blurring of unbound fluorophores. As such, standard imaging buffer conditions can be used with a wide range of fluorophores. In order to reduce background signal and maintain bound-fluorophore emission, fluorophore modulation by Forster resonance energy transfer (FRET) has been implemented in PAINT imaging [71, 72], achieving a ≈30-fold increase in localisation acquisition speed compared to traditional fluorophore PAINT. The use of photoactivatable fluorophores in combination with SPI techniques could potentially also be used to increase SNR in PAINT experiments, as discussed further in chapter 6.

1.3.4 Fast SMLM

A key limitation of SMLM compared to deterministic SR techniques is the increased time required to collect datasets. Typically thousands to hundreds of thousands of images of the sample must be recorded so that enough fluorescence events are observed to sufficiently resolve the structure of interest. The number of images required can be reduced by increasing the density of emitting fluorophores, however, ultimately the temporal resolution of traditional SMLM is limited by the Rayleigh criterion. This can be disadvantageous when imaging dynamic processes as the system is often changing faster than it can be imaged.

A number of analysis approaches have been developed to localise individual fluorophores without the need for isolated PSFs. In super-resolution optical fluctuation imaging (SOFI) [73], the integral of the second-order correlation function of each pixels intensity fluctuation in time gives a SOFI intensity to each pixel which is proportional to the squared PSF, increasing the resolution of the imaging system by a factor of $\sqrt{2}$. Deconvolution-STORM (deconSTORM) [74] analyses involves iterative deconvolutions of the raw dataset to estimate the sample. Bayesian analysis of blinking and bleaching (3B) [75] was also developed to resolve overlapping emitters by modelling the dataset as being generated by a number of fluorophores. 3B has been shown to facilitate 50 nm resolution imaging of podosome formation with $\approx$4 s temporal resolution [75].

Super-resolution radial fluctuations (SRRF) [76] is an analytical approach that enables super-resolution images to be produced from dense SMLM data and bulk labelling fluorescence imaging without fluorophore localisation. Gradient fields are computed from fluorescence intensity data and used to identify local convergence. SRRF is capable of distinguishing PSFs separated by $\approx$0,7 times their FWHM. Similar to SOFI, deconSTORM and 3B, temporal analysis is applied to further enhance resolution and so create SR reconstructions from multiple imaging frames. A resolution of $\approx$1 frame per second was achieved in live-cell imaging with a resolution of 60-120 nm.

1.3.5 Quantification in SMLM

A key advantage of SMLM compared to deterministic SR techniques is the ability to easily quantitatively analyse localisation data. It is possible to quantify deterministic datasets produced by methods such as STED and SIM. However, due to the visual nature of the output, complicated image processing is often required. In SMLM, the primary output is a

list of coordinates corresponding to the position of fluorophores within the sample. These can be used to reconstruct a SR image of the sample but are also directly compatible with a range of quantitative analysis metrics. The most common of these approaches are discussed in detail later in this chapter for both 2D and 3D-SMLM.

A disadvantage of SR images created by SMLM compared to deterministic methods is a non-trivial relation between sampling density and resolution. Unlike intensity-based images (as created by STED, SIM etc), where resolution is well defined and labelling density is typically not a limiting factor, in SMLM it is the localisation uncertainty that is well defined. The resolution of the reconstructed image is a combination of this uncertainty and the recorded sampling density. The Nyquist criterion defines the smallest feature that can be reliably resolved by coordinate-based data is given by twice the mean point-to-point distance [77]. Thus, the smallest resolvable feature size is:

$$\Delta_{Nyquist} = \frac{2}{N^{1/D}} \tag{1.4}$$

Where N is the labelling density and D is the dimension of the structure of interest. This formula predicts that 10^4 points per μm^2 are required to achieve 20 nm resolution in 2D. However, in practice fewer points are often sufficient depending on the sample geometry [18]. Other factors that affect reconstruction resolution relate to labelling inhomogeneity within biological samples (*e.g.* membrane labelling may be expected to be homogenous but clathrin-coated pits comprise a minute fraction of the overall membrane and thus high-density labelling would still result in a low overall labelling density) and labelling probe size (*e.g.* antibodies are $\approx$10-15 nm in size, which is comparable to SMLM localisation precision). Although methods such as Fourier ring correlation (FRC) [78], attempt to quantify resolution, its definition remains a contentious topic within the SMLM field [79, 80]. Resolution in 3D-SMLM can be defined by Fourier shell correlation (FSC) [81, 82]. However, the measured FSC resolution can vary between regions within the sample, with high-frequency content appearing to have a higher resolution even at the same localisation uncertainty and sampling density [83]. In the words of Dong Li and Eric Betzig: "Supreme Court Justice Potter Stewart famously stated in a case on the limits of free speech that he couldn't define hardcore pornography, but "I know it when I see it." We feel similarly about resolution." [80]. It is my opinion that resolution is rarely a useful metric for comparison in SMLM as it is greatly affected by localisation precision, labelling density and homogeneity as well as the underlying structure of the sample, making a direct comparison almost impossible.

1.3.6 SMLM PSF Fitting

In all 2D-SMLM the intensity distribution of PSFs from isolated emitters are fit with Gaussian functions to determine their centre position (figure 1.6). The choice of fitting method depends on the amount known about the form of the PSF and noise as well as time and computational expense. The computation required to fit 2D functions to data increases exponentially as the number of independent fit parameters increases. The 2D Gaussian function described in equation 1.2 has up to six parameters that can be fitted (x and y position of its centre, x and y widths, amplitude and background offset). However, prior knowledge of the system can be used to reduce the number of parameters that must be fit. For example, if the standard circularly symmetric 2D PSF is being imaged the x and y widths collapse into a single parameter. Additionally, the emission wavelength of the fluorophore can be used to estimate this width, further reducing fitting costs. Depending on the amount of information required, the amplitude and background offset can also be fixed leaving only the minimum parameters of x and y positions to fit. However, this prevents post-filtering of correct fits based on improbable values of these parameters.

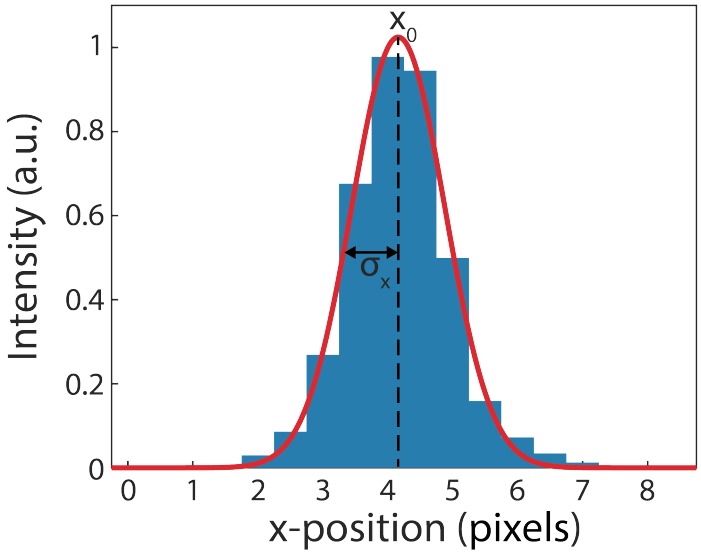

Fig. 1.6 Gaussian function fitting to isolated PSFs. An experimentally recorded PSF at 580 nm was fit to a 1D Gaussian function in MATLAB.

The two most commonly used fitting methods are least-squares criterion (LS) and maximum-likelihood estimation (MLE). In LS fitting, the squared difference between a PSF predicted by estimated parameters (a Gaussian function in most SMLM) is compared to the observed PSF for each pixel. The sum of these squared errors is minimised by varying the fit parameters. MLE fitting requires a model of the PSF and camera noise. The likelihood

of obtaining the observed PSF from the model given some initial estimated parameters is computed and maximised by varying the fit parameters. MLE provides the highest precision compared to LS at increased computational expense [84]. Due to MLE requiring detailed information on the noise present (which varies between detectors), LS is still commonly used.

The centre point of a PSF can be determined arbitrarily precisely in the absence of noise, given an unlimited number of detected photons [85]. In practice, however, fluorophores emit a relatively small number of photons and sample background is not negligible in SMLM experiments. Ultra-sensitive detectors are required to detect the signal. In addition to sample-related noise, sources of noise such as shot noise and dark current present in the detection equipment become significant. Shot noise is present in all electronic devices and is a product of random fluctuations of electric current in electronic conductors. This is due to the quantum nature of electric current in the form of electrons. Shot noise is proportional to the square root of the photocurrent from the detector, such that it becomes significant at low detection intensities, ultimately limiting detector sensitivity. Dark current noise occurs in light-sensitive devices. A small signal is emitted by the device even in the absence of illumination, mostly due to thermal vibrations in the photodetector. Dark current is minimised by cooling the detecting element within the device to reduce thermal vibrations. In modern EMCCDs the photodetector is cooled to <-70°C so that the dark current becomes comparable to shot noise.

1.4 3D Super-Resolution Fluorescence Microscopy

The vast majority of biological structures and processes occur in three dimensions and are not necessarily well-represented by two-dimensional information. 2D SR techniques collapse a 3D volume into a 2D projection. This can lead to erroneous conclusions being made that can compromise scientific understanding. This is especially true for quantitative studies where 3D structure can result in the observation of increased localisation density within homogenous distributions that can lead to clustering artefacts (figure 1.7).

The extension of SR methods to 3D solves this problem by measuring sub-diffraction limit axial information within the sample. As with 2D SR techniques, 3D SR has been achieved in a variety of ways (all with the inevitable cost of increased experimental complexity) that can be fitted into the same classifications of deterministic methods and SMLM methods.

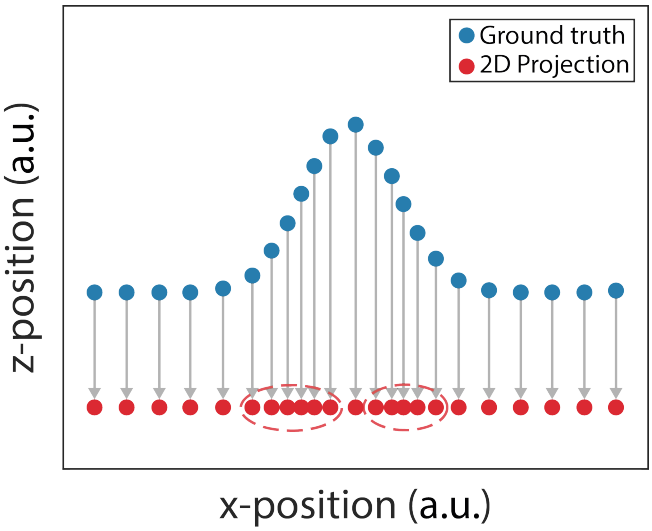

Fig. 1.7 Illustration of artefacts created by 2D imaging of 3D systems. A 3D distribution of homogeneous surface density (blue) and its 2D projection (red) is shown from the side. The 2D projection does not report a homogeneous density but instead perceives high-density regions (dashed-red areas) corresponding to changes in axial position that could be misinterpreted as clustering.

1.4.1 Deterministic 3D SR Methods

Deterministic 3D SR techniques often involve scanning excitation illumination axially though the sample. By confining the illumination volume axially to be smaller than the diffraction limit, SR information can be achieved in three dimensions. In 3D-STED, the illumination PSF can be reduced in size laterally as well as axially [19, 86]. The resulting effective PSF is now scanned in three dimensions to create a SR image of the volume of interest.

Wide-field single-plane illumination microscopy (SPIM) has also been demonstrated to achieve excitation confinement below the diffraction limit, enabling SR optical sectioning across the sample. Bessel beam plane illumination has been shown to obtain ≈300 nm isotropic wide-field resolution by scanning for whole-cell SR imaging in live samples [87]. More recently, the principles of SIM have been extended to excitation confinement in lattice light-sheet microscopy [88], employing a 2D lattice of ultra-thin illumination to scan whole-cell volumes. With this approach, fast imaging with 150 nm and 280 nm lateral and axial resolution and low photo-toxicity was achieved [89]. Further SPIM techniques are discussed in more detail in chapter 2.

As with deterministic 2D SR methods, deterministic 3D methods benefit from a fast acquisition rate compared to SMLM techniques. Optical-sectioning techniques are generally

limited in resolution compared to SMLM although 3D-STED offers comparable resolution with the use of potentially photo-toxic illumination powers.

1.4.2 3D Single-Molecule Localisation Microscopy

Within the category of 3D-SMLM, the method in which axial information is gained from the PSF of an isolated emitter can be split into two categories: 1) inferring axial position from multiple image planes and 2) PSF engineering, which are both capable of achieving ≈10 nm lateral localisation precision and ≈20 nm axial localisation precision [90]. In either case, axial information is gained at the detriment of other factors. Additional optical components reduce transmission efficiency and thus can limit sensitivity in low SNR samples. The 2D PSF is often spread over a larger area, reducing peak intensity and requiring a reduction in labelling density. Resolution is also reduced as, according to equation 1.4, a 100-fold greater number of localisations is required compared to 2D-SMLM to achieve Nyquist sampling.

Biplane [91] is a method for 3D-SMLM in which the sample is imaged simultaneously in two axial planes. The two focal planes are offset relative to each other so that a single PSF can be imaged in both. The intensity and defocus of the PSF is compared between the two planes in order to determine the axial position (figure 1.8a). To achieve this with a single objective lens, the emission signal is passed through a 50:50 beam splitter with both channels incident onto separate detector or separate areas of the same detector. The two emission paths are of different length so that they are focussed onto the detector with a constant axial offset within the sample. The depth of focus achieved by Biplane is limited by the axial size of the 2D PSF to ≈500 nm. While Biplane techniques are relatively easy to implement, requiring few additional optical components, they exhibit non-uniformity in localisation precision across their focal plane [92] and halve the detected signal, resulting in a lower lateral precision compared to 2D-SMLM. If a single detector is used, the field of view is reduced in half to accommodate the two images.

The two focal planes of Biplane SMLM have been extended upon in multifocus microscopy (MFM) [93], which simultaneously images nine axial planes within the sample. A multifocus grating is used in combination with a chromatic-correction grating and a prism to split the emission signal into nine distinct areas on a single detector, each with a focal offset of 380 nm so that the overall depth of focus is extended to ≈4 μm. As in Biplane, the emission signal is reduced as the photons comprising a single PSF are split into multiple

images while the transmission efficiency of the multifocal grating (≈65%) further reduces SNR.

One of the most technically complex and most precise 3D-SMLM technique is interferometric PALM (iPALM) [94]. iPALM combines two high-NA objective lenses to acquire additional spatial information. The emission collected by both lenses is passed through a three-way beam-splitter so that it creates interference patterns on three separate detectors as a function of the sources axial position. The intensity of a single PSF is compared between the three detectors in order to determine the axial position with greater precision than lateral precision. iPALM has been demonstrated to achieve a localisation precision of 9.5 nm laterally and 4.1 nm axially for 1,200 photons detected from gold beads across a ≈600 nm depth of focus [94]. As three detectors are used to image each PSF, iPALM does not suffer from the same axial variation in localisation precision as Biplane, achieving a more-flat profile across the depth of field [94].

The most common form of 3D SMLM is Astigmatism. Astigmatism [95] is an example of PSF engineering to gain axial information in SMLM. A cylindrical lens placed in the emission path creates two slightly axially offset planes for the x and y axis. This manifests itself as a change in ellipticity and orientation of the PSF depending on its axial position relative to the focal planes (figure 1.8b). When an emitter is positioned equidistance between the x and y focal planes, its PSF appears symmetrical. As the emitter moves towards one of the two focal planes its PSF contracts in that dimension and expands in the other, creating an ellipse. Due to a non-linear relation between axial position from a focal plane and PSF width, the position of emitters can be localised outside of the two focal planes. The astigmatic PSF is fit with a 2D Gaussian function that is not constrained to be symmetrical so that the ellipticity and orientation are extracted to determine the axial position across a ≈500 nm depth of focus. Like Biplane, astigmatism is simple to implement, as just one additional lens is added to the emission path. However, it suffers from non-uniformity in localisation precision across the focal depth [92]. This is due to the non-linear relation between axial position from a focal plane and PSF width; the width of the PSF changes more slowly close to the focal plane compared to further away from it. Astigmatism does not spread out the 2D PSF as much as other 3D-SMLM techniques and as a consequence, the SNRs are comparable to 2D-SMLM allowing for challenging samples to be imaged.

Another 3D-SMLM technique is the double-helix point-spread function. As this technique is the basis of the experimental work presented in this thesis it is discussed in detail in the next section.

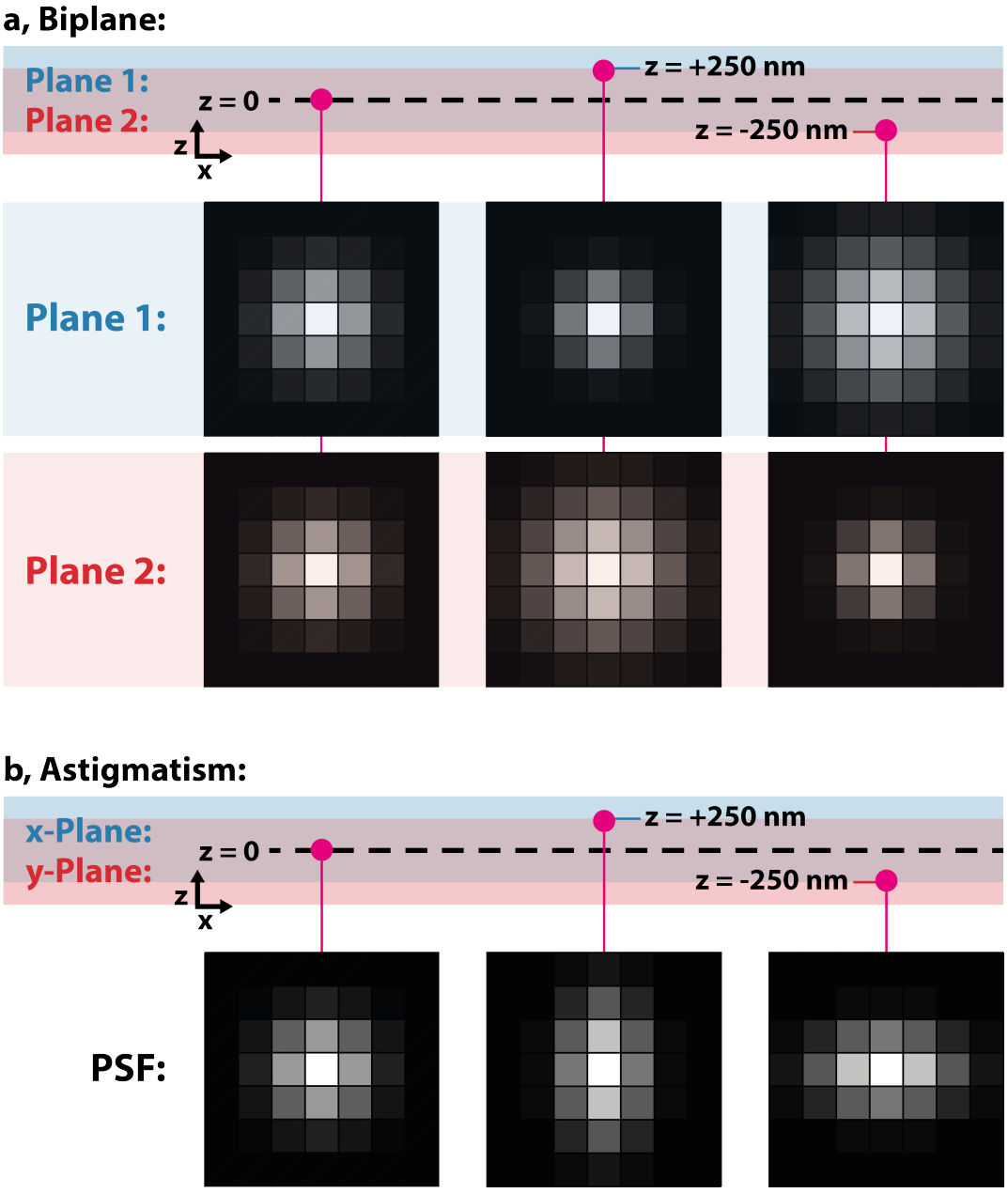

Fig. 1.8 Simulated detected PSFs for isolated emitters in the centre of the depth of focus (left), 250 nm above (middle) and 250 nm below (right) for biplane (a) and astigmatism (b) methods of 3D-SMLM.

1.5 The Double-Helix Point-Spread Function

The double-helix point-spread function (DHPSF) is another example of PSF engineering to gain axial information from a 2D PSF. The ability to encode depth into the rotation of a PSF was first demonstrated in 2006 [96] and was applied to single-molecule detection in the form of the DHPSF by tracking fluorescent microspheres in 2008 [97, 98] and single fluorophores in polymer samples in 2009 [99]. The first live-cell single-particle tracking implementation of the DHPSF was exhibited in 2010, tracking endocytosed quantum dots at the bottom surface of COLO205 cells [100] and mRNA, each tagged with 32 EGFP molecules, in *Saccharomyces cerevisiae* yeast cells [101]. Since then, the DHPSF has been used to track chromosome loci in *Saccharomyces cerevisiae* yeast [102]. The DHPSF was first demonstrated for use with PALM in 2011 at the basal surface of PtK1 cells expressing PA-GFP-tubulin that were imaged in 90% glycerol with an oil-immersion objective lens [103]. Sequential multi-target imaging was presented in 2011, resolving both the outer surface and intracellular protein structure in *Caulobacter crescentus* by a combination of super-resolution by power-dependent active intermittency (SPRAI) and PAINT imaging methods using eYFP and Nile Red fluorophores [104]. This was expanded in 2013 with multicolour imaging of eYFP, Nile Red and PAmCherry1 was demonstrated in *Caulobacter crescentus* [105]. Proof-of-concept STORM imaging in mammalian cells was presented of microtubules labelled with Alexa Fluor 647 at the basal $\sim$1 μm of BSC-1 cells in 2012 [106]. The DHPSF was first implemented with SPIM in 2014, demonstrating increased SNR when imaging fluorescent bead samples [107]. This work was extended to mammalian cell imaging with tilted light sheet illumination in 2018 [108]. A timeline listing key milestones in the development of the DHPSF, including the work presented in this thesis, is presented in figure 1.9.

The DHPSF is created by transforming the conventional 2D PSF so that its intensity distributions rotate as they propagate along the optical axis (figure 1.10). This is physically implemented by placing a specially designed phase mask (described in detail in reference [103] into the Fourier plane of a $4f$ system added into the emission path. This introduces a phase shift in the Fourier domain of the imaged PSF so that, when the emission is transformed back to the spatial domain, the conventional Airy disk of the 2D PSF is split into lobes that rotate around a midpoint corresponding to the centre of the original PSF. The angle between the two lobes linearly relates to the axial position of the emitter within the focal depth (see figure 1.10). The two lobes are fit with Gaussian functions and localised as in 2D-SMLM to precisely determine their midpoint and angle. The DHPSF can achieve a more uniform

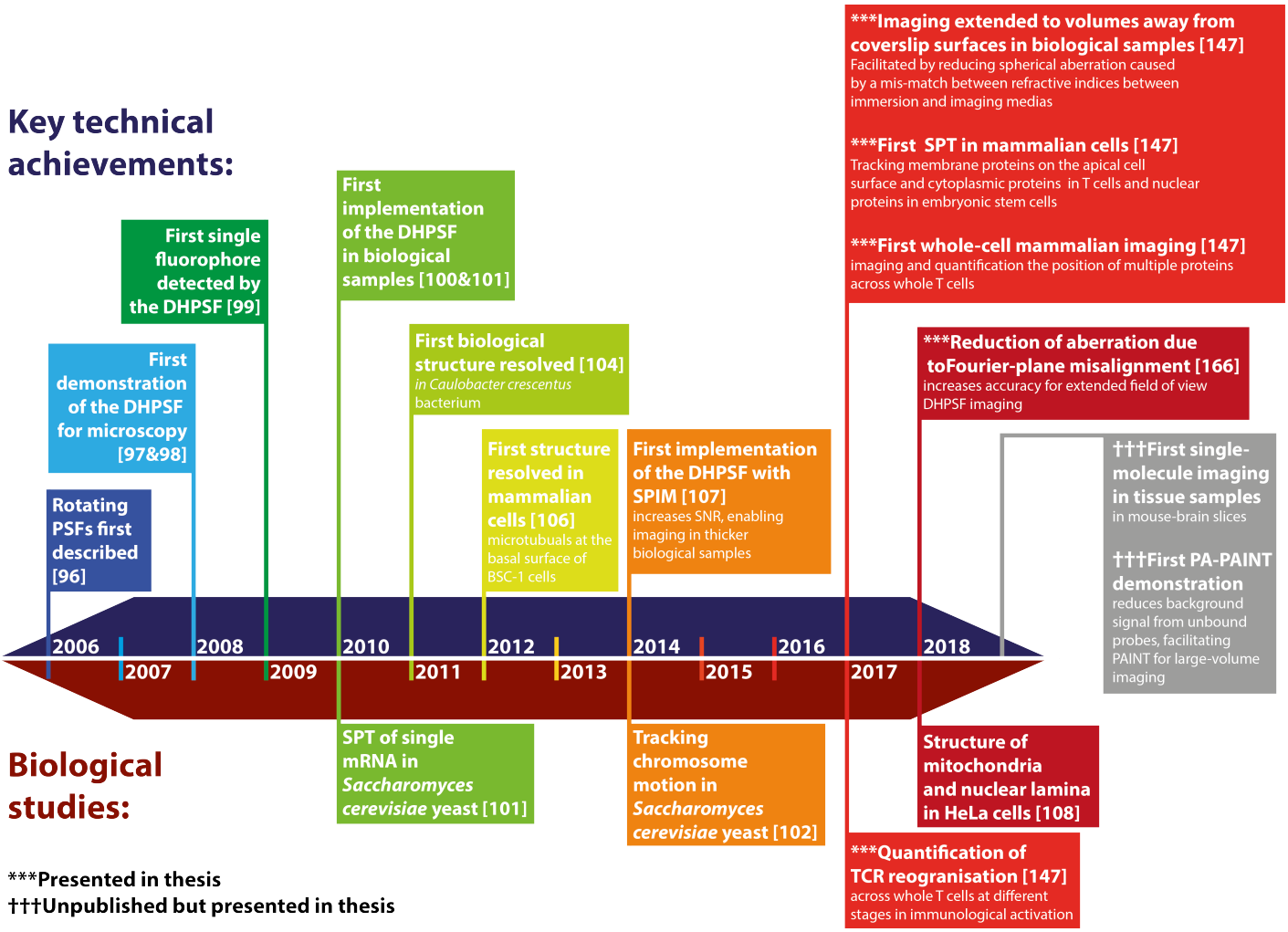

Fig. 1.9 Timeline of key milestones in the development of the DHPSF. Technical achievements are listed above the timeline and biological studies are listed below the timeline. The published and unpublished work presented in this thesis is denoted by asterisks and crosses respectively.

localisation precision of ≈10 nm laterally and ≈20 nm axially (see chapter 2) across a ≈4 μm depth of focus.

When using the DHPSF, the lateral localisation precision is reduced compared to the analogous 2D experiment as the photons collected from each emitter are split in two separate spots that are localised. Each emitter now has two lateral localisation errors associated with its position and contains half the number of photons, reducing SNR by at least a factor two. A statistical comparison of the Fisher information (a measure of the amount of information a variable holds about a parameter that affects its distribution, in this case the parameter is axial position) of biplane, astigmatism and the DHPSF 3D-SMLM techniques was conducted

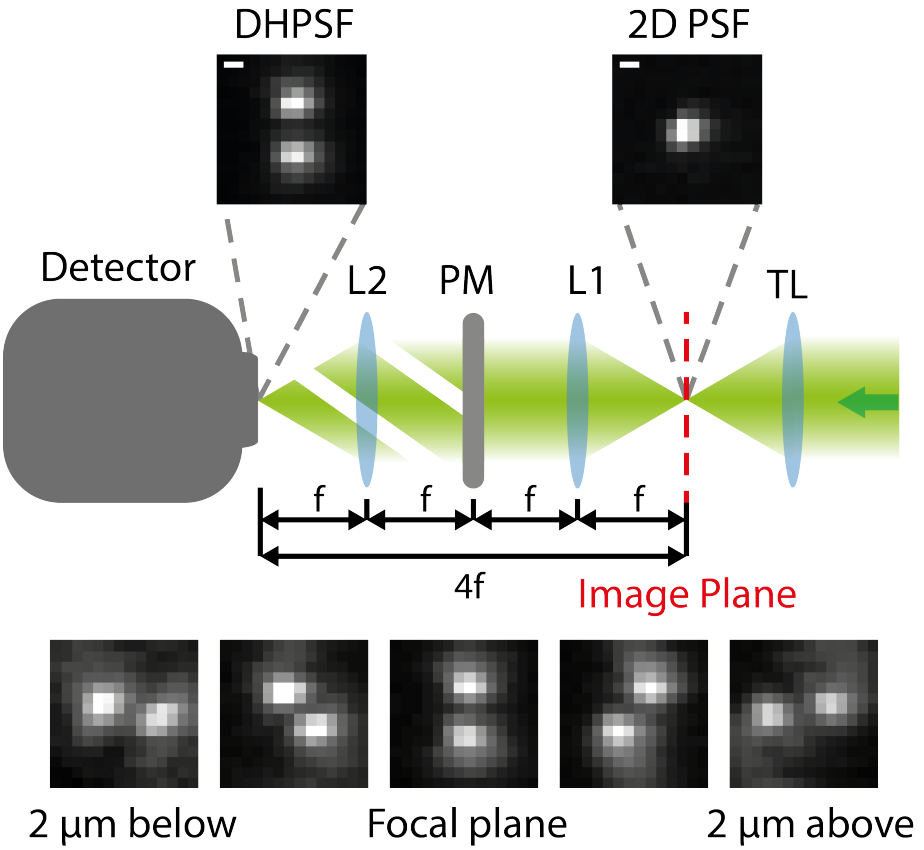

Fig. 1.10 The form and implementation of the DHPSF. The DHPSF can be implemented by the addition of a $4f$ system comprised of two lenses (L1 & L2) into the emission path of a fluorescence microscope with a DHPSF phase mask (PM) placed in the Fourier plane of the $4f$ system. The focal plane of L1 is placed in the image plane of the microscope (defined by the tube lens, TL), relaying the fluorescence image onto a detector placed a distance 4f away. Experimentally recorded example DHPSFs are shown across the ≈4 μm depth of focus.

by Badieirostami *et al.* [92]. The study found that the DHPSF provides the most constant lateral and axial precision across the depth of field. While Biplane and astigmatism exhibit a greater peak localisation precision near the centre of the focal depth in all dimensions, for high detected photon numbers (≈6,000), the DHPSF provides a greater average localisation precision across the focal volume. For low detected photons (≈1,000) Biplane provides a marginally greater average precision to the DHPSF.

1.5.1 PSF Engineering

The axial position of an emitter within the focal plane of an objective lens can be encoded into the form of the PSF by phase modulation in the Fourier domain of the emission. Placing a patterned phase mask in a plane conjugate to the back focal plane of the objective (*e.g.* the Fourier plane of a $4f$ system relaying the image plane) introduces phase aberration that can be used to reengineer the 2D PSF. The electromagnetic field in the image plane is related to that of the back focal plane by:

$$I(u,v;z,y,z) \propto \left| F\left\{ E(x',y';x,y,z) \cdot P(x',y') \right\} \right|^2 \tag{1.5}$$

Where $F\{a\}$ denotes the Fourier transform of a, $E(x',y';x,y,z)$ is the electromagnetic field at the back focal plane caused by a point source at (x,y,z) and $P(x',y')$ is the phase modulation imposed in the Fourier plane [83].

A translation of the point source in z manifests itself as a curvature of in the phase of $E(x',y')$ and $P(x',y')$ determines how this affects the image $I(u,v)$. This curvature can be approximated by [83]:

$$E(x',y';z) \propto e^A \tag{1.6}$$

Where A is given by:

$$-ikn_{im}z_{im}\sqrt{1-(NA/n_{im}\sqrt{x'^2+y'^2})^2} + ikn_s z\sqrt{1-(NA/n_s\sqrt{x'^2+y'^2})^2} \tag{1.7}$$

Where k is the wavenumber of the emission, $n_{im,s}$ is the refractive index of the glass coverslip and sample respectively, z_{im} is the position of the focal plane above the coverslip interface, NA is the numerical aperture of the objective lens and z is the axial position of the point source emitter [83].

Phase patterns, $P(x',y')$, are wavelength dependent and are designed to encode axial information into $I(u,v;x,y,z)$ by modulating the effect of curvature in $E(x',y';z)$. They can be implemented via programmable deformable mirrors (DM), lithographically etched phase

masks or spatial light modulators (SLM). DMs and SLMs have the advantage that they can be reprogrammed to dynamically change the PSF. However, DMs are limited in their resolution by the number of actuators, limiting the effectiveness of the phase pattern. SLMs are more accurately programmable but typically only work on a single polarisation of light, reducing signal by a factor two. Phase masks on the other hand offer high transmission efficiency and pattern resolution but cannot be re-patterned.

1.5.2 Alternative Phase Patterns to the DHPSF for Determining Axial Position

A variety of phase patterns (defining $P(x', y')$) have been designed to emphasize the phase curvature so that axial information can be determined. In addition to the DHPSF, the corkscrew PSF [109] employs a single rotating lobe while the self-bending PSF [110] displaces laterally as a function of axial position. These PSFs extend the depth of focus compared to the DHPSF at the cost of imaging each PSF twice with two complementary phase patterns to determine its centre position. The phase-ramp PSF [111] creates a similar PSF to the DHPSF with a simplified phase pattern at the cost of localisation precision and focal depth. Large axial range PSFs have been mathematically designed by maximising a function of the Fisher information [112], tailoring the form of the PSF to the axial size of the system and its background levels. These so called Tetrapod PSFs [113] have been demonstrated to have an axial range of $\approx$20 μm to achieve $\approx$30 nm lateral localisation precision and $\approx$50 nm axial localisation precision in high-background situations.

1.6 Quantification in SMLM

As previously mentioned, the primary output of SMLM techniques is a list of coordinates corresponding to the position of fluorophores within the sample. This output is readily compatible with quantitative analysis and can be easily imported into programming languages. While images (created by either deterministic methods or by the reconstruction of SMLM datasets) can be used to answer broad questions (*e.g.* if a certain protein is found in the nucleus of a cell or not), quantification allows for more subtle observations as well as direct comparisons to be made (*e.g.* changes in the fraction of a certain protein found inside the nucleus under different conditions). This can provide a powerful tool for probing

biological systems, which often display innate variability, providing the correct metrics are identified and adequate controls are considered. SMLM quantification methods are often bespoke depending on the system of interest. This is especially true for 3D-SMLM as there are fewer standardised analysis tools available. In these cases it is important to test the performance of the analysis on idealised simulated data sets to ensure that the output is correctly interpreted. SMLM (and 3D-SMLM) quantification tools occupy two categories: 1) spatial distribution/stoichiometry analysis typically conducted on high-density localisation datasets in fixed cells and 2) single-particle tracking (SPT) analysis conducted on live cells.

1.6.1 Quantification of Distribution/Stoichiometry in SMLM

SMLM techniques can provide a range of quantitative metrics such as counting protein expression, measuring the size and shape of protein clusters, changes in density and co-localisation. However, these studies are affected by issues such as detection efficiency [65], photo-conversion efficiency [114] and blinking artefacts [115] that must be taken into account in quantitative analysis [116]. Fluorescence intermittency artefacts are generally more prominent in STORM as each fluorophore switches between 'bright' and 'dark' states multiple times. PALM reduce this effect, with the recent Janelia Fluor dyes displaying an average of 1.4 fluorescent events [69], although a small fraction of molecules still appear $\approx$5 times.

Co-localisation of multiple labelled proteins can be conducted using multi-colour SMLM. Providing that the separate localisation lists are corrected for chromatic aberration and can be precisely aligned with fiducial markers, co-localisation can theoretically be determined at the single-protein level with precision given by the localisation uncertainty. Unfortunately, in practice this is more difficult due to the detection/emission efficiency of the different fluorophores used. Two or more colour Ripley's K tests can be implemented to provide a measure of co-localisation as well as examining the distribution of distances between the protein datasets. Cross-correlation has also been implemented to quantify co-localisation in SMLM datasets as a function of length scale [117].

Cell-wide distribution quantification can be achieved, providing information on homogeneity within the sample. This has be used to identify the presence of nanodomains in membrane protein distribution (*i.e.* the presence of highly controversial lipid rafts [118]) and can serve as a sample-wide metric of clustering. Within these analysis methods, some of the most commonly implemented tools are nearest-neighbour (NN) analysis and Ripley's

K function. In NN analysis the distribution of Cartesian distances from each localisation to its nearest localisation is compared to model distributions or between conditions. Assuming a constant localisation density, a shift towards shorter NN distances implies increased clustering. Complete spatial randomness (CSR) models of equal localisation density can be simulated to identify the maximum NN distances expected in the absence of clustering. The distribution of NN distances as a function of localisation density can be used to further identify clustering; in CSR models density and NN distance are inversely correlated but in completely clustered models the two are uncorrelated [119]. Ripley's K function quantifies overall clustering as a function of length scale. The mean number of localisations within radius r from each localisation, $N(r)$, is compared with a CSR distribution, given by $\rho\pi r^2$ for 2D imaging of a circular area. The metric $L(r)-r$ is then used to quantify the extent of clustering within the sample [120]:

$$L(r)-r=\sqrt{\frac{N(r)}{\pi\rho}}-r \tag{1.8}$$

Where ρ is the mean number of localisations per unit area. $L(r)-r>0$ implies a clustered distribution and $L(r)-r<0$ implies an anti-clustered distribution. $L(r)-r=0$ for complete spatial randomness.

Individual cluster identification and quantification is also possible with SMLM and has been demonstrated to identify the clustering state of T-cell membrane proteins [121]. However, erroneous background localisations, over-counting artefacts and detection efficiency make accurate quantification of individual clusters difficult. The relative stoichiometry of clusters can be compared directly, given a large enough sample size, by localisation number [122]. By quantifying the fluorescence intermittency kinetics of the fluorophore used under experimental conditions it is possible to estimate true cluster stoichiometry [121]. Individual clusters can be identified in a number of ways, the most common of which is density-based spatial clustering of applications with noise (DBSCAN) [123]. DBSCAN computes local density to identify clusters from background, requiring a user-defined minimum density of points to identify clusters. Other methods include Voronoi tessellation of localisations [124, 125] and Bayesian modelling [126] to identify clusters and the latter has been extended into 3D [127]. Recently, quantitative PAINT (qPAINT) [128] has been shown to provide robust 2D counting measurements as dye photophysics are decoupled from blinking kinetics in PAINT labelling. As with all analysis methods, significantly more progress has been made in 2D compared to 3D and as a result there are fewer tools for 3D quantification currently

available. Recently, Bayesian [127] and Voronoi [125] methods of 3D cluster analysis have been demonstrated, with additional tools likely to follow as 3D-SMLM becomes more widely adopted.

1.6.2 Single-Particle Tracking in SMLM

A key advantage of SMLM compared to other SR techniques is the ability to track the motion of individual fluorophores across successive frames in live cells. Single-particle tracking (SPT) provides quantitative information on the molecular dynamics of the target in question that can elucidate subtle biological phenomena such as the motion of glycine receptors on the surface of neurones [129] and the hand-over-hand motion of myosin V walking on actin [130]. More recently, 3D-SPT has been demonstrated in Saccharomyces cerevisiae using the DHPSF to track individual mRNA particles [101] to track individual mRNA and in mouse fibroblast cells using Multifocus Microscopy (MFM) also to track mRNA [131].

In order for the trajectory of individual particles to be determined the density of emitters must be low enough that individual PSFs are separated and the chance that emitters will move so that their positions are confused is low. As a result the maximum working density is related to the speed of motion being observed, with faster motion requiring lower densities. Low imaging density can be achieved with low-labelling concentration so that only a handful of targets within the sample are labelled. This can require a large number of samples to be imaged in order to obtain statistically significant results and does not provide much information on a single-cell level. By using photoactivatable fluorophores and a low level of activation, many trajectories can be extracted from single cells [132], increasing the efficiency of data acquisition and allowing for high-density diffusion maps to be produced [42]. Alternatively, PAINT labelling can be employed to achieve thousands of trajectories from a single cell in an approached named universal PAINT (uPAINT) [133], although this is experimentally more difficult to implement.

In most SPT analysis methods long trajectories are preferable as the number of times the motion of each particle is sampled increases. Consequently, SPT experiments are optimised so that a single fluorophore is localised as many times as possible before it photobleaches. Typically this is achieved by reducing the number of photons collected per exposure, either by reduced excitation power density or increasing acquisition rate depending on movement speed, at the compromise of SNR and thus localisation precision. Recent developments in

organic dyes allow for many more localisations of a single fluorophore compared to current fluorescent proteins, as such more robust quantification of motion can be obtained.

The two most common SPT tools are mean-square displacement (MSD) [134] and jump-distance (JD) [135] analysis, which are discussed in detail in chapter 4. As with distribution-quantification tools, the majority of SPT tools currently available are focused on 2D-SMLM. Both MSD and JD analysis tools have been extended into 3D-SMLM datasets (also described in chapter 4) for the work presented in chapter 4 and the corresponding MATLAB code is attached in the appendix of this thesis.

1.7 Thesis Overview

The chapters that follow describe the construction of a DHPSF microscope platform and its optimisation for imaging biologically relevant samples away from coverslip surfaces.

Chapter 2 describes the individual components of the DHPSF microscope as well as characterisation of its localisation precision and stability. Relevant illumination methods and imaging modalities are also introduced in this chapter.

Chapter 3 describes aberrations affecting the form and accuracy of the DHPSF. These are addressed and minimised to enable the use of the DHPSF in technically demanding areas of biological samples.

Chapters 4 and 5 present SPT and imaging applications of the DHPSF in a range of cell types and imaging modes that are facilitated by the extended depth of focus of the DHPSF compared to other 3D-SMLM techniques.

Finally, in chapter 6, the DHPSF is applied to quantify the nanoscale organisation of the T-cell receptor, a T-cell membrane protein that plays a key role in immune-response triggering. High-density whole-cell imaging is also demonstrated.

Chapter 2

Building and Characterising the DHPSF Platform

This chapter focusses on the building and characterisation of a fluorescence instrument capable of DHPSF imaging as well as standard 2D imaging. Individual components are listed with their function described. A schematic diagram shows a functional view of the instrument with the idea that one reading this chapter could build an equivalent imaging platform.

Quantification of the performance of the instrument is then provided with a discussion of factors affecting metrics such as stability and accuracy with solutions provided to reduce their effect. Applicable imaging methods, labelling strategies and background reduction techniques are discussed and quantified.

Contributions

Dr Steven Lee and I built the DHPSF instrument and I took and analysed all data from this instrument that is presented in this chapter. Dr Aleks Ponjavic helped to design, build and operate a compatible light-sheet illumination stage for SPI and wrote an auto-focus script to track the axial position of fiducial markers in beanshell for micromanager.

2.1 Building the DHPSF Platform

2.1.1 Components of Typical 2D Fluorescence Microscopes

This section describes the components included in the majority of 2D-fluorescence microscope platforms. Such an instrument would be capable of wide-field florescence microscopy as well as 2D-SMLM techniques. Figure 2.1 depicts an idealised microscope schematic. Firstly, the two fundamental components of any microscope, the objective lens and detector, are described. Then, the components placed in the excitation path are described in the order from photon emission to the sample. Thirdly, the components of the emission path are described in order from the sample to the detector. Finally, the components responsible for sample translation and vibration isolation of the platform are described to complete the instrument.

Objective lens

The objective lens collects the photons emitted at the sample plane. Typically, high numerical aperture (NA) lenses are used to gather the maximum signal. The highest NA lenses employ oil as an immersion liquid and can reach an NA of 1.49. State of the art water immersion lenses can reach an NA of 1.27. Infinity-corrected objective lenses output collimated light rays collected from the focal plane and allow for additional optics to be added between the objective lens and tube lens without altering the position of the image plane. In this work the majority of imaging was conducted with a Nikon 1.27 NA PLAN APO water immersion objective lens to maximise emission collection with a water immersion media.

Detector

Emitted fluorescence photons are recorded by a highly sensitive detector. Electron-multiplying charged-coupled device (EMCCD) cameras are most commonly employed in fluorescence microscopy due to their currently unparalleled quantum yield in commercially available camera-based detectors. EMCCD cameras use electron multiplication to amplify the signal generated from photons incident on the detector without amplifying shot noise and can exhibit a quantum efficiency (QE) of >90% in the visible spectrum due to their large ($\approx$16 μm $\times$ 16 μm) and back-thinned pixels. Scientific complementary metal-oxide semiconductor (sCMOS) cameras are gaining popularity within the SR community due to their affordability, superior acquisition speed (>400 frames per second, compared to $\approx$100 frames per second for EMCCD). While most sCMOS cameras are less

sensitive at very low photon numbers (reported values vary), due to their smaller pixels (≈6.5 μm × 6.5 μm) and lower QE (≈70%), recent developments claim to reach a QE of ≈95% with 11 μm x 6.5 μm pixels (Photometrics Prime 95B). We chose to employ a EMCCD camera in the design of our instrument as, at the time, sCMOS detectors were not available with comparable QE. Since then, an equivalent instrument employing a high-QE sCMOS camera has since been built at the Cambridge Advanced Imaging Centre (CAIC).

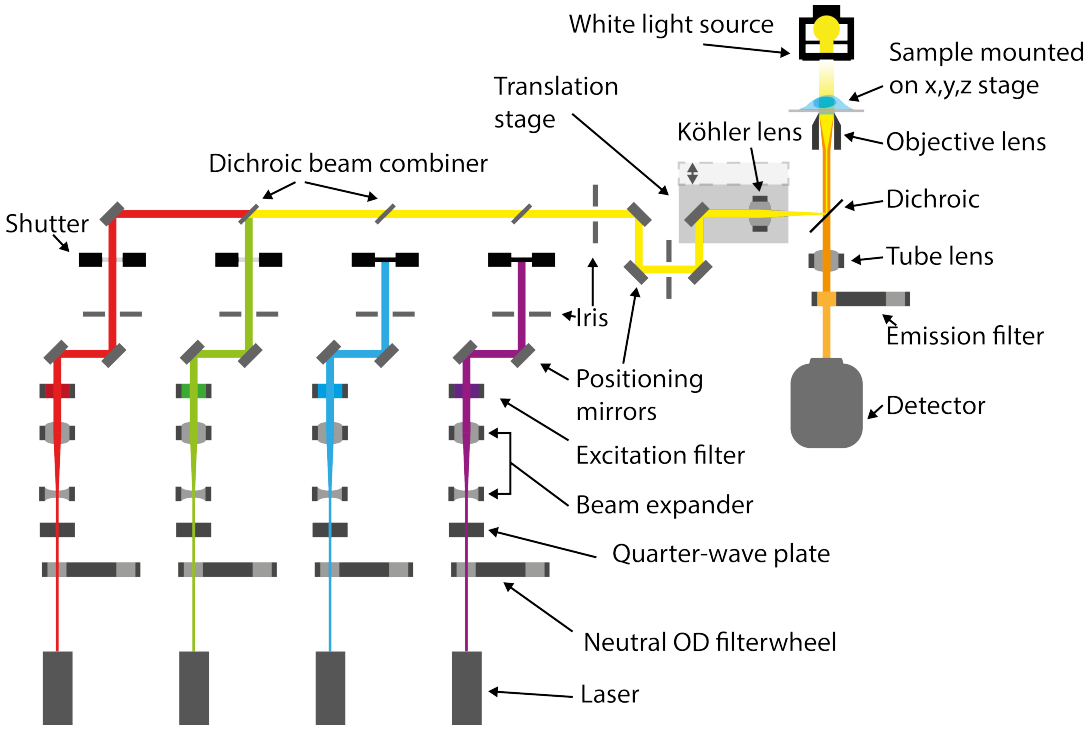

Fig. 2.1 Schematic diagram of a typical 2D fluorescence instrument. Two lasers (640 nm and 561 nm) are shown combining and illuminating a sample, whose emission is then collected and imaged onto a detector.

The Excitation Path

The excitation path involves the creation, modification and direction of excitation illumination. This illumination is incident on the sample, exciting fluorophores that are in an emissive state. The excitation path also includes activation illumination employed in PALM and STORM methodologies.

Light source

Excitation of fluorophores within the sample is achieved by high-intensity monochromatic illumination at a specific wavelength. This is typically provided by LED lasers in the power range of $\sim$100 mW.

Illumination power-density control

The power density of the excitation illumination must be controlled to optimise imaging conditions. This can be achieved via the laser itself or with neutral optical-density (OD) filters in the excitation path. OD is a measure of the transmission efficiency of a material and is defined as ($OD = -log_{10}(I_{out}/I_{in})$ where I is the intensity of light). Neutral OD filters are wavelength independent, reducing the intensity of all light passing through equally.

Polarising optics

Fluorophores are only excited by the component of light parallel to its fluorescence dipole. Circularly polarised light achieves uniform excitation of fluorescence dipole orientation within the sample. The linearly polarised output of LED lasers is typically converted to circular polarisation by a wavelength-matched quarter-wave plate (QWP). QWPs retard one orientation of polarised light by a quarter of the wavelength so that, when placed at 45° to the polarisation axis, linearly polarised light is converted to a circular polarisation.

Beam expanding optics

Beam expanding optics magnify the illumination to excite fluorophores across a larger area of the sample, increasing the field of view that can be imaged. This is often achieved by a Galilean telescope system comprised of two lenses. The first lens (of negative focal length, f_1) diverges the collimated beam before the second lens (of positive focal length, f_2) re-collimates the beam, resulting in a magnification of $M = -f_2/f_1$. The distance between the two lenses is roughly equal to the sum of the two focal lengths but is fine-tuned to achieve maximum collimation at the sample.

Excitation Filtering

Excitation filters are band-pass filters placed in the excitation path to ensure that only the desired wavelength of light is incident on the sample. Typical ODs for an excitation filter are 6-7 OD outside of the band and $\sim$0 OD inside. Excitation filters typically have a very narrow spectral band (FWHM $\sim$2 nm) to reduce unwanted illumination.

Positioning mirrors

Adjustable mirrors are used to coaxially align individual excitation paths in a combined beam path that is then directed towards the sample. Two or more adjustable mirrors are

included in each excitation path to allow for precise control of the position and direction of each laser beam separately.

Shutters

Digitally-controlled shutters are placed in each excitation path, this hardware automation allows for the use of complex combinations of laser illumination timings, for example, in photo-switching experiments.

Dichroic beam combiners

Dichroic mirrors reflect specific wavelengths of light while appearing transparent to other wavelengths when incident at a specific range of angles (usually 45 ± 1.5 degrees). A specific dichroic is placed in each excitation path to coaxially combine the excitation beams into a single combined beam path.

Wide-field excitation geometry optics

In order to achieve wide-field excitation geometries, as opposed to confocal illumination, the excitation beam is focused to the back-focal plane (BFP) of the objective lens, resulting in collimated a excitation geometry at the sample. This is implemented by the addition of a Köhler lens placed a focal length before the BFP of the objective lens. This facilitates epifluorescence illumination or total-internal reflection (TIRF) to be achieved depending on the angle of incidence of the laser beam on the coverslip-sample interface. This angle can be controlled by orthogonal translation of the Köhler lens relative to the objective lens by mounting on a single-axis translation stage.

Objective lens

In standard fluorescence microscope platforms, the final component of the excitation path, and the first of the emission path, is the objective lens (some excitation confinement techniques involve separate lenses to create narrow excitation geometries and collect the fluorescence signal, these are discussed later in this chapter).

The Emission Path

The emission path includes optics associated with the collection and detection of the fluorescence photons emitted by excited fluorophores within the sample. A generalised diagram demonstrating the spectral filtering of excitation and emission signals for imaging by dichroic beamsplitter and emission filters is presented in figure 2.2.

Separation of excitation and emission photons

A beamsplitting dichroic mirror is used to reflect the excitation path towards the objective lens while remaining transparent for the emission signal, which is of longer wavelength. This dichroic is usually mounted within the microscope body for maximum stability and can display multiple reflecting and transparent bands corresponding to typical wavelengths associated with excitation and emission respectively (figure 2.2).

Imaging the sample plane

The collimated rays output by the infinity-corrected objective lens are focussed into an image by a tube lens placed after the dichroic beamsplitter. The image plane of the platform is created in the focal plane of the tube lens, which is usually mounted within the microscope body.

Isolation of emission signal

Imaging contrast is achieved by filtering the emission path for the emission wavelength of the fluorophore of interest using a range of emission filters. The filters are chosen so that their transparency wavelength band matches the emission spectrum of the fluorophore so that the number of background photons (originating from sources such as excitation bleed-through, cell autofluorescence and Raman scattering) incident of the camera is reduced. Often a combination of band-pass and long-pass filters is used for an optimal SNR. Typical emission filters will have an $\sim$0 OD band that covers the majority of the emission spectra of the fluorophore being imaged. Outside of this band the OD of the emission filter is generally >5-6. The combined OD of the long-pass and band-pass filters is typically >10 at the excitation wavelength, where the majority of the background is present.

Detection of emitted photons

As described above, the spectrally-filtered emission is focussed to form an image on a detector at the end of the emission path.

Other Components

Additional components that are typically employed to mount the components described above and increase the stability of the system are described below. Non-essential components to improve usability and ease of alignment are also described.

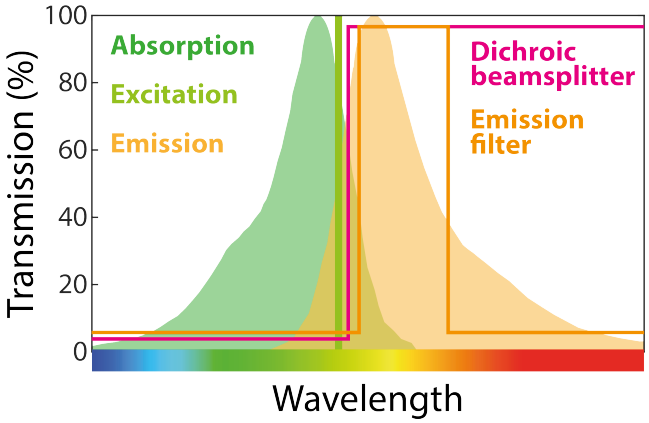

Fig. 2.2 Generalised diagram demonstrating the spectral filtering of excitation and emission photons in fluorescence imaging. The absorption and emission spectra of a typical fluorophore (Tetramethylrhodamine, green and orange respectively) are represented by filled volumes. The excitation illumination (561 nm LED laser, green line) overlaps close to the absorption maximum but is below the transmission wavelength of the dichroic beamsplitter (pink line). The emission spectrum is further filtered by an emission filter (orange line) to increase imaging contrast.

Microscope body

The microscope body mounts the objective and allows for fine control of its axial position relative to the sample, translating the objective's focal plane through the sample.

Sample-mounting components

Typically, biological samples are mounted onto a glass coverslip that is held by a sample-mounting stage. Stages are of stiff construction to reduce sample movement and vibration. Lateral translation of the sample is provided by the stage. Coarse large distance translation is achieved mechanically whereas, precise movement can be achieved by piezoelectric motors over distances of $\approx$100 μm.

Objective lens positioning control

The objective lens can be mounted onto a piezoelectric scanner that moves axially for fast and precise focal control over $\approx$100 μm with minimal relaxation effects. Such devices achieve $\pm$5 nm repeatability and $\sim$0.5 nm step resolution. These piezo scanners can be linked to a drift-correction system to maintain a constant focal plane within the sample for long-timescale imaging.

Vibration insulation

The entire instrument, including laser pathways, is mounted onto an actively damped vibration-insulation optical table. Optical tables typically damp vibration between 3 to

50 Hz, decoupling the microscope from environmental vibrations. The effect of acoustic vibration and air flow around the instrument is reduced by constructing a box around the sample. For microscopes investigating live biological processes under physiological conditions, this can be combined with an incubating unit to maintain a constant sample temperature.

Excitation alignment aids

A number of physical circular apertures or variable diameter and identical height are added into the individual laser paths and to the combined beam path to aid alignment. If a beam passes through the centre of two or more irises (without a mirror in-between) it can be determined to be aligned parallel to the optical table. The irises are positioned once all laser beams have been coaxially aligned so that in the future the beams can be re-aligned by passing through the centre of the irises in their path.

White light source

A white light illumination source can be attached to the inverted microscope base, allowing for conventional images of cells to be taken for reference.

Multi-colour optics

For multi-colour experiments, a dichroic beam splitter is placed before the emission filters to create multiple emission paths of different wavelengths. The multiple emission paths are passed through the relative emission filters and are imaged on separate detectors (figure 2.4) or on discrete areas of a single detector's sensor in a 'Dual view' system.

2.1.2 Additional Components Achieving DHPSF Transformation

To achieve the DHPSF transformation, additional optics are placed in the emission pathway of the standard fluorescence microscope shown in figure 2.1. The 2D PSF is modified by a DHPSF phase mask (shown in figure 2.3) placed in the Fourier plane of a $4f$ system of lenses before it is reimaged onto the detector.

4f systems are comprised of two lenses both of focal length f. The first lens (L_1) is placed so that its focal plane is in the original image plane of the microscope (at a distance f from the image plane). Interference effects induced by diffraction through the lens results in a Fourier transformation of the emission image being formed in the image plane of the L_1 (a distance f from the L_1), this is known as the Fourier plane. The second lens (L_2) is then placed so that its focal plane is in the Fourier plane (a distance f from the Fourier plane).

The second lens performs a reverse Fourier transformation and focusses the emission onto the detector placed in the lens' image plane (a distance f from the second lens, this a total distance of $4f$ from the microscope image plane. (figure 2.3b).

Each component of the $4f$ system is mounted into a three-axis translation stage for precise alignment. The DHPSF phase mask is placed in the Fourier plane of the $4f$ system and aligned laterally relative to the emission path so that the two lobes of the DHPSF rotate around a central position (figure 2.3d).

The designed DHPSF microscope contains two $4f$ systems that share the same first lens. An imaging-flat (radius of curvature $\sim$100 m) dichroic beam splitter placed between L_1 and the phase mask separates the emission of different colour fluorophores into the appropriate $4f$ path. The emission is then incident on a wavelength-specific phase mask before an image is formed onto two separate cameras (figure 2.4).

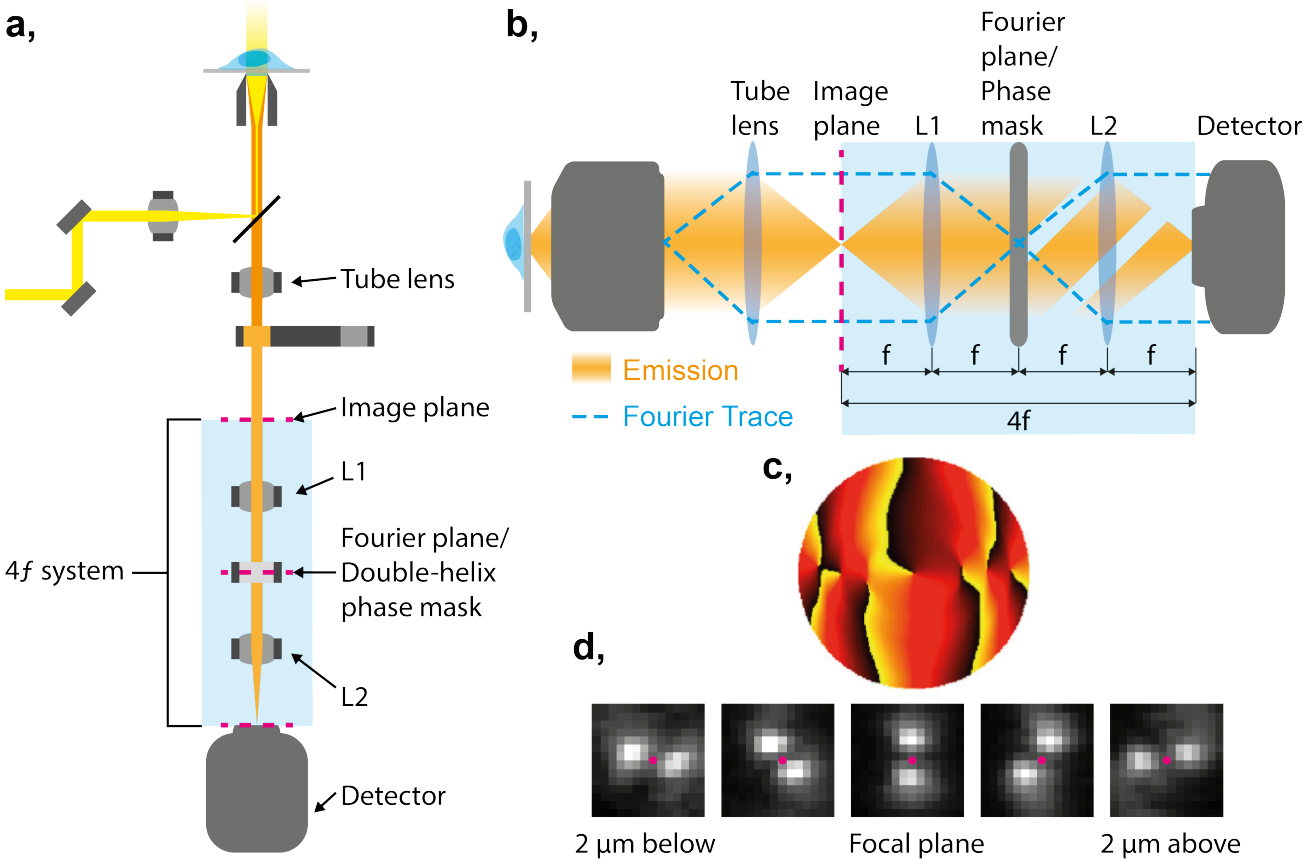

Fig. 2.3 Schematic diagram of additional optics achieving the DHPSF transformation. (a) Additional optics comprising a $4f$ system in the emission path of a typical 2D SR microscope with a DHPSF phase mask in the Fourier plane. (b) Idealised emission and Fourier trace of DHPSF emission path. (c) Surface profile of the DHPSF phase mask (Adapted from Grover *et. al.* [103] (d) Examples of DHPSFs across a $\sim$4 μm depth of field.

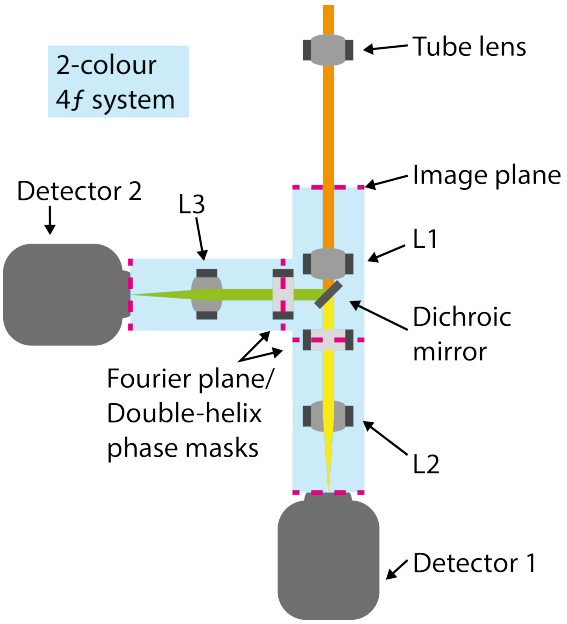

Fig. 2.4 Schematic diagram of two-colour $4f$ system facilitating two-colour DHPSF imaging. A dichroic beam splitter separates light onto two DHPSF phase masks optimised for separate emission wavelengths before the two channels are imaged onto two detectors.

2.2 Characterisation of the DHPSF Platform

This section describes the characterisation and optimisation of factors affecting the stability of the DHPSF platform. Applicable imaging methods, labelling strategies and background reduction techniques are then introduced and quantified.

2.2.1 SMLM Fitting

Throughout this work, 2D localisation data was fit by PeakFit plugin for ImageJ [136] and 3D DHPSF localisation data was fit by easy-DHPSF [137]. PeakFit was chosen due to its high scores in accuracy and detection rate in quantitative evaluation of SMLM fitting packages [138] (achieving the 4th highest accumulative score of 35 tested algorithms). PeakFit identifies maxima in an image as candidates for localisation before fitting a 2D Gaussian with specified free parameters by either LS of MLE methods.

Easy-DHPSF was the only available DHPSF fitting routine that was published from the start of the project up until the time of writing. An axial scan of static fluorescent beads provides a calibration reference of the form of the DHPSF across the depth of field. The single-molecule input data is then used to create templates of the DHPSF at six equally spaced planes within the image volume. The user then defines the image correlation thresholds used in fitting the single-molecule localisations. The two lobes of accepted DHPSFs are then fit to 2D Gaussian functions with their centre point and axial position determined to determine the position of the molecule in three dimensions. A calibration scan must be performed before each experiment as small changes in the alignment of the $4f$ system and phase mask alter the form of the DHPSF.

In the absence of mechanical sources of noise, the precision that a single molecule can be localised is ultimately determined by the detected signal above background and the physical pixels that the signal is spread over [84]. The effect of factors such as signal intensity, background noise and pixel size on localisation precision are discussed and theoretically modelled by Webb *et. al.* [85]. This study proposed a universal equation estimating the theoretical limit of precision in an optical system (equation 2.1), although this is widely regarded to overestimate achievable localisation precision. The localisation precision is shown to fall as $\frac{1}{N}$ for background noise and $\frac{1}{\sqrt{N}}$ for photon-counting noise, where N is the number of detected photons. This article also determines that the optimum ratio between pixel size and the standard deviation of a 2D PSF is $\approx$1:1 for Gaussian fitting.

$$\left\langle (\Delta x)^2 \right\rangle = \frac{s^2 + a^2/12}{N} + \frac{8\pi s^4 b^2}{a^2 N^2} \tag{2.1}$$

where a is the pixel size, s is the standard deviation of the imaged PSF, b is the number of background photons per pixel and N is the number of detected photons above background.

SMLM fitting algorithms use the fit error between the signal and fitted function to estimate a localisation precision. This estimation is purely dependent on the SNR and does not take mechanical stability beyond a single acquisition frame, thus underestimating the true precision of the instrument. The achievable localisation precision of an instrument can be quantified by repeatedly imaging static point sources and determining their perceived widths [105].

2.2.2 Mechanical Stability

The mechanical stability of a microscope is a measure of the errors induced in localisation precision due to effects such as vibration and differential thermal expansion/contraction on the various optical components in the optical train. Thus, in SMLM, the achievable precision is a convolution of both fitting errors, which depend on the number of detected photons, and the mechanical stability of the microscope, which is independent of the number of detected photons. It is possible to determine this 'true' precision by measuring the distribution of multiple localisations of individual point sources as a function of detected photons [105]. At low detected photon numbers the true precision is dominated by fit errors whereas at high detected photon numbers a plateau is reached at some combination of fit error and mechanical stability, representing the ultimate achievable localisation precision of an instrument. Long term stability can be achieved by fiducial correction of sample drift but is ultimately limited by the experimental localisation precision.

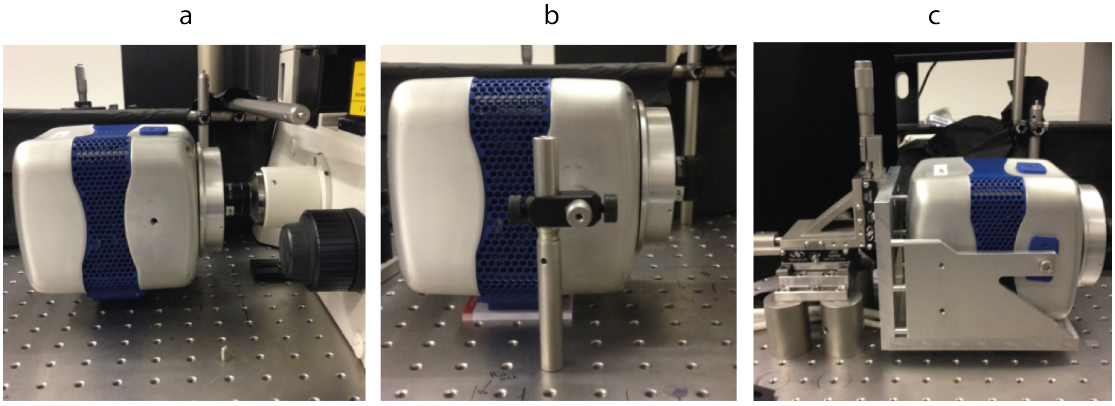

Fig. 2.5 Examples of detector mounting methods tested for maximum short-term mechanical stability.

The mechanical stability of a microscope is affected by many factors, such as the construction material, size, sturdiness of mountings, temperature fluctuations and environmental vibrations. The effect of detector mounting on localisation precision was investigated with three different mounting techniques; (a) mounted directly to the microscope base with no support, (b) mounting with 1/2" stainless steel optical posts to the optical table and (c) mounting into a custom-made aluminium cradle (figure 2.5).

The localisation precision and thus instrument stability was measured as previously described by Gahlmann *et. al.* [105]. Static diffraction-limited (100 nm) fluorescent beads (560/580 nm absoption/emission) were imaged on poly-L-lysine coated coverslips for 2,000

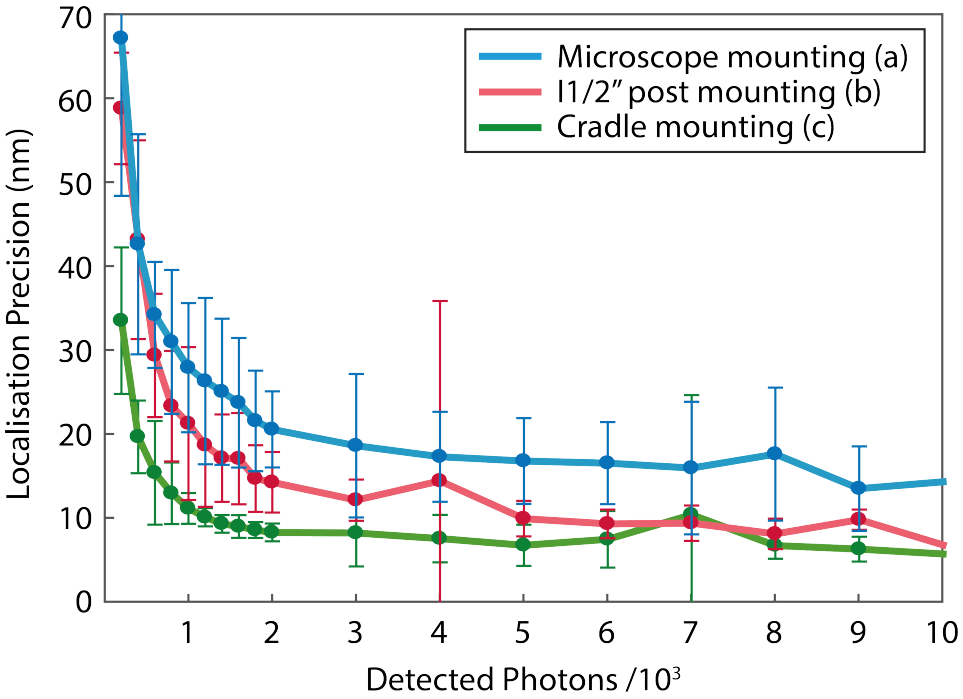

Fig. 2.6 Comparing mechanical stability of camera mounting methods. Average and standard deviation of localisation precision of static fluorescent beads imaged for 2,000 frames with a 30 ms exposure time without drift correction is plotted as a function of detected photons.

frames with an exposure of 30 ms. The stability of the microscope was improved at all detected photon values sequentially from cases (a), (b) and (c) (figure 2.6). The ultimate precision for case (a) was measured to be 16.1±0.7 nm which was reached by ≈4000 photons. For case (b), the ultimate precision was measured to be 9.6±0.3 nm by ≈3000 photons. The most stable detector mounting was case (c) with a measured localisation precision of 6.9±0.3 nm, which is reached by ≈2000 photons. This mounting was chosen for all presented experiments in this work. Figure 2.7 shows this 2D localisation precision in greater detail. A localisation precision of <10 nm is reached by ≈1000 detected photons and <20 nm by ≈500 photons (figure2.7).

2.2.3 Comparing Mechanical Stability between Instruments

To confirm that the stability of the constructed microscope (instrument A) was similar to other super-resolution instruments within the lab the same stability analysis was also conducted on three other set ups. Another custom-built inverted optical microscope from the lab was tested (instrument B). This instrument differed in that it employed an Olympus microscope

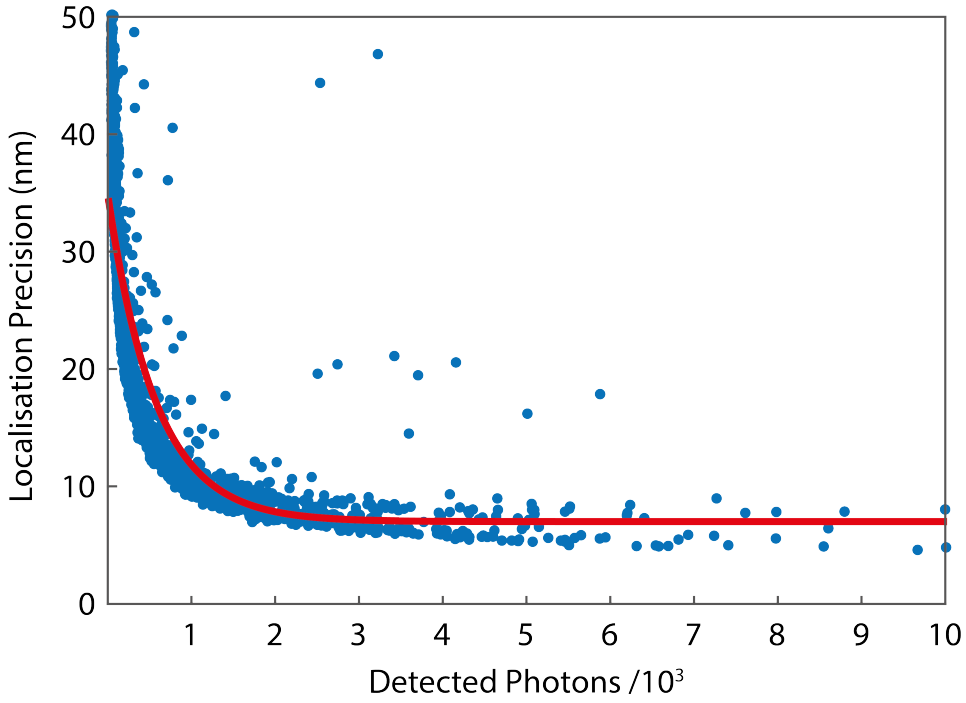

Fig. 2.7 Empirically-determined 2D localisation precision of the instrument. The distribution of localisations of individual fluorescent beads imaged for 2,000 frames with a 30 ms exposure time without drift correction is plotted as a function of the average number of detected photons per localisation.

body and oil-immersion objective lens. These were compared to a commercially available super-resolution microscope (Nikon N-STORM, instrument C) from the Gallop lab (Gurdon Institute, Cambridge). This instrument also uses an oil-immersion objective lens and EMCCD detector. Finally, a non-super-resolution instrument was investigated (instrument D). This setup was comprised of an ASI RAMM stage mounted directly to an optical table with a less-sensitive CCD detector.

Figure 2.8 compares the mechanical stability of the four instruments. The commercially available instrument C reached an ultimate precision of 7.7±0.4 nm but was surpassed by both custom-built instruments A and B which achieved an ultimate precision of 6.9±0.3 nm and 4.6±0.4 nm respectively. The non-super-resolution instrument D achieved a prevision of ≈20 nm, performing worse than all other instruments at all detected photons. This information confirms that the newly-built instrument performs as expected, reaching a comparable mechanical stability to other SMLM instruments in the lab.

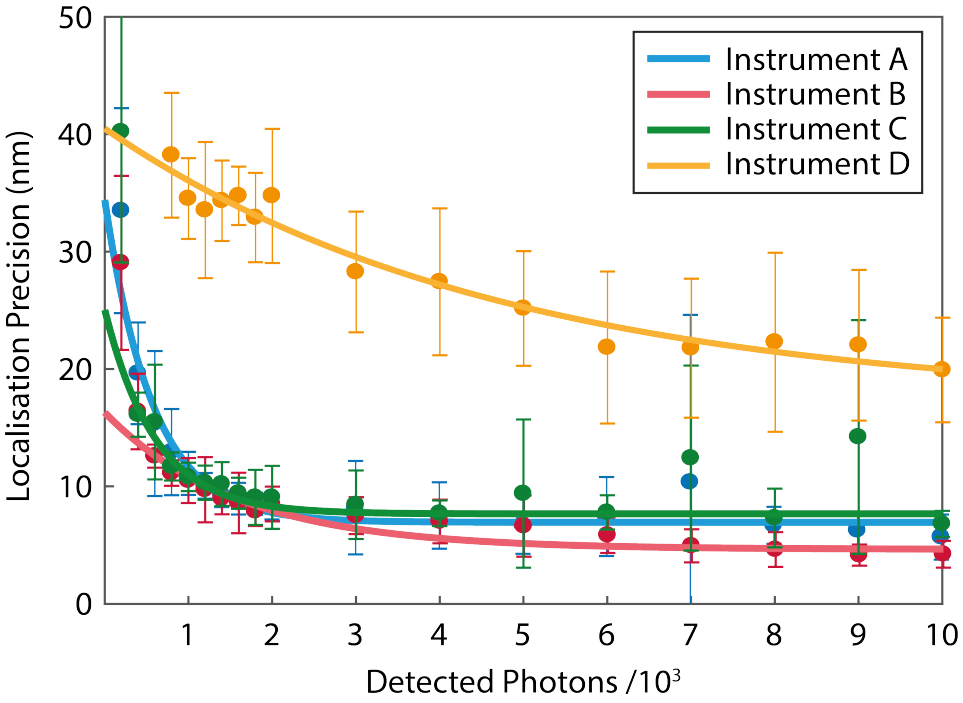

Fig. 2.8 Average and standard deviation of measured localisation precision decay for instruments A, B, C and D over a 60 second period without drift correction. Fitted exponential decays are plot to guide the eye.

2.2.4 3D Stability of the DHPSF Platform

In addition to the lateral stability measured by 2D localisation experiments, axial stability is crucial to 3D imaging techniques. The axial mechanical stability of inverted optical microscopes is typically less than the lateral stability. This is because the focusing mechanism responsible for translating the objective lens relative to the sample is more susceptible to gravity. This mechanism is usually based on rack and pinion in which the mechanical linkage that can be prone to relaxation effects. The lateral and axial stability can be directly measured using the DHPSF in an analogous experiment to the 2D stability measurements.

In order to achieve maximum axial stability, a number of steps were taken before imaging. The mechanical focus of the instrument was used only at the start of the process to find the rough focal plane, after this point all focal adjustments were conducted via the piezo objective positioner. An acoustic insulator was placed over the sample in order to reduce airflow that may arise from events such as opening/closing of the lab door. The samples were left for at least ten minutes for mechanical relaxation to occur before the focal plane was

corrected with the piezo stage. During acquisition care was taken to minimise movement within the room. These measures were taken for all imaging presented in this work with the exception of when using fiducial markers for drift correction, when less care was needed. Axial and lateral stability measurements were then plotted against detected photons and compared to 2D measurements from the same instrument (figure 2.9).

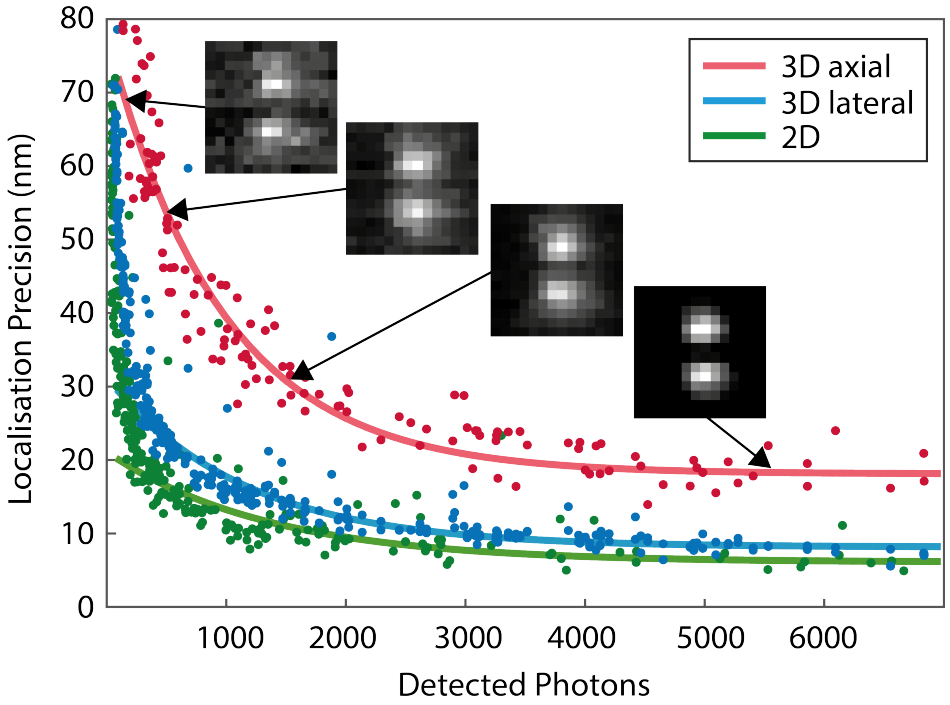

Fig. 2.9 Empirically determined localisation precision of the DHPSF instrument as a function of detected photons. Measured lateral (x&y) and axial (z) localisation precision from 2,000 frames acquired with 30 ms exposure time compared to 2D localisation precision from the same instrument without the addition of the DHPSF phase mask. Example DHPSFs are shown at their corresponding detected photon values.

The ultimate lateral localisation precision of the DHPSF instrument was measured to be 8.8±0.5 nm. The reduction in stability compared to 2D localisation is most likely due to the inherent reduction of signal and the introduction of additional optics into the emission path. The ultimate axial precision of the DHPSF instrument was measured to be 18.5±0.9 nm. This agrees well with modelled predicted values [92]. Expected photon values and the corresponding localisation precision are presented for individual fluorophores later in table 2.1.

2.2.5 Focal Drift

Drift of the focal plane is a common issue faced in extended imaging experiments. The focal plane within the sample can move so that the structure of interest is no longer in the depth of field. Causes of focal drift include thermal expansion/contraction within the microscope body and stage, as well as relaxation of the focussing mechanism mounting the objective lens. These factors can be minimised by maintaining a more constant temperature around the instrument and allowing the mechanisms to relax after movement for an extended period of time.

The focal drift of the DHPSF microscope system was measured over a 20 minute period. The mean of seven repeats was used to estimate the expected drift as a function of time (figure 2.10). The drift was found to follow the linear fit $\Delta r = (0.0044 \pm 0.0003)N + (1.3 \pm 1.8)$, where Δr is the Cartesian drift distance in nanometers and N is the number of frames (at 100 ms exposure). Using this equation, the focal plane is expected to drift by 160±13 nm each hour. While focal drift can occur in both directions, it is expected to go with gravity on most occasions as the rack and pinion system mounting the objective lens relaxes.

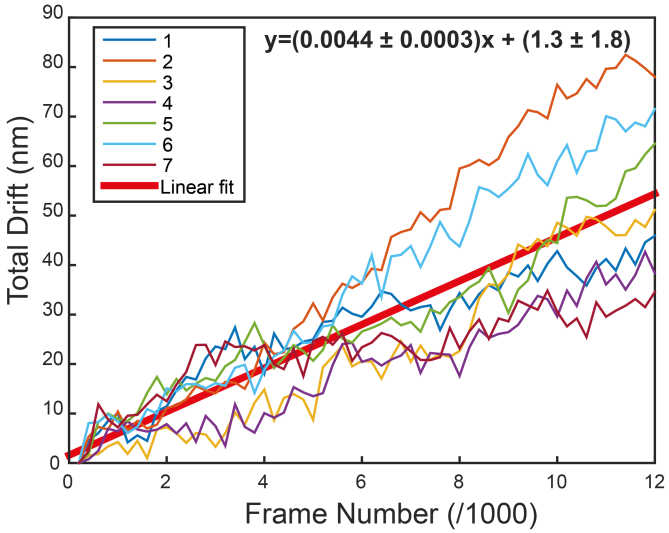

Fig. 2.10 Axial drift of the microscope platform over time. The Cartesian distance drifted by the focal plane within the sample is plotted as a function of frame number (100 ms exposure per frame) for seven repeats. A linear fit was used to estimate the expected drift as a function of time.

Focal drift can be corrected for with fiducial markers. In SMLM, fiducial markers are typically isolated diffraction-limited point sources that do not bleach during the acquisition, placed somewhere in the FOV. Polystyrene spheres coated with fluorescent dye can provide

high SNR fiducial PSFs for high-precision fiducial tracking. However, these can often saturate the dynamic range of the detector and are prone to photobleaching over long acquisition times, especially at the increased excitation laser powers typically used in DHPSF imaging. One solution to this is to use 100-200 nm gold nanoparticles, which scatter the excitation laser, as fiducial markers. This sacrifices some SNR as the scattering provides fewer detected photons compared to fluorescent beads but has the advantage that there is no photobleaching so that the acquisition length is instead limited by other factors. Fluorescent nano-diamonds are increasingly being used a fiducial markers. Point defects in their crystal structure are highly fluorescent within the visible light range and immune to photobleaching. Nano-diamonds provide greater SNR compared to gold nanoparticles but can saturate the detector at high excitation powers.

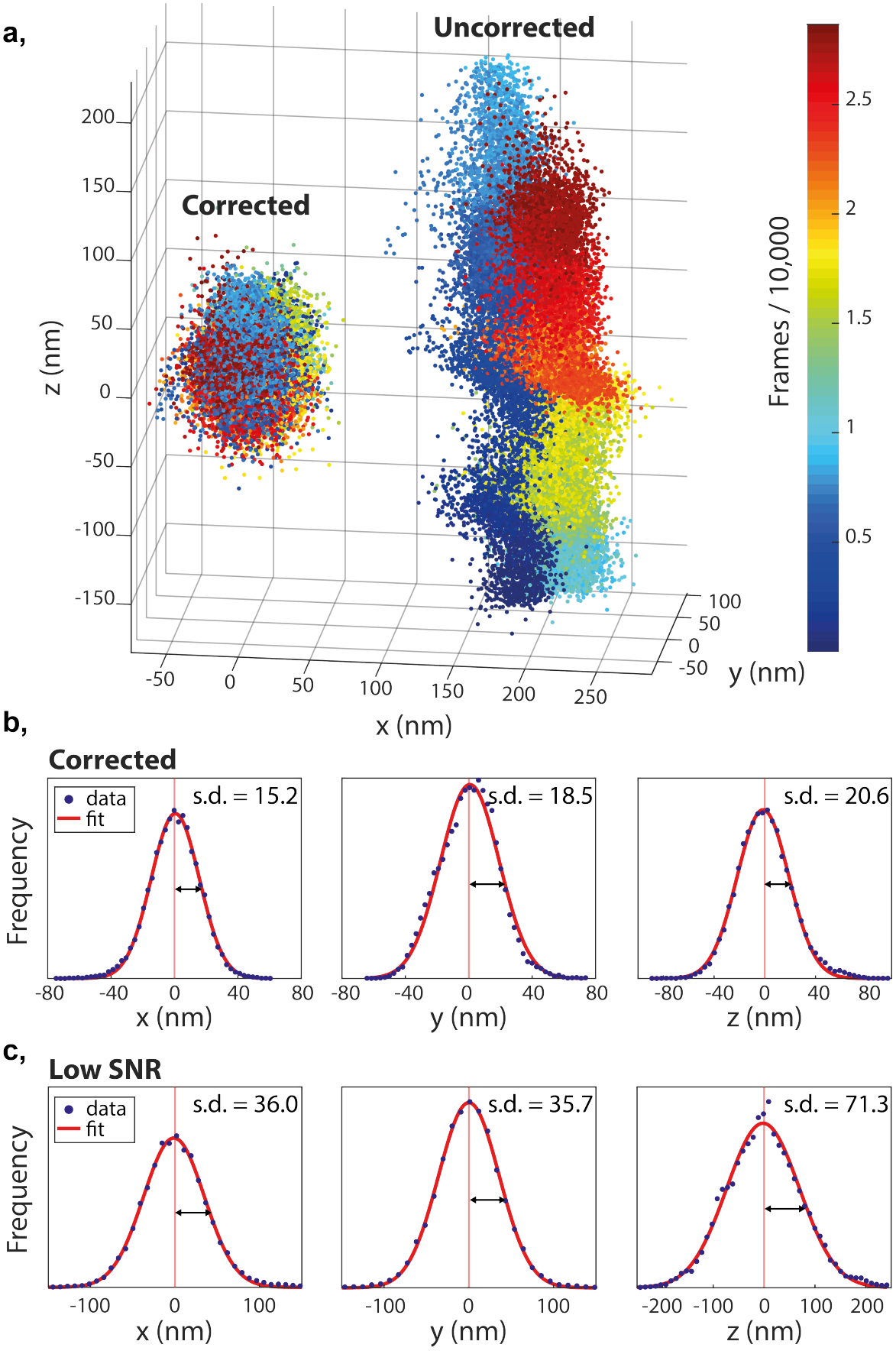

Fig. 2.11 Figure caption on following page.

Fig. 2.11 (Previous page.) Fiducial correction of axial drift. (a) Uncorrected localisations from a fiducial marker imaged for 30,000 frames coloured in time (right) and drift-corrected localisations from the same fiducial marker (left). (b) Distribution of corrected localisations in x (left), y (centre) and z (right) with fit Gaussian distributions and standard deviation quoted. (c) Distribution of corrected localisations for a low SNR ($\sim$3) fiducial marker in x (left), y (centre) and z (right) with fit Gaussian distributions and standard deviation quoted.

The precision of 3D fiducial correction was measured by imaging multiple fiducial markers for 30,000 frames with a 30 ms exposure (15 minutes total acquisition time) under typical imaging conditions. Figure 2.11 shows the motion of one of these markers before and after fiducial correction. During this acquisition the focus of the sample was roughly maintained by an auto-focus script written by Dr Aleks Ponjavic, this can be seen in the discontinuous step in axial position around frame 10,000 as the peizo-mounted objective lens is moved to return the focus to the initial position within the sample. After correction, sample drift was eliminated and the localisations were reduced to a near Gaussian distribution with standard deviations in all dimensions corresponding to typical localisation precisions presented in figure 2.9 (a standard deviation of 15.2 nm, 18.5 nm and 20.6 nm in x, y and z respectively). The same experiment was repeated at a low SNR ($\sim$3) of fiducial marker. The measured distribution after correction fit a Gaussian distribution with a standard deviation of 36.0 nm, 35.7 nm and 71.3 nm in x, y and z respectively, representing the worst case precision of fiducial correction.

2.2.6 Compatible Excitation Wavelengths

The DHPSF instrument includes multiple excitation laser lines enabling imaging of a range of fluorescent probes. A 405 nm laser provides photoactivation/modulation when applicable and 488 nm, 515 nm, 561 nm and 641 nm lasers allow for excitation of fluorophores across the visible spectra. The majority of imaging is conducted using 561 nm excitation due to the availability of bright and photo-stable fluorophores excited at this wavelength. For two-colour experiments, 641 nm or 488 nm excitation is used in conjunction with 561 nm excitation as there is little spectral overlap causing unwanted cross-excitation.

The DHPSF phase mask is wavelength specific as its thickness is tuned to cause constructive and destructive interference in the emission signal [103]. The DHPSF instrument is compatible with all possible phase masks and is currently equipped with 530 nm, 580 nm and 640 nm compatible DHPSF phase masks and the corresponding emission filters.

When designing an experiment it is important to consider possible causes of background related to excitation illumination that may arise. Certain hydrophobic pens, used to contain sample media, fluoresce at certain wavelengths. The hydrophobic ink can leach into the media and result in non-specific background fluorescence that cannot be filtered away from the emission signal of the fluorophores of interest. This issue has been found at both 488 nm and 641 nm but not 561 nm excitation with hydrophobic pens (PAP pen, GTX22601, GeneTex). A similar issue is also seen when using frame-seal slide chambers (9×9 mm, Biorad) sample containers. For all imaging with excitation away from 561 nm, this problem is overcome by employing metal sample holders (A7816, ThermoFisher), by relying on the surface tension of the sample media to form a droplet without a holder or by using PDMS chambers (MultiWell Chamber Coverslip, CWCS 8R-1.0, Grace Bio-Labs).

2.3 Background Reduction

As evident in figure 2.9, the achievable localisation precision in SMLM is not only limited by the mechanical stability of the microscope but also by the number of detected photons from individual localisations. More specifically it is the signal-to-noise ratio (SNR), defined as the number of photons above background divided by the standard deviation of the background ($SNR = \frac{S-B}{std(B)}$), which is important. Recent developments in fluorescence dyes have resulted in improved quantum yields and photostability [139, 140] allowing for increased signal to be collected. In addition, advancements in high NA objective lenses and efficient detectors (EMCCD and sCMOS, [141, 142]) have improved the ability to collect and measure this signal. Typical SMLM experiments employ a range of long-pass and band-pass optical filters to separate background photons at different wavelengths from the emission signal of the fluorophore being imaged. However, the optical filters are not perfect (∼5-6 OD) and thus a certain amount of off-wavelength photons pass through, leading to degradation of the SNR in many samples. Fluorophores excited out of the depth of focus of the microscope add to this background noise in thick samples and autofluorescence often present in biological samples [143] initially limited high-precision SMLM to the study of thinner biological samples.

As a result, a range of background-reduction techniques have been developed, facilitating SMLM studies of biological samples from proteins at the surface or within a supported lipid bilayer [144, 132, 40, 145] to whole-cell eukaryotic imaging [82, 146, 147] and thick tissue samples. These techniques include excitation-confinement amongst other approaches such as plasmonics field-confinement. These other approaches and excitation-confinement are

reviewed by Lee *et. al.* [148]. Due to their relative ease of implementation and applicability of the samples presented in this work, only excitation-confinement techniques are outlined and investigated here.

The DHPSF microscope was designed to be compatible with four illumination modes: epifluorescence, highly inclined and laminated optical sheet illumination (HILO) [58], single-plane illumination (SPI) [60, 61] and total internal reflection fluorescence illumination (TIRF) [56, 57] (figure 2.12). A trade-off between SNR and convenience is considered before each experiment, optimising data collection and quality.

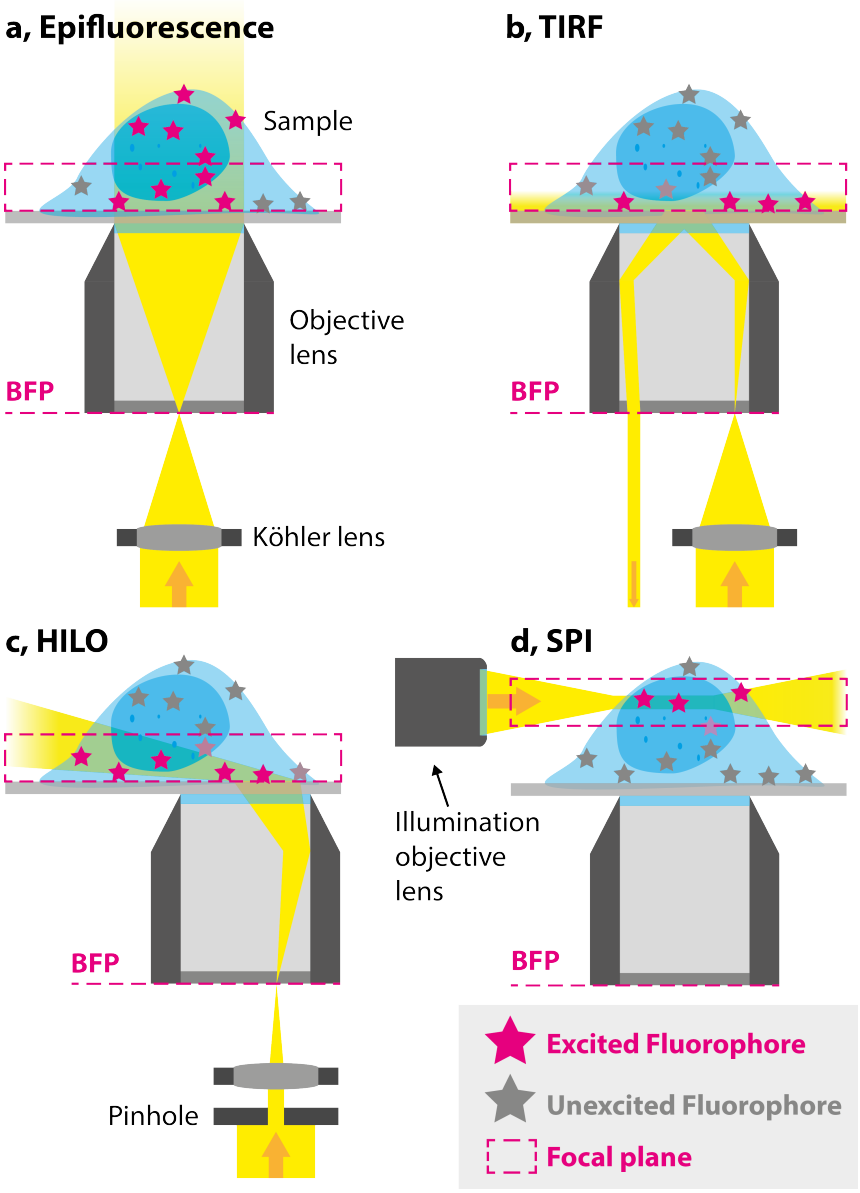

Fig. 2.12 Figure caption on following page.

Fig. 2.12 (Previous page.) Example schematic diagrams illustrating the implementation of different illumination geometries. (a) Epifluorescence illumination. Collimated light is focussed into the back focal plane (BFP) of the objective lens, illuminating all axial planes within the sample. (b) Total internal reflection fluorescence illumination (TIRF). Collimated light is focussed to the BFP of the objective lens. The beam is then translated or angled so that the angle of incidence on the coverslip/media interface is past the critical angle, creating an evanescent field that illuminates 100-300 nm into the sample. (c) Highly inclined and laminated optical sheet (HILO) illumination. As in TIRF illumination the angle of incidence of the light is changed to reduce illumination above the depth of focus. A pinhole placed before the objective lens further reduces the excitation geometry by limiting thickness of the laser beam. (d) Single-plane illumination (SPI) by typical light sheet. A second, low magnification, objective lens is used to illuminate the sample perpendicularly to the collection objective. Prior to this illumination objective lens a cylindrical lens is used to create a lateral sheet of illumination.

Epifluorescence illumination involves collimated illumination exiting the objective lens parallel to the optical axis. This is achieved by focussing the collimated laser beam to the back focal plane of the objective with a Köhler lens so that the objective lens re-collimates the illumination (figure 2.12a). This excitation geometry illuminates all axial planes within the sample simultaneously resulting in fluorophores outside of the depth of focus to be excited and emit photons that are collected by the detector but cannot be relayed to form an image by the objective lens, adding to background noise. Nonspecific background is also created from outside of the depth of field. Epifluorescence is the most simple excitation geometry to implement but also provides the lowest SNR due to its lack of sectioning. Although it is suitable for imaging high-signal and low-background samples such as fluorescent beads, epifluorescence illumination does not usually provide sufficient SNR facilitate single-molecule imaging in the majority of biological samples due to the reason described above.

In total internal reflection fluorescence (TIRF) microscopy [56] the excitation laser is incident on the coverslip-media interface at or above the critical angle so that it undergoes total internal reflection and does not propagate into the sample. Instead, an evanescent wave is created on the low refractive index side of the interface that penetrates only 100-300 nm into the sample (figure 2.12b), reducing unwanted background fluorescence outside of this volume. TIRF illumination is achieved either by changing the angle of incidence of the excitation laser into the back focal plane of the objective or by translating the beam so that it is still parallel to the optical axis but now entering the objective off-centre. TIRF is commonplace in 2D fluorescence microscopy due to its ease of implementation and optical sectioning that is well matched to the depth of field of the 2D PSF. The major disadvantage of TIRF is that

confines imaging to surfaces. As the majority of biological systems exist in a 3D volume with thickness larger than 300 nm, this limits the range of systems that can be investigated. Furthermore, the presence of a non-physiological surface can perturb extracellular membrane proteins and may not allow for the true state of the system to be determined [149–151]. In the case of 3D SMLM techniques and especially those with large depths of fields, such narrow optical sectioning is suboptimal as a large fraction of the working depth of field is not being utilised and imaging is limited to the glass/water interface. Generally speaking increasing the depth of field must come at some cost, be it experimental complexity or axial precision. Therefore when using large depth of field 3D SMLM there are few samples that benefit from TIRF illumination compared to other background reduction methods and thus the two are rarely implemented together. Standard depth of field 3D SMLM techniques such as astigmatism and biplane imaging are more compatible with TIRF illumination due to their comparable depth of field ($\sim$500 nm).

Highly inclined and laminated optical sheet illumination (HILO) [58] is implemented similarly to TIRF illumination. The excitation laser is translated so that it is incident on the coverslip-media interface at an oblique angle, however, not so far as to be past the critical angle like in TIRF (figure 2.12c). As the inclination increases the thickness of excitation geometry is reduced [59], reducing out of focus fluorescence and reportedly increasing the SNR by a factor 3.1–3.5. Limiting the diameter of the excitation beam can further reduce the excitation thickness to 5–10 μm, roughly following the relation $x = R/tan(\theta)$, where R is the radius of excitation beam and θ is the angle of incidence. An additional increase in SNR of a factor 2.2–2.9 is reported when reducing the diameter from 80 μm to 15 μm on the sample, resulting in a combined increase in SNR by a factor up to 7.6 [58]. HILO facilitates SMLM up to 20 μm into biological samples, including tissue. HILO in conjunction with DHPSF microscopy has previously been used to resolve the cytoskeletal structure of Caulobacter crescentus bacteria [104]. The key advantage of HILO is being able to significantly increase SNR to a level that facilitates SM detection in noisy biological samples without adding a great amount of experiential complexity. All samples will benefit from the SNR increase due to inclination (as also described in VAEM [59], however the additional increase related to excitation beam radius comes at a cost of a reduced field of view. In the case of small samples, such as single-cell imaging presented in this work, a 30 μm excitation diameter is sufficient so the maximum SNR can be achieved. However, when larger fields of view are required a compromise between SNR increase and excitation diameter must be reached, limiting the applicability of the technique. The minimum achievable excitation thickness (FWHM) of $\sim$6 μm is quite well matched to the depth of field of the DHPSF although there is still significant excitation of fluorophores adjacent to the focal volume that can reduce

image quality. For the DHPSF instrument the angle of inclination is altered by translating the excitation beam perpendicularly to the optical axis of the objective lens. As a consequence, the excitation maxima aligns with the centre of the focal plane as the excitation is always incident on the objective lens parallel to the optical axis (supplementary information in [58].

Single plane illumination (SPI) or light-sheet microscopy refers to a range of techniques designed to create a narrower excitation geometry via a thin sheet of light, typically running perpendicular to the optical axis so that it fills the focal plane of the objective (figure 2.12d). In the simplest systems a second objective is used to introduce the excitation beam perpendicularly to the collection objective lens. A cylindrical lens placed before the SPI objective to offset the axial focal point of the illumination beam from the lateral, resulting in sheet-like excitation geometry within the field of view. The NA of the SPI objective determines the FWHM of the sheet which can typically range between $\sim$0.5–5 μm [152]. In these systems the thickness (and thus excitation power density) can vary across the sample and the field of view is often limited in the case of very narrow sheets. Other difficulties arise from engineering a system that is capable of controlling two objective lenses in close proximity without limiting the sample geometry. One solution to this issue is single-objective SPIM (soSPIM) [153] in which excitation light is directed through the detection objective lens and reflected off micro-mirrors positioned at 45° close to the sample to achieve optical sectioning. While this method eliminates the need for a second objective lens it has less flexibility unless the position of the micro-mirror is directly controlled as demonstrated by Gebhardt *et. al.* [154]. More complicated SPIM approaches involve beam shaping by holography to form Bessel beams [155] and airy beams [156] that maintain a constant narrow thickness over much larger distances and exhibit less aberration when imaging deep within samples. Although technically more complex to implement these techniques can provide large field of view sectioning as thin as 300 nm [87]. State of the art lattice light sheet [89] when combined with structured illumination has demonstrated video-rate super-resolution microscopy on entire living cells [82, 157]. As with TIRF illumination, the DHPSF is better matched to thicker SPI techniques in order to match the $\sim$4 μm depth of field. These thicker ($\sim$2–5 μm) techniques typically provide greater sectioning compared to HILO illumination but with significantly more experimental complexity, not only from the additional optical components required but also from sample geometry issues related to the second objective lens.

In general in this work HILO excitation is used as it provides adequate optical sectioning to image the samples presented with high SNR (typically >5) without adding to experimental complexity. The SPI set up that was designed includes less stable components for sample

mounting compared to the standard mounting staged used for other techniques. The reduction in stability will have negative effects on image quality even in the presence of fiducial correction. In the case of high-background and low-signal samples SPI may be necessary for SMLM. SPI is also useful when employing 488 nm and 640 nm excitation, as there can be an increase in non-specific background fluorescence at these wavelengths compared to 561 nm.

2.4 Compatible SMLM Labelling Strategies for the DH-PSF

In principle any SMLM labelling technique that allows for the isolation of individual emitting fluorophores is compatible with the DHPSF. The DHPSF is larger than the PSFs of other SMLM techniques and therefor occupies a greater area on the detector in the conjugate image plane (∼5-fold larger compared to an analogous 2D experiment) (figure 2.13). Consequently, experiments require lower imaging concentrations so that PSFs no longer overlap and thus to obtain the same number of localisations longer acquisitions must be recorded. In this work, SMLM is achieved by a range of labelling methods including: single-molecule concentrations of fluorophores, PALM [30, 31], STORM [32, 41] and PAINT [38].

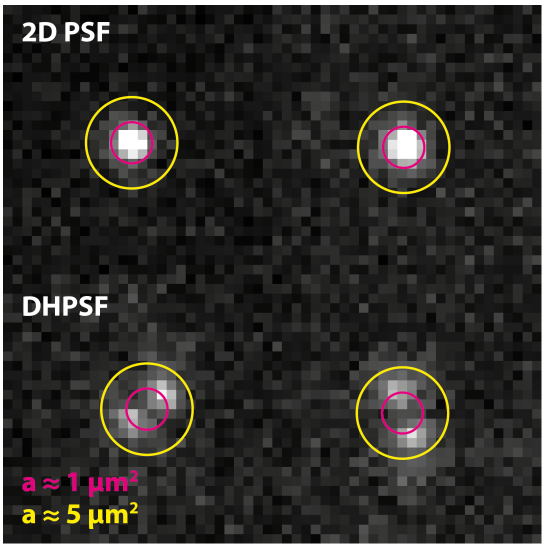

Fig. 2.13 Relative size of 2D PSF and DHPSF. Typical examples of 2D PSFs (top) and DHPSFs (bottom) with circles highlighting the approximate area occupied by a single PSF.

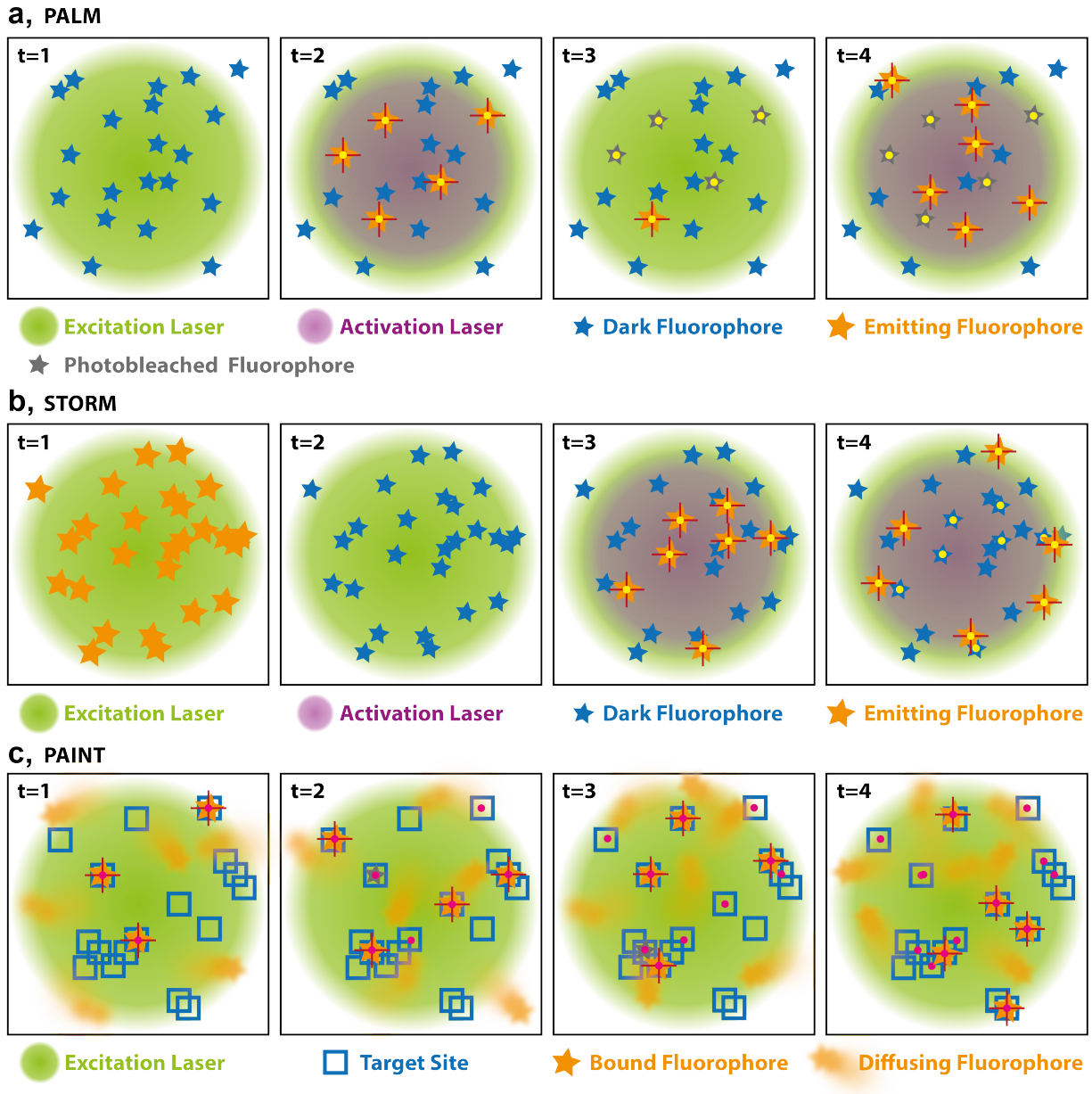

Fig. 2.14 SMLM labelling strategies. (a) General principles of photo-activation localisation microscopy (PALM). An activation laser brings 'dark' fluorophores into a 'on' state where they are localised and bleached. (b) General principles of stochastic optical reconstruction microscopy (STORM). Initially fluorescent fluorophores are bleached into a 'dark' state where an activation laser causes fluorophores to blink repeatedly until they are photobleached (in the case of Alexa Fluor 647). (c) General principles of points accumulation for imaging in nanoscale topology (PAINT). Fluorophores present in the media diffuse rapidly, blurring out their emission. When a fluorophore contacts a target site it binds transiently so that its emission PSF can be localised. Over time the same target sites are imaged multiple times.

Photo-activation localisation microscopy (PALM) [30, 31] isolates the emission of individual fluorophores by exploiting photo-activatable or photo-switchable properties of some fluorophores. These fluorophores are initially in a 'dark' state with absorption spectra not resonant with the excitation laser so that no fluorescence is observed. Upon stimulation by an activation laser (usually at 405 nm), the fluorophore converts to a fluorescently active 'on' state with absorption spectra resonant with the excitation laser and the molecule is observed until either it switches 'off' or it irreversibly photobleaches (figure 2.14a). By tuning the power and timing of the activation laser a stochastic subset of the 'dark' fluorophores can be activated. These fluorophores are imaged and subsequently photobleached before the next subset of 'dark' fluorophores are activated. The activation laser can either be pulsed to illuminate a different subset at regular intervals or be continuously incident on the sample at low power so that 'dark' fluorophores are activated at a similar rate to 'on' fluorophores photobleaching. As the number of unbleached fluorophores reduces the activation laser power can be increased so that the localisation rate remains at a constant optimal level until completion, although this can add to the non-specific background. An advantage of PALM is that the localisation rate can be precisely controlled by the power of the activation laser, allowing for a range of experiments including tracking (that typically requires a lower density of PSFs) and imaging to be conducted. In the case of certain dyes blinking is observed so that, once activated, intermittent dark-states are observed that can make stoichiometry measurements difficult. In addition, the conversion from 'dark' to 'on' state has a certain efficiency so that not all fluorophores present in the sample can be observed. For example, the fluorescent protein mEos3.2, undergoes fluorescence intermittency or 'blinks' 2.8 times on average after photoactivation and has a conversion efficiency of $\sim$40% [65]. Recent developments in organic dyes have created bright fluorophores that blink on average 1.4 times and can exhibit 95% photoactivation efficiency [69], making stoichiometry experiments more accessible. Another advantage of PALM is that, unlike STORM, no specific buffer is required to facilitate the activation, meaning that biological samples can be imaged in their typical media.

Most dyes photobleach by interaction with singlet oxygen dissolved in the imaging buffer [158]. Stochastic optical reconstruction microscopy (STORM) [32, 41] surrounds fluorophores by an oxygen-scavenging buffer, allowing excited electrons to stochastically enter a triplet or dark state. Conversely to PALM, in STORM all dyes are initially fluorescent and are sent into a dark state by the excitation laser. In the case of Alexa Fluor 647, molecules can be brought out of this dark state multiple times by 405 nm illumination (typically achieving $\sim$17 switching events per Alexa Fluor 647 molecule with 405 nm illumination or $\sim$8 without 405 nm illumination [159] (figure 2.14b). The distribution

of switching event numbers can make stoichiometry measurements difficult in STORM, especially when attempting to count low numbers of targets. Similarly to PALM, the localisation rate can be turned with activation laser power in order to achieve optimal imaging. A disadvantage of STORM is that the buffers required to make different fluorophores blink may be harmful to living cells, reducing the applicability of STORM to imaging in live cells. An advantage of STORM compared to PALM for imaging is that each fluorophore is localised multiple times so that higher localisation densities can be achieved, creating higher-resolution reconstructions. This is especially useful for determining the distribution of low-expression targets if stoichiometry measurements are not important.

Points accumulation for imaging in nanoscale topology (PAINT) [38] can achieve a near-unlimited number of localisations of a single target by maintaining a supply of diffusive imaging probe in the solution of the sample being imaged. The imaging probe (which can be a fluorophore itself or is tagged to one) binds transiently to the target of interest. When the probe is unbound fast Brownian motion blurs its emission out on the detector but when it is bound to its target the emission is able to form a tight PSF on the detector and the position can be localised (figure 2.14c). In the case of some fluorophores such as Nile red [160, 161], which binds non-specifically to hydrophobic regions such as the space between lipids in plasma membranes, the emissive properties are changed upon binding allowing for additional rejection of non-bound probes. As the binding is transient, photobleached fluorophores are replaced by unbleached fluorophores and imaging can continue indefinitely achieving 10^6-10^9 localisations from a single cell [82]. DNA-PAINT [39, 162] is a variant of PAINT that uses short 'imaging' oligonucleotides tagged with fluorescent dyes to achieve target-specific PAINT imaging. The target protein of interest within a biological sample is expressed with a short 'docking' strand of single-stranded DNA. A complimentary 'imaging' strand of DNA is added to the sample and transiently duplexes to the docking strand. The primary disadvantage of all PAINT methods is dramatically increased background fluorescence due to unbound fluorophores present in the media. As a consequence, excitation confinement techniques are of increased importance compared to all other labelling strategies. The primary advantage of PAINT is the ability to record very high localisation densities in order to increase reconstruction resolution. In theory, DNA-PAINT allows for accurate stoichiometry measurements, being able to distinguish between monomers, dimers and larger clusters from the blinking rate of each target [128]. However, it has so far been technically difficult to implement. As DNA-PAINT imaging on intracellular targets requires cell-membrane permeability it is not applicable to live biological samples. However, there is no reason why live cell imaging is not possible when considering extracellular targets such as

the majority of membrane proteins. Such experiments could allow for statistically significant diffusion analysis on an individual cell basis.

In this work all three labelling strategies are presented with the addition of labelling with a non-modulatable fluorophore at a low labelling level so that even when all fluorophores are emitting their PSFs do not overlap. All live cell work was conducted in this method or with PALM whereas fixed cell work was conducted in PALM, STORM or PAINT modes depending on the aim of the experiment.

2.5 Compatible Fluorophores for the DHPSF

Due to the photon-splitting nature and transmission inefficiencies in the additional optics of the DHPSF compared to 2D SMLM, the DHPSF is typically only compatible with brighter (defined as quantum efficiency multiplied by extinction coefficient) fluorophores. This can be somewhat mitigated with the use of SNR increasing techniques as previously discussed, however, low quantum efficiency fluorophores, such as GFP, can still be challenging to image with the DHPSF. The fluorophores used in this work are listed in table 2.1 with expected detected photons at 30 ms exposure under typical imaging conditions and the corresponding localisation precisions quoted. These fluorophores were chosen as they represent some of the brightest and most commonly used products that are commonly available and, excluding mEos3.2, are compatible with NHS ester labelling of antibodies.

Flurophore	**Expected photons at 30 ms**	**5th and 95th percentile (photons)**	**Lateral Localisation Precision (nm)**	**Axial Localisation Precision (nm)**	**Absorption Maximum (nm)**	**Excitation Wavelength (nm)**
mEos3.2	350	250, 700	26±2	59±5	571	561
TMR	850	450, 1,550	19±2	43±5	555	561
JF549	900	600, 1,400	19±2	43±5	549	561
PA-JF549	2,000	1,000, ,5,000	13±2	26±2	552	561
AlexaFluor 647	1,900	1,200 4,000	14±2	26±2	650	640

Table 2.1 Experimentally measured number of detected photons of all fluorophores presented in this work with corresponding localisation precision, required excitation laser and compatible SMLM techniques.

2.6 Discussion

At the time of building, in 2014-15, the DHPSF instrument built in the lab was one of the first such instruments in Europe. The instrument was designed to be capable of both 3D DHPSF imaging and standard 2D imaging by removing the DHPSF phase-mask. This is often useful in range finding and proof of concept experiments due to the greatly reduced fitting times required for 2D imaging. The instrument is flexible in its application due to having multiple laser lines (405 nm, 488 nm, 515 nm, 561 nm and 640 nm) and interchangeable filter sets. The image path contains two $4f$ systems facilitating simultaneous two-colour imaging experiments. Drawbacks of the instrument include significant focal drift from the microscope body. This has been somewhat mitigated with the use of fiducial correction and automated live correction, however, newer microscope bodies such as the Nikon Perfect Focus System allow for increased focal stability without increasing experimental complexity by adding fiducial markers. Due to the reduction in signal inherent to DHPSF imaging the collecting power of the objective lens and sensitivity of the detector is of great importance. At the time of writing the instrument contains the highest NA water objective (1.27 Nikon PLAN APO) and most sensitive EMCCD camera commercially available but in the near future there may be scope to further upgrade these components, reducing the DHPSF's key limitation of signal collection. The most useful improvement to the microscope system would be automation. Currently, finding areas of interest (such as cells and especially those with fiducial markers within the field of view) and focussing the microscope are conducted manually, requiring an operator in between acquisitions. Throughput could be improved significantly if all aspects of imaging could be automated, as recently demonstrated for 3D STORM imaging by Beghin *et. al.* [163].

More generally, the most obvious improvement to the DHPSF technique as a whole is related to fitting of the raw data. Currently the only published method of reconstructing DHPSF data is easy-DHPSF [137], which is slow compared to 2D fitting algorithms and requires user-defined thresholds to separate noise from true PSFs, making it incompatible with batch-processing. In 2016 the Single-Molecule Localization Microscopy Symposium ran a software benchmarking competition encouraging the development of DHPSF fitting algorithms with many of the entrants outperforming easy-DHPSF on test data sets. However, at the time of writing none of these options have been published or distributed. Dr Leila Muresan, at the Cambridge Advanced Imaging Centre, is attempting to develop steerable filters as an alternative to the template-matching used in easy DHPSF to eliminate the need for user-defined thresholds. Additionally, a 'quick and dirty' alternative fitting routine was

written by Dr Aleks Ponjavic within the lab using PeakFit to find individual localisations relating to lobes of the DHPSF before linking together localisations in MATLAB to approximate the 3D position of fluorophores. This fitting routine is typically a factor 10 faster than easy-DHPSF but is subject to increased background localisations and localisation precision. As a result, this method is only used to save time providing an initial overview of preliminary data before all final data sets are analysed with easy-DHPSF. Wang *et. al.* use a cepstrum-based reconstruction scheme to deconvolve wide-field DHPSF images into traditional 2D images with additional 3D information, extending the depth of field of diffraction-limited imaging [164]. A similar approach could potentially improve DHPSF identification by deconvolving DHPSF data into traditional 2D data, where PSF identification is simpler and the library of developed processing techniques is far more developed. Once the DHPSFs had been identified SM fitting to the original DHPSF data would provide 3D SR information.

The key advantages of the DHPSF compared to other 3D SMLM techniques is the increased depth of field and isotropic resolution. Astigmatism and biplane methods are typically limited to a working depth of field of $\sim$500 nm, defined by the focal depth of the objective, whereas the depth of field of the DHPSF can be up to 4 μm. In terms of implementation, astigmatism microscopy is the easiest to implement as it requires just the addition of a cylindrical lens into the emission path. Biplane microscopy can be more difficult to implement as the path length of both channels must be precisely set in order to offset the two focal planes. Dual-objective biplane methods are additionally complex as two high-power objective lenses must be held in close proximity above and below the sample, limiting sample geometry. The DHPSF method is between the two in implementation difficulty. The $4f$ system requires somewhat precise alignment and the position of the phase mask is very important. However, as global shifts in the PSF are corrected for by the calibration, so as long as the phase mask is placed in the Fourier plane and the additional optics are broadly aligned, the DHPSF is functional. Multifocus microscopy (MFM) [93], which has been demonstrated to achieve a $\sim$4 μm depth of field by splitting the emission path onto nine separate areas of the detector, requires more precise alignment of additional optics and restricts the maximum field of view to $\sim$20 μm in published raw datasets.

The DHPSF instrument is capable of operating in both an imaging mode and a tracking mode, as described and demonstrated in chapters four and five respectively. The work completed on extending the DHPSF to imaging large volumes is described in chapter three.

2.7 Methodology

DHPSF Microscope

A bespoke microscope capable of achieving the DHPSF transformation was designed and built incorporating two EMCCD detectors and a 1.2NA water immersion lens or 1.27NA water immersion lens mounted on a scanning piezo stage. The water immersion lens provides $\sim$4 μm depth of field and is capable of imaging PSFs away from the coverslip surface. (see chapter 3 for more details).

405 nm, 488 nm, 515 nm, Cobolt), 561 nm and 640 nm laser beams were circularly polarised, expanded, collimated and aligned coaxially before being focussed onto the back aperture of the objective lens mounted onto an inverted microscope frame. The fluorescence signal was separated from the excitation beams into the emission path by a quad-band dichroic mirror. In the emission path, a wavelength-specific phase mask placed in the Fourier-plane of a $4f$ system performed the double-helix PSF transformation. In two colour experiments an additional dichroic mirror was placed in the emission path to separate the signal originating from the two different fluorophores. Long-pass filter and band-pass filters placed just before the detector were used to isolate the imaged fluorescence emission from background fluorescence. Finally, an EMCCD camera recorded the emission signal for later analysis.

Micromanager control software [165] was used to control individual laser shutters and camera acquisition time. Manually operated optical density filters in each laser line were used to control laser power incident on the sample. For 2D imaging the same set up was used with the exception of excluding the DHPSF phase masks.

DHPSF-Microscope Components

Lasers 405 nm (120 mW, iBeam smart-405-s, Toptica), 488 nm (240 mW, Cobalt MLD, Cobalt) 515 nm (400 mW, Cobalt Fandango 150, Cobalt), 561 nm (200 mW, Cobolt Jive 100, Cobolt) and 640 nm (200 mW, iBeam smart-640-s).

Neutral density filter Wheel containing 0.2, 0.3, 0.4, 0.5, 0.6, 1.0, 2.0, 3.0 and 4.0 OD Ø1" filters (FW2AND, THORLABS).

Wavelength-specific quarter-wave plate 405 nm, 488 nm, 515 nm, 561 nm and 633 nm (WPQ10M, THORLABS).

Beam expanders Ø1" concave and convex N-BK7 lenses, anti-reflection coated 350-700 nm. Focal lengths of -30 mm and 200 mm for 405 nm, 488 nm, 515 nm and 641 nm excitation paths. Ø1" concave and convex N-BK7 lenses, anti-reflection coated 350-700 nm. Focal lengths of -75 mm and 200 mm for 561 nm excitation path (Thorlabs).

Shutters and controller (SH05 & SC10, THORLABS).

Excitation filters (FF01-405/10-25, LL01-488-25, LL01-514-25, LL02-561-25, FF01-640/14-25, Semrock).

Köhler lens Ø1" focal length 300 mm N-BK7 Plano-Convex lens, anti-reflection coated 350-700 nm (LA1484-A).

Dichroic beam combiners (Di02-R561-25x36, Di02-R514-25x36, Di02-R405-25x36, Semrock).

White light source (M590L3-C5).

Microscope body (Eclipse Ti-U, Nikon).

Beamsplitting dichroic (Di01-R405/488/561/635-25x36, Semrock).

Objective lens (1.2 NA Plan Apo VC 60×, 1.27 NA Plan Apo VC 60× or 1.45 NA CFI Apo TIRF 60×).

Objective lens piezo translation (P-726 PIFOC, PI).

Sample mounting stage (HLD117, Prior Scientific) with bespoke aluminium inset (Department of Chemistry workshop).

4f system lenses Ø2" focal length 200 mm N-BK7 Plano-Convex lenses, anti-reflection coated 350-700 nm (LA1979-A).

Three-axis translation stages (PT3(A)/M).

Emission filters For 488 imaging (FF01-496/LP-25 & FF01-525/15-25, Semrock). For 515 imaging (FF01-515/LP-25 & FF01-582/75-25, Semrock). For 561 imaging (BLP02-561R-25 & FF01-580/14-25, Semrock). For 640 imaging (BLP01-647R-25 & FF02-675/67-25, Semrock).

DHPSF phase mask (DoubleHelix Optics) for 530 nm, 580 nm and 650 nm wavelength emission.

EMCCD detector (Evolve 512 Delta, Photometrics).

Calibrating the DHPSF

In order to calibrate the relationship between rotation of the DHPSF and axial position within the depth of focus, diffraction-limited fluorescence beads were imaged at the appropriate wavelength while being scanned through the depth of focus. For all work presented in this thesis, calibration was achieved by imaging 100 nm Tetraspeck fluorescently labelled polystyrene beads (T7279, ThermoFisher).

A solution of 100 μL of a $\sim 3.6\times10^8$ particles/mL solution of fluorescent beads in phosphate-buffered saline (PBS) (2810305, MP Biomedical) was prepared and filtered (0.22 μm Millex-GP syringe filter unit, Millipore). Argon-plasma cleaned (PDC-002, Harrick Plasma) microscope slides (24×50 mm borosilicate, thickness No. 1, Brand or 22×22 mm borosilicate, thickness No. 1, VWR) were coated with 0.01% poly-L-lysine (PLL) (molecular mass 150–300 kDa; P4832, Sigma) for 30 minutes and washed with filtered PBS before adding the diluted beads. After 2 minutes at room temperature the slides were washed in filtered PBS and imaged using the DHPSF microscope. The piezo stage was used to scan the objective lens axially through the sample in 40-50 nm steps across 4 μm, recording ten 30 ms exposure acquisitions at each step.

Determination of Localisation Precision

Fluorescent beads, prepared as in DHPSF calibration, were imaged for 2,000 frames with 30 ms exposure with and without the inclusion of the phase mask in the imaging path at a range of laser powers such that the emission signal of the beads covered the dynamic range of the EMCCD using a method previously described [105] Beads were localised using PeakFit for 2D images and easy-DHPSF for DHPSF images. An algorithm was written in MATLAB to analyse the output localisations, separating localisation from individual beads via basic cluster analysis. A histogram of the position of each bead's localisations in each dimension was plotted and fit to a Normal distribution. The standard deviation of the fit Gaussian function gives the localisation precision in each dimension. This value was then plotted

against the mean number of detected photons per frame for each bead. An exponential decay with the form $Y = Ae^{x/t} + C$ was fit to this data, where C represents the ultimate stability of the instrument and t the speed at which this localisation precision is reached.

Measurement of Focal Drift

Fluorescent beads, prepared as in DHPSF calibration, were imaged for 30,000 frames with 30 ms exposure by the DHPSF microscope. An auto-focus script roughly maintained the focus of the sample by periodically checking the angle between the lobes of the DHPSF of the fiducial marker and moving the piezo stage to return to the original position.

Fiducial correction was then applied to correct the position of the marker with the distribution of the corrected position plot via a histogram in all three dimensions. A Gaussian function was fit and used to extract the standard deviation of this distribution in x, y and z. The SNR was reduced by lowering the laser power so that the fiducial marker was close to the detection limit and the experiment was repeated.

Chapter 3

Reducing Aberrations in the DHPSF Away from the Coverslip

This chapter describes work conducted towards reducing specific aberrations present when imaging with the DHPSF. First, in collaboration with the O'Holleran group in CAIC, the effect of Fourier-plane misalignment is addressed and a solution to minimise this aberration is provided. Then a description of how spherical aberrations in the DHPSF that are present when imaging away from the coverslip can be reduced, extending the DHPSF to imaging large volumes. Quantification of the form of the DHPSF before and after this aberration reduction is provided and the trade-offs of the methodology are discussed.

Contributions

Dr Steven Lee and I designed the experiments presented in this chapter. All experiments were conducted and analysed by me. Sohaib Abdul Rehman and Dr Kevin O'holleran identified and modelled the aberrations caused by phase mask misplacement. Sohaib helped to take data relating to Fourier-plane shift and advised about analysis.

Named Publications Relating to this Chapter

- Three-Dimensional Super-Resolution in Eukaryotic Cells Using the Double-Helix Point Spread Function. **Alexander R. Carr**, Aleks Ponjavic, Srinjan Basu, James McColl, Ana Mafalda Santos, Simon Davis, Ernest D. Laue, David Klenerman and Steve F. Lee. Biophysical Journal, 2017.
- Maximizing the field of view and accuracy in 3D Single Molecule Localization Microscopy. Sohaib Abdul Rehman, **Alexander R. Carr**, Martin O. Lenz, Steven F. Lee and Kevin O'Holleran. Optics Express, 2018.

3.1 Compensation of Fourier Plane shift by Phase-Mask Translation

The majority of modern microscopes employ infinity-corrected objective lenses which output collimated light rays collected from the focal plane. These rays are then focussed to an image in the image plane by a tube lens. As a result, the exact distance between the back focal plane (BFP) of the objective lens and the tube lens is not crucial for the majority of 2D localisation microscopy. This is useful as additional optics can be added between the objective and tube lenses (in infinity space) without moving the image plane. However, in the case of 3D imaging techniques, the position of the tube lens is more important as it can result is a displacement of the Fourier plane in $4f$ systems (figure 3.1a&b). If a phase-modifying component (such as the DHPSF phase mask) is placed out of the Fourier plane of the objective lens, point sources away from the central focal plane are laterally shifted relative to the optic (figure 3.1c), which results in a spatially varying PSF. The cause of this shift is discussed further by S.A. Rehman *et. al.* [166].

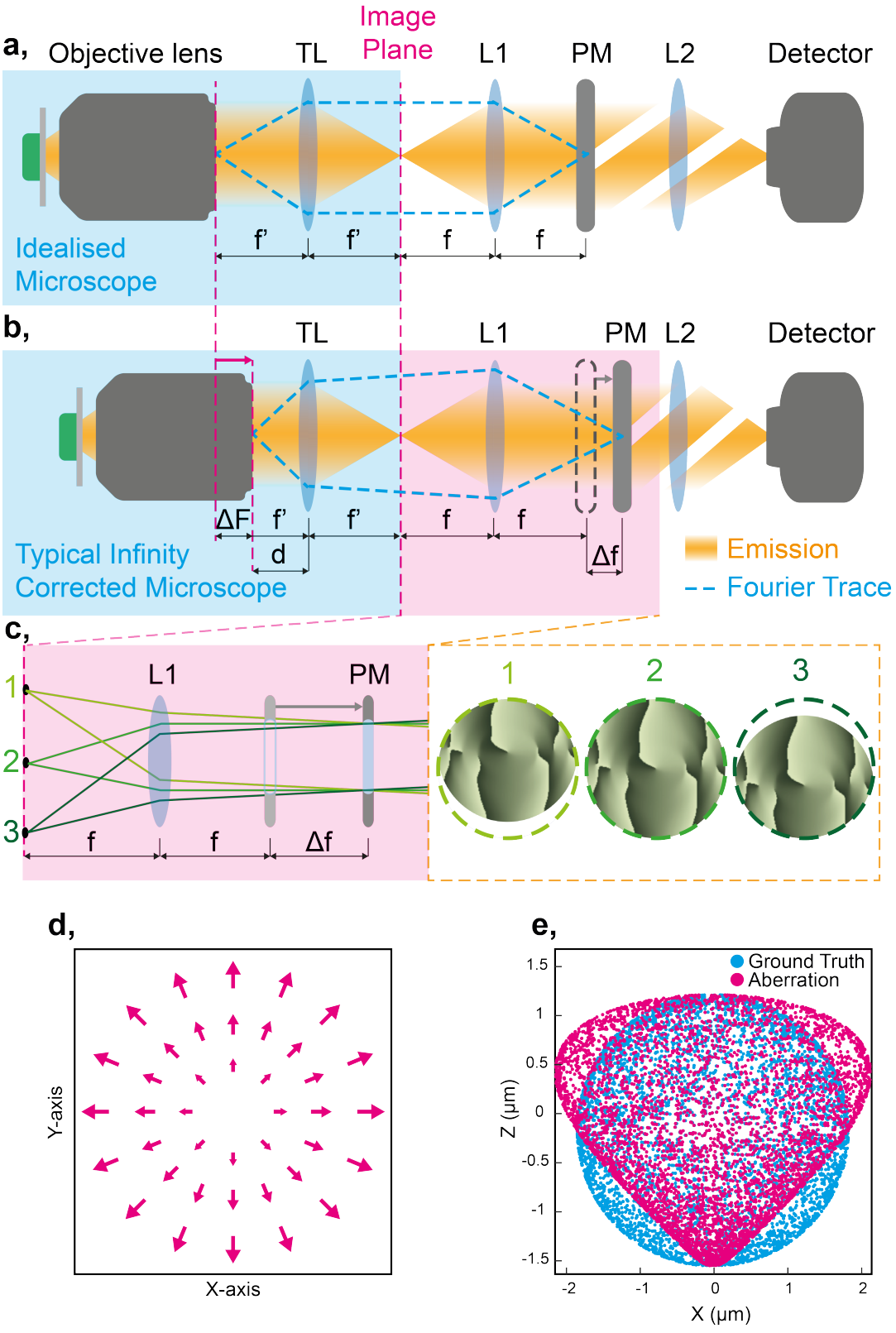

Fig. 3.1 Figure caption on following page.

Fig. 3.1 (Previous page.) The effect of Fourier plane misalignment on DHPSF imaging. $4f$ system (L1&L2) emission paths for an idealised microscope (a) and a typical infinity corrected microscope (b). A shift in the distance between the back-focal plane of the objective lens and the tube lens (TL) causes a translation of the Fourier plane and thus the phase mask (PM) should be translated accordingly. (c) Ray trace of the emission of three points within the FOV overlapping in the true Fourier plane of the system. (d) Simulated radial displacements of the DHPSF for a 35 mm mismatch between PM and Fourier plane. (e) Simulated displaying the effect of radial distortion across the depth of field on SMLM image reconstruction when imaging a spherical sample (errors exaggerated 10-fold). The aberration acts to contract the reconstruction below the centre of the focal plane and to expand it above the centre of the focal plane.

The effect of Fourier-plane misalignment on localisation reconstruction is that localisations are shifted radially with a magnitude and direction determined by both the position of the fluorophore laterally from the image centre and the distance away from the axial midpoint (figure 3.1d). This acts to compress the reconstruction below the focal midpoint and expand it above the focal midpoint (figure 3.1e). This can be particularly important when precise comparisons are being made between large distances or when successive focal planes are aligned to form a composite image. In literature, the phase mask of DHPSF systems is routinely shown to be in the focal plane of the relay lenses [98, 99, 92], indicating that this aberration is commonplace within DHPSF data. Moreover, in work published by Diezmann *et al.* post-correcting field-dependent aberrations in the DHPSF, a similar radial displacement is seen [167]. In the supplementary information of this study an approximately 70 nm radial shift is shown at an axial depth of 600 nm, suggesting that phase mask has been placed in the centre of the $4f$ system rather than in the true Fourier plane.

For our DHPSF instrument, when the DHPSF phase mask was placed in the expected Fourier plane (i.e. the centre of the $4f$ systems), the lateral shift of beads across the field of view was measured to reach 120 nm by 1.5 μm above and below the centre of the focal plane. This shift was reduced to $\sim$50 nm when the phase mask was moved closer to the true Fourier plane (figure 3.2). In this case the lateral shift of the DHPSF was minimised empirically and thus was limited by the ability to see a change in DHPSF centre point compared to the EMCCD's pixels. It is important to note that this shift relates to a loss of accuracy and not a loss of precision within localisation fitting. Repeatedly localised fluorophores/objects will exhibit broadly similar distributions across the field of view, however, the precise distance between points far apart in the field of view will be expanded/contracted in relation to their axial position. The effect this shift has on localisation data is further discussed by S.A. Rehman *et. al.* [166]. In experiments that require precise measuring (a precision of <50 nm)

of large distances (>∼5 μm) between points or accurate stitching together of multiple planes, this effect can be further minimised by more-precise phase mask placement. However, for all experiments presented in the following chapters the loss of accuracy is negligible. This work was published in 2018 in Optics Express [166].

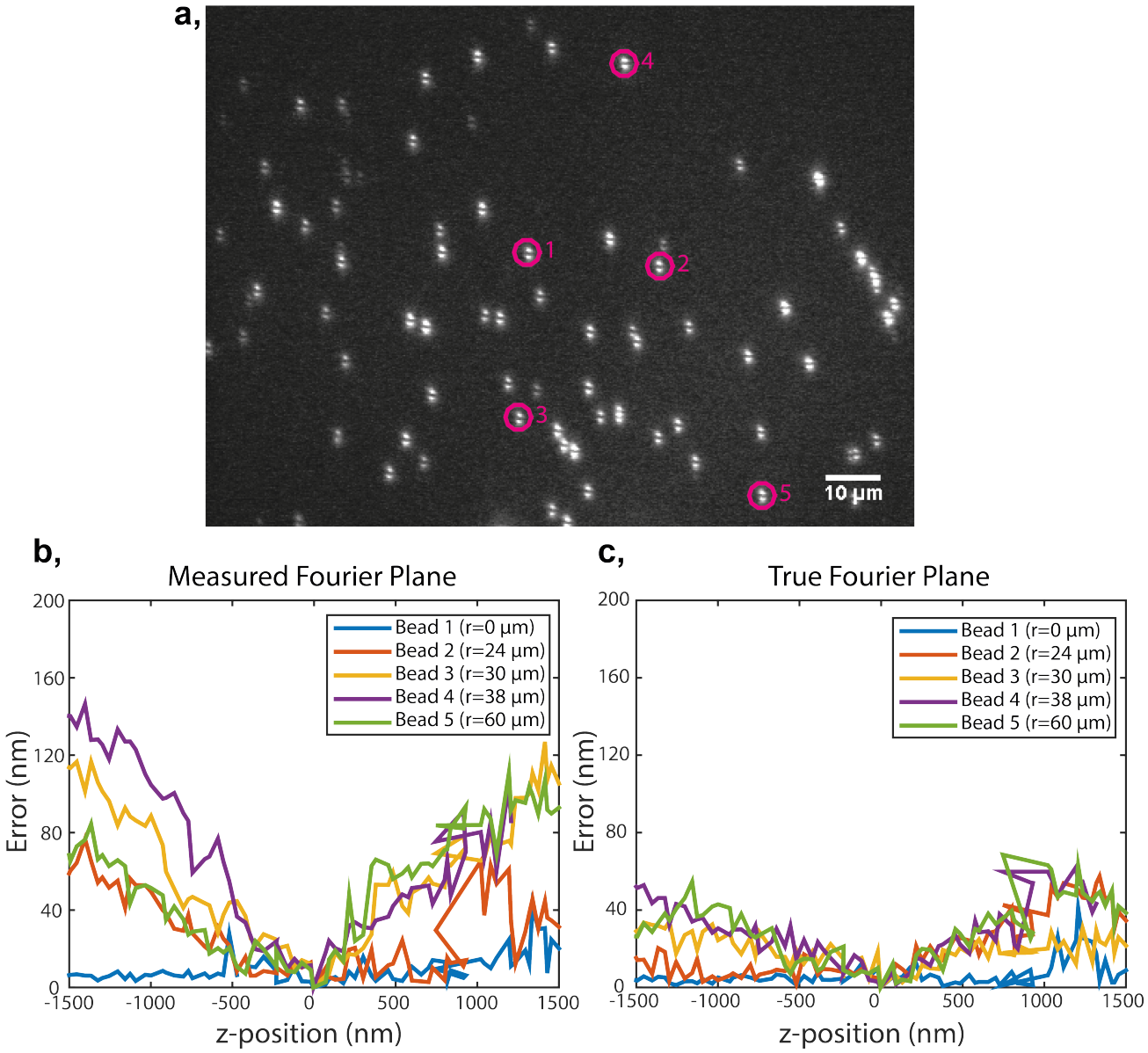

Fig. 3.2 Correction of errors due to Fourier-plane misalignment. (a) Raw data of DHPSF identifying the individual fluorescent beads analysed in (b) and (c). (b) Total axial displacement error across a 3 μm depth of field for five fluorescent beads across the FOV when the DHPSF phase mask is placed in the centre of the $4f$ system. (c) Total axial displacement error across a 3 μm depth of field for the same five fluorescent beads across the FOV when the DHPSF phase mask is placed in the true Fourier plane.

3.2 Reducing Spherical Aberration Away from the Coverslip

In the absence of aberration, the DHPSF rotates linearly as a function of depth within the depth of field so that measuring the angle between lobes corresponds to the true depth within the sample. As aberration is introduced the DHPSF is degraded, spreading out the lobes and altering the rotation [97, 168]. This not only results in a reduction of signal but also in a discrepancy between the apparent depth and true depth.

Spherical aberration (SA) is characterised by the axial spreading out of the PSF of an optical system so that rays are not all focussed to the exact same point. SA is induced when different rays effectively travel different distances due to variations in refractive index between their respective paths. This is the case when imaging a sample with an immersion objective lens that employs an immersion media with a different refractive index to the sample being imaged, with the effect being exaggerated with increased axial depth into the sample, as shown in figure 3.3.

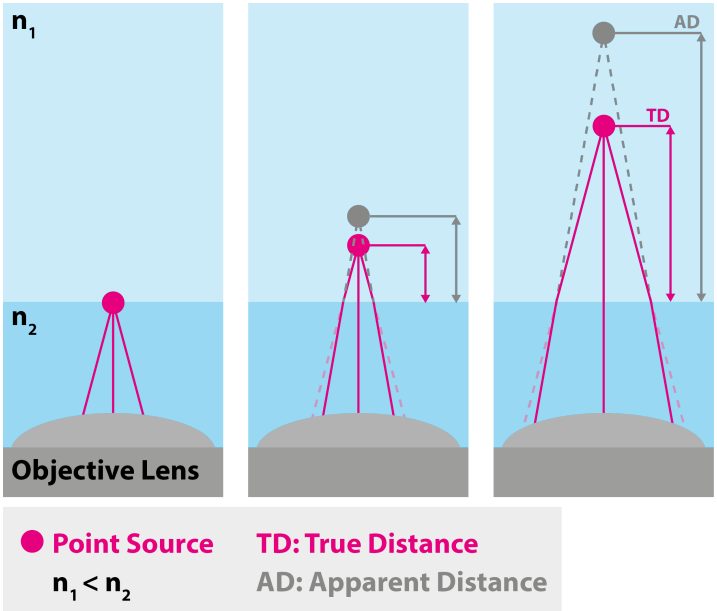

Fig. 3.3 Ray diagram of an immersion objective lens imaging point sources in a sample of different refractive index representing sample media and immersion liquid/coverslip (approximating $n_{immersion} = n_{coverslip}$). A change in refractive index results in a discrepancy between true distance and apparent distance from the interface.

In DHPSF imaging, the mismatch of refractive index between immersion oil (n=1.515), used for high numerical-aperture (NA) objective lenses, and typical sample media ($n \approx$1.33) degrades the DHPSFs when imaging away from the surface (figure 3.4). With increased axial depth, an asymmetry in the rotation of the DHPSF is induced [101] before the form of the two lobes is completely degraded [147] so that fitting cannot be conducted. Theoretical modelling of the DHPSF estimates a discrepancy of 800 nm between true depth and apparent depth at the centre of a focal plane positioned 50 μm above from the coverslip surface, when imaging in water with an oil immersion objective lens [168].

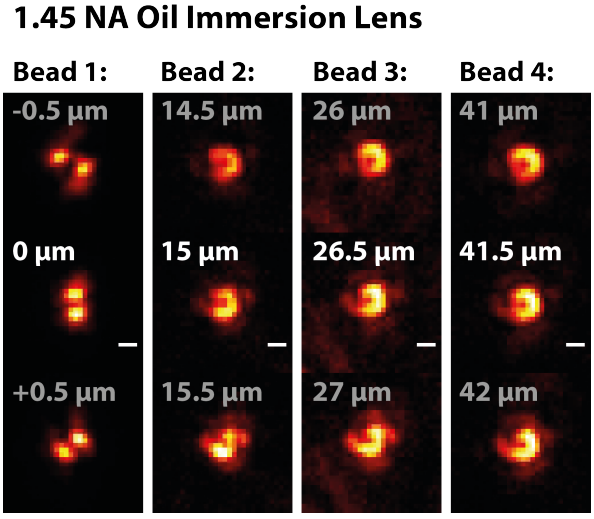

Fig. 3.4 DHPSFs at increasing axial depths. Example DHPSFs from 100 nm fluorescent beads when imaged with a 1.45 NA Plan Apo TIRF oil immersion objective lens at a range of axial depths. Fluorescent beads were suspended in 1% agarose solution ($n \approx$1.33). Labels represent the distance above the coverslip of each image plane. Scale bars are all 1 μm.

As the refractive index of biological samples is typically close to that of water (n_{water}=1.33, $n_{HeLa-cell} \approx$1.37 [169], $n_{bovine-muscle-tissue} \approx$1.38 [170]), SA is introduced when imaging away from the coverslip surface with an oil immersion objective lens. This has limited the working range of DHPSF imaging to volumes at the coverslip surface, making it incompatible with most aspects of eukaryotic cell imaging. Previously, the DHPSF had only been shown to image smaller prokaryotes and the basal surface of eukaryotic cells [101, 100, 106, 103, 104]. However, in addition to recent developments in whole-cell imaging [82, 146], large-volume imaging away from the coverslip with the DHPSF is motivated by biology. Many biological processes in eukaryotes occur away from the coverslip surface, in the nucleus or cytoplasm, outside of the axial range of previous DHPSF imaging methodologies. Interactions between membrane proteins and coated-coverslip surfaces may also perturb resting-state dynamics

and organisation [171, 150, 151]. In many cases the apical membrane may provide a more physiological representation of membrane protein distributions.

3.3 Matching the Refractive Index of Media and Immersion Liquid

The effect of refractive-index mismatch between immersion liquid and sample media on imaging above the coverslip was identified by Hell *et. al.* in confocal microscopy [172, 173]. In this case, oil or glycerol was used as media to match the refractive index with the immersion oil and reduce spherical aberration away from the surface. For biological samples it is more convenient to employ a water-immersion objective lens in order to match the refractive indexes, at the cost of some collecting power. Collecting power goes as NA^2. The theoretical difference in collecting power between a 1.45 NA and 1.2 NA lens is a factor 0.685 and was measured to be 0.676 by 5,000 2D localisations of fluorescent bead PSFs at constant excitation power. When imaging in aqueous media (e.g. agarose and most sample media) with a water immersion objective lens, the form of the DHPSF is preserved further than 50 μm above the surface (figure 3.5) due to the reduction of SA. Fixed biological samples display a higher refractive index (typically $\approx$1.4) and thus may be better matched by the use of silicone oil immersion objective lenses ($n_{silicone}$ =1.41), however, in practise water immersion lenses have proven suitable for imaging away from the coverslip in live and fixed tissue samples.

3.4 Quantification of Aberration away from the Coverslip

The effect of SA away from the coverslip was investigated by imaging fluorescent beads suspended in a gel solution with a refractive index close to water. The fluorescent beads were scanned through the depth of focus of the objective lens at 50 nm intervals via a piezo motor. A 1.45 NA oil immersion objective lens was used to image fluorescent beads with a focal plane centred at the surface and 5 μm, 15 μm and 30 μm above the surface. The relation between the angle of the DHPSF and axial position of the stage was plot so that an angle of 0 degrees corresponded to the mid-point of the focal plane ($z = 0\mu$m) for three repeats at each focal depth (figure 3.6). No localisations could be fit when the focal plane was positioned 30 μm above the coverslip. At 5 μm above the coverslip the angle matches well

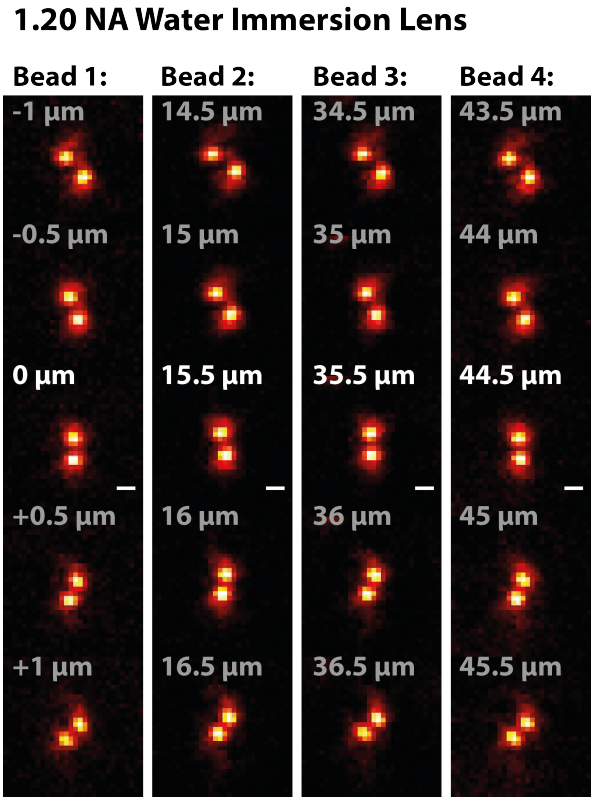

Fig. 3.5 DHPSFs at increasing axial depths. Example DHPSFs from 100 nm fluorescent beads when imaged with a 1.20 NA Plan Apo water-immersion objective lens at a range of axial depths. Fluorescent beads were suspended in 1% agarose solution ($n \approx 1.33$). Labels represent the distance above the coverslip of each image plane. Scale bars are all 1 μm.

to those recorded at the coverslip for negative depths (below the centre of the focal plane). For positive depths (above the centre of the focal pane), the angle was significantly less when imaging above the coverslip (at +1.5 μm the angle was -63° when imaging at the coverslip and -54° when imaging 5 μm above the coverslip). This is consistent with theoretical and experimental data presented by Ghosh *et. al.* [168] for the case of increasing SA. When imaging 15 μm above the coverslip, the curve flattens out further, deviating from the surface case above and below the centre of the focal plane (the difference in angle was +15° and -12° at +1.5 μm and -1.5 μm respectively). The rotation rate was reduced with increased distance from the coverslip, corresponding to an increase in the depth of field as the apparent depth and true depth are separated by SA, as shown in figure 3.3.

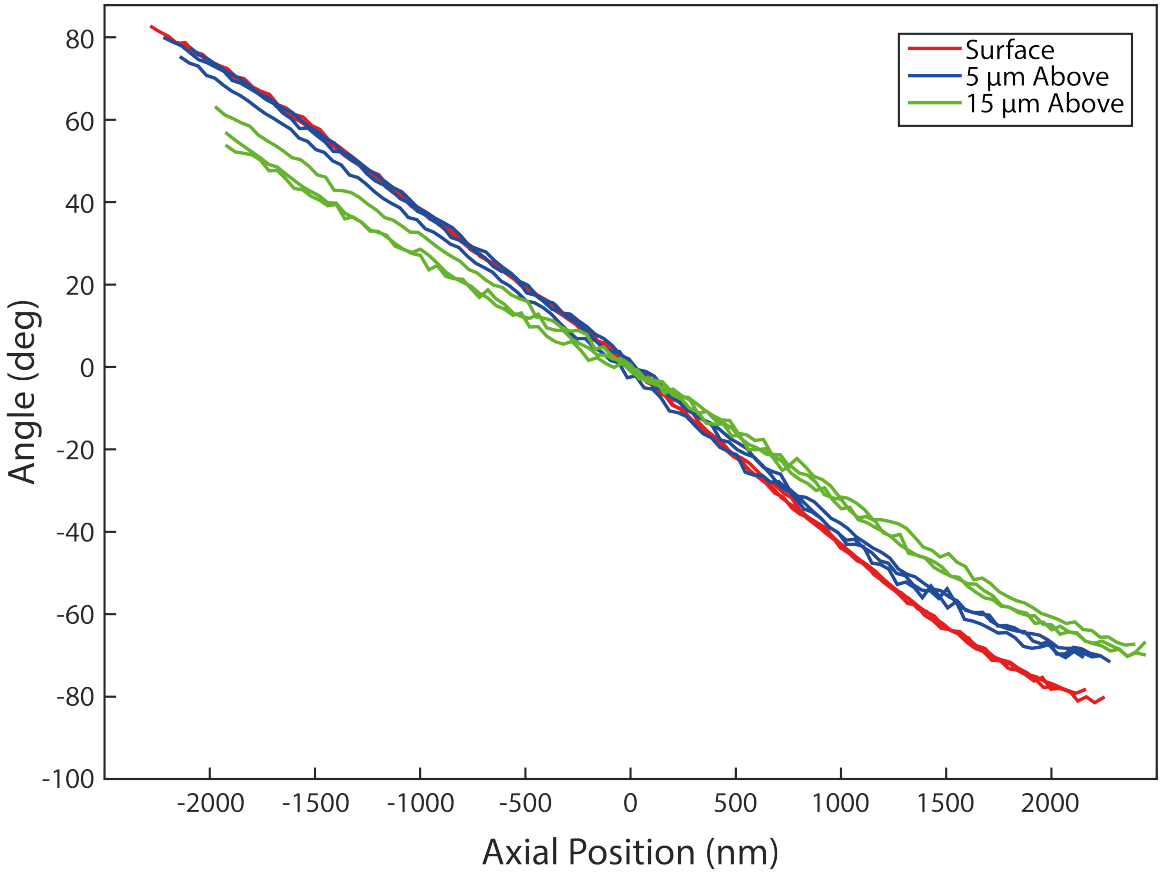

Fig. 3.6 The effect of increased spherical aberration due to imaging above the coverslip with a mismatch of refractive indices on the rotation of the DHPSF. A 1.45 NA oil immersion lens was used to image fluorescent beads suspended in aqueous gel ($n \approx n_{water}$) at a range of depths above the coverslip with the DHPSF in 50 nm axial steps throughout the depth of focus. The angle between DHPSF lobes as a function of axial position within the depth of focus is plot for three repeats of beads at the coverslip surface (red), 5 μm above (blue) and 15 μm above (green) the coverslip surface. An angle of 0° is taken to represent the centre of the focal depth (z = 0 nm).

A 1.2 NA water immersion objective lens was used to scan fluorescent beads suspended in gel solution to better match the refractive indices of the immersion liquid and gel. The focal plane was centred at the surface and 15 μm, 30 μm and 45 μm above the coverslip surface. The angle between the lobes of the DHPSF was plot against the axial position of the stage so that an angle of 0 degrees corresponded to the mid-point of the focal plane (z=0 μm) for three repeats at each focal depth (figure 3.7a). It was possible to fit the DHPSF at all axial distances with no obvious deterioration of the form of the DHPSF by eye. The curves plotted for all axial distances above the coverslip overlapped at all axial positions, indicating that there was no significant distortion of the depth of focus with increased distance from the coverslip.

The total 3D Cartesian error between each fluorescent bead was investigated using easy DHPSF with a bead at the surface used as the calibration stack in order set thresholds to identify localisations in the remaining bead data. The total Cartesian error was determined at each 50 nm axial step for each bead using the mean position of localisations from the respective image plane in x, y and z with the equation $r = \sqrt{r_x^2 + r_y^2 + r_z^2}$, where r is the total Cartesian error, and $r_{x,y,z}$ are the mean displacement in x, y and z respectively. The Cartesian position of the bead at $z = 0$ nm was considered as the origin in displacement calculations. The produced plot of axial position and Cartesian error (figure 3.7b) showed significant localisation errors increasing towards the periphery of the depth of focus, reaching $\approx$100 nm at the extremes. However, no significant differences in error were seen between beads at different distances away from the coverslip. These errors are within the range expected for non-fiducial corrected experiments and would likely be brought to within the localisation precision limits should fiducially correction be implemented. This work was published in 2017 in the Biophysical Journal [147].

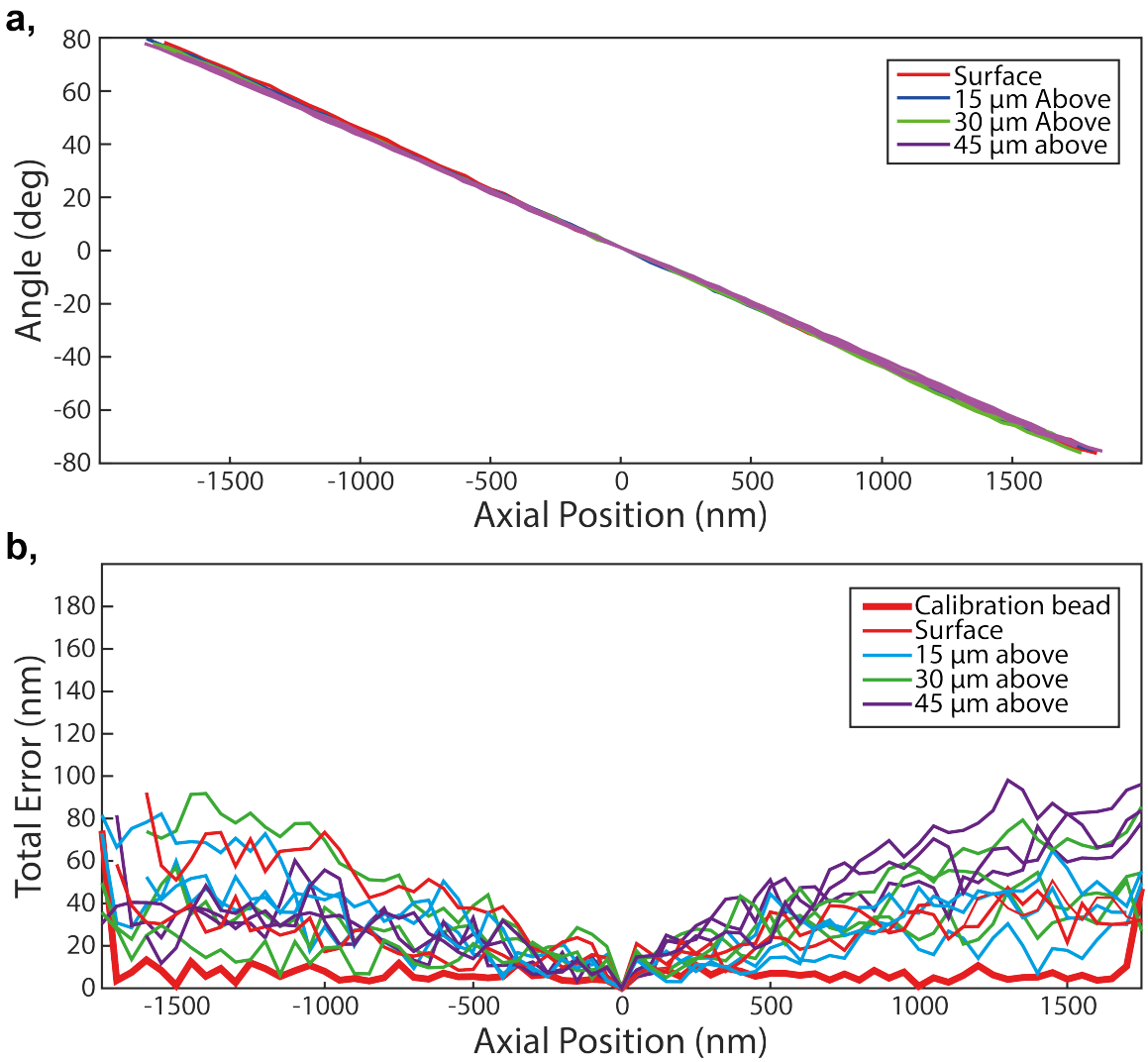

Fig. 3.7 The effect of imaging above the coverslip with matched refractive indices on the rotation of the DHPSF. A 1.27 NA water immersion lens was used to image fluorescent beads suspended in aqueous gel ($n \approx n_{water}$) at a range of depths above the coverslip with the DHPSF in 50 nm axial steps throughout the depth of focus. (a) The angle between DHPSF lobes as a function of axial position within the depth of focus is plot for three repeats of beads at the coverslip surface (red), 15 μm above (blue), 30 μm above (green) and 45 μm above (purple) the coverslip surface. An angle of 0° is taken to represent the centre of the focal depth (z = 0 nm). (b) Total Cartesian error as a function of axial depth the bead data shown in (a). The bead located at the surface that was used to create templates for fitting in easy DHSPF is highlighted (thick red line).

3.5 Discussion

Reducing aberration is important for any imaging system in order to preserve image quality across the sample as well as factors such as usable field-of-view (FOV). Aberration can be particularly damaging for super-resolution techniques due to the small length scales being investigated and thus many studies have focussed on its reduction, especially in 2D [174–176]. Although a number of studies have been published addressing aberration in the DHPSF system [167, 168] the field is still relatively unknown. The cause of the lateral-shifting aberration was not previously known, as demonstrated by characteristic radially-increasing lateral errors quantified but not reduced by Diezmann *et al.* [167]. While the work presented in this chapter focusses on the effect of Fourier plane translation on the DHPSF, the cause and solution apply to all PSF engineering techniques employing infinity-corrected optics. In the case of the DHPSF, a reduction in this spatially-varying aberration reduces systematic lateral and axial errors, extending the usable FOV so that the excitation geometry is now the limiting factor [166]. Reducing this aberration is important for imaging employing successive image-planes with the DHPSF. The lateral contraction at the bottom of the focal volume would overlap with the lateral expansion at the top of the focal volume, resulting in potential misalignment of up to $\sim$400 nm for a radius of 21 μm if the phase mask is positioned in the centre of the two $4f$ lenses as opposed to the Fourier plane [166].

Infinity corrected optics are routinely employed in modern microscope setups as additional optics such as polarisers can be added into the emission path without effecting the position of the image plane. This allows for more flexible microscope design but can have unwanted effects for phase-modifying imaging modalities as the back focal plane of the objective lens no longer aligns with the focal plane of the tube lens. This has the effect of separating the conjugate back focal plane with the Fourier plane of the system. When designing a microscope employing phase-modifying optics (as required for PSF engineering), this separation should be measured to ensure optimal instrument performance. The exact position of the Fourier plane is also dependent on the wavelength of light due to chromatic aberration and thus optics should be moved accordingly when imaging at different wavelengths. The approximate position of the Fourier plane within a $4f$ system can be found by eye by passing collimated light down the objective lens and minimizing the spot created within the $4f$ system. More precise alignment requires measurement of the rotation of the DHPSF across the field of view to minimise relative motion between PSFs. It is possible to envision an analysis tool that would identify and analyse the relative motion of DHPSFs from fluorescent beads as they are scanned through the focal plane of the microscope. This could

provide a quantitative metric on the alignment of the phase mask with the Fourier plane that could be used to rigorously locate the optimal alignment of the system.

3.5.1 Consequences of Employing Water-Immersion Lenses

The reduction of SA away from the surface comes with trade-offs. The primary disadvantage of employing a water immersion lens over an oil immersion lens is a sacrifice of collecting power. As previously stated, a factor 0.685 reduction of signal is expected. Due to the photon-splitting nature of the DHPSF this is of increased importance as it further limits the sensitivity of the technique to low SNR samples. For newer bright organic dyes this is typically not a limiting factor, however, for dimmer fluorescent proteins, such as GFP, this reduction in signal can be critical. Another issue is the evaporation of the immersion media for water immersion lenses. This can limit the duration of very long experiments ($>\approx$5 hours) and lead to additional focal drift. Immersion oils with a refractive index matched to water can be used to eliminate this effect when long acquisitions are required. Advantages of using water as an immersion liquid include ease of cleaning and a reduction in the relaxation time when the focal plane is moved due to the reduced viscosity of water compared to oil. The depth of focus of the DHPSF is affected by the NA of the objective lens (as well as by the emission wavelength, λ). Ghosh *et. al.* calculate that the rate of rotation of the DHPSF is proportional to $\approx \lambda n_a$ [168], so that swapping from a 1.45 NA oil immersion lens to a 1.27 NA water immersion lens should result in a 14% increase in rotation rate. However, a $\approx$5% reduction in rotation rate was observed for the data presented in figures 3.6&3.7 over a 3 μm axial range. This is likely due to unspecified differences between lens constructions.

Reducing SA away from the coverslip in biological samples by employing a water immersion objective lens facilitates DHPSF imaging in a range of previously inaccessible areas, such as the apical cell surface, the cytoplasm and nucleus of cells [147]. Whole-cell imaging is also made possible by stitching together neighbouring image planes distributed across large volumes. The true physiological state of protein dynamics on the cell membrane can be investigated on the apical surface of cells, away from interactions with coated coverslip surfaces that may have perturbative effects [171, 150, 151]. This advancement allows for a greater range of biological processes to be investigated by the DHPSF, adding to the versatility of the technique as a biophysical tool.

Applications of the DHPSF in technically demanding areas of cells, away from the coverslip surface, are described and demonstrated in chapters 4 and 5.

3.6 Methodology

Measurement of Error due to Fourier Plane Shift

In order to measure the localisation error caused by misalignment of the DHPSF phase mask outside of the Fourier plane, fluorescent beads (T7279, ThermoFisher) were imaged across the depth of focus at a range of lateral positions across the field of view. The same beads were axially scanned through the focus with the phase mask placed in the midpoint between the two lenses in the $4f$ systems (the theoretical Fourier plane) and in the true Fourier plane. The true Fourier plane was found by minimising lateral shift during rotation across the field of view empirically in iterative steps. The lateral position of each bead at the middle of the focus (z =0 nm) was taken as its origin and the total Cartesian distance from the origin for each bead was recorded at each axial position as the error.

Imaging the DHPSF Away from the coverslip Surface

Fluorescent beads (T7279, ThermoFisher) were suspended in either agarose (A9414, Sigma) or phytagel (P8169, Sigma) and imaged with the DHPSF with 561 nm excitation. For suspension in agarose, a 1% solution of agarose in 2 mL of filtered (0.22 μm Millex-GP syringe filter unit, Millipore) phosphate-buffered saline (PBS) (2810305, MP Biomedical) was heated until boiling and kept at 40°C until use. For suspension in phytagel, a 1% solution of pytagel and 2 mL of filtered PBS was heated until boiling and kept at 70°C. For both solutions, 0.5 μL of a 1.8 x 10^{11} particles/mL solution of fluorescent beads (T7279, ThermoFisher) was added to 100 μL of gel solution at temperature. 50 μL of the mixture was then deposited onto argon-plasma cleaned (PDC-002, Harrick Plasma) coverslips (22$\times$22 mm borosilicate, thickness No. 1, VW) and allowed to cool to room temperature. The slides were then mounted onto the DHPSF instrument and the piezo stage was used to determine the distance above the coverslip and scan the objective axially through the depth of focus. Ten 30 ms exposures were recorded at each 50 nm step for all fluorescent beads at a range of axial depths into the sample.

Quantifying Signal Reduction Between Water and Oil Immersion Objective Lenses

Fluorescent beads on Poly-L-lysine (PLL) (molecular mass 150–300 kDa; P4832, Sigma) coated coverslips were imaged without the DHPSF phase mask at the coverslip surface with both a 1.45 NA oil immersion objective lens (1.45 NA CFI Apo TIRF 60×, Nikon) and a 1.20 NA water immersion objective lens (1.2 NA Plan Apo VC 60×, Nikon). Ten fields of view were imaged in each case for at 30 ms exposure, collecting ten frames at each location. PeakFit [136] was used to fit the observed 2D PSFs and extract the mean number of photons detected per localisation.

Chapter 4

Single-Particle Tracking Applications of the DHPSF

This chapter focusses on 3D tracking of individual proteins in areas previously inaccessible to the DHPSF. The reduction of spherical aberration away from the surface described in chapter 3 facilitates tracking of single particles in live cells away from the coverslip. Single-particle tracking experiments are presented for a range of target proteins, including membrane-bound, cytoplasmic and nuclear proteins, for cell in suspension and adherent cells. Finally the applicability of the DHPSF to single-molecule tracking is discussed.

Contributions

Dr Steven Lee and I designed all experiments presented in this chapter. I conducted all experiments and analysed all data. All diffusion analysis and simulation code was written by myself in MATLAB. Dr James McColl maintained T cell samples and assisted with T-cell labelling. Dr Srinjan Basu and the Laue group provided all labelled ES cell samples and helped to design the preliminary tracking experiments presented in figure 4.11.

Named Publications Relating to this Chapter

- Three-Dimensional Super-Resolution in Eukaryotic Cells Using the Double-Helix Point Spread Function. **Alexander R. Carr**, Aleks Ponjavic, Srinjan Basu, James McColl, Ana Mafalda Santos, Simon Davis, Ernest D. Laue, David Klenerman and Steve F. Lee. Biophysical Journal, 2017.

4.1 Tracking away from the Coverslip Surface

The DHPSF has previously been used to track mRNA labelled by association with the fluorescent protein EGFP in yeast cells [101] as well as quantum dots diffusing in 80% glycerol and at the coverslip surface of colon-derived cells [100]. These studies have been confined to imaging at the coverslip surface or in high-n_a media (1.44 n_a for 80% glycerol) to due to spherical aberration present when imaging away from the coverslip caused by a mismatch in refractive index between the immersion liquid (1.52 n_a for immersion oil) and imaging sample ($\approx$1.33 n_a for water-based media and cells). However, there is also strong research interest in SPT in live cells away from the coverslip surface [177, 131, 113] for which the DHPSF was previously incompatible due to increased spherical aberration. The reduction of spherical aberration, when imaging away from the coverslip described in chapter 3, by matching the refractive index of the immersion media and sample, facilitates live-cell SPT with the DHPSF across large volumes [147]. This enables SPT studies of protein motion and binding kinetics at the apical surface of cells, away from potential interactions with unphysiological surfaces. It also enables SPT studies in the nucleus of mammalian cells, where 2D techniques typically perform poorly due to non-flat sample geometries.

4.2 3D Single-Particle Tracking Tools

Although a range of SPT tools are freely available for 2D localisation data, 3D-SPT tools are not yet well established and distributed. The two most common diffusion-analysis tools are mean-square displacement (MSD) [134] and jump-distance (JD) [178] analysis. Both MSD and JD analysis determine diffusion coefficients by linking localisation data in time to identify trajectories of individual fluorophores. A range of studies have focussed on dealing

with aspects such as fluorophore blinking, platform drift and crossing/overlapping trajectories [179–181].

MSD analysis calculates diffusion coefficients by plotting the mean-square displacement of trajectories from their origin for a given time interval Δt [182–185]. The shape of the MSD curves produced provides information on the nature of the diffusion. For example: a linear correlation between MSD and Δt indicates free Brownian motion, a plateau in the curve indicates confined diffusion and an increasing slope indicates directed motion such as active transport [186, 187]. MSD analysis can be conducted on individual trajectories by considering multiple start points or an ensemble of many trajectories to provide information about the overall diffusion population. However, as the analysis generally averages over all points within a trajectory transitions between diffusion states (such as a change from Brownian motion to active transport or an increase in diffusion coefficicent) can be obscured [188]. Similarly MSD analysis is not well suited to identifying subpopulations of diffusion states, although it can still be used to separate large differences in diffusion populations. MSD analysis becomes susceptible to inaccuracies when trajectories are short, as is often the case when imaging fluorescent proteins, as multiple start points cannot be considered from each trajectory [134]. As a rough guide, M. J. Saxton proposed that the maximum time interval considered should not exceed one-quarter of the total number of steps within a trajectory [134]. Therefore, if a minimum of four points are used to fit the MSD curve a minimum trajectory length of 16 time steps is required.

When experimental conditions limit trajectory length, an alternative method to analyse SPT data is jump distance (JD) analysis [178, 189–192]. In JD analysis, the distribution of Cartesian distances between successive localisations (jumps) within all trajectories is compared to a theoretically-derived probability function. By including multiple populations with different diffusion coefficients and fractions into the probability function it is possible to distinguish different diffusion subpopulations with greater accuracy than MSD methods. As JD analysis does not consider individual trajectories it does not provide information on the type of diffusion being exhibited (free, confined or active motion), additionally it provides less-accurate estimates for absolute values of diffusion coefficient, compared to MSD, for the majority of datasets as positional uncertainty errors are not averaged out within trajectories.

In this work, both MSD and JD analysis was extended to 3D-SMLM for 3D-SPT analysis of DHPSF datasets. The input for both methods was designed to be a list of 3D coordinates so that it is compatible with any 3D-SMLM technique or 2D-SMLM datasets by setting the axial position to a fixed value. The number of dimensions exhibited by the motion is also an

input parameter, altering the analysis to account for diffusion bound to a surface (2D motion in a 3D space) or full 3D diffusion (3D motion in a 3D space). The diffusion analysis was coded in MATLAB and is appended to this thesis.

4.3 Extending Mean-Squared Displacement Analysis to 3D

An algorithm performing MSD analysis on 3D localisation data was written in MATLAB by extending a method previously published by Weimann *et. al.* [135] into three dimensions (code available in appendix). However, unlike the previous code, the written analysis does not include its own fitting functions but instead operates on input localisation data (rather than raw image data). This makes the code applicable to localisation data from any SMLM source, in either 2D or 3D.

In 2D, the MSD for a given time interval $n\Delta t$ is defined as:

$$MSD(n\Delta t) = \frac{1}{l-n}\sum_{i=1}^{l-n}[x(i+n)-x(i)]^2+[y(i+n)-y(i)]^2 \tag{4.1}$$

Where l is the trajectory length, Δt is the time step between successive image frames and x and y are the 2D spatial coordinates of the particle.

In 3D this is extended to:

$$MSD(n\Delta t) = \frac{1}{l-n}\sum_{i=1}^{l-n}[x(i+n)-x(i)]^2+[y(i+n)-y(i)]^2+[z(i+n)-z(i)]^2 \tag{4.2}$$

Where x, y and z are the 3D spatial coordinates of the particle.

This MSD as a function of time interval, $n\Delta t$, is related to the short-range diffusion coefficient by:

$$MSD(n\Delta t) = 2qDn\Delta t + 2q\sigma^2 \tag{4.3}$$

Where q is the number of dimensions of diffusion present (3 for 3D diffusion or 2 for membrane-bound diffusion), D is the diffusion coefficient and σ is the localisation precision of the SMLM technique. In the case of 3D-SMLM, in which the lateral and axial localisation

precisions are generally different, σ is a convolution of the localisation precision in each dimension.

In order to extract the diffusion coefficient of individual trajectories a linear fit was conducted on the first four points of the MSD plot described by equation 4.3. Only trajectories with >16 localisations were used in this analysis since the maximum time lag should not exceed a quarter of the total trajectory length [134]. Ensemble diffusion coefficients were determined by calculating the mean MSD for each time interval between all trajectories, with errors given by the standard deviation.

4.3.1 Benchmarking Mean-Squared Displacement Analysis

In order to verify the results from the written MSD analysis algorithm, its performance was tested on a 2D data set and compared to the output of the previously published MSD code from Weimann *et. al.* For benchmarking purposes only, a 2D TIRF dataset of the membrane-bound T-cell receptor (TCR) complex tagged with tetramethylrhodamine (TMR) via a HaloTag diffusing on the basal surface of 12 Jurkat T cells sat onto passivating-coated coverslips was passed to both codes with the output MSD curves compared (figure 4.1) (see chapter 6 for a detailed introduction to T-cells and the adaptive immune response). For 2D analysis the axial position of all localisations was input as 0 nm to satisfy the data input format requirements of the code. The Weimann code output a 2D Diffusion coefficient of 0.046 ± 0.002 μm^2/s and the written code output $0.046\pm0.002\mu$m^2/s. All points on the MSD curves are within error and the calculated MSD curves agree well. The two lines do not match perfectly, most likely due to minor discrepancies between the position lists produced by each fitting protocol. The Weiman code includes its own fitting routines in MATLAB whereas the Peakfit plugin for ImageJ [136] was used to fit the raw 2D dataset for the written analysis code.

Next, the performance of the code was benchmarked against simulated 3D datasets (see chapter 4 methodology for more details) across a range of diffusion coefficients expected from biological samples ($\approx$0.1 μm^2/s for membrane-bound proteins and $\approx$1 μm^2/s for unbound diffusion). The effect of trajectory length and localisation precision on the performance of the analysis was investigated by distributing points randomly in space and displacing each point in 3 dimensions by a distance randomly sampled from a normal distribution with a width equal to the expected one-dimensional MSD for each frame, given by:

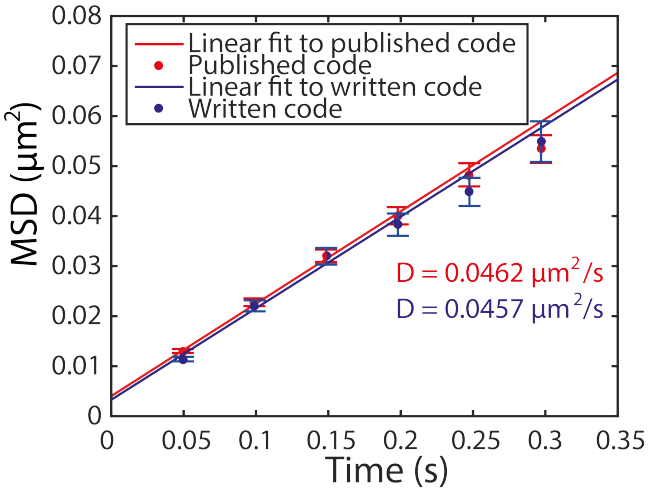

Fig. 4.1 Benchmarking MSD analysis against previously published code. A 2D data set of a membrane protein diffusing on the basal surface of Jurkat T cells was compared to a previously published MSD analysis algorithm.

$$MSD = \sqrt{2D\Delta t} \tag{4.4}$$

For each time step an addition displacement was added to all dimensions to simulate the effect of localisation precision of the instrument. This distance was sampled from a normal distribution centred at zero with a width equal to the measured lateral localisation precision in x and y and the measured axial localisation precision in z, for a simulated number of detected photons (see chapter 2). Unless stated otherwise, the number of simulated time steps was 16 per trajectory and the number of photons was assumed to be 1,000. The recall of the algorithm was calculated and compared to the simulated diffusion coefficients using:

$$Recall = \frac{D_{calculated}}{D_{simulated}} \tag{4.5}$$

The effect of the number of tracks analysed on recall was investigated by simulating trajectories with an experimentally determined localisation precision at a range of diffusion coefficients (figure 4.2a). 20 simulations with a 30 ms time step (as used in the majority of imaging experiments) were used to determine the mean recall value and standard deviation at each number of trajectories. The mean error in recall ($|1 - Recall|$), was less than 0.02 after 100 trajectories are considered and the standard deviation of recall was below 0.05 after 200 trajectories were considered, for all simulated diffusion coefficients. This indicates that

after 200 trajectories of minimal length (16 time steps) are analysed the algorithm is robust for diffusion coefficients of as slow as 0.01 $\mu m^2/s$, with fewer trajectories required for faster diffusion coefficients.

The effect of localisation precision determined by the number of detected photons on recall was investigated by simulating trajectories at a range of different diffusion coefficients (figure 4.2b). 20 simulations of 400 trajectories with a 30 ms time step were used to determine the mean recall and standard deviation at each number of detected photons. The mean error in recall was below 0.02 after 100 detected photons, which is below the detection limit of the microscope, for all simulated diffusion coefficients. The standard deviation of recall was below 0.05 for simulated diffusion coefficients of >=0.1 $\mu m^2/s$ at all considered detected photon numbers. For a simulated diffusion coefficient of 0.01 $\mu m^2/s$, $\sim$500 detected photons resulted in a standard deviation in recall of <0.05. This indicates that, at all experimentally feasible detected photon numbers, analysing 400 trajectories of minimal length (16 time steps) is robust for diffusion coefficients >=0.1 $\mu m^2/s$. For robust analysis of diffusion coefficients as low as 0.01 $\mu m^2/s$ a mean detected photons of >500 is required. This information was used to define a minimum number of detected photons for tracking experiments presented in this thesis of 500.

4.3.2 Identifying Bound and Unbound Trajectories

Additional functionality separating trajectories displaying bound/confined motion (*e.g.* static particles) from unbound/Brownian diffusion was implemented into the diffusion analysis code. Erroneous bound events are can be an issue in live-cell SPT experiments. By only considering unbound motion for samples known to exhibit only free or partially confined diffusion the impact of these erroneous trajectories can be reduced. This also acts as a useful tool in separating diffusion populations in systems exhibiting both bound and unbound motion, such as chromatin-remodelling proteins in embryonic stem cells [193], as the two populations can be analysed separately. In order to separate bound and unbound trajectories the individual MSD curves of all trajectories were compared to a linear fit to the first four points. Trajectories whose MSD curve did not fit well to a linear fit, by measure of R^2 value, were considered to be bound. Simulated trajectories were considered in order to determine the threshold value of R^2 to best separate the two populations. 600 trajectories were simulated as before for diffusion coefficients of 0 $\mu m^2/s$, 0.1 $\mu m^2/s$ and 0.7 $\mu m^2/s$, representing typical values for bound, membrane diffusion and 3D unbound trajectories respectively, each with axial and lateral localisation precisions centred at expected values for 500 detected photons.

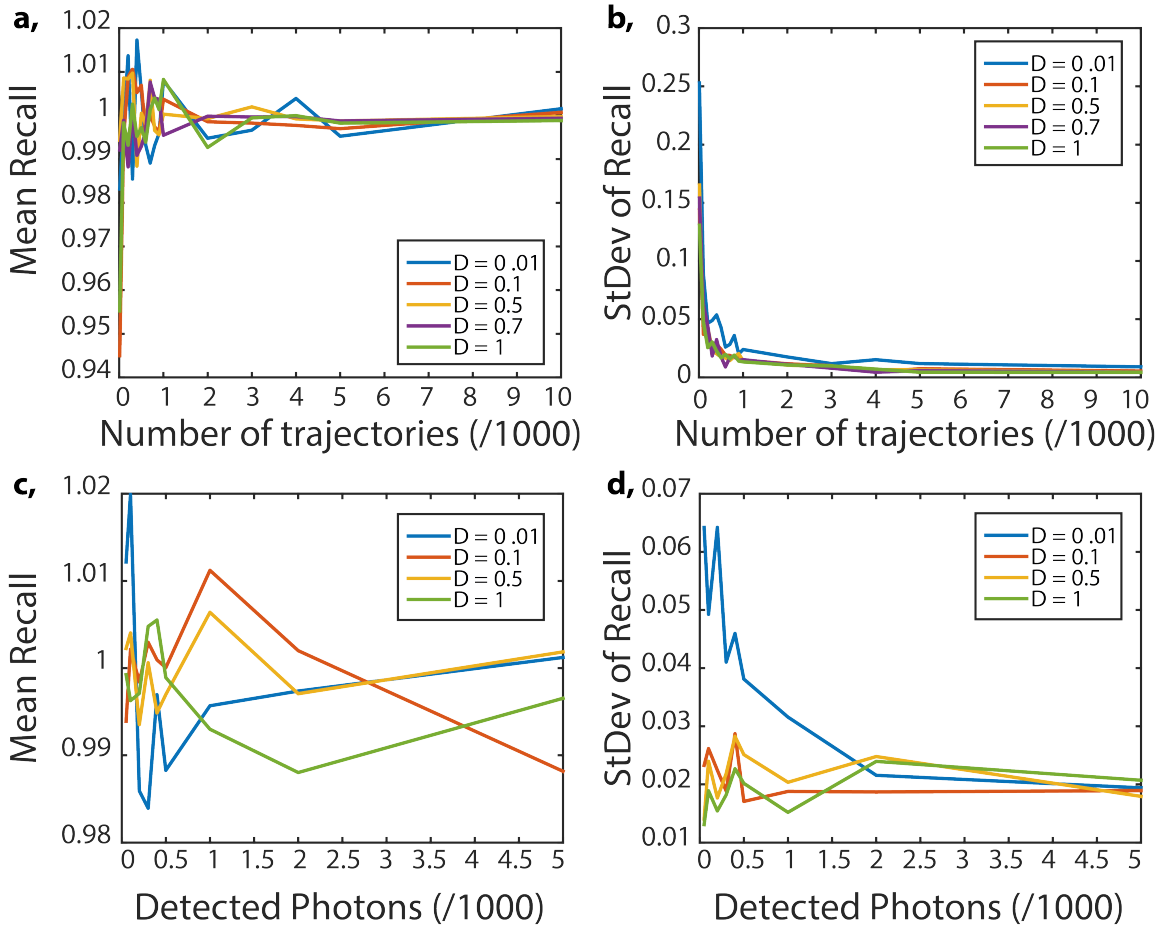

Fig. 4.2 Benchmarking MSD analysis against simulated 3D SPT trajectory data. (a) Mean recall in simulated diffusion coefficients from 20 simulated datasets at a range of diffusion coefficients as a function of the number of trajectories considered. (b) Standard deviation of recall as a function of the number of trajectories considered. (c) Mean recall in simulated diffusion coefficients from 20 simulated datasets at a range of diffusion coefficients as a function of 3D localisation precision determined by the number of detected photons per localisation. (d) Standard deviation of recall as a function of localisation precision.

For each trajectory the first four points of the MSD was fit with a linear function and the R^2 value recorded. A cumulative histogram of R^2 for each population was created (figure 4.3). An R^2 value of 0.85 was determined to give the most accurate identification of diffusion state, identifying >90% of unbound and bound trajectories correctly.

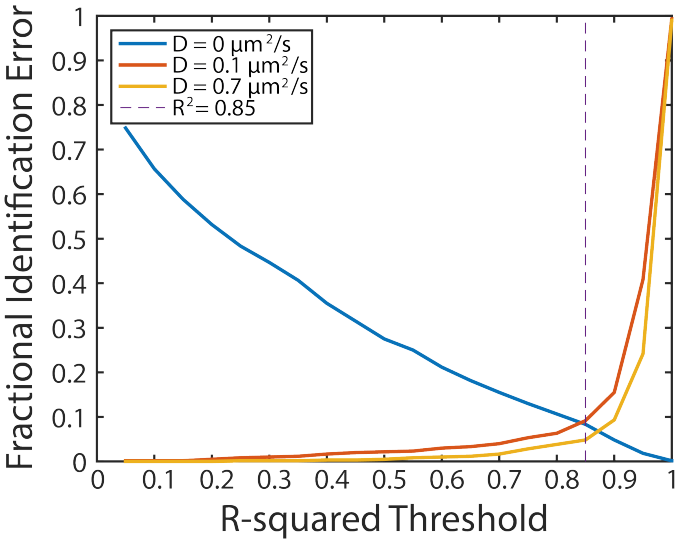

Fig. 4.3 Separating bound and unbound trajectories by R^2 value of linear fit to individual MSD curves. The fraction of simulated tracks from three diffusion populations that were misidentified as a function of the threshold value of R^2 is plot. The dashed line at $R^2 = 0.85$ represents the optimal threshold used in later SPT analysis.

4.4 Extending Jump Distance Analysis into 3D

JD analysis in 2D and 3D was added into the written algorithm. For 2D JD, the method provided by the previously Weimann code was followed [135]. For 3D, this method was extended to account for the modified probability distribution of Brownian motion in 2D compared to 3D. In 2D free-space diffusion the probability of a particle with a diffusion coefficient D displacing a distance r in time t is given by:

$$P(r,t) = \frac{r}{2Dt} e^{-r^2/4Dt} \tag{4.6}$$

Thus the normalised cumulative probability distribution of jump distances in 2D is given by [135]:

$$C(r,t) = 1 - e^{-r^2/4Dt} \tag{4.7}$$

In 3D free-space diffusion the probability of a particle with a diffusion coefficient D displacing a distance r in time t is given by:

$$P(r,t) = \frac{4\pi r^2}{(4\pi Dt)^{\frac{3}{2}}} e^{-r^2/4Dt} \tag{4.8}$$

By integration, the normalised cumulative probability distribution of jump distances in 3D is given by:

$$C(r,t) = \frac{8\pi Dt}{(4\pi Dt)^{\frac{3}{2}}} [\sqrt{(\pi Dt) erf(\frac{r}{\sqrt{\pi Dt}})} - re^{-r^2/4Dt}] \tag{4.9}$$

Where $erf()$ is the error function. Validation of equation 4.9 is shown for simulated 3D trajectories with experimentally determined localisation precision in figure 4.4.

The cumulative distribution of jump distances extracted from 3D-SPT tracking data is fit to a number of populations of equation 4.9 with different diffusion coefficients and fractions. Up to three populations are considered by the written code with the fewest number of populations that produces a good fit taken as the final answer.

4.4.1 Benchmarking Jump Distance Analysis

JD analysis is highly sensitive to localisation errors as, unlike in MSD analysis, the absolute distance of each jump is considered without any information about direction. As a result, when the localisation precision is comparable to the distance moved between each time step significant overestimations of the diffusion coefficient can occur. The effect of localisation precision on jump distance analysis was investigated by simulating static trajectories (see chapter 4 methodology for more details) with localisation precisions sampled from experimentally determined values at a range of detected photon numbers (figure 4.5a). The cumulative histograms of jump distances extracted from 20 repeats of ten particles at 300 time points separated by 30 ms (3,000 jumps) were fit to equation 4.9 in order to determine an idealised apparent diffusion coefficient. At 500 detected photons, a typical value for DHPSF SPT experiments as a compromise between SNR and track length, a diffusion coefficient of 0.035 μm^2/s was observed for a time step of 30 ms. The apparent diffusion

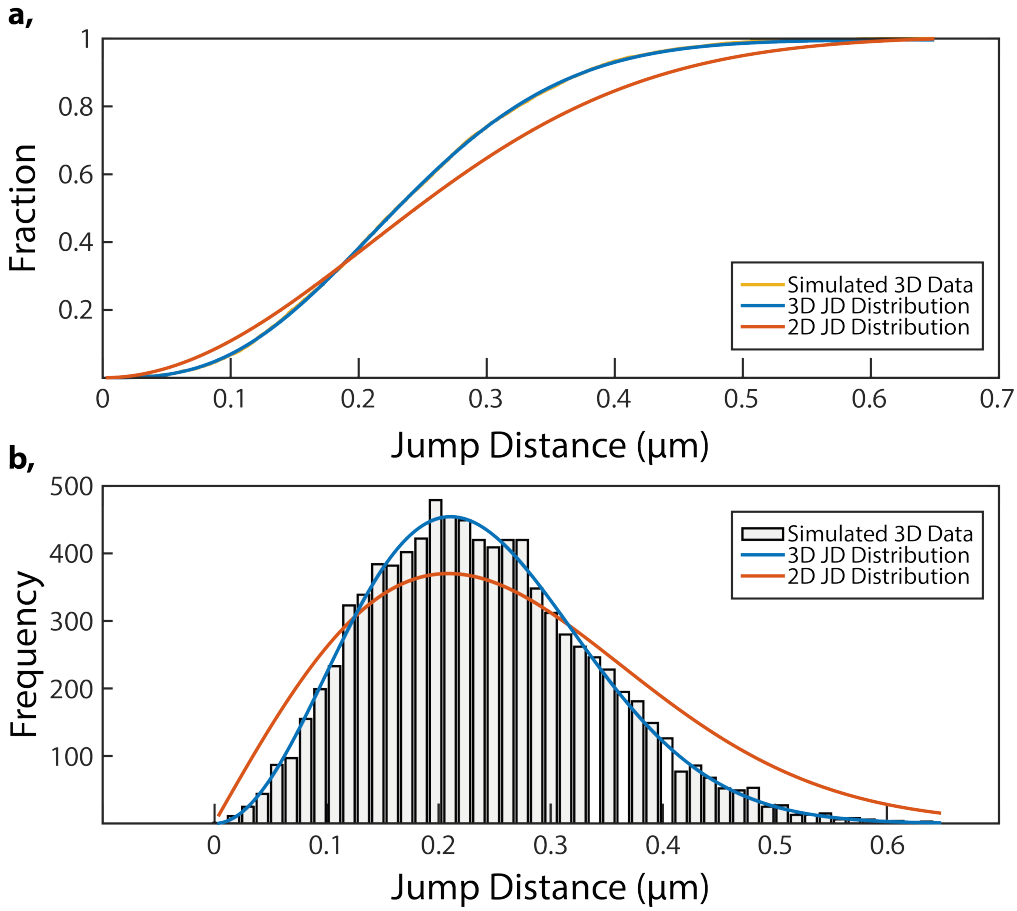

Fig. 4.4 Validation of 3D jump distance probability distribution vs 2D distribution for simulated trajectory data. 10,000 jump distances were simulated with a diffusion coefficient of 0.5 $\mu m^2/s$ and an experimentally determined localisation precision at 500 detected photons (25 nm laterally and 50 nm axially). The diffusion coefficient was calculated to be 0.5575 $\mu m^2/s$. (a) Cumulative histogram of simulated jump distances with fitted 3D (blue) and 2D (red) distributions as described in equation 4.9 and 4.7, respectively (data, yellow, obscured by 3D fit line). (b) Histogram of simulated jump distances with fitted 3D and 2D distributions given by the gradient of the lines plot in (a).

coefficient fell to 0.01 $\mu m^2/s$ by 1,700 detected photons, representing an $\sim$10% error for typical membrane-bound protein diffusion.

The effect of the number of jumps considered on recall was investigated by simulating trajectories with an experimentally determined localisation precision at 500 detected photons for a range of diffusion coefficients (figure 4.5b&c). 20 simulations with a 30ms time step were used to determine the mean and standard deviation of recall with increasing number of jumps. Due to the apparent diffusion coefficient quantified above for 500 detected photons

and a 30 ms time step, JD analysis performed poorly in terms of mean recall for simulated diffusion coefficients of 0.01 $\mu m^2/s$ and 0.1 $\mu m^2/s$, achieving a mean recall of $\approx$4.5 and $\approx$1.5 respectively at all jump numbers considered. Faster simulated diffusion coefficients were more accurately returned as the localisation precision constituted a smaller fraction of the total movement between time steps. At simulated diffusion coefficients of 0.5 $\mu m^2/s$ and 1 $\mu m^2/s$ a mean recall of $\approx$1.1 and $\approx$1.05 were achieved at all number of jumps. The standard deviation of recall was consistently below 0.05 after $\approx$1,000 jumps for all but the slowest diffusion coefficient (0.01 $\mu m^2/s$), which stabilised at $\approx$0.1 after $\approx$2,000 jumps. This analysis indicates that JD analysis is prone to systematic errors in diffusion coefficient estimations when localisation errors comprise a significant fraction of the distance travelled between time points but is relatively robust to the number of trajectories considered.

Next, the effect of localisation precision as a function of detected photons on recall was investigated for 3000 simulated jumps (figure 4.5d&e). 20 repeats of ten particles each with ten, 30 ms time steps at a range of simulated diffusion coefficients and experimentally determined localisation precision (see chapter 2) at a range of detected photon numbers. At higher detected photons, the recall of JD analysis is improved for slow diffusion coefficients (0.01 $\mu m^2/s$ and 0.1 $\mu m^2/s$). However, for faster moving diffusion coefficients (0.5 $\mu m^2/s$ and 1 $\mu m^2/s$) the number of detected photons has very little influence on recall. This is unsurprising as the localisation uncertainty comprises a greater fraction of the observed motion for slower diffusion compared to faster diffusion. Therefore, a reduction in localisation uncertainty will have a proportionally greater effect on the uncertainty of movement for slow diffusion as the distances moved are comparable to the uncertainty. For fast diffusion the localisation uncertainty is already insignificant at low detected photons compared to the total distance moved so the improvement is small.

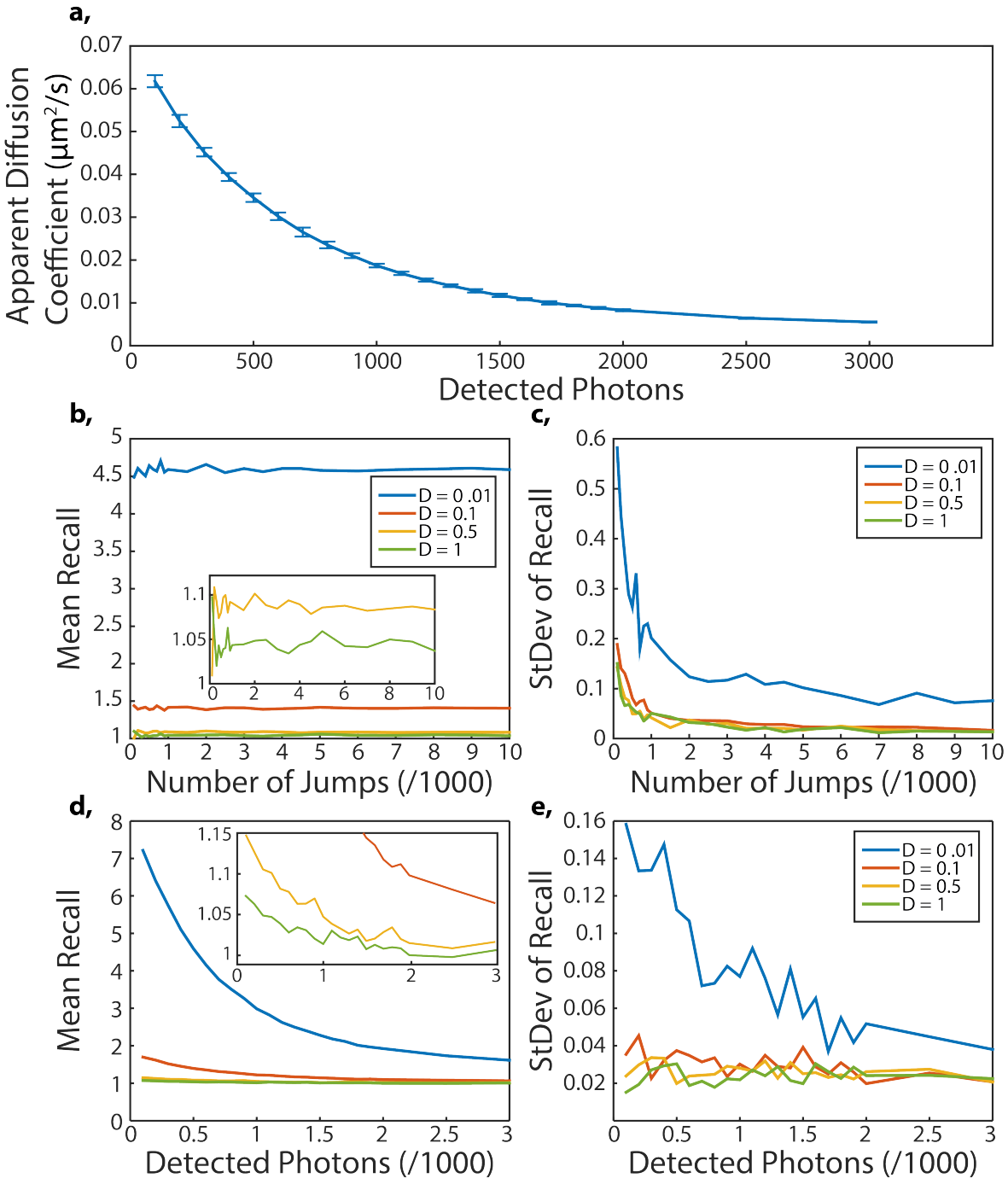

Fig. 4.5 Benchmarking jump distance analysis on simulated 3D SPT trajectory data. (a) The apparent diffusion coefficient measured by JD analysis on simulated static particles with localisation uncertainty experimentally determined by the number of detected photons. (b) Mean recall in simulated diffusion coefficient from 20 simulated datasets at a range of diffusion coefficients as a function of the number jumps considered. (c) Standard deviation of recall as a function of the number of jumps considered. (d) Mean recall in simulated diffusion coefficients from 20 simulated datasets at a range of diffusion coefficients as a function of the number of detected photons (colour scheme described in all other legends). (e) Standard deviation of recall as a function of the number of detected photons.

4.4.2 Identifying Diffusion Populations

One of the key benefits of JD analysis is its ability to resolve individual diffusion populations that may be present within a sample. Up to three diffusion populations can be fit with the analysis code. This could be extended to any combination of 2D and 3D diffusion populations if necessary. The performance of the code in separating diffusion population was evaluated with idealised simulated datasets comprised of populations with different diffusion coefficient (figure 4.6). 20 repeats were conducted to find the mean and standard deviation of diffusion coefficient and fraction assigned to each population at three different numbers of jumps (1,000, 10,000 and 100,000). An experimentally determined localisation uncertainty was included for 500 detected photons in order to emulate typical experimental conditions. Two diffusion distributions were analysed, the first with equal fractions of 1 μm^2/s, 0.1 μm^2/s and 0.01 μm^2/s diffusing populations (figure 4.6a&b) and the second with equal fractions of 1 μm^2/s, 0.5 μm^2/s and 0.1 μm^2/s diffusing populations (figure 4.6c&d).

Fig. 4.6 (Following page.) Identifying diffusion populations in simulated 3D SPT trajectory data. 20 datasets for two distributions of diffusion populations were simulated: $D_1 = 1\mu$m^2/s, $D_2 = 0.1\mu$m^2/s and $D_3 = 0.01\mu$m^2/s in equal fractions and $D_1 = 1\mu$m^2/s, $D_2 = 0.5\mu$m^2/s and $D_3 = 0.1\mu$m^2/s in equal fractions at 1,000, 10,000 and 100,000 jumps. (a) Mean and standard deviation of diffusion coefficients and fractions for the first distribution output by JD analysis. (b) Examples of one, two and three population fits to the simulated datasets for the first distribution. Individual diffusion populations are labelled. (c) Mean and standard deviation of diffusion coefficients and fractions for the second distribution output by JD analysis. (d) Examples of one, two and three population fits to the simulated datasets for the second distribution. Individual diffusion populations are labelled.

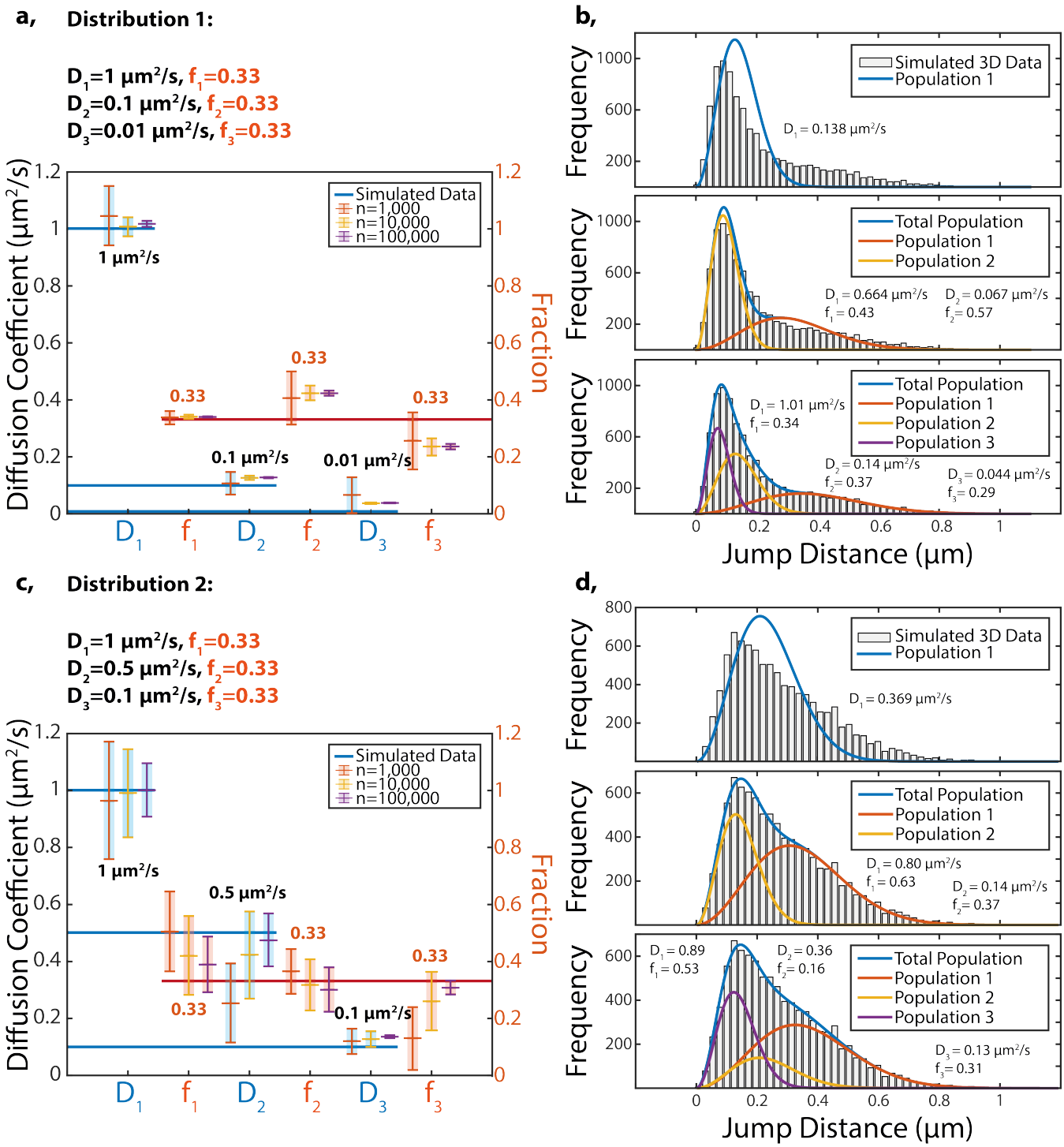

Fig. 4.6 Figure caption on previous page.

The diffusion coefficients of the first distribution (figure 4.6a&b) were returned well even at 1,000 considered jumps ($D_1 = 1.05 \pm 0.10 \mu m^2/s$, $f_1 = 0.34 \pm 0.02$, $D_2 = 0.11 \pm 0.04 \mu m^2/s$, $f_2 = 0.41 \pm 0.09$, $D_3 = 0.07 \pm 0.06 \mu m^2/s$, $f_3 = 0.26 \pm 0.10$), with errors reducing at high jump numbers. At all jump numbers the fraction of the second and third population were overestimated and underestimated respectively, although the true value was within error for the 1,000 jump case. This is likely due to the localisation uncertainty appearing to increase the diffusion coefficient for slow-moving particles.

The second distribution (figure 4.6c&d) was less well identified with greater errors for each measurement. At 1,000 total jumps the distribution was identified to be $D_1 = 0.97 \pm 0.20 \mu m^2/s$, $f_1 = 0.51 \pm 0.14$, $D_2 = 0.25 \pm 0.14 \mu m^2/s$, $f_2 = 0.37 \pm 0.08$, $D_3 = 0.12 \pm 0.04 \mu m^2/s$, $f_3 = 0.13 \pm 0.11$. However at greater jump numbers the distribution could be better resolved with $D_1 = 1.00 \pm 0.09 \mu m^2/s$, $f_1 = 0.39 \pm 0.10$, $D_2 = 0.48 \pm 0.09 \mu m^2/s$, $f_2 = 0.30 \pm 0.08$, $D_3 = 0.136 \pm 0.005 \mu m^2/s$, $f_3 = 0.31 \pm 0.02$ at 100,000 jumps.

Subfigures 4.6b&d show examples of one, two and three populations fit to both distributions for 10,000 jumps. For the first distribution (figure 4.6b), the three population fit matches the simulated diffusion coefficients and fractions within the error expected (quantified in figure 4.5a at 500 detected photons). The first overall distribution of JD does not match well to either one or two populations. However, the second distribution (figure 4.6d) does not match the simulated diffusion coefficients and fractions within expected errors and the overall distribution is well represented by both two and three population fits. In this case it would be difficult to judge from the data if two or three populations were present even though the populations are more distinct than in the first distribution. This indicates that the performance of the JD analysis could be influenced by the underlying distribution present in the sample.

4.5 Implications of MSD and JD for 3D Single-Particle Tracking

The metrics of interest, the underlying truth of the system and the experimental data available dictate whether MSD or JD is the better analysis tool. In both cases accuracy is improved as more data is collected, however, the nature of the trajectory data can influence the accuracy of JD and MSD differently. For example, if many short trajectories are collected, as if typically the case for SPT of fluorescent proteins, JD analysis can be effective while MSD requires at

least 16 time steps in each trajectory and may not be applicable. JD considers each time step individually and thus is not affected by track length but rather the total number of jumps.

JD is prone to systematic errors when the localisation uncertainty is comparable to the expected distance moved due to diffusion. This can limit its applicability to high-SNR systems or fast moving targets. In MSD localisation uncertainty errors are averaged out within trajectories, leading to a more uniform performance across the range of diffusion coefficients expected from biological systems. In the majority of SPT experiments a compromise between SNR (relating to localisation precision) and track length must be found. Once the minimum number of photons required to be detected by the SPT instrument is reached, MSD analysis is relatively more robust to the number of detected photons compared to JD analysis, allowing for longer tracks to be recorded without sacrificing recall for most biologically relevant diffusion coefficients. In 3D localisation errors are typically increased compared to 2D and an additional dimension of error is present, decreasing the effectiveness of JD analysis more significantly compared to MSD analysis.

JD analysis is better-suited to separating multiple populations of diffusion coefficient that may be present in some biological systems. For example, JD analysis could provide information on the ratio of membrane-bound to cytoplasmic instances of a protein within a cell with less data compared to MSD analysis as each trajectory is sampled multiple times. Given a sufficient number of trajectories, MSD analysis is capable of providing the same information; however this is not always possible, especially if quantification is required for individual cells. MSD analysis has the added advantage of providing information on the type of motion exhibited by individual trajectories, identifying free diffusion, confined motion and active transport. In this way additional diffusion populations can be identified that may be hidden in JD analysis.

While many analysis tools are available for 2D SPT and there is an extensive list of publications investigating many aspects of analysis [194, 195], the resources for 3D SPT are comparatively lacking. For example, the effect of sampling error caused by motion blur as a particle diffuses within the exposure time of the detector [196] and by the pixel-based nature of camera detectors [197] on 2D MSD analysis have been studied but not yet extended into 3D. With the recent emergence of 3D-SPT instrumentation, 3D analysis techniques will follow in due time.

For the imaging conditions presented in the following applications, MSD analysis proves more reliable at returning diffusion coefficients. JD analysis proved less reliable in practice, with its performance varying depending on the underlying composition of the diffusion

populations of idealised datasets. As a result, MSD analysis was chosen as the preferred analysis tool in all presented applications. All algorithms described above are attached as appendices.

The following sections describe the application of 3D SPT using the DHPSF in previously inaccessible regions away from the coverslip surface (see chapter 3). To our knowledge, these examples are the first implantation of the DHPSF for SPT away from surface in eukaryotes.

4.6 Single-Particle Tracking on the Apical Surface and in the Cytoplasm of T cells

Previous SPT studies on T-cell membrane proteins have been conducted in 2D, either focussing at the coverslip surface [198] or at the apical membrane on non-flat geometries [199]. Imaging at the coverslip surface flattens out the membrane but potentially introduces unwanted interactions between the proteins of interest and the surface [150, 151]. 2D analysis of movement on non-flat surfaces may obscure the true behaviour of the target and cause simple diffusion to show apparently complex patterns that can be misinterpreted for incorrect conclusions [149]. The surface of T cells exhibits a wide range of complicated 3D nanoscale structure including membrane 'ruffles' and pseudopodia [200, 201], adding a 3D component to the diffusion of membrane-bound proteins and necessitating the use of 3D SPT techniques. The movement of cytoplasmic and nuclear proteins is also not well represented by 2D projections due to the inherent 3D nature of cells and inhomogeneity in their internal structure.

In order to demonstrate the SPT capabilities of the DHPSF in traditionally demanding areas of cells, membrane-bound and cytoplasmic T-cell proteins were imaged on the top $\approx$4 μm of live Jurkat T cells sat on passivating IgG-coated coverslips (figure 4.7). The membrane-associated T cell receptor (TCR) was imaged as it diffused over the nanostructure of the apical surface of live Jurkat T cells and the intracellular protein Zap70 was imaged inside live Jurkat T cells (figure 4.7b). Both proteins were tagged via a HaloTag ligand labelled with TMR fluorescent dye. MSD analysis measured the mean diffusion coefficient of the TCR to be $0.110 \pm 0.007 \mu m^2/s$ (424 trajectories across 15 cells), whereas the mean diffusion coefficient of Zap70 was measured to be $1.34 \pm 0.04 \mu m^2/s$ (435 trajectories across six cells). The precision of diffusion measurements was estimated by imaging static TCR at the apical surface in fixed Jurkat cells and was found to be $0.008 \pm 0.002 \mu m^2/s$ (132

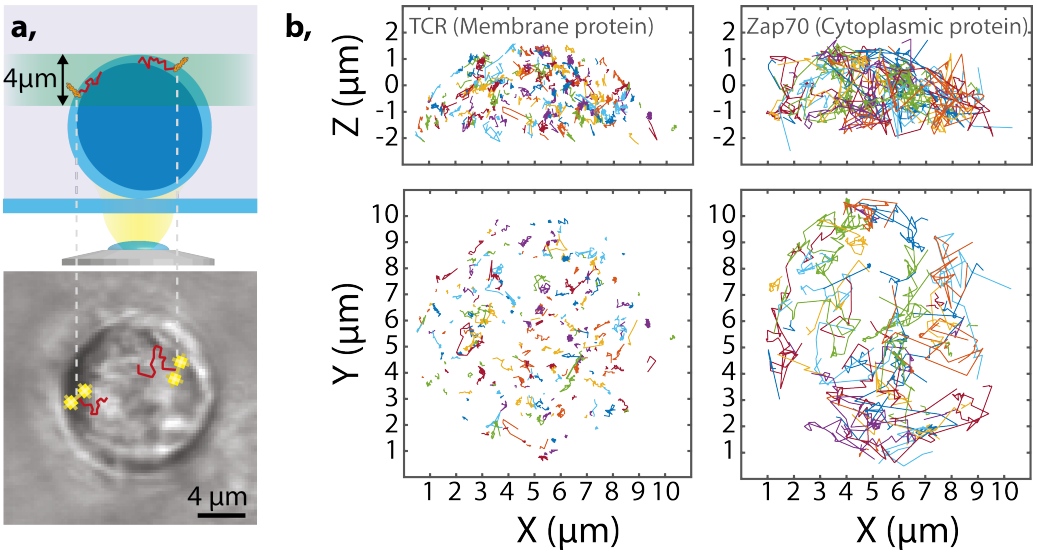

Fig. 4.7 SPT of membrane-bound and intracellular proteins in live human T cells. (a) Schematic of experimental setup for 3D SPT of T-cell proteins away from the coverslip with the DHPSF (top). A white light imaging of a live T cell viewed with the DHPSF phase-mask is shown with example DHPSFs (bottom). (b) Representative side-on and top-down views of trajectories of membrane-bound (TCR, left) and intracellular (Zap70, right) proteins at the apical surface.

trajectories across 6 cells), agreeing well with the observed errors in live-cell TCR diffusion. The MSD plot for the TCR fit well to a straight line, indicating free diffusion, whereas the MSD plot for Zap70 fell below the straight line fit to the first four points of the MSD curve at higher time intervals, indicating a degree of confinement, most likely corresponding to confinement within the cell volume (figure 4.8).

The determined TCR diffusion coefficient is significantly higher than previously reported values obtained from the apical surface of Jurkat T cells. James *et. al.* measured a diffusion coefficient of $0.06 \pm 0.01 \mu m^2/s$ for TCR by fluorescence correlation spectroscopy [199]. MSD analysis of a 2D x-y-projection of our 3D trajectory data reports a mean diffusion coefficient of $0.064 \pm 0.004/mu m^2/s$, which is in good agreement with previously reported values. No specific value for cytoplasmic Zap70 could be found for comparison although a study by Sloan-Lancaster *et. al.* report cytoplasmic Zap70 to diffuse faster than 1 $\mu m^2/s$, the upper limit measurable by their FRAP instrument [202].

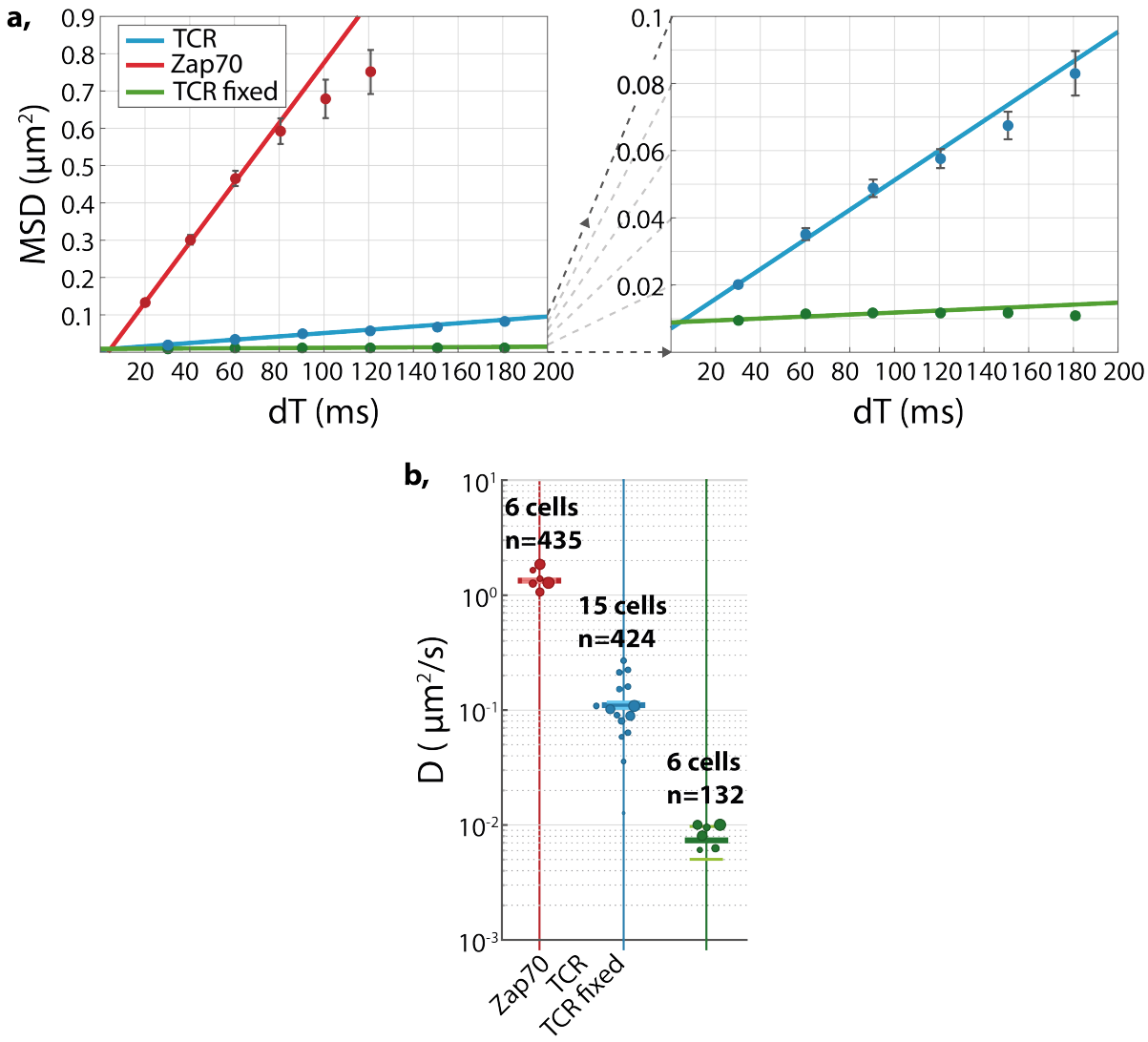

Fig. 4.8 MSD analysis of membrane-bound, intracellular and static T cell proteins. (a) MSD plots for Zap70 (intracellular) and TCR (membrane-bound) live and fixed with linear fits to the first four points. A magnification highlighting the MSD curves for live and fixed TCR diffusion is shown to the right. (b) Ensemble diffusion coefficients for Zap70 and TCR live and fixed determined by MSD analysis (horizontal bars) with cell-to-cell variation (circles) and total number of trajectories analysed. The size of the circles is proportional to the number of trajectories obtained from the cell. Small circles represent cells with fewer trajectories while large circles represent cells with many trajectories. The number of trajectories ranges from ∼30-140 per cell for Zap70 and ∼5-40 for TCR due to cell-to-cell variation.

4.6.1 3D Diffusion Measurements in Comparison to 2D Models for Membrane Surfaces

In order to confirm the importance of 3D SPT compared to 2D for tracking membrane-bound targets, trajectories were simulated on the top surface of smooth spheres with a diffusion coefficient of 0.1 μm^2/s and experimentally determined localisation uncertainty (figure 4.9a&b). 250 trajectories were simulated over five spheres, each with a 20 time steps. The MSD of the trajectories was analysed in 3D and from a 2D projection to measure the apparent difference in diffusion coefficient. The 3D MSD analysis reported a mean diffusion coefficient of $0.103 \pm 0.003 \mu$m^2/s while 2D MSD analysis reported a mean diffusion coefficient of $0.078 \pm 0.003 \mu$m^2/s. The ratio of 3D to 2D diffusion coefficient is 1.34 ± 0.02, which represents a systematic error caused by the curvature of a sphere.

MSD analysis was conducted on a 2D projection of the live membrane-bound TCR data presented in figure 4.8. 3D MSD analysis previously reported a mean diffusion coefficient of $1.110/pm0.007 \mu$m^2/s while 2D MSD analysis reported a mean diffusion coefficient of $0.064 \pm 0.004 \mu$m^2/s (figure 4.9d). The ratio between 3D and 2D diffusion coefficient is 1.72 ± 0.22, which is considerably larger than expected from diffusion on the top of a smooth sphere. This increase originates from movement away from a spherical surface which can be seen in figure 4.9c and is likely caused by ruffles and pseudopodia in the outer T cell membrane. A previous study of T cell morphology via electron microscopy determined an analogous 'roughness factor' of 1.8 to account for the effect of T-cell morphology in 2D diffusion measurements [200], which has since been used to correct for 3D effects in T cell membrane protein diffusion studies [203, 204]. This measurement is in good agreement with the ratio between 2D and 3D diffusion measurements determined from the TCR dataset. The current study represents a case where 3D SPT, facilitated by the DHPSF, is essential for accurately representing protein dynamics in complex 3D environments. This work was published in 2017 in the Biophysical Journal [147].

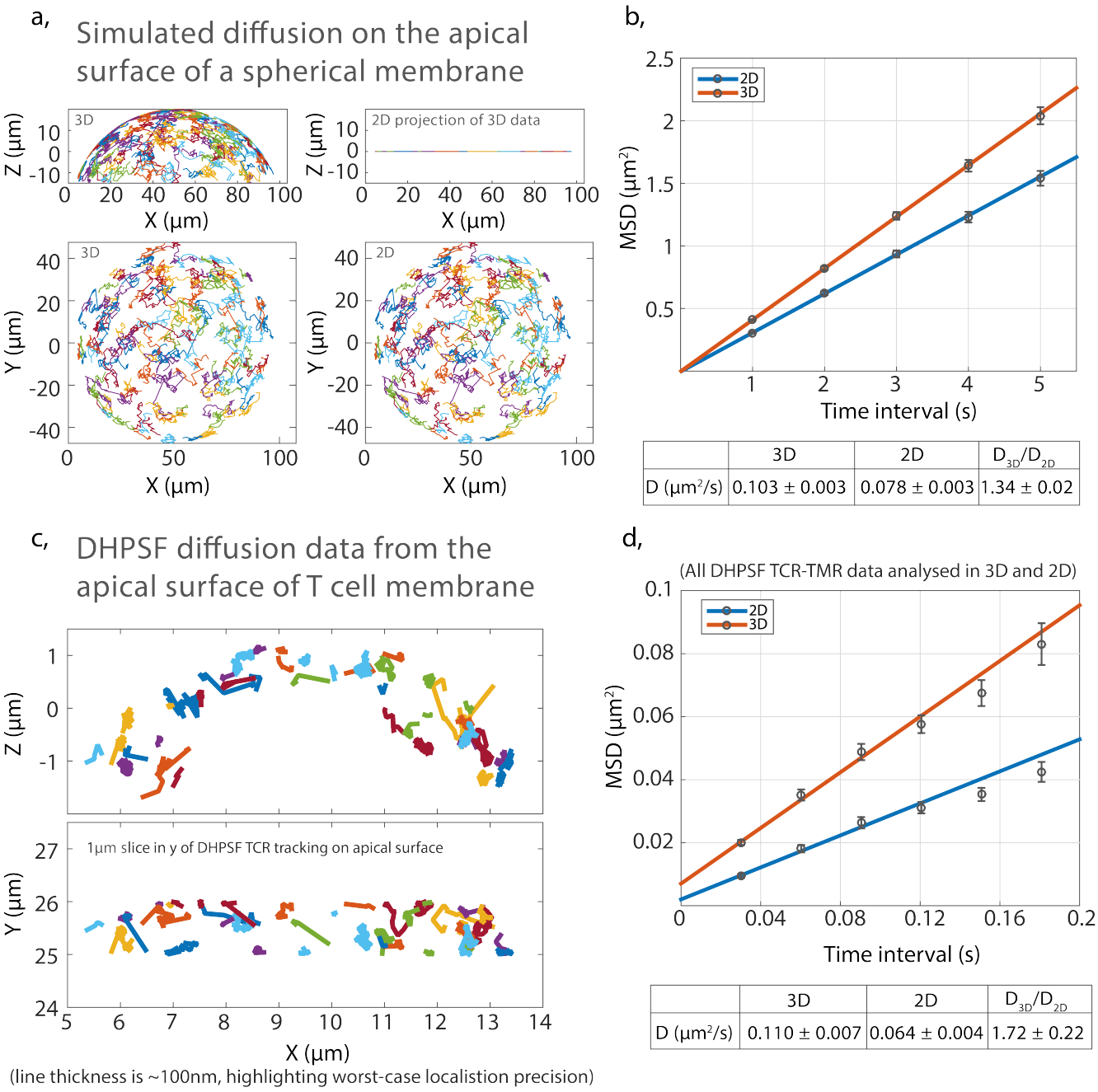

	3D	2D	D_{3D}/D_{2D}
D (μm²/s)	0.103 ± 0.003	0.078 ± 0.003	1.34 ± 0.02

	3D	2D	D_{3D}/D_{2D}
D (μm²/s)	0.110 ± 0.007	0.064 ± 0.004	1.72 ± 0.22

Fig. 4.9 2D MSD analysis of 3D motion. (a) top-down and side-on views of simulated 3D trajectories on the top surface of a sphere and corresponding 2D projection. (b) MSD plot for simulated diffusion on a spherical surface analysed in 2D and 3D. (c) Representative top-down and side-on view of membrane-bound 3D DHPSF trajectories from a 1 μm lateral slice of the apical surface of a T cell. The thickness of the trajectories is rendered as ~100 nm to represent the worse-case localisation uncertainty. Unlike the simulated trajectories, these trajectories are seen to exhibit significant radial movement, away from a model sphere. (d) MSD plot for membrane-bound diffusion analysed in 2D and 3D. The ratio between 3D and 2D diffusion coefficients is greater than expected from diffusion on a spherical surface.

4.7 Single-Particle Tracking in the Nucleus of Embryonic Stem Cells

In order to demonstrate the applicability of the DHPSF to SPT of nuclear proteins in vivo and across cell types (suspension and adherent cells) we investigated the chromatin remodeler CHD4, a nuclear protein known to play a critical role in embryonic stem cell (ES) pluripotency as part of the larger nucleosome remodelling and deacetylase (NuRD) complex [205]. A previous 2D SPT study showed that CHD4 occupies two diffusion states in near-equal ratios: bound to chromatin and a fast-moving state [193]. The same study reported that the removal of the nuclear protein methyl-CpG Binding Domain Protein 3 (MBD3) resulted in a $\sim$25% increase in the diffusion coefficient of the fast-moving population of CHD4 compared to wildtype cells. Due to the limited nominal focal plane of conventional 2D SPT ($\sim$500 nm) and the fast 3D motion of nuclear proteins, this study was unable to record trajectories with enough time points for MSD analysis. Instead JD analysis was used to quantify the motion of a 2D-projection of the true motion. 3D SPT and the large depth of field afforded by the DHPSF allow for longer trajectories to be collected and thus for more robust and detailed MSD diffusion analysis to be conducted.

We used the DHPSF to track nuclear CHD4 tagged with HaloTag ligand labelled with JF549 fluorescent dye in wildtype mouse ES cells and MBD3 null mouse ES cells (figure 4.10). As described in figure 4.3, MSD analysis was be used to identify freely-diffusing trajectories with $\sim$90% recall, allowing for the two populations of CHD4 diffusion to be separated. The mean diffusion coefficient of unbound CHD4 was determined to be $0.60 \pm 0.01 \mu m^2/s$ in wildtype cells (851 trajectories over 58 cells) and $0.75 \pm 0.03 \mu m^2/s$ in MBD3 null cells (1212 trajectories over 26 cells), exhibiting the same $\sim$25% increase previously reported [193]. Both MSD plots exhibited linearity for the first four points but fall below the fit by the sixth time point (figure 4.10c), indicating a small degree of confinement most likely caused by the boundary of the nucleus. The mean diffusion coefficient of bound CHD4 by nature did not fit well to a straight line and thus no meaningful diffusion could be measured. The bound diffusion coefficient of CHD4 was measured to be $0.06 \pm 0.03 \mu m^2/s$ for wildtype cells and $0.07 \pm 0.03 \mu m^2/s$ MBD3 null cells. This work was published in 2017 in the Biophysical Journal [147].

These results are being followed up in a study of additional components of the NuRD complex by Dr Srinjan Basu in the Laue group (Biochemistry Department, University of Cambridge). Structural links between components as well as how the entire complex

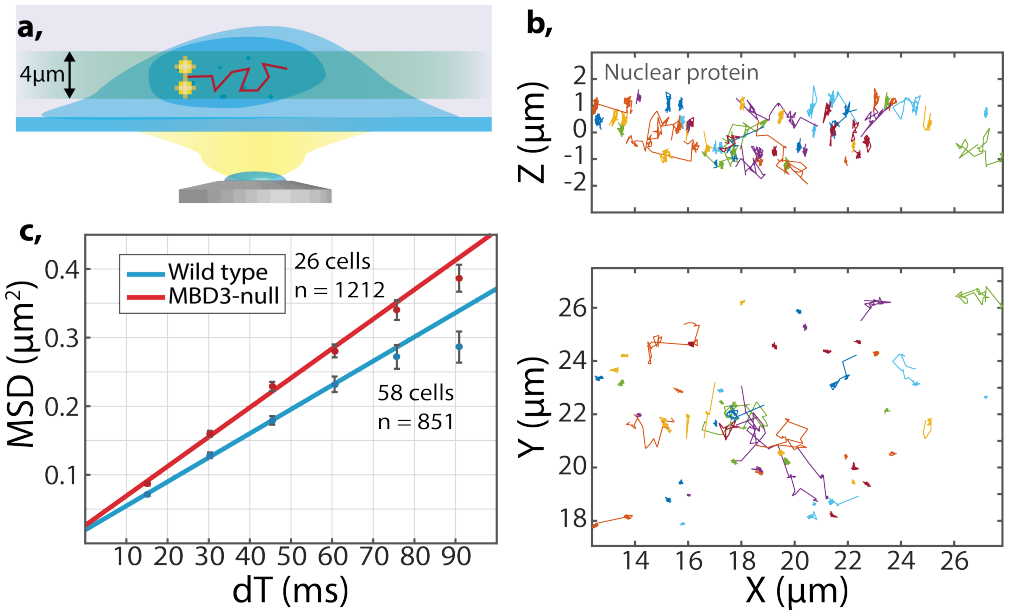

Fig. 4.10 SPT of CHD4 nuclear protein using the DHPSF in live mouse ES cells. (a) Schematic of experimental procedure for SPT in the nucleus of ES cells using the DHPSF. (b) Side-on and top-down view of CHD4 trajectories from a $\sim$4 μm thick section within an ES cell nucleus. The bound and unbound populations of CHD4 can clearly be seen. (c) MSD plot for unbound trajectories in wildtype and MBD3 null cells with linear fit to the first four points.

assembles and which sub-complexes exist are being probed by analysis of relative diffusion coefficients and binding times in a range of knock-out cell lines. SPT data for the chromatin remodeling complex constituent proteins CHD4, MBD3 and MTA was analysed by MSD (figure 4.11).

For CHD4, wildtype cells and MBD3 and GATAD2A knock-out cells were imaged with CHD4 labelled with PAJF549 via HaloTag ligand (figure 4.11a&d). In wildtype cells, the mean diffusion coefficient of unbound CHD4 was determined to be $0.619 \pm 0.022 \mu m^2/s$ (2,539 trajectories) with an unbound fraction of 0.36. In MBD3 null cells, the mean diffusion coefficient of unbound CHD4 was determined to be $0.73 \pm 0.04 \mu m^2/s$ (2,474 trajectories) with an unbound fraction of 0.36, agreeing well with the data presented in figure 4.10. In GATAD2A null cells, the mean diffusion coefficient of unbound CHD4 was determined to be $0.554 \pm 0.022 \mu m^2/s$ (3,636 trajectories) with an unbound fraction of 0.32.

For MBD3, wildtype cells and CHD4 and GATAD2A knock-out cells were imaged with MBD3 labelled with PAJF549 via HaloTag ligand (figure 4.11b&e). In wildtype cells, the mean diffusion coefficient of unbound MBD3 was determined to be $0.60 \pm 0.03 \mu m^2/s$

(1,828 trajectories) with an unbound fraction of 0.31. In CHD4 null cells, the mean diffusion coefficient of unbound MBD3 was determined to be $0.429 \pm 0.018 \mu m^2/s$ (909 trajectories) with an unbound fraction of 0.31. In GATAD2A null cells, the mean diffusion coefficient of unbound MBD3 was determined to be $0.711 \pm 0.025 \mu m^2/s$ (1,531 trajectories) with an unbound fraction of 0.34.

For MTA3, another component of the NuRD complex, wildtype cells and CHD4, GATAD2A and MBD3 knock-out cells were imaged with MTA3 labelled with PAJF549 via HaloTag ligand (figure 4.11d&f). In wildtype cells, the mean diffusion coefficient of unbound MTA3 was determined to be $1.13 \pm 0.08 \mu m^2/s$ (94 trajectories) with an unbound fraction of 0.28. In CHD4 null cells, the mean diffusion coefficient of unbound MTA3 was determined to be $1.30 \pm 0.05 \mu m^2/s$ (145 trajectories) with an unbound fraction of 0.50. In GATAD2A null cells, the mean diffusion coefficient of unbound MTA3 was determined to be $0.91 \pm 0.04 \mu m^2/s$ (472 trajectories) with an unbound fraction of 0.45. In MBD3 null cells, the mean diffusion coefficient of unbound MTA3 was determined to be $0.93 \pm 0.04 \mu m^2/s$ (222 trajectories) with an unbound fraction of 0.53. For all MTA3 cells a low number of trajectories were recorded, likely due to low expression of MTA3-HaloTag. Due to biological variation a greater number of trajectories should be collected to accurately represent the overall distribution.

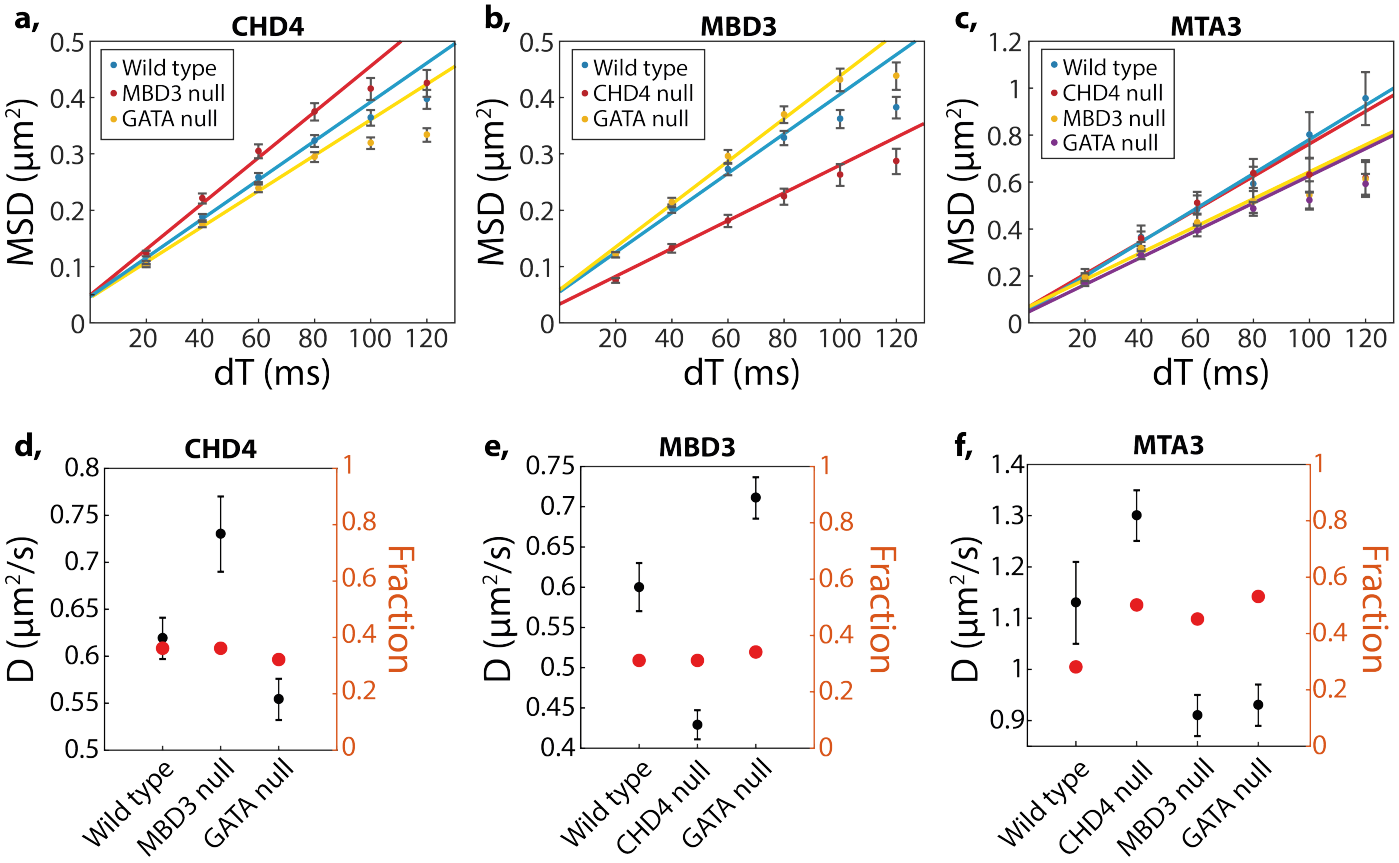

Fig. 4.11 3D SPT using the DHPSF for components of the NuRD complex in live embryonic stem cells. (a-c) MSD plots for CHD4, MBD3 and MTA3 proteins for wildtype cells and a range of knock-out cells. (d-f) Determined mean diffusion coefficient of unbound populations of CHD4, MBD3 and MTA3. The fraction of trajectories determined to be unbound is plot for each cell line.

4.8 Discussion

The presented applications show that the DHPSF can be used to perform 3D SPT in situations where 2D SPT typically performs poorly: at the apical cell surface and in the nuclei of living cells. Previously the DHPSF has been applied to tracking mRNA in Saccharomyces cerevisiae in which MSD analysis was used to determine a mean diffusion coefficient of 0.040 μm^2/s [101]. This result, coupled with the presented measured diffusion coefficients, demonstrates the ability of the DHPSF to track particles with a wide range of diffusion coefficients.

4.8.1 3D Single-Particle Tracking with the DHPSF for membrane-bound targets

As shown, 2D projections can obscure components of motions associated with membrane nanostructure when tracking membrane-bound targets, making it easy to draw erroneous conclusions. For example, diffusion on the surface of microvilli orientated parallel to the optical axis would appear static in 2D and could be misinterpreted as a binding event. In the absence of membrane ruffles on the basal surface, it is possible to accurately represent diffusion with 2D SPT when imaging at the coverslip surface. However, interactions with unphysiological hard-coated surfaces can perturb the resting dynamics of membrane proteins [150, 151, 171]. This effect is especially relevant for membrane-bound proteins with significant extracellular domains such as the T-cell membrane proteins TCR and CD45 [206]. The DHPSF provides an elegant solution for SPT of membrane-bound targets in their natural state as it is capable of imaging large volumes away at the apical surface of biological samples on non-flat geometries. Even tracking membrane-bound targets diffusing at the coverslip surface, membrane ruffles may cause significant axial variation [151] that necessitate 3D-SPT.

4.8.2 3D Single-Particle Tracking with the DHPSF for cytoplasmic and nuclear targets

Fast-moving 3D diffusion is also not well represented in 2D, as it is highly likely that the target will leave the imaging volume during acquisition, dramatically shortening recorded trajectories. When tracking CHD4 with the DHPSF, MSD analysis was able to show that the diffusing population was largely freely diffusing as opposed to being actively transported or confined. This observation was not possible in previous 2D experiments as only short trajectories could be recorded [193] and provides additional information on the native behaviour of the protein.

4.8.3 Advantages and disadvantages of the DHPSF for Single-Particle Tracking

Compared to commonly implemented 3D SPT techniques, such as Astigmatism and Biplane microscopy, the DHPSF offers an increased depth of field of $\sim$4 μm compared to $\sim$500

nm and consequently is capable of recording longer trajectories. Other 3D SPT techniques, such as off-focus imaging [207] and Tetrapod-PSF engineering [113], are capable of imaging over large depths of fields, achieving $\sim$3 μm and up to 20 μm depths of field respectively. These techniques also afford the ability to record long tracks with high precision at the cost of an increased size of PSF and reduced signal collection. Astigmatism and Biplane represent some of the smallest 3D PSFs while also providing the shallowest focal depth. The DHPSF provides a compromise between PSF size and depth of field that is useful in a wide range of SPT applications, occupying a $\sim$5 fold larger area compared to 2D imaging (in comparison the Tetrapod PSF can take up a $\sim$200 fold larger area at the periphery of the depth of field). Imaging techniques that increase the size of the PSF require fewer molecules to be simultaneously fluorescent so that their PSFs don't overlap, reducing the labelling density that can be imaged and thus increasing the acquisition time to record the same number of trajectories. Multifocus microscopy (MFM) has been demonstrated for 3D SPT [93, 208]. The $\sim$4 μm depth of field of MFM is comparable to that of the DHPSF while the size of the PSF is comparable to Biplane imaging, allowing for higher densities of molecules to be imaged compared to the DHPSF. In the case of MFM the trade-off is instead in field of view as the image is split into nine components on the same detector, reducing the amount of data that can be simultaneously collected.

As a PSF is spread over more pixels (as is required for extended depth of field 3D SPT) the SNR is reduced as the photons are also spread out. Currently, brighter organic dyes provide the best candidates for 3D SPT due to their increased quantum efficiency and photostability compared to fluorescent proteins [69]. As more photons are required to localise a single emitter when using the DHPSF compared to 2D SPT one must either sacrifice time resolution (with longer exposure) or use higher laser activation powers (to excite more photons per unit time and thus reduce trajectory length) to image the same samples. For the DHPSF, SPT experiments with individual fluorescent proteins cannot currently employ MSD analysis due to reduced track lengths. This limitation can be circumvented by tagging the target with multiple fluorescent proteins. Thompson *et. al.* labelled mRNA-protein complexes with $\sim$32 EGFP molecules for SPT with the DHPSF [101]. Another option is to employ JD analysis for fluorescent protein SPT studies. As discussed above, JD analysis is currently less robust for 3D localisation techniques due to the increased number of positional uncertainty errors but is applicable to short trajectories.

The DHPSF is well suited to SPT in almost all situations so long as organic dyes can be used. 3D SPT is beneficial compared to 2D SPT in all situations containing non-flat geometries. In photon-limited imaging cases other 3D SPT techniques that sacrifice less

SNR, such as astigmatism, may be better-suited than the DHPSF. With 3D SMLM techniques becoming more widespread, 3D SPT is likely to become more prevalent, motivating the development of more advanced diffusion analysis methods in the near future. Although not yet explored, the DHPSF should be compatible with analysis methods such as motion-blur analysis [209] that are routine for 2D SPT.

4.9 Methodology

Simulating Trajectory Data

Idealised SPT trajectories were created in MATLAB by simulating a random walk. First particles were randomly distributed in x, y and z. At each time step every particle was moved in all dimensions by a distance sampled from a normal distribution centred at the expected 1D MSD given by: $MSD_{1D} = 2Ddt$. After the trajectory was created the position of each simulated localisation was displaced in x, y and z by a distance sampled from a normal distribution centred at 0 nm and with given by experimentally determined axial (for x and y) and lateral (for z) localisation precision for a given number of detected photons. The MATLAB code is attached in the appendix as part of the 3D tracking section.

2D SPT of TCR diffusing at the coverslip surface of T cells

Before imaging, $\sim 10^6$ T cells expressing TCR-β-HaloTag were labelled with Halo ligand-TMR (G8251,Promega) for 30 minutes at 37°C. The cells were then subjected to three washes in filtered (0.22 μm Millex-GP syringe filter unit, Millipore) Phosphate-buffered saline (PBS) (2810305, MP Biomedical) followed by 30 min incubation in T cell medium (RMPI medium (11835-063, Life Technologies) supplemented with 10% fetal calf serum (FBS, GE Healthcare), 1% sodium pyruvate (Sigma), 1% antibiotics (pen step, Sigma) and 2% glutamin (Sigma). The cells were then centrifuged at 600×g for 2 minutes and resuspended in 200 μL of filtered PBS. Meanwhile glass coverslips (24x50 mm borosilicate, thickness No. 1, Brand) were cleaned with argon plasma (PDC-002, Harrick Plasma) for 10 min and coated with nonspecific immunoglobulin G (IgG) (IgG, Jackson Immunoresearch Europe) for 30 min. The coverslips were washed three times with filtered PBS before 20-100 μL of labelled T cells added and allowed to settle on the surface for ∼5 min.

The sample was imaged in 2D on the DHPSF platform with the phase mask removed so that the $4f$ system relayed the image plane onto the camera without affecting the PSF. A 60x 1.45 NA oil-immersion objective lens (CFI Apo TIRF 60x Oil, Nikon) was used to provide TIRF illumination with 561 nm laser excitation (200 mW, Cobalt Jive 100, Cobalt). A quadband dichroic and longpasss and bandpass filters were used to separate the emission signal (Di01-R405/488/561/ 635-25x36, and BLP02- 561R-25 and FF01-580/14-25, respectively, Semrock) before the detector. An exposure time of 30 ms was used to track

the position of the TCR until all fluorophores had photobleached. Fitting was conducted using PeakFit (GDSC SMLM single-molecule plugins) [136] before the localisations were analysed in the bespoke MSD analysis code in MATLAB.

3D SPT at the apical surface of T cells

Before imaging, $\sim 10^6$ T cells expressing TCR-β-HaloTag or Zap70-HaloTag were labelled with 0.5-5 nM Halo ligand-TMR for 30 min at 37°C. The cells were then subjected to three washes in twice filtered PBS (involving centrifugation at 600×g for 2 min) followed by 30 min incubation in T cell medium. The cells were then resuspended in 200 μL of filtered PBS. The cells were imaged live or were fixed in 4% paraformaldehyde (Sigma) and 0.2% glutaraldehyde (Sigma) for 60 min at room temperature. Meanwhile glass coverslips (24x50 mm borosilicate, thickness No. 1, Brand) were cleaned with argon plasma for 10 min and coated with nonspecific IgG for 30 min for live-cell imaging and Poly-L-lysine (PLL) (molecular mass 150–300 kDa; P4832, Sigma) for 20 min for fixed-cell imaging. The coverslips were washed three times with filtered PBS before 20-100 μL of labelled T cells added and allowed to settle on the surface for ∼5 min.

Samples were imaged on the DHPSF platform employing a 60x 1.20 NA water-immersion objective lens (Plan Apo VC 60x, Nikon) as described in chapter 2. Continuous 561 nm excitation was incident on the sample in HILO geometry with a power density of ∼940 W/cm^2 measured before the objective lens by powermeter (PM100D, ThorLabs). A quad-band dichroic and longpasss and bandpass filters were used to separate the emission signal (Di01-R405/488/561/ 635-25x36, and BLP02- 561R-25 and FF01-580/14-25, respectively, Semrock) before the detector. An exposure time of 30 ms was used to image TCR in live and fixed cells and an exposure time of 10 ms was used to image Zap70 until no more localisations were seen (typically <10,000 frames for all cases). DHPSF fitting was conducted with easy-DHPSF [210] in MATLAB before localisation data was analysed in the bespoke MSD analysis code in MATLAB.

3D SPT in the nucleus of ES cells

Two days before imaging, cells were passaged onto 35 mm glass-bottom dishes (No. 1.0, MatTek) in phenol red-free serum and mLIF conditions as described in previous work (24). The cells were incubated with 0.5-5 nM Halo ligand-JF549 (6147/5, Tocris) for 15 min,

followed by two washes in filtered PBS. Cells were imaged in phenol-red free serum and mLIF conditions containing 5-10 mM Trolox (53188-07-1, Sigma).

Samples were imaged on the DHPSF platform employing a 60x 1.20 NA water-immersion objective lens (Plan Apo VC 60x, Nikon). Continuous 561 nm excitation was incident on the sample in HILO geometry with a power density of $\sim$500 W/cm^2. A quadband dichroic and longpasss and bandpass filters were used to separate the emission signal (Di01-R405/488/561/635-25x36, and BLP02- 561R-25 and FF01-580/14-25, respectively, Semrock) before the detector. An exposure time of 15 ms was used to record the motion of the labelled protein for 20,000 frames. DHPSF fitting was conducted with easy-DHPSF [210] in MATLAB before localisation data was analysed in the bespoke MSD analysis code in MATLAB.

For the data presented in figure 4.11, cells were incubated with 5 nM Halo ligand-PAJF549 (6149, Tocris) for 15 min, followed by 2 washes in filtered PBS. Cells were imaged in in phenol-red free serum and mLIF conditions containing 5-10 mM Trolox. These samples were imaged as described above but with simultaneous 561 nm ($\sim$500 W/cm^2) and 405 nm ($\sim$50 W/cm^2) lasers incident in HILO geometry to provide photoactivation of the fluorophore. An exposure time of 20 ms was used to record the motion of the labelled proteins for 20,000 frames. DHPSF fitting was conducted with easy-DHPSF [210] in MATLAB before localisation data was analysed in the bespoke MSD analysis code in MATLAB.

Chapter 5

Imaging Applications of the DHPSF in Eukaryotic Cells

This chapter focusses on the application of the DHPSF for 3D SMLM to previously inaccessible regions of biological samples. The reduction of spherical aberration away from the surface, described in Chapter 3, facilitates single-molecule imaging and quantification in live and fixed cells away from the coverslip. DHPSF imaging experiments, imaging away from the coverslip surface, are presented to address questions in a range of biological samples including suspension cells, adherent cells and tissue. Whole-cell imaging is demonstrated with fitted 3D meshes used to visualise morphological changes upon T-cell activation. This approach is extended to investigate the reorganisation of T-cell membrane proteins. These were quantified and corrected for biases caused by cell morphology. Finally, quantification of protein organisation is demonstrated in a number of other biological samples before the applicability of the DHPSF to imaging is discussed.

Contributions

Dr Steven Lee and I designed all the experiments presented in this chapter, with input by Dr Aleks Ponjavic for T-cell related experiments. All experiments were conducted and analysed by myself. I fitted the cell meshes created the cell-specific special randomness models in MATLAB and wrote the nearest-neighbour analysis code in MATLAB. Dr James McColl assisted with T-cell labelling and maintained T-cell lines. Dr Aleks Ponjavic labelled

T-cells with Alexa647 and made GLOX solutions periodically during STORM imaging experiments. Dr Yu Zhang provided labelled and fixed HELA cell samples with expressing (K-ras)-mEos3.2. Dr Yu Ye provided labelled and fixed HEK cell samples expressing proteasome-mEos3.2. Vlad Anton, from the Seth Grant group provided labelled and fixed mouse brain samples expressing PSD95-mEos3.2 and assisted with imaging by navigating brain samples in a white-light imaging mode. All 3D figures were rendered by me in either MATLAB or ViSP.

Named Publications Relating to this Chapter

- Three-Dimensional Super-Resolution in Eukaryotic Cells Using the Double-Helix Point Spread Function. **Alexander R. Carr**, Aleks Ponjavic, Srinjan Basu, James McColl, Ana Mafalda Santos, Simon Davis, Ernest D. Laue, David Klenerman and Steve F. Lee. Biophysical Journal, 2017.
- A Cell-Topology Based Mechanism for Antigen Discrimination by T Cells. Ricardo A. Fernandes*, Kristina A. Ganzinger*, Justin Tzou, Peter Jonsson, Steven F Lee, Matthieu Palayret, Ana Mafalda Santos, **Alexander R. Carr**, Aleks Ponjavic, Veronica T. Chang, Charlotte Macleod, B. Christoffer Lagerholm, Alan E. Lindsay, Omer Dushek, Andreas Tilevik, Simon J. Davis, David Klenerman. (In submission at Nature Immunology)

5.1 Imaging Large Volumes in 3D with the DHPSF

Although other 3D-SMLM techniques have used to study biological systems away from the coverslip surface [131], the majority of previous imaging studies employing the DHPSF have been limited to imaging at the coverslip surface. Tubulin-PA-GFP has been imaged at the basal surface of Rat Kangaroo Kidney EpithelialPtK1 cells [103], microtubules labelled with secondary antibody-Alexa647 have been imaged over the bottom $\sim$1 μm of African green monkey kidney BSC-1 cells [106] and eYFP, PAmCherry1 and Nile Red have been imaged in the bacterium Caulobacter crescentus at the coverslip surface [104, 105]. More recently DHPSF imaging has been conducted above the coverslip surface with an oil-immersion lens and light-sheet excitation confinement, imaging a $\sim$6 μm thick volume in human HeLa cells without aberration correction [108]. As described in chapter 3, spherical aberration present

when imaging above the coverslip degrades the DHPSF, reducing localisation precision and affecting the rotation rate of the lobes as a function of axial depth. Reducing spherical aberration by matching the refractive index of the immersion media of the objective lens to the sample facilitates robust SMLM deep into biological samples and as a consequence, a greater range of biological samples and questions can be probed with the DHPSF. A number of applications of the DHPSF for imaging away from the coverslip areas are demonstrated and are presented organised by biological sample type into three groups: 1) suspension cells (T cells), 2) adherent cells and 3) tissue sections.

5.2 3D Imaging in T Cells

T cells are a type of lymphocyte (white blood cell) that are central to adaptive immunity. $CD4^+$ T cells initiate the adaptive immune response by recognising spcific foreign particles (antigens) presented by major histocompatibility complexs (MHCs) on the surface of antigen presenting cells (APCs) with a highly variable T-cell receptor (TCR) on the cell surface [211–213]. The TCR is comprised of two hetero-dimers of cluster of differentiation 3 (CD3) co-receptor that associates with TCR-α, TCR-β chains and a ζ-chain to form the TCR complex. Another protein involved in T-cell signalling is cluster of differentiation 28 (CD28), a T-cell specific membrane protein that promotes cell proliferation and survival. The spatial distribution of T-cell membrane proteins is known to play a key role in initiating and sustaining an immune response [206, 214–216], with a single TCR-MHC complex being capable of triggering a response [217]. Therefore, it is imperative to develop imaging methodologies that are capable of recording these distributions at the single-molecule level and under physiological conditions. The aim of this work was to demonstrate the applicability of the DHPSF to investigate the protein distributions across whole-cell volumes as well as to visualise the underlying morphology of the plasma membrane. To this end, immortalised $CD4^+$ Jurkat T cells were used to demonstrate the methodology. For a more-detailed introduction to T-cells and the adaptive immune response see chapter 6.

The localisation precision of the DHPSF ($\sim$10-25 nm laterally and $\sim$20-60 nm axially) allows for individual fluorescently-labelled proteins to be resolved within biological samples below the diffraction limit. The membrane-bound TCR-β was expressed in Jurkat T cells with a HaloTag. This was labelled with Halo ligand-TMR and imaged on the surface of fixed T cells on a coverslip surface. Thus, individual TCR molecules could be resolved (figure 5.1), facilitating super-resolution mapping of protein organisation. To demonstrate

the compatibility of the DHPSF with large-volume imaging, whole T cells were imaged in multiple image planes.

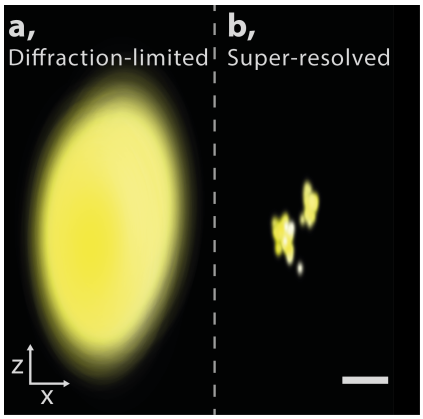

Fig. 5.1 The DHPSF is capable of resolving individual labelled proteins below the diffraction limit. Jurkat cells expressing TCR-HaloTag were labelled with Halo ligand-TMR and imaged with the DHPSF. A comparison between diffraction-limited (a) and super-resolved (b) rendering of two isolated clusters of localisations originating from individual TCR molecules separated by $\sim$300 nm. Scale bar is 300 nm.

5.2.1 Imaging Multiple Image Planes within a Sample

Due to the large depth of field of the DHPSF, extended structures can be imaged with a single imaging plane. However, eukaryotes are typically larger than $\sim$4 μm and, thus, in order to image a whole cell multiple focal planes must be acquired. As discussed in chapter 3, reducing spherical aberration away from the coverslip by matching the refractive index of immersion media and sample allows for extended imaging with the DHPSF >50 μm into biological samples [147]. This, coupled with reducing spatially varying aberration resulting from Fourier-plane misalignment [166], enables super-resolution imaging of whole-cell samples by stitching together successive image planes within the sample.

The lateral position of successive image planes relative to each other was examined by measuring the apparent displacement of fluorescent beads suspended above the coverslip surface in Phyta gel solution with refractive index equal to water. Approximately 200 beads, sampled across multiple $\sim$100 μm wide fields of view, were imaged each in two image planes. The beads were positioned towards the top of the depth of field and imaged for 100 frames at 30 ms. The objective lens was then moved 2.5 μm towards the sample, so that the beads were within the detection volume, and the same beads were imaged again for 100

frames. This process was repeated 60 times with an average of 3.3 fluorescent beads in each field of view.

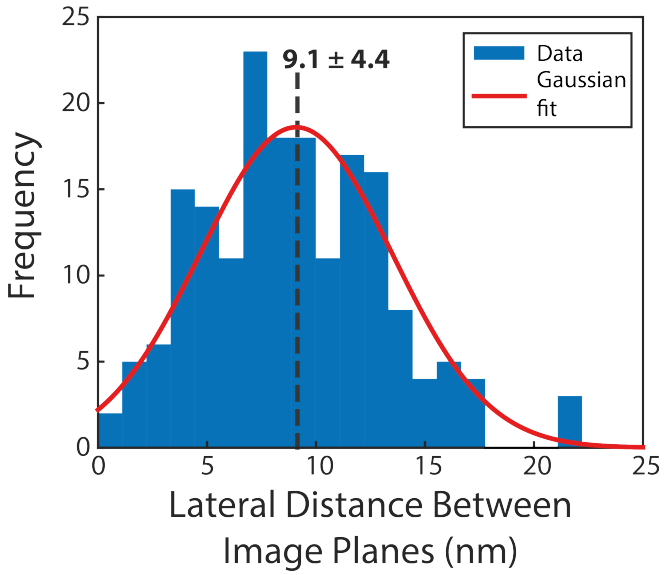

Fig. 5.2 Lateral offset between successive image planes is comparable to expected localisation errors. A histogram of the measured Cartesian lateral offset for fluorescent beads imaged in successive image planes axially separated by 2.5 μm. A 1D Gaussian function was fit to the data (red line) in order to extract the centre position and width.

The mean position of each bead was compared between successive image planes with the Cartesian distance between the two plotted as a histogram (Figure 5.2). A 1-dimensional Gaussian function was fitted to this distribution to extract the centre position and width. It was determined that an axial offset of 2.5 μm resulted in a 9.1 ± 4.4 nm lateral displacement. This value is comparable to the lateral localisation precision of the DHPSF and less than expected lateral errors for a single image plane in the Fourier plane-aligned DHPSF platform measured in chapter 3 [166]. Assuming this error is systematic and axially linear; a total lateral displacement of 55 nm would be expected between the basal and apical surfaces of a typical T cell ($\sim$15 μm thickness). Although this may not be the case, this error would be small compared to the volume being imaged.

When imaging a single plane, the localisation density recorded within the sample falls to zero at the periphery of the depth of field due to the form of the DHPSF and in part to a reduction in collection efficiency of the objective lens. In order to achieve the most-flat localisation density across volumes spanning multiple image planes the optimal axial offset between planes was investigated by imaging fluorescently labelled proteins in fixed Jurkat T cells. The density of localisations recorded from a single plane was measured by imaging the

membrane-bound protein TCR labelled with TMR via a HaloTag in the central plane of five Jurkat T cells (figure 5.3). The central plane was chosen as it exhibits the lowest geometric variation in membrane area across the depth of field, assuming a spherical cell. The axial distribution of localisation density correlated well to the axial intensity distribution calibrated by easy-DHPSF (figure 5.3b). This is to be expected as the ability to localise PSFs is directly related to the number of detected photons above background. It should be noted that the distribution varies depending on the alignment of the DHPSF and is not identical between experiments.

An approximation of the density distribution, removing noise at the centre of the depth of field (shown in figure 5.3a), was used as an example image plane to determine the optimal axial offset between image planes. The sum of two identical approximate distributions was plotted with a relative offset between the two of 2-5 μm in 500 nm steps. The mean localisation density from a 4 μm section including the interface between the two approximate image planes was plotted as a function of the offset (figure 5.3c). A relative localisation density of one indicates a flat localisation density between at the interface of the two planes. An axial offset of 3-3.5 μm (or $\sim$75% of the working depth of field) between successive image planes was found to give the most-flat localisation density at the interface between planes with a <10% change in localisation density. In all experiments employing multiple image planes, an offset between successive image planes of 3 μm was chosen unless an offset of 3.5 μm would reduce the total number of image planes.

5.2.2 Whole-Cell Imaging of T cells

Jurkat T cells expressing the membrane protein CD28 fused to mEos3.2 wer was investigated across entire Jurkat T cells to demonstrate the capability of the DHPSF for mammalian whole-cell imaging. Whole-cell super-resolution imaging of Jurkat T cells was achieved by imaging between three and five axial planes separated by 3 μm across the sample by translation of the objective lens with a piezo stage (figure 5.4). Jurkat T cells expressing the membrane protein CD28 fused to mEos3.2 were fixed in suspension and imaged on the coverslip in a PALM mode with HILO laser excitation on the DHPSF platform (figure 5.5). Approximately 20,000 frames were acquired at 100 ms exposure (as described in chapter 2), corresponding to an expected maximum drift of 89$\pm$8 nm. Imaging conditions were optimised so that mEos3.2 fluorescence events typically lasted 1-2 frames, with very few events lasting >5 frames (0.5 s). Approximately 5,000 localisations were collected across a single T cell, after filtering for repeat localisations of the same fluorescence event (see

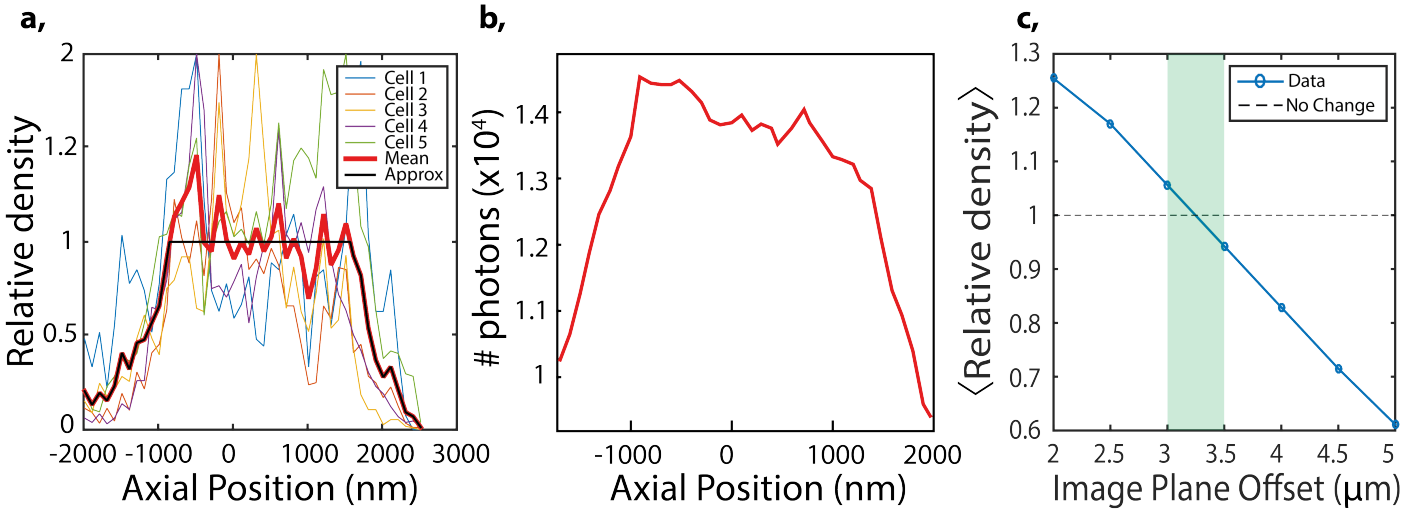

Fig. 5.3 Optimal axial offset between successive image planes to reduce localisation density variation. (a) Localisation density of TCR-TMR localisations across a single image plane from five cells with average (red) and approximate (black) distributions. (b) Number of photons detected from a single DHPSF across the depth of field during DHPSF calibration by easy-DHPSF. (c) Relative localisation density across a 4 μm thick section at the interface of two successive simulated image planes as a function of axial offset between planes. The highlighted green area indicates the optimal range of axial offset achieving the most-flat localisation density.

chapter 5 methodology for a detailed description) in time (0.5 s) and space (500 nm), with each CD28 molecule expected to be localised 2.8 times due to the fluorescence intermittency of mEos3.2 [65]. This is significantly lower than the number of CD28 molecules expected on Jurkat T cells (∼20,000, determined by fluorescence-activated cell sorting (FACS) by the Davis group). The overall detection efficiency is related to a number of factors including: mEos3.2 folding efficiency (40% [65]), the fraction of the cell volume that is being imaged at one time (assuming that the entire cell is illuminated by both activation and excitation lasers, ∼25%) and the detection efficiency of the imaging system. The combination of the first two factors leads to the estimate that 1/10 of CD28 molecules would be localised by an idealised microscope, ie ∼2,000 CD28 molecules per cell, corresponding to 5,600 localisations after mEos3.2 blinking. This figure is close to the recorded localisations (4,910) and thus the detection efficiency of the DHPSF can be determined to be ∼90% for mEos3.2, although varying expression levels of CD28-mEos3.2 between cells make this a crude estimation. Imaged whole T cells appear largely spherical with no obvious large-scale organisation of CD28 (figure 5.5b). A localisation density can be estimated assuming a sphere with radius 6.5 μm and a roughness factor of 1.8 [200], as determined by electron microscopy, to be ≈5

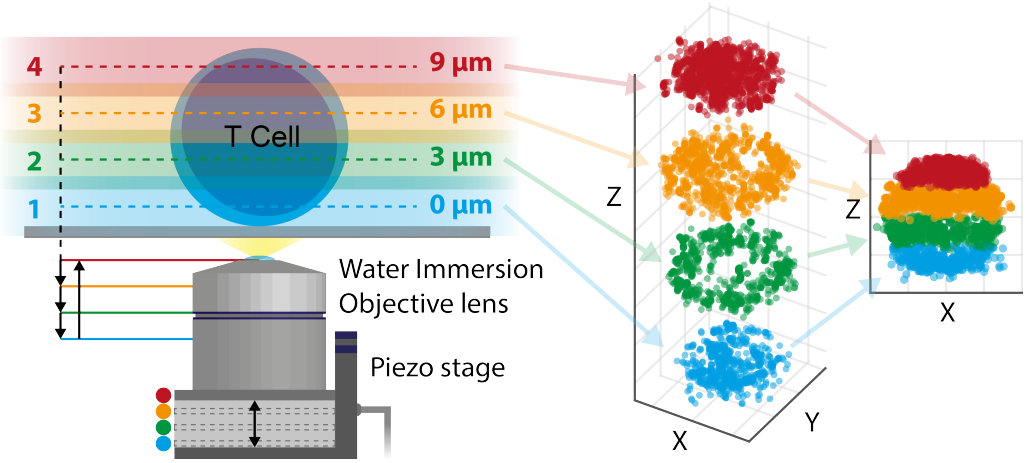

Fig. 5.4 Schematic diagram of experimental procedure for whole-cell imaging with a water-immersion objective lens. A 60x 1.2 NA water immersion objective lens was mounted on a piezo stage. Localisations are collected from 3-5 axial planes across the cell sample and recombined into a single large-volume reconstruction.

localisations/*mu*m^2. This localisation density is not enough to resolve any fine structure of the plasma membrane of the T cells.

Fig. 5.5 (Following page.) Super-resolution whole-cell reconstructions of CD28 membrane protein labelled with mEos3.2 in Jurkat T cells using the DHPSF. (a i) Highlighted Jurkat T cell expressing CD28-mEos3.2 imaged with the DHPSF (4,910 localisations). Localisations are colour coded by axial height from the coverslip and rendered with isotropic 3D Gaussian distributions with experimentally measured localisation precision for ∼350 photons detected. (a ii) Top-down and side-on views of the localisations presented in (a i) rendered with 100 nm localisation precision for visibility. Scale bars in (a) are 4 μm. (b) Additional reconstructions of whole-cell CD28-mEos3.2 localisation data. Top down (b i) and side-on (b ii) views are rendered with 200 nm localisation precision for visibility. Scale bars in (b) are 5 μm.

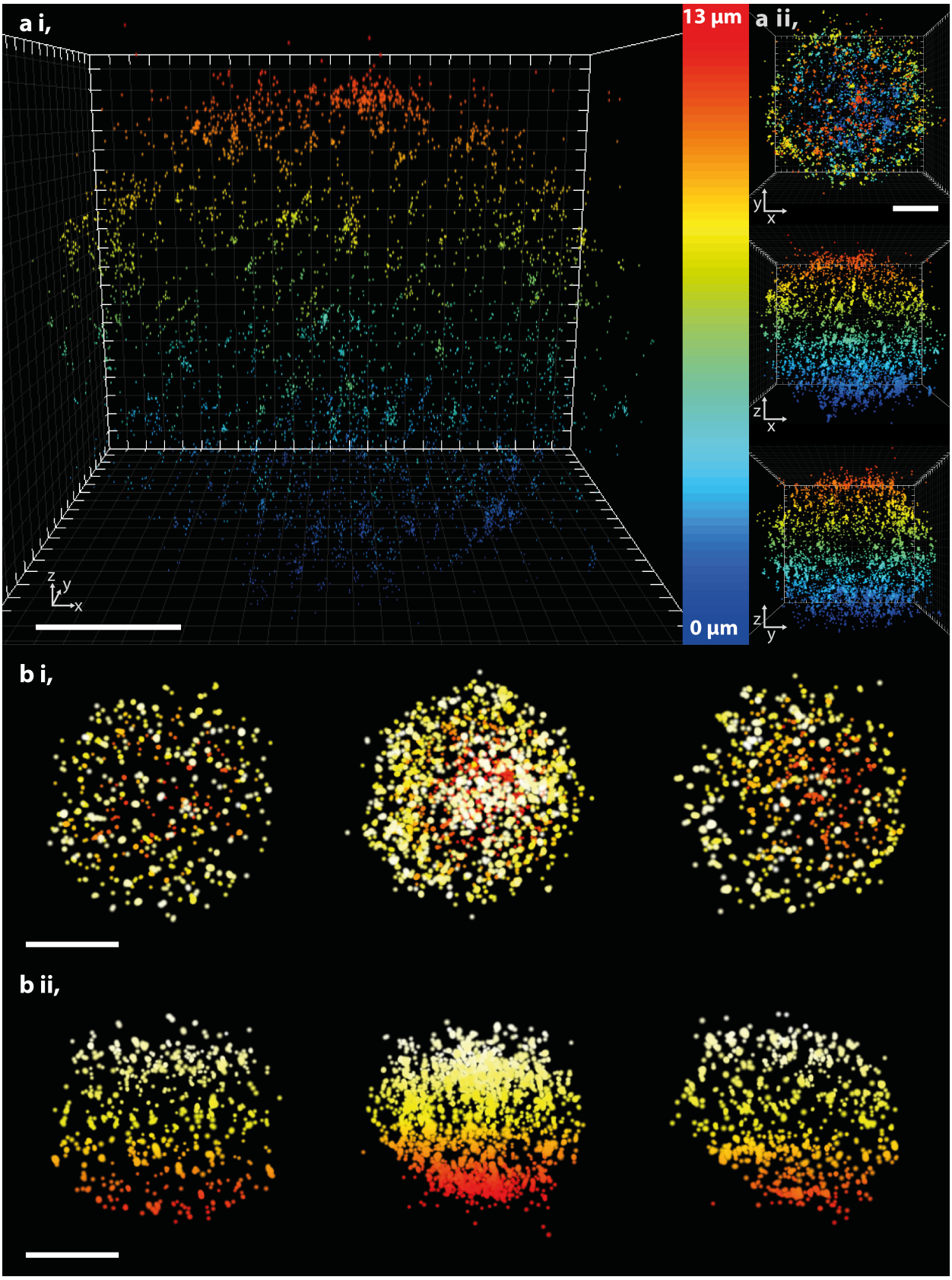

Fig. 5.5 Figure caption on previous page.

A key advantage of SMLM techniques compared to other SR imaging methodologies is the ability to provide quantitative information about the spatial distribution of the target at the single-molecule level within the sample. To demonstrate the importance of 3D-SMLM for T cell membrane-protein imaging the distribution of nearest neighbour (NN) distances between CD28 molecules was investigated. Repeat localisations of the same fluorophore were removed by filtering in space and time. The CD28 localisation data presented in figure 5.5a was filtered for repeat localisations of the same mEos3.2 molecule within a radius of 1200 nm acquired within three seconds of each other to account for the fluorescence intermittency of mEos3.2. The NN distance between the remaining CD28 localisations was then calculated and plotted as a cumulative histogram (figure 5.6). 27% of CD28 molecules were revealed to be <250 nm apart, with 63% <500 nm apart. This measurement highlights the advantage of SMLM techniques compared to confocal microscopy and other diffraction-limited techniques for quantification of protein distributions at the single-protein level as when using diffraction-limited techniques a significant fraction of proteins would not be able to be resolved.

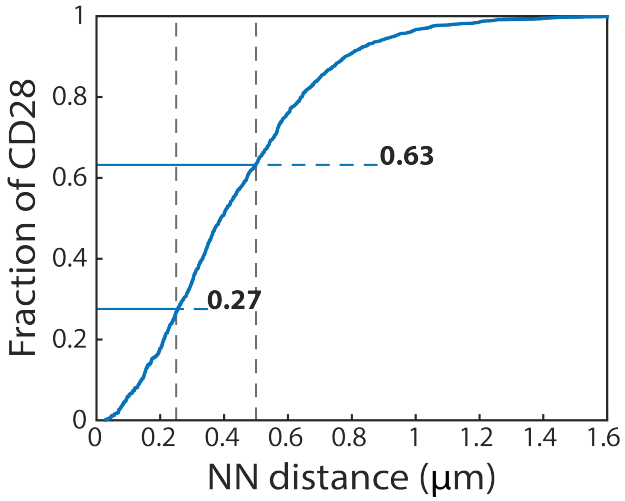

Fig. 5.6 Cumulative histogram of the nearest neighbour distance between CD28 molecules across whole Jurkat T cells. ∼3,000 CD28 molecules were recorded. The two dashed lines indicate distances of 250 nm and 500 nm with the corresponding fraction labelled.

5.2.3 Visualisation of Large-Scale Membrane Reorganisation over Whole T Cells

T cells have been shown to undergo morphological changes [171] and redistribution of membrane proteins [218, 206, 216] upon immunological stimulation. A key protein in this

process is the TCR. Immunologically-activating antibodies (OKT3) bind to CD3 subunits of the TCR, cross linking TCR complexes and activating the T cell and causing a reorganisation of the T-cell membrane [211, 219, 212]. The DHPSF was used to resolve the distribution of the TCR across whole Jurkat T cells imaged in 3-5 axial planes at distict time points during immunological activation. Fixed Jurkat T cells expressing TCR-β-HaloTag were labelled with TMR-Halo ligand and fixed at three time points during immunological activation: 1) resting (*i.e.* in solution in the absence of OKT3), 2) after 5 min contacting an OKT3-coated surface and 3) after 10 min contacting an OKT3-coated surface. The three samples were imaged on the DHPSF platform.

The approximate position of the outer membrane of each cell was determined by fitting 3D meshes to the localisation data (figure 5.7). Using functions included in Meshlab software (http://meshlab.sourceforge.net), the 3D localisation datasets were converted into an object mesh. For each point 50-200 neighbours, depending on localisation density, were considered to estimate a normal vector perpendicular to the surface. These points and their normals were then used to build a surface using the Poisson surface reconstruction approach [220, 221], which solves an approximate indicator function of the object by fitting its gradient to the input normal. Meshes checked by eye and then uniformly sampled, creating an even distribution of vertices for simplicity. More detailed instructions are provided in the methodology section at the end of this chapter. To demonstrate this methodology, a mesh was fitted to the CD28-mEos3.2 whole-cell data presented in figure 5.5a. The accuracy of these meshes is related to the localisation density. At relatively low sampling densities, as is the case for the presented CD28 dataset, this approach is able to distinguish large-scale morphology but not resolve membrane nanostructure such as dynamic finger-like protrusions (*i.e.* pseudopodia) and ruffles that have been observed by other optical microscopy techniques [89]. In the dataset presented in figure 5.7 some localisations are observed >1 μm away from the cell mesh, most likely corresponding to long pseudopodia or internal stores but could also be accounted for in part by erroneous localisations resulting from overlapping DHPSFs. Internal localisations do not affect mesh fitting as the Poisson surface reconstruction approach initially estimates the mesh volume to contain all points before shrinking it down for the best fit. As such, this approach is applicable to estimating volumes from membrane-bound and intracellular localisation datasets.

The mean position of the outer membrane of fixed Jurkat T cells was extracted by fitting meshes to whole-cell TCR localisation datasets from the three time points (figure 5.8). These cell meshes were used to visualise large-scale morphological changes during T cell activation. Although five cells were imaged for each time point, due to the low-throughput of the mesh

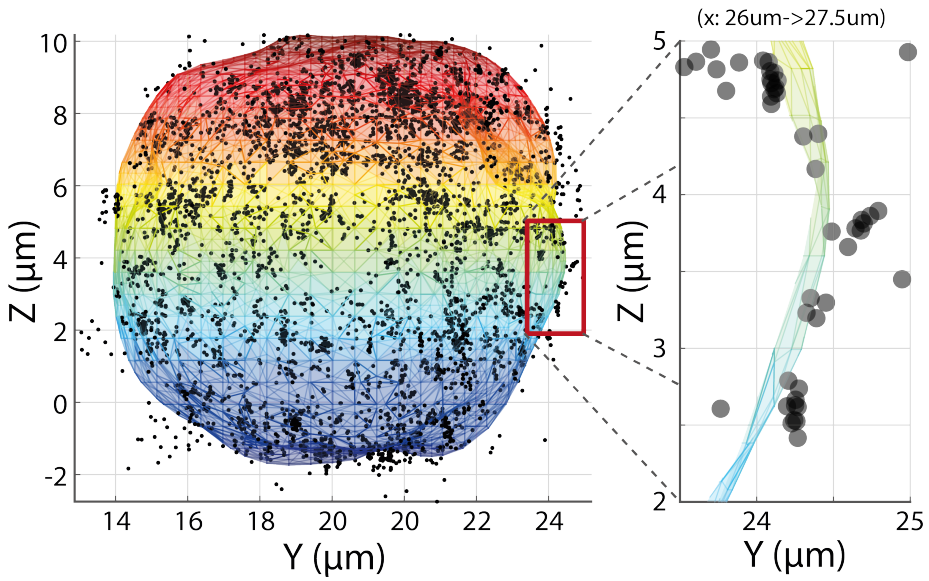

Fig. 5.7 Mesh fitting to whole-cell localisation data. Whole-cell CD28 localisation data was fit with a mesh to approximate the outer membrane surface. Individual CD28-mEos3.2 localisations are rendered as grey spheres and the fitted cell mesh coloured axially for visibility. The inset highlights a 1.5 μm thick section of the mesh following localisation data.

fitting process only the highest localisation density dataset in each condition was fitted with a mesh. The produced cell meshes validate the methodology and allowed for quantification to be conducted on a cell by cell basis. Substantial morphological differences were observed between resting T cells (fixed in suspension) versus those fixed after contacting activating-coated surfaces. In suspension, the cell mesh appeared smooth and spherical, whereas cells that had been contacting the surface for 5 min had less uniform cell meshes that exhibited flattening and extension of the basal surface. Much larger spreading was seen for cells contacting the surface for 10 min. For the three time points, the vertex densities of the cell meshes presented in figure 5.8 were 5.1, 4.9 and 2.8 vertices/μm^2 with 0.4, 0.7 and 0.8 localisations per vertex, respectively.

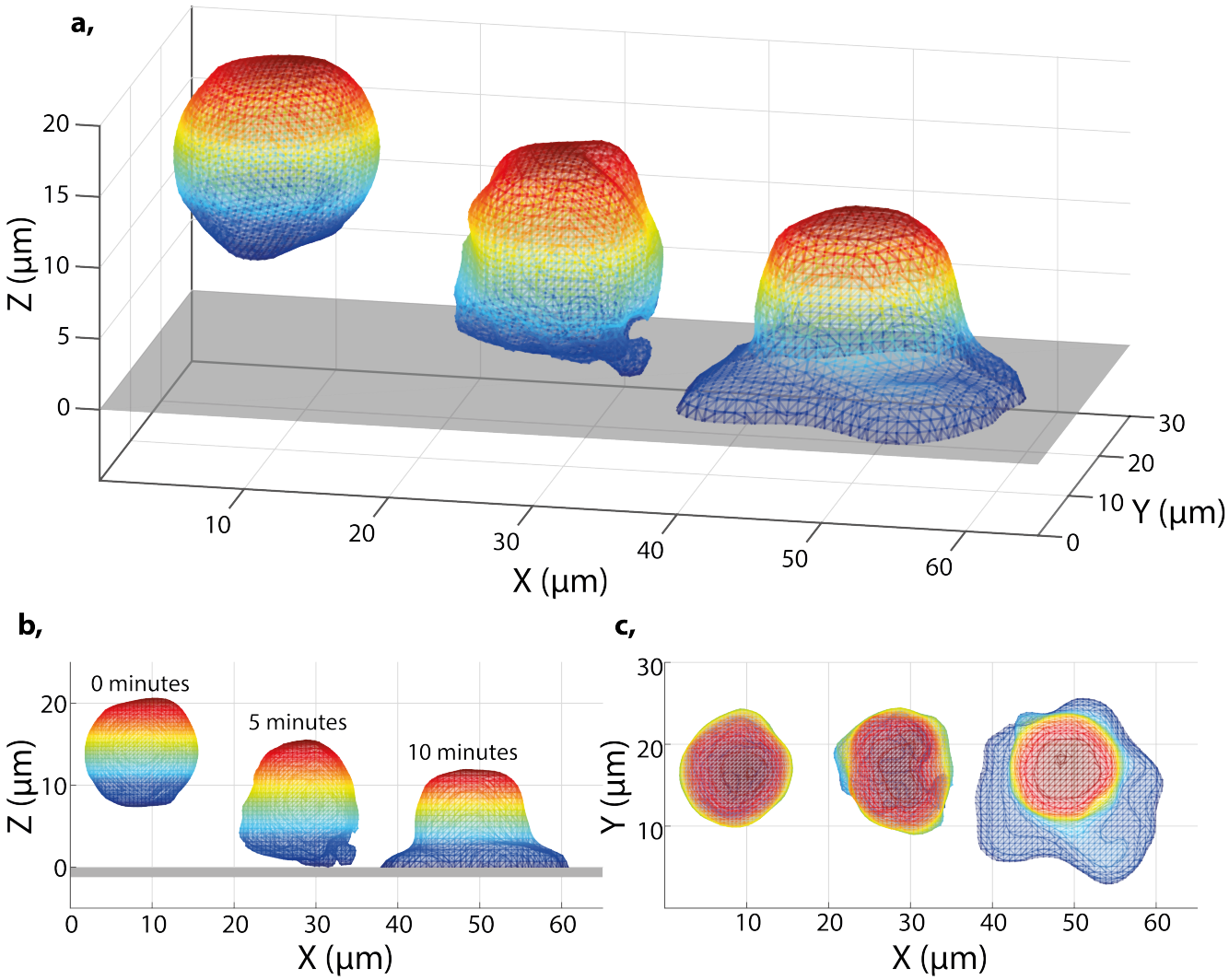

Fig. 5.8 Visualisation of large-scale morphological changes of Jurkat T cells on activating-coated surfaces by mesh fitting to whole-cell 3D localisation data. (a) Meshes were fitted to DHPSF whole-cell TCR localisation datasets of three Jurkat T cells tagged with HaloTag-TMR. Cells were fixed in solution (left, 1,149 localisations), 5 min after contacting an OKT3-coated surface (centre, 2,495 localisations) or 10 min after contacting an OKT3-coated surface (right, 2,397 localisations). Large-scale reorganisation of the outer membrane caused by immune-response triggering and the formation of an immunological synapse is visualised at three distinct stages. Side-on (b) and top-down (c) views are provided. Cells are coloured by axial position and the flat grey surface represents the coated coverslip of the experiment. The cell fixed in suspension has been rendered away from the coverslip to emphasize its resting state.

5.2.4 Quantification of Large-Scale Reorganisation over Whole T Cells

A key advantage of SMLM methodologies compared to imaged-based SR techniques is the ability readily obtain quantitative metrics. This is demonstrated by quantifying the reorganisation of the TCR across entire Jurkat T cells. The accuracy of the cell meshes was determined by analysis of the CD28 localisation dataset and corresponding cell mesh presented in figure 5.7. While a significant fraction of CD28 molecules are observed internally due to degradation/creation machinery and internal stores, there should be no CD28 molecules observed extracellularly. Any CD28 molecules that are observed outside the mesh must therefore related to membrane structure that is not resolved by the mesh rather than internal sources. By considering only CD28 molecules located outside of the cell mesh, a membrane-bound fraction can be isolated and used to determine the precision of the fitted mesh. After filtering for repeat localisations of the same fluorophore in space (500 nm) and time (1 s), a cumulative histogram was created from the distance from each CD28 molecule located outside of the cell mesh to the nearest cell-mesh vertex (figure 5.9). $\sim$95% of these CD28 molecules were located <1 μm from the cell mesh. A distance of 1 μm from the corresponding cell mesh was chosen as a threshold to separate membrane-associated and intracellular molecules

Fig. 5.9 (Following page.) Quantification of membrane-bound and intracellular TCRs during T-cell activation. Cumulative histograms of distance away from fitted cell meshes for the three cells presented in figure 5.8. The grey dashed lines at 1,000 nm indicate the threshold used to estimate membrane-bound localisations. The distribution of the TCR differs significantly between the resting cell (blue lines) and the two activated cells (red and orange lines). (a) Cumulative histogram of the distance from the corresponding cell mesh for extracellularly localised CD28 localisation data presented in 5.7. (b) Cumulative histogram of the distance from the mesh of all TCR molecules to the corresponding cell meshes. (c) Cumulative histogram of the distance from the mesh including only TCR molecules localised inside the mesh as a fraction of total number of detected TCR molecules. (d) Cumulative histogram of the distance from the mesh including only TCR molecules localised outside the mesh as a fraction of total number of detected TCR molecules. (e) Cumulative histograms of the distance from the mesh of intracellular TCR molecules as a fraction of the number of detected TCR molecules determined to be inside the fitted mesh. (f) Cumulative histograms of the distance from the mesh of extracellular TCR molecules as a fraction of the number of detected TCR molecules determined to be outside of the fitted mesh.

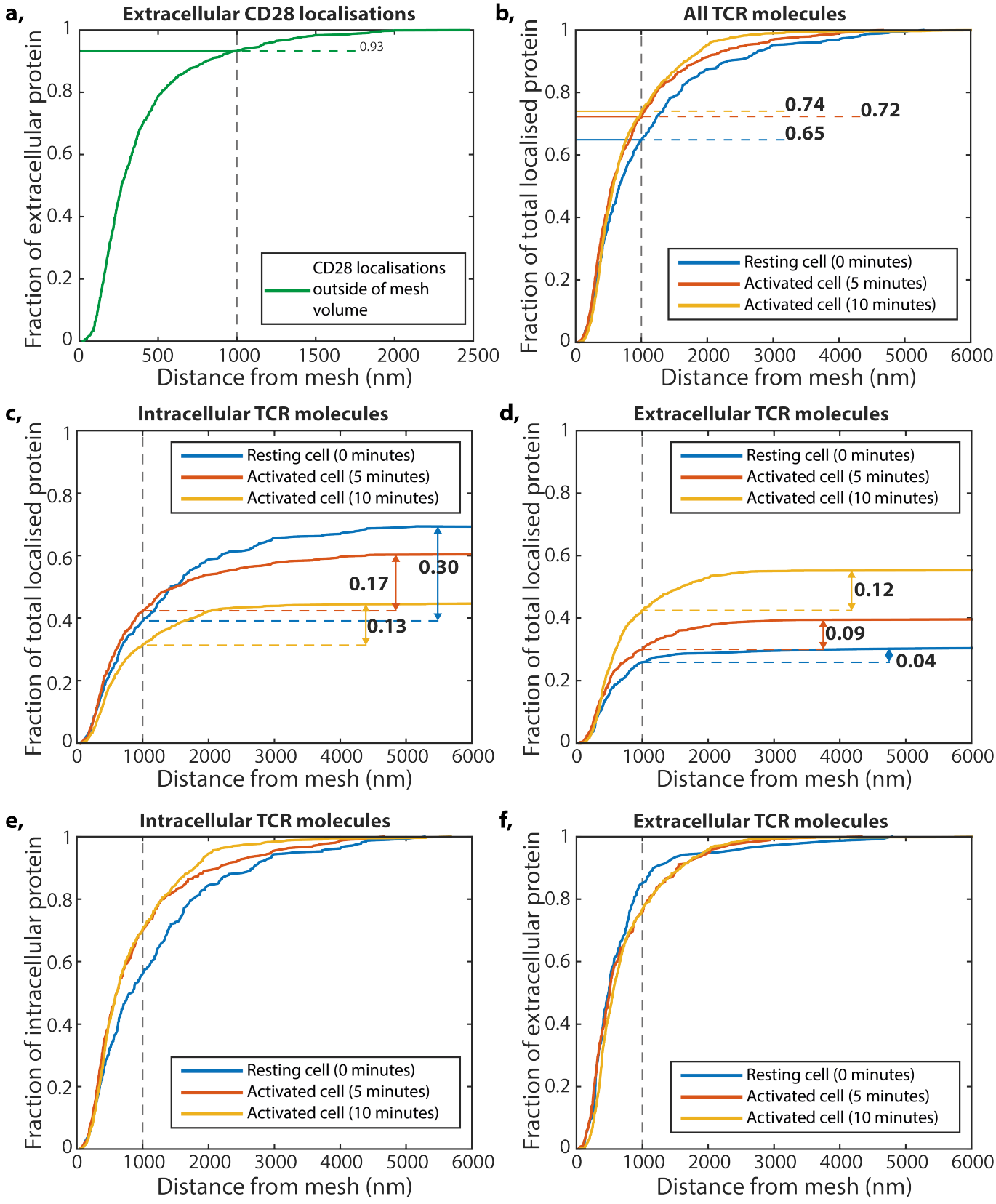

Fig. 5.9 Figure caption on previous page.

Cell-surface meshes were used to quantify the membrane-bound and cytoplasmic fractions of localised TCR molecules at distinct time points during immunological activation (figure 5.9). The localisation datasets were filtered in space (500 nm) and time (1 s) to remove repeat localisations of the same fluorophore. The distance from each remaining localisation to the nearest vertex in the corresponding cell mesh was used to separate membrane-bound and cytoplasmic TCR molecules. A cumulative histogram of these distances was created for each of the three cells presented in figure 5.8. For the resting cell, 65% of all TCR molecules were determined to be membrane-associated. For the two activated cells, fixed after 5 and 10 min, 72% and 74% of all TCR molecules were determined to be membrane-associated respectively (figure 5.9b). The fraction of all localisations over 1 μm from the mesh inside the volume (intracellular localisations) decreased in the case of the activated cells compared to the resting cell. 17% and 13% of TCR molecules were localised intracellularly after 5 and 10 minutes on an activating surface respectively, compared to 30% in the resting cell (figure 5.9c). The fraction of all localisations over 1 μm from the mesh outside the volume increased in the activated cells compared to the resting cell. 9% and 12% of TCR molecules were localised after 5 and 10 minutes on an activating surface respectively, compared to 4% in the resting cell (figure 5.9d). These 'extracellular' TCR molecules are likely associated with pseudopodia longer than 1 μm known to be present on the outer membrane of human T cells [201]. Although n=1, these data are consistent with previous studies supporting the notion that immunological stimulation causes intracellular TCRs held in internal stores to be recruited to the outer membrane in Jurkat T cells [222, 223]. This is likely to be an active process as the T cell attempts to form an immunological synapse [224, 225].

5.2.5 Cell-Specific Complete Spatial Randomness Models

Changes in cell morphology can affect the observed distribution of proteins, creating artefacts that can be misinterpreted as reorganisation or obscuring true reorganisation events. For example, the distribution of inter-protein distances across whole cell SMLM datasets is highly dependent on the shape of the cell itself. Mostly round cells have a uniform axial distribution of inter-protein distance due to their symmetry, while other morphologies result in non-trivial axial distributions. Cell-surface meshes can be used to decouple protein organisation from morphology in quantitative analysis. Additional quantification of TCR reorganisation during T-cell activation was conducted by correcting the distribution of inter-TCR distances for cell morphology changes.

To calculate the inter-protein distances within the whole-cell TCR datasets an algorithm was written in MATLAB. First, repeat localisations originating from the sample fluorophore were removed by filtering in space (500 nm) and time (1 s). For each remaining localisation, the distance to all other localisations was calculated and used to create a histogram. The peak value of these histograms, representing the modal inter-protein distance, was recorded. The mean and standard deviation of this inter-protein distance was plotted as a function of axial depth within the sample in 500 nm steps for all localisations in the three samples (figure 5.10a-c).

In order to correct for cell shape, cell-specific complete spatial randomness models were created from the cell meshes. For each cell, a model distribution representing localisation data of proteins distributed entirely on the outer membrane (no intracellular protein) was created by randomly sampling a number of vertices equal to the number of unique TCRs observed from the cell mesh. Each point was randomly translated by between -250 nm and 250 nm with equal probability to determine error limits. An additional displacement was sampled from a normal distribution in all dimensions to represent localisation uncertainty. This displacement was centred by the measured localisation precisions laterally and axially for the mean number of detected photons from the dataset ($\sim$1,350 photons with 100 ms exposure corresponding to $\sim$15 nm laterally and $\sim$30 nm axially). The inter-protein distance analysis was conducted on 1,000 instances of model datasets for each cell, taking the mean and the 5th and 95th percentiles to create error limits. The deviation of the true inter-protein distance from the model inter-protein distance provides information about how well the membrane-bound model fits as a whole (figure 5.10d-f).

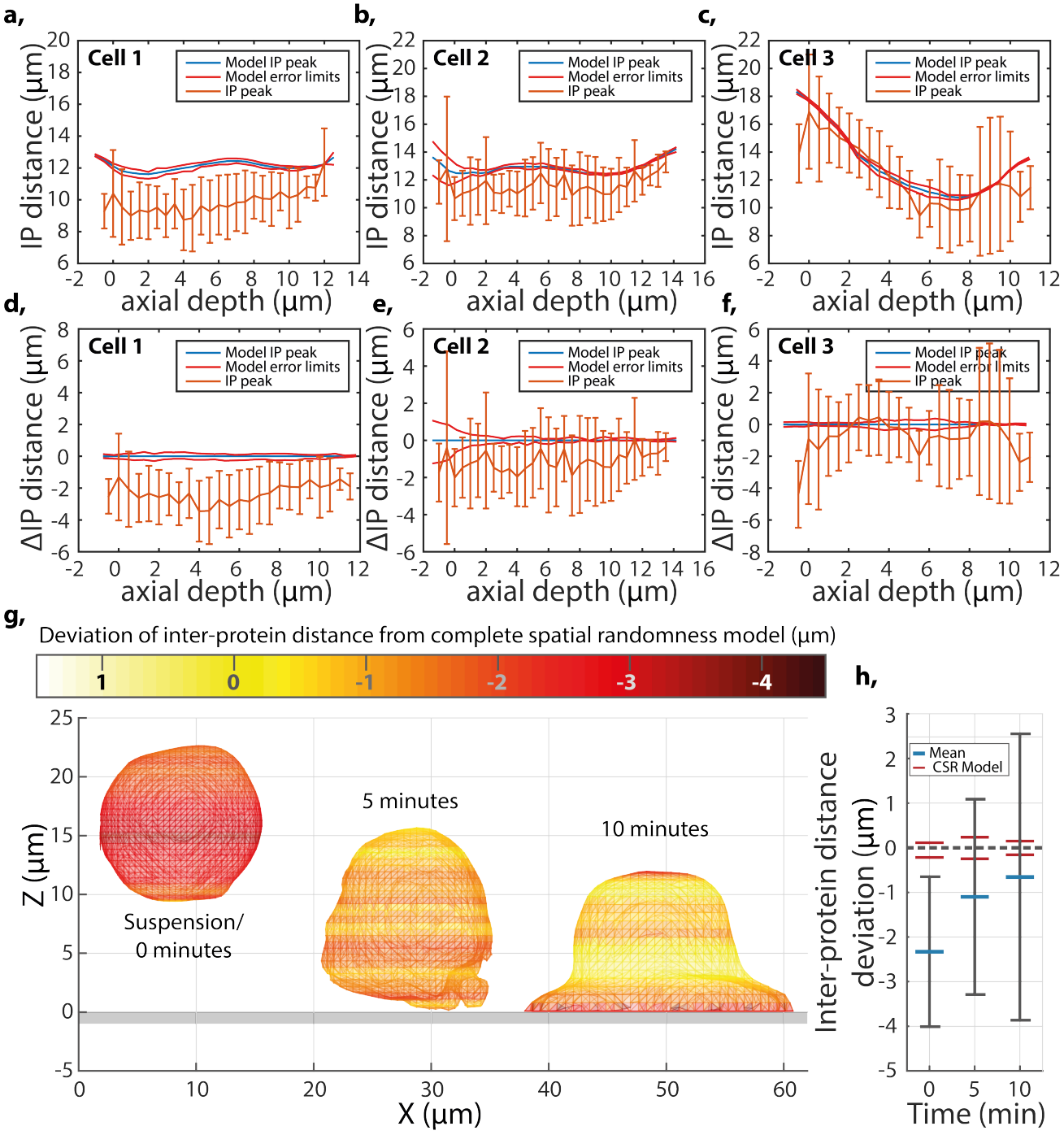

Fig. 5.10 Figure caption on following page.

Fig. 5.10 (Previous page.) Correcting for the effect of morphology on inter-protein distance distribution. (a-c) Inter-protein distribution as a function of axial depth for the three cells presented in figure 8. Membrane-bound CRS model inter-protein distributions from the corresponding cell meshes are plot with 5th and 95th percentile error limits (blue and red solid lines). (d-f) Deviation from the membrane-bound CSR model of inter-protein distance distributions for the three cells as a function of axial depth. (g) Side-on view of cell meshes presented in figure 8 coloured axially by deviation of inter-protein distance from a CSR model of a membrane-bound protein; with yellow indicating no deviation from model system, and red/black indicating a reduction in peak inter-protein distance compared to the model system. Stripes are observed as the deviation of inter-protein distance varies across the axial depth of the cells, however these are within error as shown in d-f. (h) Mean and standard deviation of inter-protein distance deviation from CSR model of inter-protein distance over the entire cell for each cell shown in (g).

The overall inter-protein distance distribution of the TCR was found to be significantly smaller from that predicted by the membrane-bound CSR model, implying that a significant fraction of the TCR was localised intracellularly. In contrast, the mean inter-protein distribution of the TCR in both activated cells overlapped substantially with the corresponding membrane-bound CSR models, indicating a reduction in the intracellular fraction upon activation (figure 5.10h). These results support the analysis of membrane-bound and cytoplasmic TCR fractions presented in figure 5.9. The cell meshes were coloured axially with the calculated inter-protein distance deviation from the relevant CSR model (figure 5.10g). In all three cells, no significant axial dependence of the inter-protein distance distribution was seen (figure 5.10a-g), indicating that this is a global effect rather than a directed process, recruiting the TCR to the immunological synapse. This analysis demonstrates that the DHPSF can resolve relatively small redistributions of molecules across whole cells, such as the transfer of proteins from the cytosol to the cell surface. In the case of low-expressing proteins (*e.g.*, the TCR), a small number of molecules moving from the cell cytoplasm to the cell membrane could significantly affect the overall distribution. This work was published in 2017 in the Biophysical Journal [147].

5.2.6 STORM Imaging of CD45 Resolves Membrane Nanostructure

The nano-scale organisation of proteins on the surface of T cells is known to play an important role in immunological triggering [218, 206]. Cluster of differentiation 45 (CD45) is a membrane-bound tyrosine phosphatase that dephosphorylates the TCR in order to maintain a low net level of TCR posphorylation [226, 216]. Upon T-cell activation CD45 is excluded from contacts with coated surfaces [227] and between cells [216, 228, 229]. Membrane pseudopodia are thought to play a role in T cell activation, scanning multiple contacts at once. Exclusion of CD45 at the tip of T cell pseudopodia upon contact with an antigen-presenting cell is hypothesised to lead to immunological triggering when the exclusion zone is >200 nm in radius ('A cell-topography based mechanism for antigen discrimination by T cells' currently in submission at Nature Immunology). It is unknown if such exclusion exists at the end of membrane pseudopodia prior to contact. A methodology was developed to investigate this by imaging CD45 on the apical membrane surface of Jurkat T cells fixed in suspension in a resting state. In order to resolve individual pseudopodia, STORM labelling was chosen to repeatedly sample individual proteins and thus increase the localisation density and reduce the effect of the detection efficiency that may lead to missed events. Pseudopodia are expected to be of $\sim$250 nm diameter and so should be resolvable by the DHPSF given sufficient localisation density, providing information on the existence of pre-exclusion zones at the tip of pseudopodia.

Jurkat T cells were labelled with Alexa647-CD45 antibodies (Gap8.3, anti-CD45) and imaged in a STORM mode in a GLOX STORM buffer (figure 5.11). Constant 641 nm and 405 nm illumination was incident in a HILO configuration at $\sim$1 kW/cm^2 and 0.1 kW/cm^2 respectively. 100 nm gold nanoparticles were used for fiducial correction. 240,000 frames were recorded for three cells with an exposure time of 30 ms with 220,000$\pm$80,000 localisations recorded per cell. Acquisitions were limited to $\sim$2 hours due to degradation of the GLOX buffer when exposure to oxygen present in the air. This applications highlights the reduced localisation density required to achieve isolated emitters with the DHPSF compared to other techniques that employ a smaller PSF. However, the increased depth of field allows for large psuedopodia to be imaged in a single focal plane.

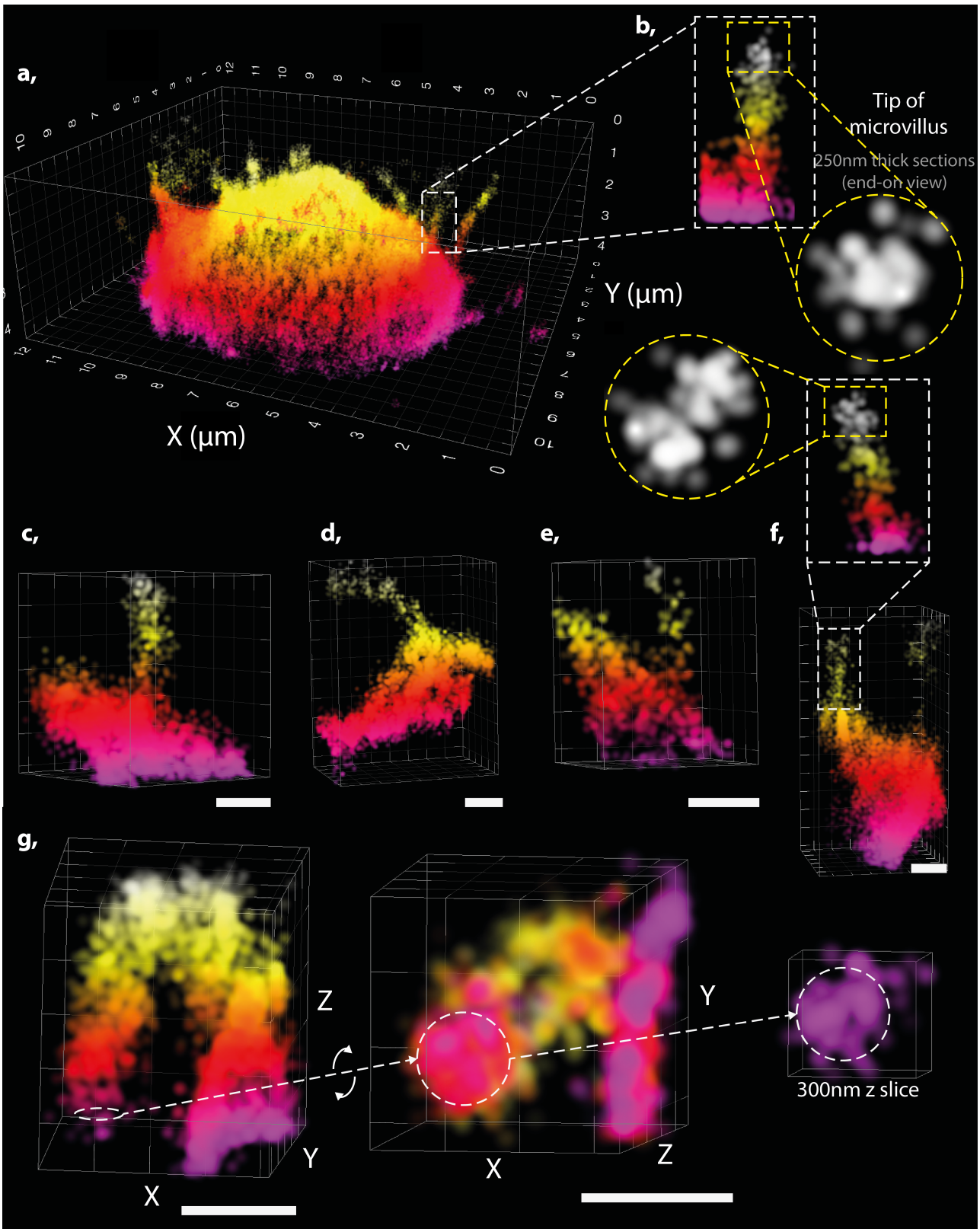

Fig. 5.11 Figure caption on following page.

Fig. 5.11 (Previous page.) STORM imaging of CD45 on the apical surface of Jurkat T cells with the DHPSF. (a) $\sim$4 μm thick section of the CD45 imaged at apical surface of a Jurkat T cell. Localisations are coloured axially for visibility. (b) Individual pseudopodium from (a) highlighted with a 250 nm section at the tip rendered in an end-on view (dashed yellow circle). No obvious segregation is observed. (c-e) Individual pseudopodium from other Jurkat T cells. (f) Additional highlighted pseudopodia from (a) highlighted with a 250 nm section at the tip rendered in an end-on view (dashed yellow circle). No obvious segregation is observed. (g) An individual pseudopodium rendered side-on and end-on with a 300 nm section shown. All scale bars are 500 nm.

Membrane nanostructure of pseudopodia could be resolved due to the increased localisation density caused by the increased expression of CD45 compared to the TCR and by repeat blinking events observed in STORM. Pseudopodia were observed to be $\sim$250-300 nm in diameter which agrees well with previous EM data [201, 200] but did not appear hollow, as would be expected. This could be due to the presence of structure below the localisation precision of the DHPSF platform or a lack of rigidity in the membrane causing a small amount of motion relative to the cell body. No obvious segregation zones were seen at the tip of pseudopodia, regardless of pseudopodia length, and the CD45 appeared largely uniformly distributed across the outer membrane. This result, combined with 2D imaging displaying a lack of CD45 segregation at very early stage contacts (data not shown but included in submitted manuscript), support the idea that CD45 is not excluded from the tips of pseudopodia in resting T cells. This observation is compatible with previous studies indicating that CD45 exclusion is a cause rather than a consequence of T-cell triggering [226, 227, 216].

5.3 3D Imaging in Adherent Cells

In order to demonstrate the applicability of the DHPSF to 3D-SMLM in a wide-range of biological samples, imaging was conducted in adherent cell types in addition to the suspension cells previously presented. Adherent cells do not permit coverslip cleaning immediately prior to imaging, increasing non-specific background and thus typically represent a more difficult system to image than suspension cells.

5.3.1 Imaging the 3D Distribution of K-ras in HeLa Cells

The overall distribution of specific proteins within a cell has traditionally been difficult to determine at the single molecule level as reduced depths of field do not always cover a significant fraction of the sample and thus require focal-plane scanning to collect a representative image. Without excitation confinement matched to the depth of field, fluorophores outside of the imaging volume are photobleached and thus cannot be detected. Most 3D-SMLM techniques require narrow ($\sim$500 nm) excitation confinement to match their depth of field in order to achieve adequate localisation density. The large depth of field of the DHPSF allows for the distribution of specific proteins across a significant fraction of individual cells to be simultaneously imaged, reducing the need for image-plane scanning in quantitative studies.

Ras proteins are small GTPases that exist in inactive GDP-bound and active GTP-bound states and regulate cell proliferation and differentiation by signalling though a number of pathways [230]. Three isoforms of Ras are expressed in human cells: K-ras, H-ras, N-ras. Ras protein malfunction is common in tumorigenesis with K-ras mutation observed in 86% of cases in humans [231]. K-ras attaches to the inner leaflet of plasma membrane through a C-terminal membrane anchor. On the plasma membrane, K-ras proteins diffuse laterally as monomers and dimers and assemble into higher order oligomers and nanoclusters [232]. Recent evidence suggests that in healthy cells K-ras is in part organised in specific nanodomains on the plasma membrane, furthermore, changes in the membrane potential were inferred to lead to spatial reorganisation of K-ras [233, 234]. However, the complete picture of the distribution of K-ras on the outer membrane and the inner endomembrane remains unclear. It has been proposed that K-ras nanoclusters provide platforms for effector binding and signal transduction, thus promoting cell proliferation and survival [235]. Understand the spatiotemporal distribution of K-ras across the cell has the potential to inform the development of new targeting strategies that may have significant therapeutic implications.

In order to investigate the distribution of K-ras proteins across HeLa cells, the DHPSF was used to perform 3D-SMLM of (K-ras)-mEos3.2 across a $\sim$3.5 μm section in the central plane of HeLa cells (figure 5.12). 200 nm gold nanoparticles were added to the sample to act as fiducial markers. The gold nanoparticles stuck to the cells without requiring additional coating and were washed out of solution before imaging. Cells were imaged for $\sim$100,000 frames with 100 ms exposure and constant low-power 405 nm illumination until no more mEos3.2 was observed. Large-scale structures were observed (figure 5.12c), most likely corresponding to K-ras distributed on the outer membrane and components of the endomembrane.

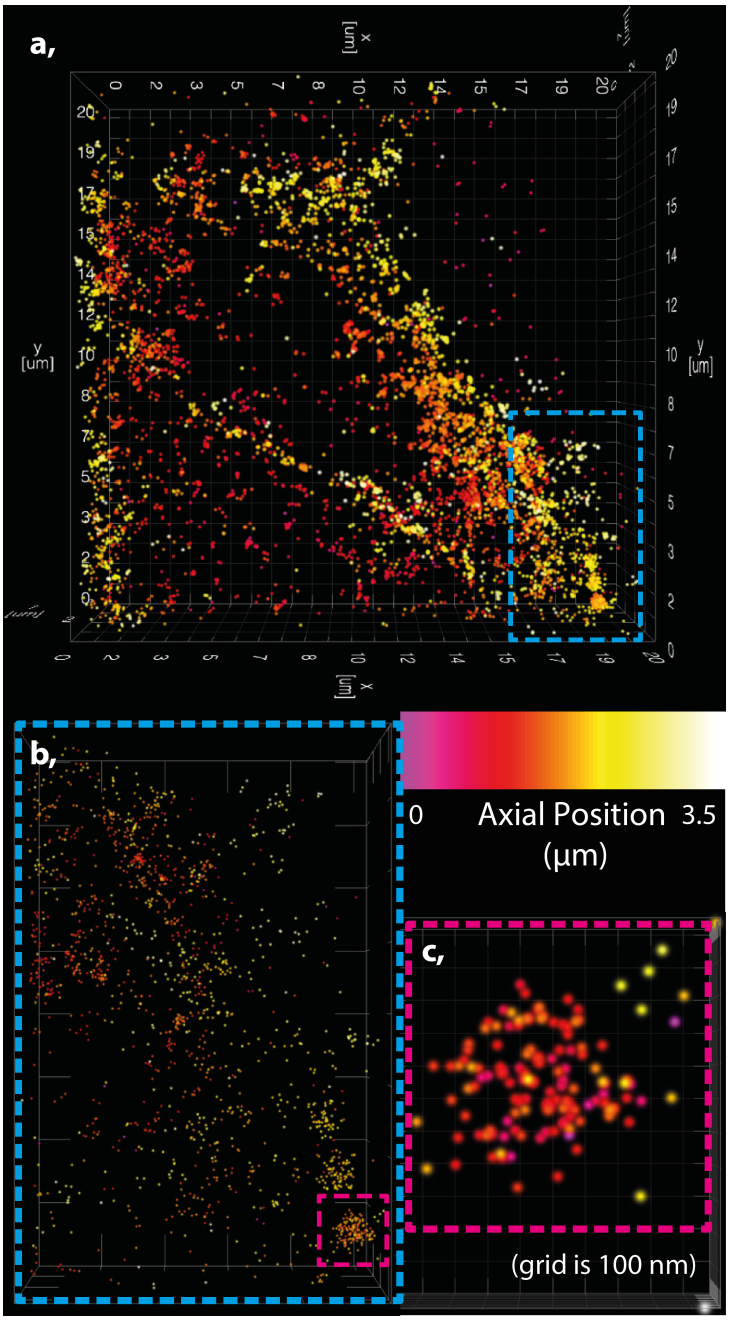

Fig. 5.12 DHPSF imaging of K-ras shows 3D organisation within HeLa cells. (a) K-ras distribution through ∼3.5 μm thick section in the central plane of a HeLa cell. Repeat localisations of the same fluorescence event were filtered. Localisations are rendered with 100 nm precision for visibility and coloured as a function of axial position. (b) Highlighted area from (a) (blue-dashed box). Localisations are rendered with experimentally determined precision of ∼25 nm laterally and ∼50 nm axially. (c) Highlighted large-order cluster of K-ras (pink-dashed box from (b)).

The redistribution of K-ras upon a change in membrane potential was investigated by imaging HeLa cells before and after membrane depolarisation caused by the addition of potassium. The plasma membrane of dividing and onocogenically transformed cells, that exhibit increased proliferation, are more depolarised than quiescent cells [230]. Therefore, membrane depolarisation is expected to result in an increased level of K-ras clustering in wildtype cells, increasing the promotion of proliferation and survival.

In order to investigate this hypothesis, 12 cells were imaged in control conditions and 9 cells stimulated by high potassium potassium (100 mM) were imaged as described above. Repeat localisations were removed. In order to investigate small-scale clustering, the number of localisations within 100 nm of each localisation within a 4 μm x 5 μm area from each cell was investigated. To enable direct comparison, the localisation density in each region was matched to the lowest density region (1,595 per μm^2 laterally) by considering the first 31,900 localisations recorded from each region (the minimum number recorded for any region). The fraction of localisations was plotted as a function of the number of neighbouring localisations within 100 nm (figure 5.13). Stimulated cells were observed to have more neighbours than the control condition. This result indicates that membrane depolarisation results in increased K-ras nanocluster formation. As dividing and oncogenic cells exhibit membrane depolarisation relative to quiescent cells, this result is consistent with the notion that K-ras nanoclusters promote cell proliferation and survival. This could be studied further by investigating oncogenic mutant cells with the same methodology, as a positive control.

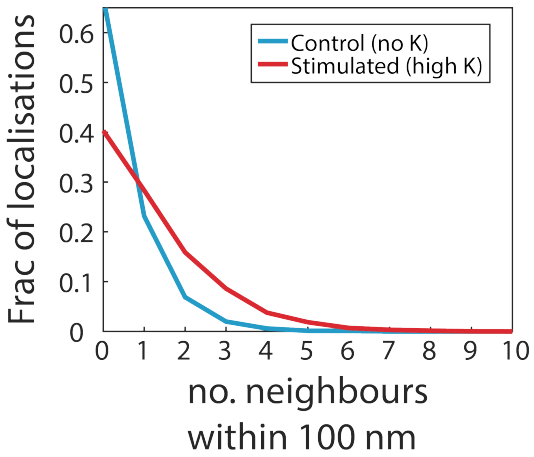

Fig. 5.13 Number of nearest neighbours within 100 nm of K-ras localisations in HeLa cells. 20 μm^2 areas of localisations from control cells (no potassium in buffer, 12 cells) and stimulated cells (high potassium in buffer, 9 cells) were analysed. The localisation density was matched (1,595 localisations per 20 μm^2) and the number of neighbours within 100 nm of each localisation was plot as a fraction of the total number of localisations.

5.3.2 Imaging the 3D Distribution of Proteasomes in HEK Cells

Another application that benefits from the increased depth of field of the DHPSF is imaging the 3D distribution of the proteasome across a significant fraction of human embryonic kidney (HEK) cells. The proteasome is a large multi-subunit protease involved in proteolysis as a key part of the cell degradation machinery [236, 237]. Despite its importance, the cellular distribution is less well studied and published data suggests that the proteasome distribution may be distinctive based on cell type and cell cycle phase [238]. The proteasome was observed to be distributed throughout the nucleus and cytoplasm in mammalian cells in 2000 [239]. However, this organisation was not studied at the single-molecule level, reducing the potential for quantitative analysis. Using the DHPSF, the distribution of the proteasome was imaged through a central plane of HEK cells expressing proteasome subunits (proteasome core-particle subunit (Pre1) and proteasome regulatory-particle subunit (RPN1)) fused to mEos3.2.

Two separate subunits of the proteasome labelled with mEos3.2 were imaged across a $\sim$4 μm thick section towards the top of fixed adherent HEK cells (figure 5.14). HILO illumination of 561 nm and 405 nm lasers was constantly incident on the sample to image in a PALM mode. Fluorescent nanodiamonds were added to the fixed sample prior to imaging for fiducial tracking as they were found to provide a higher SNR compared to gold nanoparticles. The nanodiamonds stuck to the cells without additional coating and were washed out of solution prior to imaging. For the three cells presented in figure 5.14, 200,000 frames were acquired with a 50 ms exposure time. Between 16,000 and 20,000 localisations were recorded from each cell after filtering for repeat localisation in time (0.5 s) and space (300 nm). Proteasomes were observed to be distributed across the entire cell in both labelling conditions, agreeing with 2D imaging of the same cell types conducted by Dr Yu Ye on a separate super-resolution instrument. No obvious order was seen in the localisation data in any case. Proteasomes were observed ubiquitously within the nucleus and cytoplasm, agreeing with previously published data [238]. Changes in density were seen within the centre of the cells in all cases, potentially corresponding to a reduced density within the nucleus compared to the cytoplasm. However, in these experiments, this could not be confirmed as no nuclear staining was implemented. Two-colour imaging of the proteasome and the nuclear envelope could allow for the relative concentrations between the two environments to be compared in future studies, providing an appropriate labelling strategy is developed to image the nuclear envelope.

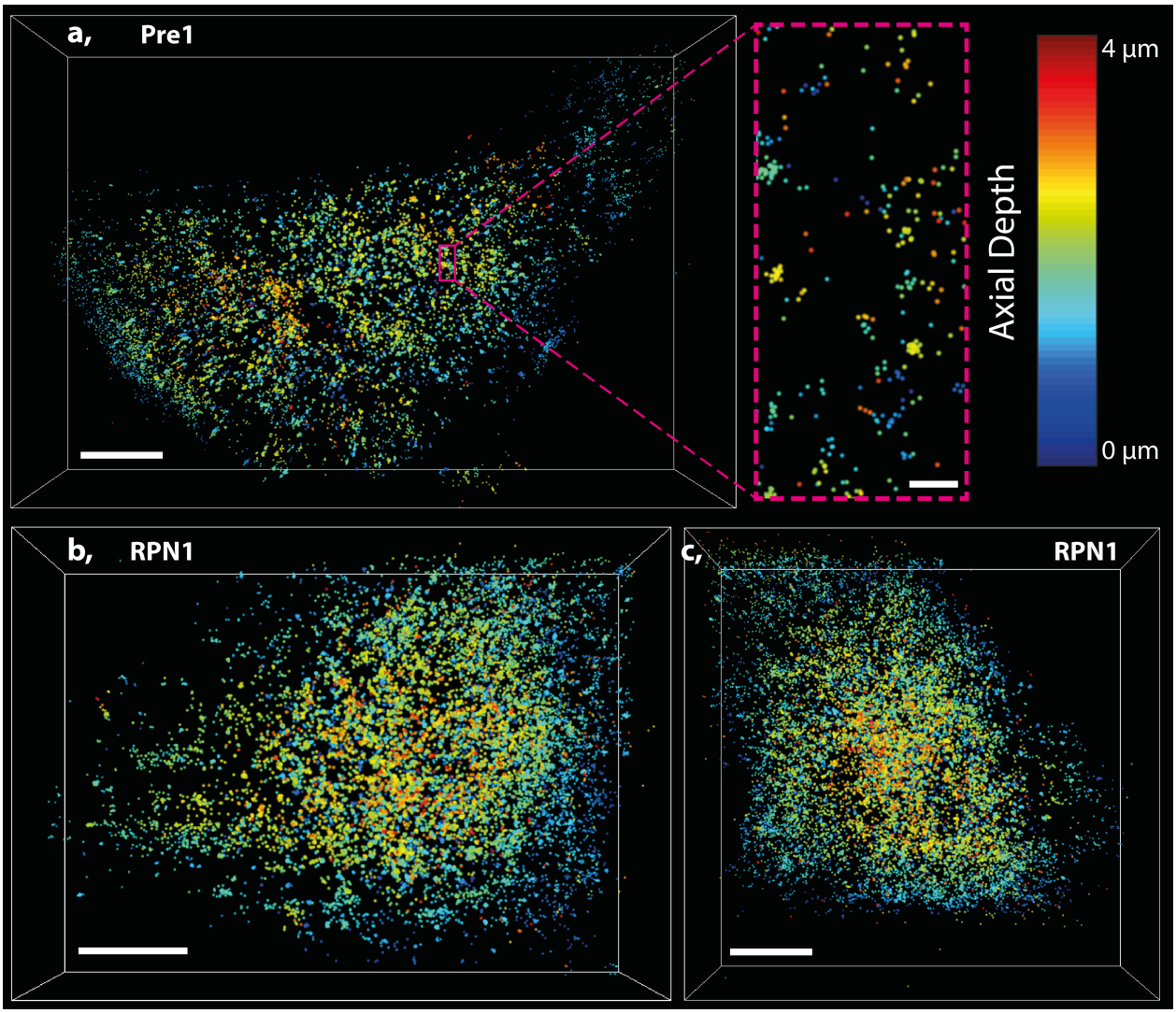

Fig. 5.14 DHPSF imaging of proteasomes shows the 3D distribution in HEK cells. (a) Proteasome core-particle subunit (Pre1) tagged with mEos3.2 was imaged through a ∼4 μm thick volume towards the apical surface of a HEK cell. 15,878 localisations were recorded after spatial and temporal filtering. A highlighted region is shown with localisations rendered with experimentally determined precision (∼25 nm laterally and ∼50 nm axially). (b&c) Two cells expressing proteasome regulatory particle subunit (RPN1) tagged with mEos3.2 were imaged. 17,275 and 20,020 localisations were collected respectively after spatial and temporal filtering. In (a-c) whole cell volumes, localisations are rendered with 100 nm FWHM for visibility. Scale bars for (a-c) are 10 μm and 500 nm in the highlighted region from (a). All localisations are coloured axially from 0 μm (blue) to 4 μm (red).

5.4 Quantifying Cluster Size and Shape in Mouse Brain Tissue

Tissue slices represent a more physiological sample for the majority of biological systems but have traditionally proven challenging to image. Background fluorescence is increased due to the increased sample thickness compared to cells cultured adherently or in suspension and the pre-defined sample geometry is typically less compatible with specialised sample chambers often required for light-sheet excitation confinement techniques. To demonstrate the ability of the DHPSF to image in tissue samples without complex sample preparation, postsynaptic density protein 95 (PSD95) fused to mEos3.2 was imaged in fixed brain tissue samples taken from transgenic mice. In the brain, signal transduction occurs at synapses between two neurons via the release of signalling molecules (neurotransmitters) from the presynaptic neurone, which bind and activate receptors on the postsynaptic neurone (figure 5.15a). These receptors are held in place by a dense protein scaffold known as the postsynaptic density (PSD) (containing PSD95). A previous 2D-SMLM study of $\sim$100,000 synapses in transgenic mice showed that PSD95 exists in nanoclusters that make up a basic structural unit of the excitatory synapse [122]. PSDs were observed to be up to 600 nm in diameter and comprised of 1-3 nanoclusters of $\sim$100 nm diameter. However, the 3D structure and organisation of the PSDs was not determined. These length scales are within the localisation precision of the DHPSF and thus additional information on PSD structure could be obtained with its application. Additionally, due to the large depth of field compared to 2D-SMLM and robust counting potential of the DHPSF many more synapses can be simultaneously imaged, although acquisition rate is reduced due to the increased size of the DHPSF on the detector.

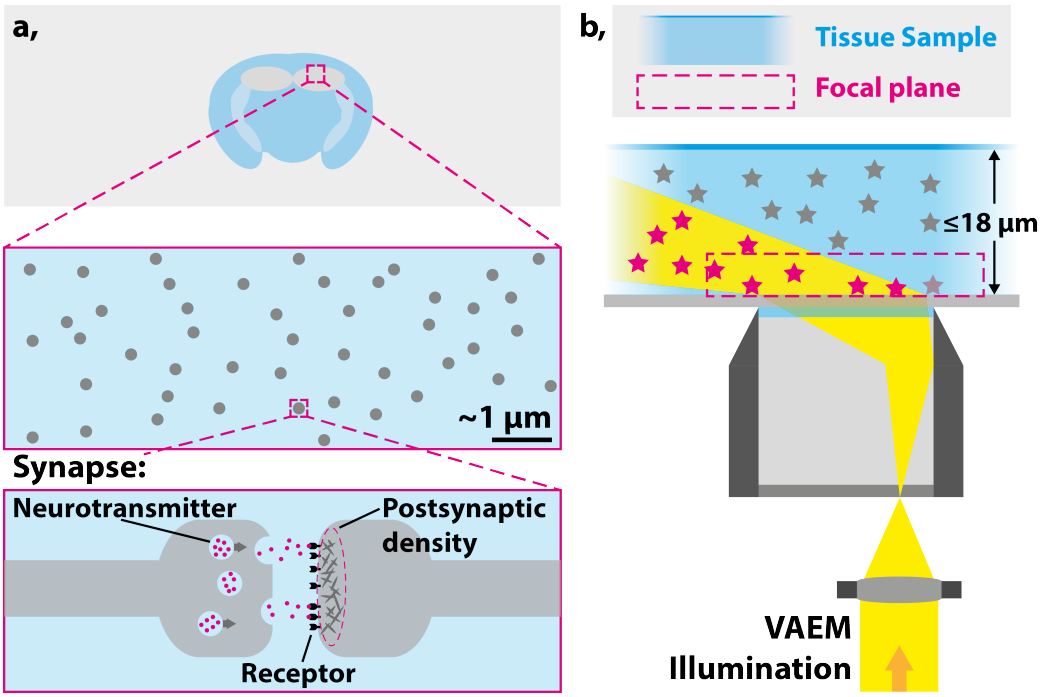

Fig. 5.15 Schematic of experimental set up for imaging fixed tissue slices. (a) Schematic of fixed brain slice on a coverslip (top) with highlighted region in the hippocampus containing individual synapses (middle) and a simplified cartoon of a synapse showing the postsynaptic density (bottom). (b) Side-on view of experimental set up using VAEM excitation to image mEos3.2 molecules (star shapes) at the bottom ∼4 μm of fixed brain tissue slices. Tissue samples with up to 18 μm thickness were imaged, although in practise any thickness slice is compatible with the set up.

Tissue samples expressing PSD95-mEos3.2 with thicknesses ranging from 18 μm to 6 μm were imaged with the DHPSF in a PALM mode with VAEM [59] excitation. A water immersion lens was chosen over an oil immersion lens as it better matched the expected refractive index of the brain sections (typically ≈1.4). Although spherical aberration was expected, the form of the DHPSF remained robust when imaging at the top surface of 18 μm thick brain sections. In order to reduce any unwanted aberration-induced effects, focal planes were placed at the bottom of the brain sections so that the coverslip surface was in the periphery (see figure 5.15b). The background signal and number of detected photons per localisation was quantified under identical imaging conditions for 18 μm, 8 μm and 6 μm thick brain sections (figure 5.16). Initial detected background photon values were ∼26 photons/pixel, ∼17 photons/pixel and ∼17 photon/pixel respectively. After 250 seconds the background had fallen to ∼17 photons/pixel, ∼12 photons/pixel and ∼11 photons/pixel respectively. However, for 6 μm thick sections holes in the brain sections could be seen by white-light illumination in some areas. The number of detected photons from 15,000

localisations recorded from the bottom ∼4 μm of each section thickness was unchanged with all samples resulting in ∼460±150 photons per localisation, corresponding to a localisation precision of ∼25 nm and ∼50 nm laterally and axially (see chapter 2). These data indicate that thinner tissue samples result in better imaging conditions although the difference between 8 μm and 6 μm thickness is marginal and 6 μm thick sections proved less reliable to create. Ideally tissue sections should be as thin as possible without compromising structural integrity.

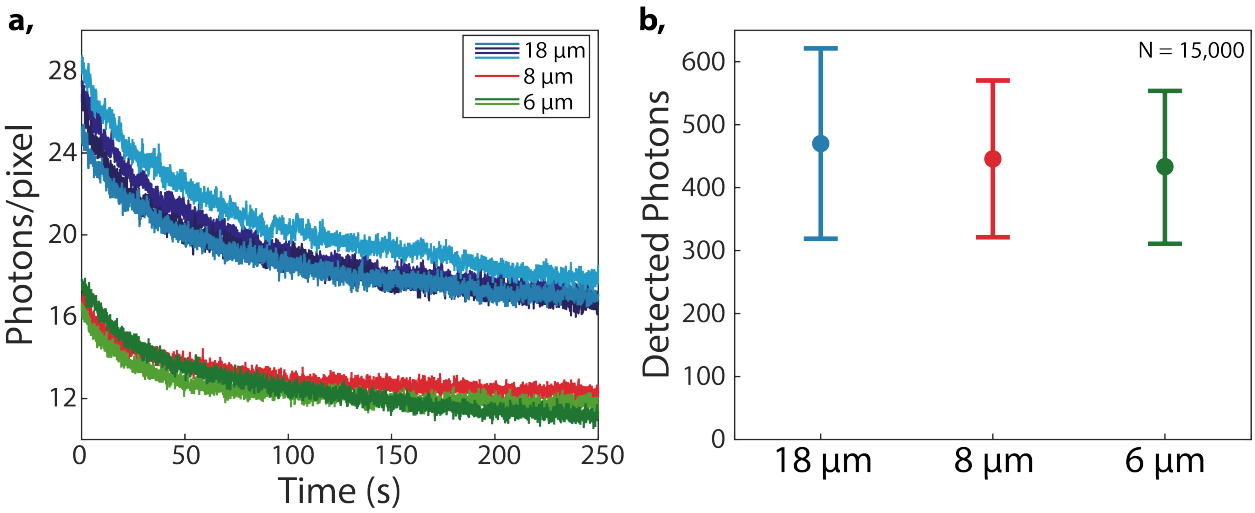

Fig. 5.16 Quantifying background and detected photons in tissue samples of varying thickness. (a) Detected background photons per pixel over 250 seconds under identical imaging conditions for 18 μm thick (blue), 8 μm thick (red) and 6 μm thick (green) tissue samples. (b) Mean and standard deviation of detected photons for 15,000 mEos3.2 localisations under identical imaging conditions for 18 μm thick (blue), 8 μm thick (red) and 6 μm thick (green) tissue samples.

In these preliminary experiments individual synapses could be seen (figure 5.17). No fiducial correction was implemented so it is likely that the focus drifted by ∼40 nm (see chapter 2) over the acquisitions (250 seconds). In future experiments, fiducial correction should be employed as extended acquisition times are required to image all PSD95-mEos3.2 within the image volume. Figure 5.17 shows a ∼65 μm x 65 μm x 3.4 μm volume of PSD95-mEos3.2 imaged in the CA1 radiatum region of the hippocampus from an 8 μm thick mouse brain section. An exposure time of 50 ms was used and 10,247 localisations were recorded in 250 seconds across ∼1,200 PSDs. Individual PSDs appeared to be ∼100 nm laterally in diameter, agreeing well with previous data [122]. Due to a lack of fiducial correction axial measurements were less reliable and PSDs appeared axially elongated, indicating a degree of focal drift. This work was used to optimise imaging conditions for future brain-slice data collection.

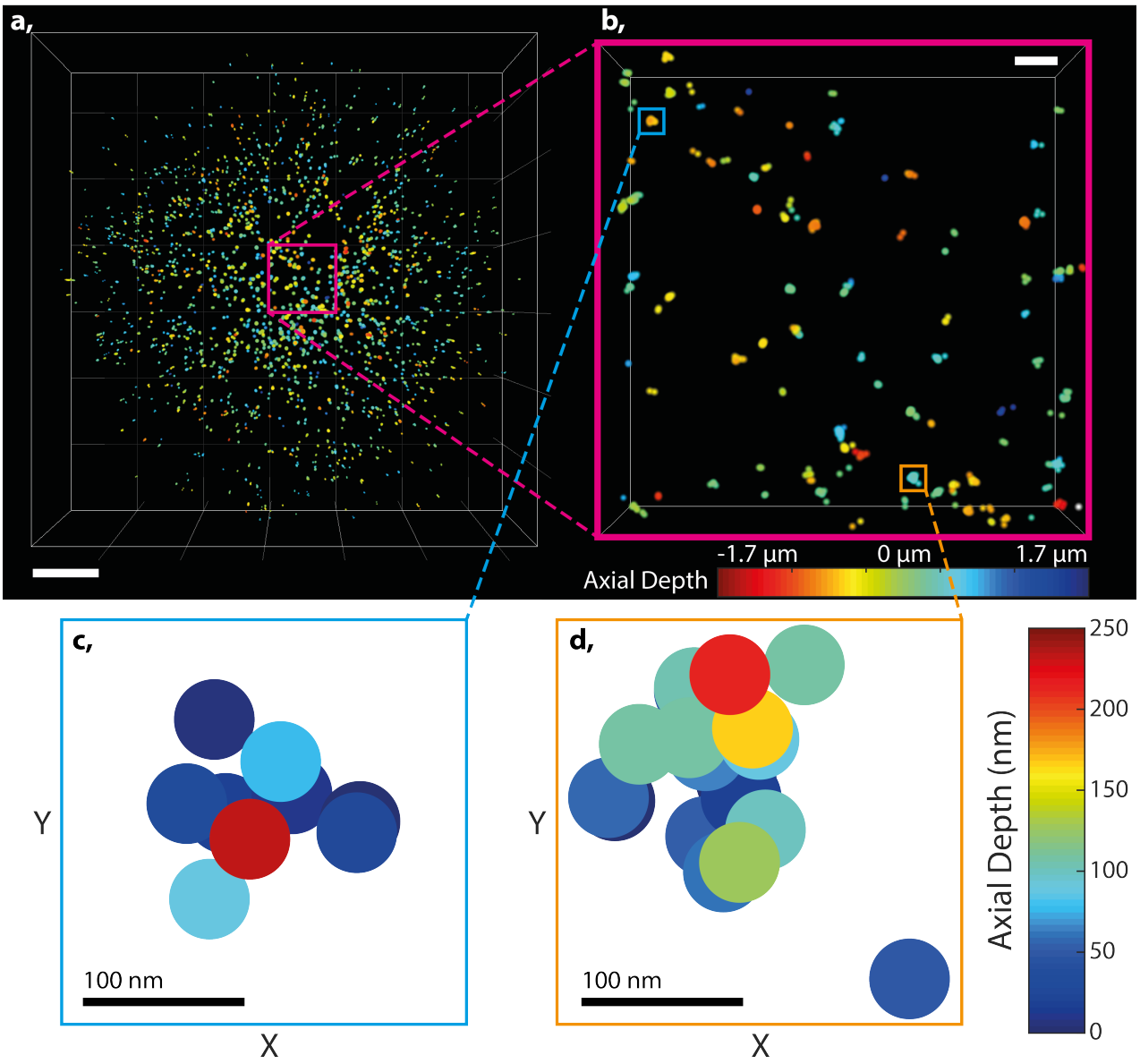

Fig. 5.17 PSD95-mEos3.2 in the CA1 radiatum imaged in fixed mouse-brain tissue with the DHPSF. (a) 10,247 localisations from a ∼65 μm x 65 μm x 3.4 μm image volume within the CA1 radiatum. Localisations were rendered with a 200 nm FWHM for visibility. Grid lines and scale bar are 10 μm. (b) Highlighted 10 μm x 10 μm x 3.4 μm volume from (a). Individual post-synaptic densities can be clearly seen across the depth of field. Localisations are rendered with a 100 nm FWHM for visibility. Scale bar is 1 μm. (c&d) Individual post-synaptic densities highlighted from (b) plot with radius equal to the expected lateral localisation precision of the DHPSF (25 nm). The structures are ∼100 nm in diameter laterally. A lack of fiducial correction makes axial measurement inaccurate but localisations are seen over ∼250 nm axially for both cases.

5.5 Discussion

3D super-resolution imaging is gaining popularity with the recent emergence of techniques such as lattice light-sheet enabled SIM [89, 240] and increased publications from 3D-SMLM [83, 82, 208, 241]. The work presented in this chapter demonstrates that the DHPSF is applicable to a wide range of imaging studies away from the coverslip, where 2D methods typically perform poorly. We show that the DHPSF is compatible with imaging suspension cells, adherent cells and tissue samples and is compatible with a number of imaging modalities including PALM and STORM. We also employed a range of labelling strategies including: expression of fluorescent proteins, HaloTag ligands and antibody labelling with either 561 nm or 641 nm laser excitation. We achieved the first implementation of the DHPSF for large-volume imaging with multiple image planes covering whole eukaryotic cells [147], which has since been extended to higher localisation densities [108].

Three different biological systems were investigated: Firstly, whole T-cell volumes were imaged with minimal aberration by employing a water-immersion objective lens. In addition to observing morphological changes, T-cell protein redistribution was quantified upon immunological stimulation across entire T cells and compared to cell-specific model distributions. High-resolution topological maps of the apical surface of fixed T cells were created by STORM imaging of membrane-bound CD45 with antibody labelling, allowing for membrane nanostructure to be investigated. Secondly, the overall distribution of specific proteins was imaged across $\sim$4 μm thick sections of fixed adherent cells in a single image plane using a photoactivatable fluorescent protein. This enabled quantification of the redistribution of K-ras protein upon changes in membrane potential in HeLa cells and in HEK cells the localisation of the proteasome within cells was determined. Finally, individual post-synaptic densities could be resolved deep into fixed mouse-brain tissue samples by imaging PSD95-mEos3.2 in a PALM mode. In all of the presented cases HILO or VAEM excitation proved sufficient excitation confinement to facilitate single-molecule imaging. As a result, imaging is compatible with almost all sample geometries as a single objective lens can be used for excitation and emission collection.

In theory the DHPSF provides a slightly worse localisation precision compared to Biplane 3D-SMLM methods at low SNR [92], although it is more consistent though the depth of field. Astigmatism 3D-SMLM is expected to result in the worst localisation precision of the three techniques in all dimensions at all SNR levels [92]. However fitting routines for Astigmatism and Biplane are more developed than the single method available for the DHPSF.

Astigmatism and Biplane are currently more robust to fitting in noisy datasets as they do not require template matching or user-defined thresholds for individual datasets. The result of this is that Astigmatism and Biplane are more likely to achieve a localisation precision closer to their theoretical limits in difficult to image samples compared to the DHPSF. Consequently, the DHPSF should be reserved for imaging high-SNR samples or for situations that require an extended depth of field, as in the applications presented in this chapter. As mentioned in chapter 2, additional DHPSF fitting methods are in development that should improve its performance and applicability for low-SNR samples.

Advantages of the DHPSF for 3D Imaging

A key feature of SMLM is quantification. 3D techniques provide more information on the position of individual fluorophores compared to 2D techniques, which facilitates more robust quantification, at the cost of increased experimental complexity. The DHPSF exhibits a more consistent localisation precision across the depth of field compared to Astigmatism and Biplane 3D SMLM techniques [92], allowing for more reliable quantification across the depth of field. One example in which this could be important is quantifying the size of PSD95 nanocluster in brain tissue. Homogenous nanoclusters would appear homogeneously sized across the depth of field for the DHPSF. Whereas a $\sim$10 nm increase in localisation precision at the focal periphery is expected for both Astigmatism and Biplane [92] and would cause nanoclusters to appear $\sim$20 nm larger in diameter at the periphery compared to those located at the centre of the focal plane. Multifocus microscopy (MFM) gains axial information by comparing the 2D PSF between multiple image planes, as in Biplane, suggesting that it will exhibit a similar axial distribution of localisation precision, although this not been investigated.

The increased depth of field of the DHPSF ($\sim$4 μm) compared to other commonly used 3D SMLM techniques ($\sim$500 nm for astigmatism and Biplane) affords the advantage of collecting more data from a single image plane. This allows for extended structures to be contained in a single image plane (*e.g.* entire pseudopodia spanning several micrometres on the apical surface of T cells) and for a significant fraction of a cell to be imaged simultaneously, reducing the need for imaging multiple planes within a cell and avoiding the increase in experimental and analytical complexity associated with stitching together successive frames. This was especially important for imaging K-ras and proteasomes in adherent cells as a single DHPSF image plane covered $\sim$50% of a typical cell volume, whereas other methods would be expected to cover $\sim$6-7%. The increased depth of field also enabled $\sim$8 times more

PSDs to be imaged in a single image plane compared to the previous 2D study, reducing the number of acquisitions required accordingly to properly catalogue PSD subtypes. Although other Tetrapod PSFs offer an even larger depth of field (<20 μm) [113], this comes at the cost of increased localisation uncertainty and PSF size, reducing working imaging concentrations. The DHPSF represents a compromise between depth of field and PSF size that is well suited to the majority of cell imaging and track applications.

Light-sheet illumination has been combined with the DHPSF to increase SNR [107] and has recently been demonstrated for cell imaging [108]. The DHPSF is particularly well-suited to imaging with simple light-sheet systems which typical have an axial thickness of 2-3 μm [61]. The comparable depth of field of the DHPSF allows for all simultaneous fluorescence events across the sample to be recorded as out-of-focus fluorophores are not excited. This has the effect of increasing localisation density and facilitating accurate stoichiometry measurements in PALM experiments (depending on the activation efficiency and blinking kinetics of the fluorophore). To achieve the same conditions with typical 3D-SMLM techniques ultra-thin excitation geometries could be employed at the cost of significant technical complexity. Bessel and Airy beam light-sheet methodologies [87, 242] offer a comparable thickness to 2D, Astigmatism and Biplane methods, although additional excitation maxima can be present outside of the depth of field, reducing the counting efficiency of the experiment.

5.5.1 Disadvantages and Difficulties of the DHPSF for 3D Imaging

As the DHPSF occupies a significantly greater area on the detector compared to the PSFs of Astigmatism, Biplane and MFM techniques, a lower density of emitting fluorophores can be simultaneously imaged before their PSFs begin to overlap and can no longer be resolved. Consequently, a relative sacrifice of either localisation density (by reducing labelling density) or acquisition duration must be made. For most cases it is preferable to increase acquisition time by increasing the fraction of time that fluorophores spend in their ‘dark’ state. In PALM this can be achieved by reducing the intensity of the activation illumination, so long as thermal activation is not limiting. In STORM this can be achieved, depending on the fluorophore, by optimising the composition of the buffers and/or reducing the activation intensity. For PAINT reducing the concentration of the probe in the buffer reduces the fraction of time that each target is visible and thus increases the ‘dark’ state. As shown in chapter 2, the DHPSF is $\sim$5-fold larger compared to an analogous 2D PSF. As a general

rule, for optimal density localisations rates should be reduced by this factor compared to 2D experiments.

Another factor that must be considered when using 3D-SMLM is the reduction of signal compared to 2D imaging. For the DHPSF, this is in part due to the photons comprising a 2D PSF being split into the two lobes of the DHPSF as well as due to transmission losses from the additional optics creating the DHPSF transformation. This effect is exacerbated in the presented applications by the use a water-immersion objective lens instead of a high-NA oil-immersion objective lens, which is expected to result in a factor 0.685 reduction in collecting power (see chapter 3). In practice $\sim$43% of the 2D PSF photons were observed in each lobe. Additionally, water-immersion lenses collect background signal from a larger volume, further reducing SNR. The result of these factors is that samples with low signal or high background can be more difficult to image compared to 2D, requiring careful experimental optimisation or the introduction of narrower excitation confinement. This is especially true for PAINT imaging, due to the increased background signal caused by freely-diffusing fluorophores in solution, or when imaging fluorescent proteins. However, modern organic dyes are generally bright enough for DHPSF-SMLM outside of PAINT, providing the background fluorescence of the sample is low. This can be optimised with the fixation protocol as well as imaging buffer composition (especially in STORM). For all examples shown, formaldehyde-paraformaldehyde fixation provided the lowest background signal compared to methanol-ethanol fixation. For imaging at the basal surface of low-SNR samples, where spherical aberration is not an issue, an oil-immersion lens can be employed to increase signal and reduce background.

Data processing is another disadvantage of the DHPSF compared to more standard Gaussian fitting used in 2D SMLM, Astigmatism, Biplane and MFM techniques. The only published DHPSF fitting method (easy-DHPSF [137]) is computationally expensive and not compatible with batch processing due to template fitting and user-defined thresholds. As a result, processing raw datasets is time consuming and can limit productivity in studies requiring long acquisitions of large regions, as is the case for the proposed study of PSD95 in the mouse brain hippocampus. Acceleration of the fitting process and removing the need for user-defined thresholds would drastically improve throughput in future studies and represents a key step towards wide-spread adoption of the DHPSF.

A less fundamental limitation of the DHPSF is its sensitivity to phase-mask alignment. The position of the phase mask must be optimised to reduce lateral movement as the DHPSF is scanned axially before every experiment. This makes the platform less user friendly but

also makes experiments that require the phase mask to be changed or removed when imaging the same sample difficult. For example, in the current form of the instrument, experiments employing sequential two-colour DHPSF imaging with one detector are not possible and swapping from DHPSF imaging to 2D can only be achieved once per sample as swapping back would require the DHPSF to be recalibrated. For samples with fiducial markers, a single fiducial could be used to recalibrate the DHPSF although this would take additional time and add complexity. The ideal solution is to ensure that the phase mask is in precisely the same position before and after being swapped so that the form of the DHPSF is maintained and recalibration is not required. Automation of the phase-mask alignment process would significantly increase usability but would require motorised mountings which are currently not in place on the platform. This limitation applies to all PSF-engineering techniques requiring direct measurement of the PSF for calibration such as Astigmatism and Tetrapod PSFs.

5.5.2 Potential Improvements to Current Instrumentation

As discussed above, the potential to swap in and out DHPSF phase masks mid-experiment without the need to recalibrate the form of the DHPSF would be useful. In the current set up the phase mask is mounted on a 3-axis translation stage to allow for its position to be adjusted manually. A robust turret system mounted on a 3-axis translation stage could allow for separate phase masks to be swapped in and out of the emission path, facilitating sequential multicolour and 2D imaging on the same detector. However, the stability of the transition would have to be measured. Another potential solution would be to position the phase mask with large travel range and precise movement stages (*e.g.* walker piezo stages). These stages would be able to return to previously determined positions with high repeatability so that the DHPSF exhibits the same form. Again, the reproducibility of the system would need to be thoroughly tested before use.

When imaging white-light through the DHPSF phase mask the image appears distorted as each point is subject to the double-helix phase transformation. This can make it difficult to identify specific areas of the sample and can obscure fine detail that could provide information about the condition of individual cells. The ability to swap between 2D and 3D imaging would also be useful for a number of other applications such as aligning bulk labelling of cellular structures (*e.g.* nuclear envelope staining, lysosome staining etc.) with 3D-SMLM data sets. This could be achieved with a single detector without moving the phase mask by diverting the emission to an alternative path. As the emission path is particularly sensitive to

phase distortions, ultra-flat mirrors should be used. At least one additional lens would also be required to compensate for the increased path length so that the image planes of both paths coincide on the detector. If this system can be implemented in stable and easy-to-use manner the usability of the instrument would be greatly increased as experiments could be optimised in a 2D mode before swapping to the more challenging DHPSF mode.

Currently the DHPSF instrument is set up to facilitate simultaneous two-colour imaging with two detectors and two phase masks sharing the first lens of their respective 4f systems (see figure 2.4 in chapter 2). At the time of writing this has not been fully exploited due to issues controlling both EMCCD cameras with micromanager making data acquisition unstable. In order for simultaneous two-colour imaging to be realised on the current instrument data handling from two cameras must be properly implemented. Correction for chromatic aberration must also be applied. As gold nanoparticles and nanodiamonds are fluorescence across a broad wavelength range, multiple fiducial markers in the field of view would allow for direct aberration correction and drift correction. Simultaneous two-colour imaging with the DHPSF has been demonstrated by the Moerner lab [105], but in practice the presented multicolour cell imaging was achieved sequentially.

Fiducial markers are often a consideration for 3D imaging. When imaging away from the surface it becomes more complicated to position fiducial markers within the imaging volume without their PSFs overlapping with areas of interest within the sample. In the work presented in this chapter, fiducial markers were added to fixed adherent cell samples and naturally stuck to the surface of cells. Free markers diffusing in the solution were then washed away so that they did not interfere with imaging. The added concentration was tuned so that typically there was $\sim$1 marker per field of view after washing. The sample was then manually searched for areas to image in which the cells looked healthy and a fiducial marker was present that did not obstruct the area of interest. Depending on the condition of the sample this sometimes took a considerable amount of time. Data acquisition could be improved by positioning fiducial markers away from the surface and away from the cells or in a gel matrix (depending on the pore size relative to the fiducial markers). Another solution implemented by the Moerner group is using a large depth-of-field PSF to periodically image fiducial markers placed on the surface, out of the DHPSF image plane [108]. In this approach a programmable deformable mirror is used in place of the phase mask to swap between DHPSFs and Tetrapod PSFs at the expense of signal transmission as deformable mirrors only operate on one lateral polarisation axis. The same effect could be achieved without this loss of signal with multiple imaging paths.

5.5.3 Concluding Remarks

The applications presented in this chapter demonstrate the ubiquity of the DHPSF for SMLM imaging away from the surface in a range of cell types and labelling methodologies. For all experiments the methodology best-suited to obtain the desired information should be chosen. For 3D SR imaging studies this decision is based partly on the labelling methods available (*e.g.* organic dyes or fluorescent proteins), which affect the SNR of the sample, and the nature of the question being asked. If dynamic processes need to be visualised, a methodology with sufficient time resolution must be used. Deterministic 3D-SR techniques generally offer greater time resolution compared to SMLM and are thus better suited to following changing systems. 3D-STED offers video-rate imaging with similar resolution to 3D-SMLM techniques but is less compatible with quantification, especially relating to stoichiometry measurements. Experimental complexity should also be taken into account when deciding which technique to use. Deterministic SR typically requires more complex instrumentation in the excitation path compared to wide-field 3D-SMLM, which typically use collimated laser excitation with little or no additional optics. Astigmatism is the easiest 3D-SMLM technique to implement in the emission path as it requires a single astigmatic lens. Other techniques such as Biplane, MFM and iPALM require precise alignment of path lengths to achieve axial localisation. The DHPSF lies in between these two categories in complexity, requiring a simple 4f system consisting of two lenses and a phase mask. The $\sim$4 μm depth of field of the DHPSF and MFM enable imaging of many structures in a single image place, reducing the experimental complexity associated with focal-plane scanning for structures larger than $\sim$500 nm axially.

A number of projects utilising the DHPSF have been planned including: 1) 3D tracking and imaging of K-ras proteins in normal and K-ras mutant cell types, 2) 3D organisation of proteasomes relative to membrane structure under membrane polarisation and 3) 3D imaging of the distribution of PSDs across the hippocampus in mice brain sections. Another two DHPSF platforms are being built in the department in collaboration with the Lee group to address more specific questions.

A more detailed application of the technique to address T-cell protein clustering relative to membrane nanostructure is demonstrated in chapter 6.

5.6 Methodology

Measuring Lateral Shift Between Axial Planes

Fluorescent beads (T7279, ThermoFisher) were suspended in phytagel (P8169, Sigma)and imaged with the DHPSF with 561 nm excitation. A 1% solution of pytagel and 2 mL of filtered (0.22 μm Millex-GP syringe filter unit, Millipore) phosphate-buffered saline (PBS) (2810305, MP Biomedical)) was heated until boiling and kept at 70°C. 0.5 μL of a 1.8×10^{11} particles/mL solution of 0.1 μm fluorescent beads was added to 100 μL of gel solution at temperature. 50 μL of the mixture was then deposited onto argon-plasma cleaned (PDC-002, Harrick Plasma) coverslips (22×22 mm borosilicate, thickness No. 1, VWR) and allowed to cool to room temperature. The slides were then mounted onto the DHPSF instrument and the piezo stage was used to determine the distance above the coverslip and move the objective axially by 2.5 μm. 100 frames were acquired at each image plane before moving to the next. This was repeated 60 times, acquiring a total of 12,000 frames at 30 ms exposure. DHPSF fitting was conducted with easy-DHPSF [210] in MATLAB.

Imaging CD28-mEos3.2 in T cells

Before imaging $\sim10^6$ T cells expressing CD28-mEos3.2 were centrifuged at 600×g for 2 min and suspended in 1 mL of fixing solution (filtered PBS with 4% formaldehyde (Sigma) and 0.2% glutaraldehyde (Sigma)). The cells were left at room temperature for 60 min before washing three times in filtered PBS involving centrifugation. The cells were resuspended in 200 μL of filtered PBS. Meanwhile, glass slides (22×22 mm borosilicate, thickness No. 1, VWR) were argon-plasma cleaned and coated with poly-L-lysine (PLL) (molecular mass 150–300 kDa; P4832, Sigma) for 30 min. The slides were washed three times in filtered PBS with 20-100 μL of filtered PBS left on each slide. 20 μL of the fixed cells was then added and allowed to settle for ∼5-10 min.

The sample was imaged on the DHPSF platform employing a 60x 1.20 NA water-immersion objective lens (Plan Apo VC 60x, Nikon). Continuous 561 nm and 405 nm excitation was incident on the sample in HILO geometry with a power density of ∼1 kW/cm^2 and ∼5 W/cm^2 respectively. A quadband dichroic and longpasss and bandpass filters were used to separate the emission signal (Di01-R405/488/561/ 635-25x36, and BLP02- 561R-25

and FF01-580/14-25, respectively, Semrock) before the detector. An exposure time of 100 ms was used. DHPSF fitting was conducted with easy-DHPSF [210] in MATLAB.

Imaging TCR-TMR in T cells

Before imaging, $\sim 10^6$ T cells expressing TCR-β HaloTag-tagged proteins were labelled with 0.5-5 nM Halo ligand-TMR (G8251,Promega) for 30 min at 37°C. The cells were then subjected to three washes in filtered PBS.

To image resting T cells, the cells were fixed in suspension in 4% paraformaldehyde and 0.2% glutaraldehyde for 60 min. Before imaging, the T cells were centrifuged and resuspended in 200 μL of filtered PBS. To image fixed cells during immunological triggering events, argon-plasma-cleaned slides (24$\times$50 mm borosilicate, thickness No. 1, Brand) were coated with activating OKT3 (10 mM/mL; Davis group, Weatherall Institute for Molecular Medicine, University of Oxford) for 20 min. Labelled live cells were added to the surface and allowed to settle for 5 or 10 min before the media was removed and replaced with 200 μL of fixing solution for 60 min. The glass slides were then gently washed with filtered PBS.

The samples were all imaged on the DHPSF platform employing a 60x 1.20 NA water-immersion objective lens (Plan Apo VC 60x, Nikon). Continuous 561 nm excitation was incident on the sample in HILO geometry with a power density of $\sim$940 W/cm^2. A quadband dichroic and longpasss and bandpass filters were used to separate the emission signal (Di01-R405/488/561/ 635-25x36, and BLP02-561R-25 and FF01-580/14-25, respectively, Semrock) before the detector. An exposure time of 100 ms was used. DHPSF fitting was conducted with easy-DHPSF [210] in MATLAB.

Whole-Cell Scanning

To image whole cells, the focal plane was axially scanned through the sample in 3–3.5 μm steps via the piezo-mounted objective. 100 frames were acquired at each position before moving to the next position. This process was repeated until no more localisations were observed, typically $\sim$50 times. The recorded localisations were offset axially by the distance to their respective image plane. In this case no fiducial correction was used as the expected drift was judged to be small compared to the distances being investigated.

Mesh Fitting to Localisation Data

Using a standard method and functions included in Meshlab (http://meshlab.sourceforge.net) 3D localisation data was converted into an object mesh via the following steps:

1. Import localisation data as point cloud into meshlab from '.xyz' file type
2. Create normals to each localisation

   The built in 'Compute Normals for Point Set' function in the 'Normals, Curvatures and Orientation' tab of the 'Filters' menu was used. An input number of neighbours ranging between 50 and 200 depending on localisation density.
3. Reconstruct a surface mesh using the Poisson surface approach

   The built in 'Surface Reconstruction: Poisson' function in the 'Remeshing, Simplification and Reconstruction' tab of the 'Filters' menu was used. Typically, an 'Octree Depth' of 10, a 'Solver Divide' of 6, a 'Samples per Node' of 1 and a 'Surface Offsetting' of 1 were selected but these parameters were adjusted slightly between datasets for best results.
4. Uniformly sample the mesh

   The built in 'Uniform Mesh Resampling' function in the 'Remeshing, Simplification and Reconstruction' tab of the 'Filters' menu was used

GLOX STORM Buffer Preparation

GLOX STORM buffer was prepared by adding 50 mg/ml glucose (Sigma), 0.02-0.05 mg/ml catalase (Sigma), 0.8 mg/ml glucose oxidase (Sigma) and 7 mg/ml MEA (Sigma) to filtered PBS. GLOX solution was prepared and filtered (0.22 μm Millex-GP syringe filter unit, Millipore) immediately prior to imaging and used for a maximum of two hours before fresh buffer was made.

Imaging CD45-Alexa Flour 647 in T cells

$\sim 10^6$ T cells were labelled with 200 nM Alexa Fluor 647 (A20006,ThermoFisher) CD45 antibodies (Gap8.3, anti-CD45; Davis group, Weatherall Institute for Molecular Medicine,

University of Oxford) on ice for 25 minutes. Cells were then washed three times in filtered PBS (involving centrifugation). Labelled T cells were fixed in 4% paraformaldehyde and 0.2% glutaraldehyde for 60 minutes at room temperature. The fixed cells were washed three times in filtered PBS and suspended in GLOX STORM buffer. Coverslips (22×22 mm borosilicate, thickness No. 1, VWR) were coated with PLL (molecular mass 150–300 kDa; P4832, Sigma) for 10 minutes, before a 1:100 dilution of 100 nm gold nanoparticles (753688, Sigma) was added for 2 minutes. Coverslips were washed three times with filtered PBS and 50 μL of the fixed cells were placed onto the coated coverslips and allowed to settle. The sample was imaged with a 1.27 NA 60x water-immersion objective lens (Plan Apo VC 60x, Nikon). A quadband dichroic and longpasss and bandpass filters were used to separate the emission signal (Di01-R405/488/561/ 635-25x36, and BLP02-647R-25 and FF01-675/67-25, respectively, Semrock) before the detector. Fixed T cells were imaged for 200,000 frames with continuous 640 nm and 405 nm HILO excitation and a 30 ms exposure. DHPSF fitting was conducted with easy-DHPSF [210] in MATLAB. After reconstruction, a rolling-mean of the fiducial marker's position over 50 frames was used to correct for drift in x, y and z.

Imaging (K-ras)-mEos3.2 in HeLa Cells

Fixed HeLa cells samples expressing (K-ras)-mEos3.2 were provided in filtered PBS by Dr Yu Zhang. The buffer was replaced with a 1:20 dilution of 200 nm gold nanoparticles (746657, Sigma) in filtered PBS and left for ∼30 seconds. The sample was carefully washed three times with filtered PBS before 1 mL of filtered PBS was added to the sample.

The sample was imaged on the DHPSF platform employing a 60x 1.27 NA water-immersion objective lens (Plan Apo VC 60x, Nikon). Continuous 561 nm and 405 nm excitation was incident on the sample in HILO geometry with a power density of ∼1.2 kW/cm^2 for 561 nm. An initial power density of ∼5 W/cm^2 was used for 405 nm that was manually increased by changing optical density filters to maintain a relatively consistent localisation rate. A quadband dichroic and longpasss and bandpass filters were used to separate the emission signal (Di01-R405/488/561/ 635-25x36, and BLP02-561R-25 and FF01-580/14-25, respectively, Semrock) before the detector. An exposure time of 100 ms was used. Typically 100,000–120,000 frames were recorded, depending on the number of mEos3.2 events. DHPSF fitting was conducted with easy-DHPSF [210] in MATLAB. After reconstruction, a rolling-mean of the fiducial marker's position over 50 frames was used to correct for drift in x, y and z.

Imaging Proteasomes-mEos3.2 in HEK cells

Fixed HEK cells expressing proteasome-mEos3.2 were provided in filtered PBS by Dr Yu Ye. Two different proteasome subunits tagged with mEos3.2 were analysed 1) core-particle subunit (Pre1) and 2) regulatory-particle subunit (RPN1). The buffer was replaced with a 1:100 dilution of fluorescent nanodiamonds (798134, Sigma) in filtered PBS and left for 2 minutes. The sample was carefully washed three times with filtered PBS before 1 mL of filtered PBS was wazzed onto the sample.

The sample was imaged on the DHPSF platform employing a 60x 1.27 NA water-immersion objective lens (Plan Apo VC 60x, Nikon). Continuous 561 nm and 405 nm excitation was incident on the sample in HILO geometry with a power density of $\sim$1.2 kW/cm^2 for 561 nm. An initial power density of $\sim$5 W/cm^2 was used for 405 nm that was manually increased by changing optical density filters to maintain a relatively consistent localisation rate. A quadband dichroic and longpasss and bandpass filters were used to separate the emission signal (Di01-R405/488/561/ 635-25x36, and BLP02-561R-25 and FF01-580/14-25, respectively, Semrock) before the detector. An exposure time of 50 ms was used. Typically $\sim$200,000 frames were recorded, depending on the number of mEos3.2 events. DHPSF fitting was conducted with easy-DHPSF [210] in MATLAB. After reconstruction, a rolling-mean of the fiducial marker's position over 50 frames was used to correct for drift in x, y and z.

Imaging PSD95-mEos3.2 in Fixed Mouse Brain Sections

Fixed brain slices were sectioned with a range of thicknesses and placed onto coverslips (24 x 50 mm borosilicate, thickness No. 1, Brand) by Vlad Anton in Edinburgh. Samples were dried and frozen. Before imaging, samples were defrosted and 1 mL of filtered PBS was added on top of the section. The sample was left for 10 minutes to equilibrate. The sample was then placed on the DHPSF platform and imaged with a 60x 1.27 NA water-immersion objective lens (Plan Apo VC 60x, Nikon). White-light illumination allowed Vlad Anton to navigate to specific regions of the hippocampus. Once an area was found, continuous 561 nm and 405 nm excitation was incident on the sample in VAEM geometry with a power density of $\sim$1 kW/cm^2 and $\sim$5 W/cm^2 respectively. The focal plane was placed so that the coverslip surface was at the periphery to reduce spherical aberration. A quadband dichroic and longpasss and bandpass filters were used to separate the emission signal (Di01-R405/488/561/

635-25x36, and BLP02-561R-25 and FF01-580/14-25, respectively, Semrock) before the detector. An exposure time of 50 ms was determined to provide optimal conditions. A range of buffers were tested for maximum SNR. Optimal conditions were found when $\sim$1 mL of filtered PBS made from D_2O was added on top of the brain sections due to an increase in quantum yield of fluorophores in heavy water [243, 244]. For each region, 5,000 frames were collected before moving laterally to a new area. DHPSF fitting was conducted with easy-DHPSF [210] in MATLAB.

Chapter 6

Quantifying the Distribution of the T-Cell Receptor in the Presence of Membrane Nanostructure on Jurkat and Primary T Cells

This chapter describes work done to image and quantify the clustering state of the T-cell Receptor (TCR) in an immortalised $CD4^+$ cell line (Jurkat) and primary $CD4^+$ T cells with the DHPSF 3D super-resolution microscope away from the coverslip surface. High-density whole-cell imaging of the outer membrane of Jurkat T cells was achieved using PAINT imaging and labelled via wheat germ agglutinin tagged with photoativatable-JaneliaFluor549 (PA-JF549). Finally, sequential multi-target imaging of the position of the TCR and the outer membrane of Jurkat and primary T cells facilitates quantification of the clustering state of the TCR on the complicated 3D topography of resting T cells, fixed in suspension, using the spatial point statistics tool - Ripley's K analysis, applied in all three dimensions.

Contributions

Dr Steven Lee, Dr Aleks Ponjavic, Dr Mafalda Santos and I designed all experiments presented in this chapter. All DHPSF experiments were conducted by me. Dr Aleks Ponjavic wrote the autofocus script in beanshell used for maintaining a constant focal plane within the

sample. Antibody and fabs labelling was conducted by Dr Aleks Ponjavic in Cambridge or by Dr Mafalda Santos in the Weatherall Institute of Molecular Medicine in Oxford. HaloTag antibodies and fabs were provided by the Davis group. Dr Mafalda Santos provided fixed and labelled primary cells from the Davis group. I rendered all presented SMLM datasets in ViSP or MATLAB and wrote all clustering analysis code in MATLAB. PA-JF549 conjugated to a HaloTag ligand was a kind gift from Dr Marco di Antonio.

6.1 Introduction to the Molecular Basis of T-Cell Activation

All organisms are constantly under attack by parasites and pathogens. Different solutions to the problem of protecting against disease have evolved including the passive barriers [245] (*e.g.* skin in mammals and exoskeletons in insects) and selective apoptosis in plants [246]. Animals have developed a complex defence mechanism, the immune system, to protect against foreign elements such as parasites or infection with pathogens. To function properly, the immune system must be able to detect and destroy a wide range of pathogens that may attack the organism by very different mechanisms. Therefore, in complex organisms the immune system has evolved many components and, as the immune system is by nature destructive, the fundamental challenge is to distinguish self from non-self.

All vertebrates share a common immune system comprised of two complementary branches; the innate immune system and the adaptive immune system. The innate immune system is classified by an unspecific and immediate generic response to pathogens. This can be achieved by pathogen-associated pattern recognition [247] or distress signals from damaged or stressed cells that can trigger a local inflammatory response that aims to contain and clear infection [248]. The innate immune system does not confer long-lasting immunity against specific pathogens but instead acts without memory in future infections. In contrast, the adaptive immune system, which is discussed in detail below, confers long-lasting immunity.

6.1.1 The Adaptive Immune System

The adaptive immune system is characterised by its specificity, its delayed effect ($\sim$4 days post infection), its increased strength compared to the innate immune system and its memory of past infection, allowing for a quicker response against future infections. An adaptive immune system based on lymphocytes appeared roughly 500 million years ago in jawless fish. These lymphocytes have since divided into two distinct populations of T and B cells in all higher vertebrates [249].

Although often described as separate, the adaptive and innate immune systems are inter-dependent parts of the same system. For example, after detection and phagocytosis of a pathogen, antigen-presenting cells (APCs) of the innate immune system present short peptide fragments from the lysis of pathogens on major histocompatibility complexes (MHCs) present on their plasma membrane. These specific peptide fragments are recognised by T cells in the adaptive immune response, initiating a specific response against the infection.

The two populations of lymphocyte of the adaptive immune system express specific antigen recognition complexes on their surfaces, respectively known as the B-cell receptor and T-cell receptor (TCR) but occupy different roles in the response to pathogens. B cells are involved in the humoral response. Once a B cell is activated by recognition of its specific antigen (and after binding of a $CD4^+$ T cell) proliferation and differentiation into plasma cells is stimulated. These plasma cells manufacture and release specific monoclonal antibodies into the extracellular fluid that bind to the specific antigen and neutralise pathogens [249].

T cells serve a number of functions in the cell-mediated response; they can recognise and kill cells expressing non-self antigens on their surface and stimulate other cell types associated with the adaptive immune response [249]. Each T cell expresses a single unique variation of TCR that recognises and bind to MHC molecules presenting a different specific non-self antigen fragment. The type of MHC molecule that is bound determines the subtype of T cell [211]. $CD8^+$ T cells bind to class I MHC molecules presenting their complementary antigen fragment that are expressed on the surface of almost all cells within the body as they report the range of proteins that are being degraded by their internal machinery. Upon binding, activated $CD8^+$ T cells kill cells that are infected with the specific pathogen by inducing programmed cell death. $CD4^+$ T cells bind to class II MHC molecules presenting their complementary antigen fragment that are expressed on the surface of professional APCs. Activated $CD4^+$ T cells can stimulate other processes by releasing a range of cytokines. These cytokine

signals include activating macrophages, stimulating the maturation of complementary B cells, recruiting neutrophils and stimulating activation of complementary $CD8^+$ T cells [211].

Due to their essential role as effectors and orchestrators within the immune response, T cells remain a key area of interest. Dysfunction of the adaptive immune system by misrecognition as self as non-self or vice versa can lead to auto-immune disease or a failure to respond to potentially deadly infection. Therefore, understanding the mechanisms governing the activation process has major relevance for the design of immune-therapeutics.

6.1.2 The T-Cell Receptor

The T-cell receptor (TCR) plays a key role in the T-cell activation process and the decision, at a single-cell or even single-protein [250, 217] level, whether to initiate an immune response. While the stoichiometry of the TCR is still not yet fully understood [251], it is known to be comprised of several subunits (figure 6.1): a highly variable hetero-dimer of TCR-$\alpha\beta$, that is responsible for antigen recognition and whose intracellular domain is almost non-existent, as well as three invariant transmembrane proteins collectively known as cluster of differentiation 3 (CD3) [252]. These CD3 proteins include two hetero-dimers, CD3$\varepsilon\delta$ and CD$\gamma\varepsilon$, that contain a single intracellular immunoreceptor tyrosine-based activation motif (ITAM), and the homo-dimer CD3$\zeta\zeta$, that contains six ITAMs [253]. TCR ITAM phosphorylation by tyrosine kinases, such as Lymphocyte-specific protein tyrosine kinase (Lck), is known to be essential in the initiation of downstream signalling and the eventual initiation of an adaptive immune response [254].

The TCR is capable of transducing a signal across the membrane with an unmatched combination of specificity and sensitivity [255]. It has been suggested the a single TCR-MHC binding event can lead to immune-response triggering [256–258, 217], even in the presence of the 10^5-10^6 non-complementary MHC molecules that are present on the surface of APCs [250]. Although the ligand recognition and the later stages of the adaptive immune response (*e.g.* the formation of the immunological synapse and downstream signalling) are well described, a consensus of the mechanisms resulting in TCR phosphorylation has not yet been reached [219].

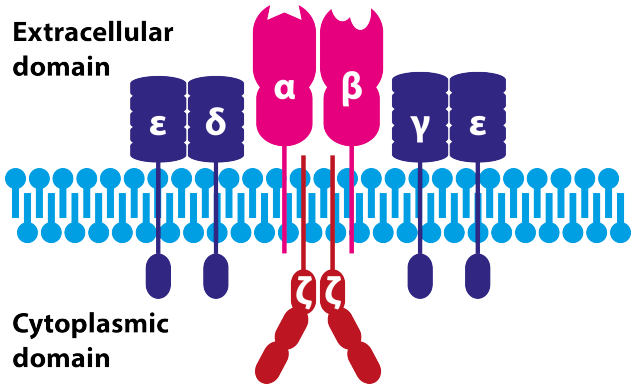

Fig. 6.1 The T-cell receptor complex (TCR) is comprised of TCR-$\alpha\beta$ hetero-dimer (magenta), CD3$\varepsilon\delta$ and CD3$\gamma\varepsilon$ hetero-dimers (navy) and CD3$\zeta\zeta$ homo-dimer (red). The TCR is a transmembrane complex with eight intracellular immunoreceptor tyrosine-based activation motifs (ITAMs) (rounded rectangles).

6.1.3 Molecular Models for TCR Triggering

Three models describing the signal transduction upon formation of the TCR-MHC complex have been proposed; aggregation, conformational change and kinetic-segregation. The evidence supporting each of these models is reviewed in detail in ref. [219].

Aggregation of TCR complexes following TCR-MHC binding could lead to enhanced phosphorylation as their cytoplasmic ITAM domains are held in close-proximity, facilitating cross-phosphorylation or the recruitment of tyrosine kinases. Indeed, artificial aggregation of TCRs by soluble antibodies such as OKT3 which binds CD3ε, has been demonstrated to elicit T-cell activation [259]. However, surface densities of complementary MHC ligands on APCs are not sufficient to form significant aggregates and the TCR is capable of triggering in the presence of very few MHCs [256–258, 217]. The presence of clusters formed of 10-100 TCRs is well documented after TCR triggering [214, 260], however if this is a cause or a consequence of TCR triggering and if TCR clusters exist in the resting cell remains unclear.

Conformation change describes the mechanism by which many ligands interact with receptors [261]. In this model, the binding of a ligand to a receptor stabilises an alternative conformation of the receptor that exposes some catalytic motif that was hidden in the initial conformation or results in autophosphorylation. However, in the case of the TCR this is unlikely to describe the activation process as the TCR lacks intrinsic tyrosine kinase domains for autophosphorylation [226]. There is some evidence of a conformation change of the TCR-α chain upon MHC binding [262], however, it is not clear how this change could affect the phosphorylation of ITAMs on the CD intracellular domains of the CD3 components. An

additional conformation-change model involving receptor deformation caused by binding forces has been proposed [263]. This force-driven change is postulated to expose CD3ε ITAMs that could be hidden within the lipid bilayer of the plasma membrane, increasing TCR phosphorylation.

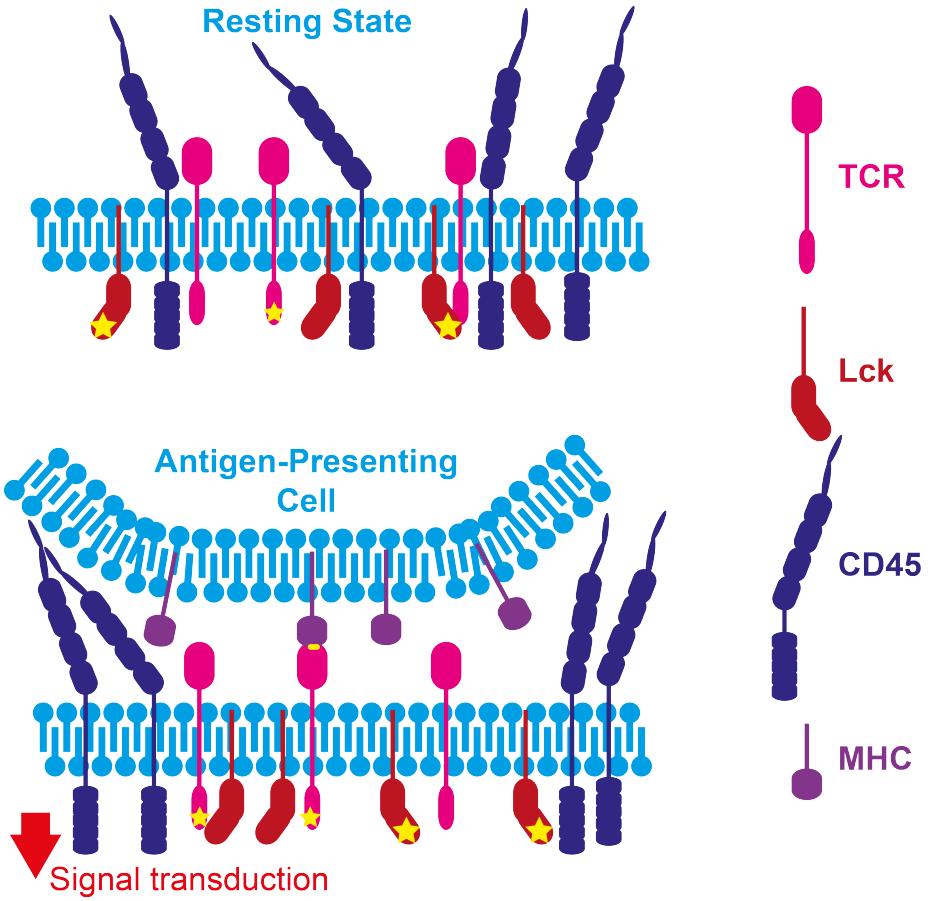

Fig. 6.2 Schematic cartoon of the kinetic segregation model. In the resting state (top), the TCR is constantly phosphorylated and dephosphorylated by freely diffusing Lck and CD45 in the T-cell plasma membrane, achieving a low net level of TCR phosphorylation (stars). When the TCR binds to an MHC complex on the surface of an antigen-presenting cell, a close contact in formed (bottom). This excludes phosphatases with a large extracellular domain (CD45) but not kinases with a small extracellular domain (Lck), resulting in a local increase in TCR phosphorylation and thus TCR triggering.

The kinetic-segregation model was proposed by Davis *et. al.* in 1996 [264] as an alternative explanation to the aggregation model of TCR triggering. The kinetic segregation model states that physical redistribution of receptors on the surface of T cells leads to a segregation of membrane proteins based on the sizes of their extracellular domains that inhibits normal signal transduction across the membrane (figure 6.2). In a resting T cell, the

TCR is continuously phosphorylated and dephosphorylated by free kinase and phosphatases proteins in the T cell membrane, such as Lck and CD45 respectively. The result is a low but stable level of TRC phosphorylation. When a TCR complex binds to an MHC on the surface of an APC, the membranes of the T cell and APC are held in close proximity by small adhesion proteins such as CD2, forming close-contact zones [206]. Membrane proteins with large extracellular domains, such as CD45 [265], cannot enter the close-contact zone while molecules with small or no extracellular domain, such as Lck, are less affected. CD45 is no longer able to dephosphorylate the TCR, resulting in a local net phosphorylation and, in turn, triggering of the immune response via 'downstream' signalling with the recruitment of Zap70 [212]. Recently, key predictions of the kinetic-segregation model have been demonstrated including: the requirement for CD45 and Lck segregation in reconstituted systems [215], ligand-independent TCR triggering [227] and the presence of CD45 exclusion zones in activating cell contacts [216].

6.2 The Spatial Distribution of the T-Cell Receptor

The spatial distribution of the TCR upon T-cell activation has been well studied [266–268]. Post-activation, TCR clusters form and are transported towards the immunological synapse by filamentous actin [269]. However, the spatial distribution of the TCR in the resting T cell is not well defined.

Recently there have been a number of 2D single-molecule localisation microscopy (SMLM) studies aiming to investigate the clustering state of the TCR on the plasma membrane of resting T cells [52]. Hu *et. al.* reported that the TCR exists in clusters of approximately 5-15 molecules by dSTORM at coverslip surfaces [121]. Pageon *et. al.* determined that the 70% of TCRs are associated with clusters comprised of $\sim$20 TCRs per cluster and $\sim$20 clusters per μm^2 by PALM imaging at the basal surface of CD4$^+$ T cells. However this study was conducted on T cells contacting poly-L-lysine (PLL) coated surfaces, which have been shown to promote T-cell activation [150], potentially resulting in a redistribution towards clustering. Another study by Rossboth *et. al.* employing label-density-variation SMLM [270] and STED microscopy determined that the TCR is randomly distributed in resting CD4$^+$ T cells, and does not form nanoclusters until after activation. Additionally, the TCR was observed to be monomeric at the apical cell surface of CD4$^+$ T cells by two-colour coincidence detection (TCCD) [199]. There is also a recent focus on the functional role of T-cell membrane nanostructure in immune-response triggering [271, 171]. One study by

Jung *et. al.* reported that the TCR is not randomly distributed across the plasma membrane but rather is preferentially located in membrane protrusions [201].

It is clear that the spatial distribution and redistribution of the TCR plays a fundamental role in immune-response triggering. These conflicting reports highlight the need for additional investigation into the resting state of the T-cell membrane.

6.3 Imaging the Spatial Distribution of T-Cell Membrane Proteins with the DHPSF

As discussed in chapter 5, clustering is not necessarily well represented by 2D imaging as axial structure within the sample can cause artefacts. Interactions with coated surfaces can influence the behaviour of membrane proteins [150, 151]. Thereofore, in order to investigate the stoichiometry of T-cell membrane proteins in the resting state 3D-SMLM techniques are required. Recent developments 3D cluster identification [127, 125] demonstrate the applicability of 3D-SMLM for quantification of the clustering state of proteins on non-flat geometries. The extended depth of field of the DHPSF compared to the majority of 3D-SMLM techniques, its robust counting ability (demonstrated in chapter 5) and the reduction of spherical aberration away from the surface make it an ideal candidate to measure the distribution of proteins in traditionally difficult to image areas of biological samples, away from coated surfaces. Duel labelling of T-cell membrane proteins and the position of the outer membrane can be used to disentangle the effect of cell morphology on perceived clustering, facilitating unbiased quantification of 3D clustering. We have developed methodology to address these factors, both of which are described below.

As shown before, the DHPSF is capable of observing the majority of expected fluorescence events within a sample, however, other factors can prevent this from representing the entire distribution. In PALM, the activation/folding efficiency of the fluorophore used can result is <50% of the protein of interest being localised [64]. In STORM, multiple fluorescence events are observed from each fluorophore with a distribution of ‘blinks’ spanning an order of magnitude [65]. This makes counting unreliable as individual fluorophores at the tail of this distribution can be mistaken as clusters. In low-expression proteins (such as the TCR), the presence of a few erroneous clusters can have a significant effect on the overall distribution.

The newly developed photoactivatable-JaneliaFluor (PA-JF) fluorophores report an activation efficiency (the fraction of fluorophores that photoactivate into an emissive state) of <50% in solution, which can be increased depending on its environment, and display a mean of 1.4 fluorescence events per fluorophore [69]. The activation efficiency is increased to $\sim$90% and $\sim$76% for PA-JF549 and PA-JF646 respectively when bound to a HaloTag [69], making these fluorophores well-suited for imaging the majority of the population of interest with a sample, providing they can be attached to a HaloTag.

In order to image the membrane-bound TCRs of T cells, antibody/antigen-binding fragment (fab) labelling was chosen as it allows for imaging in primary cells and reduces the fraction of localisations observed from intracellular proteins unrelated to membrane organisation. This required antibodies/fabs to be created with a HaloTag, limiting the application of the methodology. TCR-fabs binding to CD3 domains expressing a HaloTag were created by the Davis group to test the methodology and quantify the distribution of the TCR. Additional HaloTag-fabs for CD2 and CD45 T-cell membrane proteins are under construction by the Davis lab and will be investigated in future projects. With these TCR-fabs the distribution of the TCR across $\sim$4 μm thick sections of Jurkat and primary T cells can be imaged with high efficiency.

Fiducial markers are required to track stage drift in three dimensions for long acquisition times. Typically this is achieved by attached non-bleaching markers, such reflecting gold nanoparticles [272] or fluorescent nanodiamonds [201], to the coverslip surface with Poly-L-Lysine (PLL). When imaging away from the surface these markers are not within the field of view and thus complicated methodologies are required to periodically check the position of the marker. This can be achieved by moving the focal plane between the sample and the coverslip surface, although this may introduce additional errors due to relaxation effects after movement and the viscosity of the immersion liquid. Another solution is to swap the PSF to a larger depth of focus PSF such as the Tetrapod PSF periodically during imaging to include the coverslip surface in the depth of field [108]. This approach requires a programmable spatial light modulator to implement and, like the previous example, does not provide continuous tracking of stage drift as the fiducial markers are only imaged periodically. The ideal solution should include stable fiducial markers within the image plane of the sample, away from the coverslip. This can be achieved by suspending fiducial markers in an agarose gel solution. However, the pore size of the agarose matrix is $\sim$100 nm [273] so smaller fiducial markers, such as nanodiamonds which are typically $\sim$3 nm, are not trapped. Even larger, 200 nm, gold nanoparticles were prone to motion within the agarose gel when reflecting high-power illumination, most likely due to heating and optical forces. Fiducial markers are also prone

to adhering to cell membranes in live and fixed cells, obscuring data collection. As a result, suspension of fiducial markers in agarose was deemed not reliable for long acquisition lengths and an alternative solution was found.

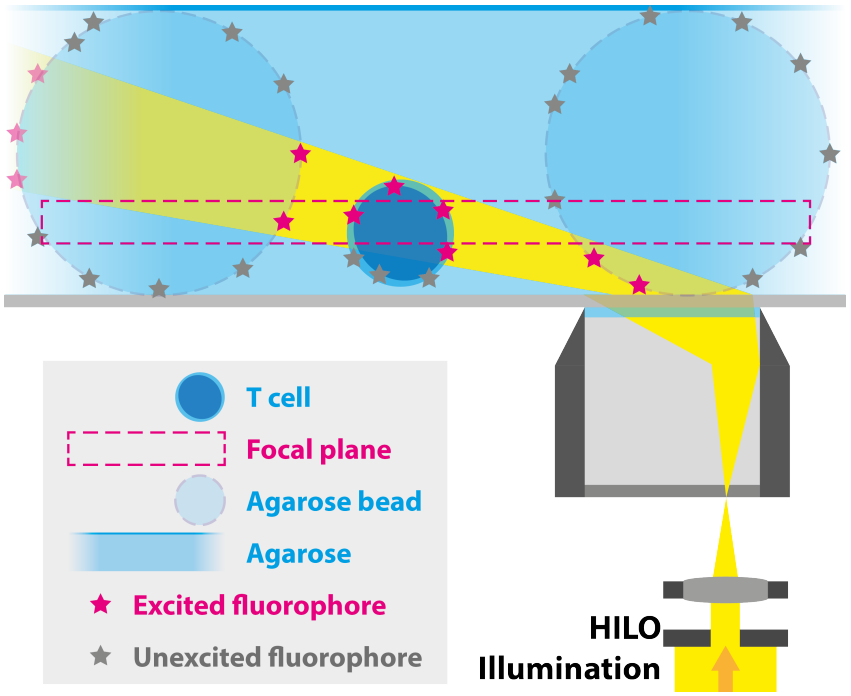

Fig. 6.3 Cartoon schematic of experimental set up for imaging T cells away from the coverslip surface with fiducial markers. 50 μm agarose beads were coated with fluorescent nanodiamonds and immobilised within an agarose gel along with the T cells. HILO illumination allowed for multiple fiducial markers to be imaged simultaneously with T-cell samples.

A novel solution for immobilising fiducial markers within the imaging volume when imaging away from coverslip surface was found. 50 μm diameter agarose beads were coated with fluorescent nanodiamonds, and attached using PLL. These labelled beads were added to cell samples and allowed to settle on the coverslip surface. The beads would not adhere to the surface but instead remained mobile. The sample was heated to 37°C and the imaging buffer was diluted with a 1:1 solution of 2% agarose. Once allowed to settle again, the mixture was cooled to room temperature to immobilise the agarose beads within the $\sim$1% agarose gel. The resulting sample contained fluorescent nanodiamonds distributed on the surface of the agarose beads, up to 50 μm away from the surface (figure 6.3). Cells that were sat near to an agarose bead (visible by white-light illumination) typically had at least one isolated fiducial marker within the field of view, allowing for extended acquisitions to be conducted.

The stability of the fiducial markers was measured by imaging two nanodiamonds attached to two different agarose beads for 2.5 hours. One image with 30 ms exposure time

was recorded every 300 ms. The rolling mean position of the first fiducial marker from 50 frames was used to correct for stage drift at each frame. A 1D Gaussian function was fit to a histogram of the position of the same fiducial marker, after correction, to extract the standard deviation for x, y and z, corresponding to the localisation precision of the DHPSF. Then the rolling mean position of the second marker from 50 frames was used to correct for stage drift. Another 1D Gaussian function was fit to a histogram of the position of the first marker, after correction, to extract the standard deviation for x, y and z. The difference between the two values should relate to the relative stability between the two fiducial markers (figure 6.4). The procedure was repeated, correcting the second marker by the position of the first. The mean axial and lateral precision was with self-correction was measured to be 12 nm and 16 nm respectively, agreeing well with the measured localisation precision of the DHPSF (see chapter 2). The mean axial and lateral precision with correction by a second marker was measured to be 17 nm and 20 nm respectively. The increased width of the second-corrected distributions could be related to movement of the agarose beads within the agarose matrix that they are set in. This result indicates that the agarose beads are stable within the gel to $\sim$5 nm over 2.5 hours, providing sufficient fiducial correction even for very long acquisitions (>10 hours).

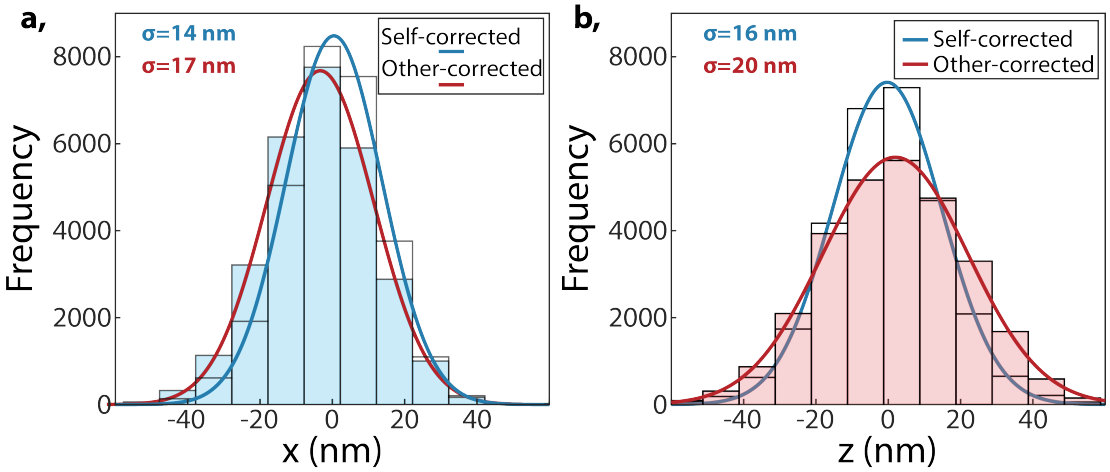

Fig. 6.4 Measuring the stability of fiducial markers suspended away from the coverslip surface. In the setup described in figure 6.3, the position of two fiducial markers on separate agarose beads was used to track for stage drift. The position of each bead was adjusted by a rolling mean of 50 sequential positions of itself (blue curve) and of the second marker (red curve). A Gaussian function was fit to a histogram of the x-position (a) and z-positions (b) of a fiducial marker after the two separate drift corrections to extract a precision for each distribution. The difference between the two relates to the stability of the fiducial markers relative to each other.

6.3.1 Imaging the TCR on the Outer Membrane of T Cells

The TCR was labelled with anti-CD3 fabs fused to PA-JF549 and imaged in a PALM mode, at the top surface of Jurkat T cells that were fixed in suspension and suspended in 1% agarose gel (figure 6.5). Constant 561 nm and 405 nm illumination was incident in a HILO geometry. Fluorescent nanodiamonds were used for drift correction and were implanted as illustrated in figure 6.3. Typically >30,000 frames were acquired with an exposure time of 30 ms until no more fluorescent events were observed. 3,400±900 localisations of the TCR were recorded from a single image plane after filtering for repeat localisations of the same fluorophore in space (500 nm) and time (1 second). Jurkat T cells express 20,000 – 40,000 copies of the TCR (determined by FACs in the Davies group). Approximately 25% of the cell is contained within the imaging volume and the activation efficiency of PA-JF549 is ∼90% when bond to a HaloTag [69], predicting that ∼4,500 - 9,000 localisations of the TCR should be possible. The reduction in observed TCR molecules may be caused by dissociation of the fabs during the labelling, washing and fixation protocol. Other factors that could affect this include the labelling efficiency of the fab with PA-JF549, which could not be determined by Ultraviolet-visible spectroscopy (UV-Vis) as the absorption of the non-fluorescent forms of PA-JF549 coincide with that of the fabs, and the true activation efficiency of PA-JF549, which has been shown to be highly variable and sensitive to local environment [69].

6.4 Imaging T-cell Membrane Nanostructure

A number of labelling methods to image the position of the outer membrane of T cells with high localisation density have previously been demonstrated. Fluorophores have been attached to lipids that are inserted into the membrane [274], however, this requires live-cell labelling that may perturb the resting state of the T cell. Lipophilic dyes such as Di(L,O,D) and CellMask deliver relatively uniform membrane labelling by interacting with the lipid bilayer [275], however, these dyes typically have a low quantum yield and thus do not lend themselves well to SMLM. Lectins, such as wheat germ agglutinin (WGA), non-specifically crosslink sugars on the membrane proteins. Fluorescently-labelled WGA has been used as a membrane probe, achieving $>10^6$ localisations from a single-cell membrane via PAINT labelling [82].

A drawback of PAINT labelling is increased background signal due to unbound fluorophores present in the imaging buffer. This can be counteracted with the use of environ-

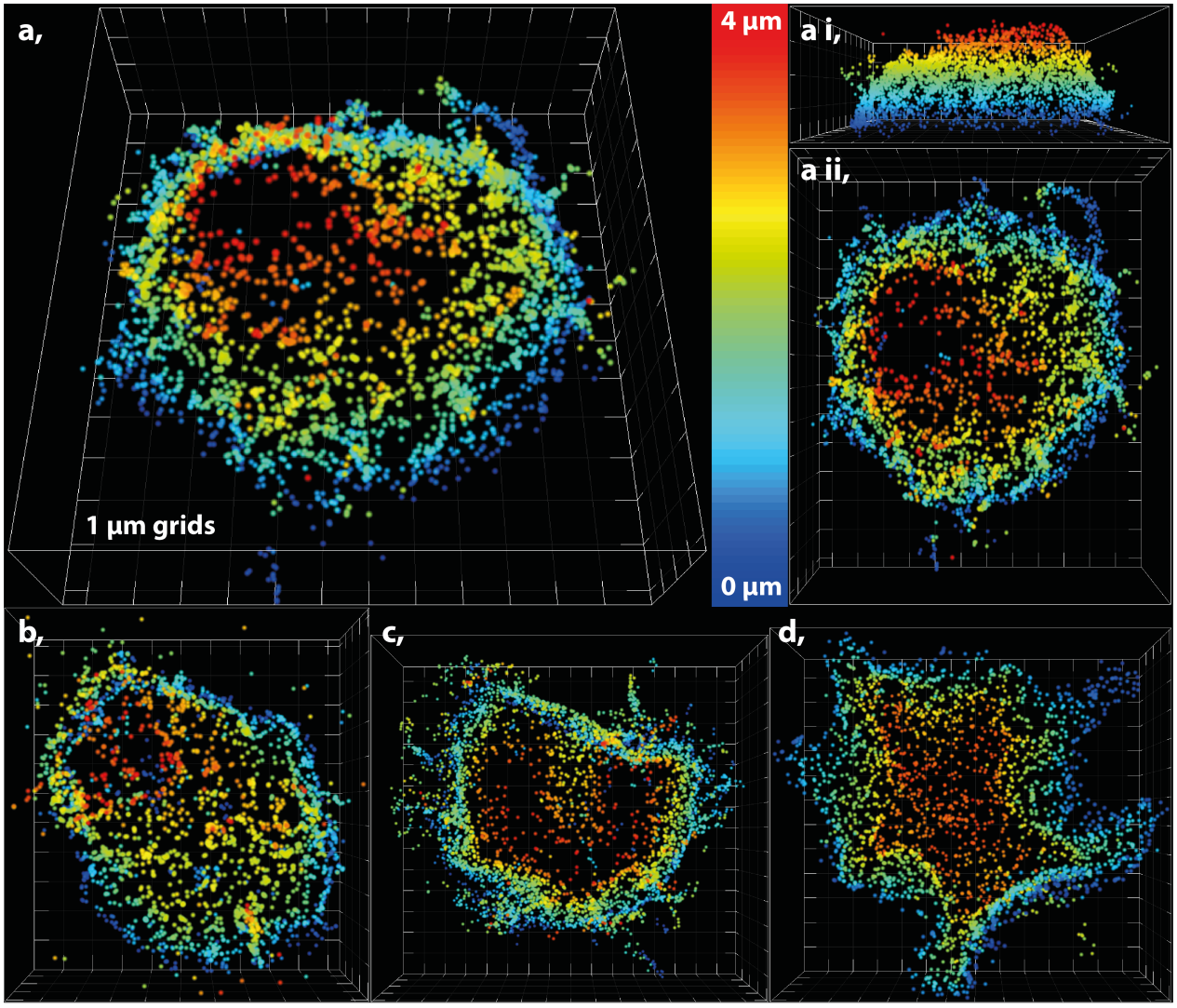

Fig. 6.5 PALM imaging the TCR on the apical surface of Jurkat T cells with the DHPSF. (a) A ∼4 μm thick section imaged at the apical surface of a Jurkat T cell labelled by anti-CD3 fabs fused to PA-JF549. (n=3,721) (a i&ii) top-down and side-on views of the cell presented in (a). (b-d) Additional examples of TCR imaged at the surface of Jurkat T cells (n=2,635, 4,557 and 2730 respectively). All localisations are coloured axially across the 4 μm depth of focus of the DHPSF and are rendered with 100 nm FWHM for visibility. Ticks and grid lines are 1 μm.

mentally sensitive probes that changes their absorption/emission upon binding to the target of interest (*e.g.* Nile Red binds to hydrophobic regions and modifies it's emission spectra depending on the hydrophobicity of the local environment [51] and FRET-PAINT involves labelling the target with both donor and acceptor fluorophores, resulting in FRET energy transfer and emission when both are bound to the target of interest [71, 72]). Without such

labelling strategies, the increased background fluorescence makes PAINT-based imaging impractical for large-volume imaging techniques such as the DHPSF without narrow excitation confinement. Low fluorophore concentrations are required so that individual bound fluorescence events can be distinguished above background, reducing the localisation rate and extending acquisition to unfeasible lengths in order to obtain sufficient labelling density. Light-sheet excitation confinement reduces the excitation geometry to a similar size to the focal depth of the DHPSF but increases experimental complexity, reducing throughput.

By employing a photoactivatable fluorophore in PAINT labelling and confining the activation and excitation geometry, out of focus fluorescence can be reduced without reducing the concentration of probes in the imaging buffer as only fluorophores close to the focal plane are likely to be activated and fluoresce. Thus, the majority of fluorophores within the sample do not contribute to background. This variant of PAINT, referred to as photoactivatable-PAINT (PA-PAINT), allows for fast localisation rates with minimal background by employing HILO illumination for both activation and excitation lasers. This technique achieves approximately one localisation of WGA-(PA-JF549) per frame across the top $\sim$4 μm of fixed T-cell membrane surfaces with signal-to-noise ratio (SNR) >5 for a 30ms exposure time (figure 6.6), an equivalent of $\sim$30 localisations per second. PA-PAINT facilitates high-density labelling of specific targets with large-volume 3D-SMLM imaging techniques with minimal additional experimental complexity compared to PALM.

The outer membrane of primary T cells that were fixed in suspension was labelled with WGA tagged with PA-JF549 in a PA-PAINT mode, at the top surface of Jurkat T cells suspended in 1% agarose gel (figure 6.7). Constant 561 nm and 405 nm illuminations were incident in a HILO geometry. Fluorescent nanodiamonds were used for drift correction and were implanted as described illustrated in figure 6.3. During long acquisitions, the focal plane is prone to drifting outside of the initial field of view. In order to maintain a stable focal plane within the sample a bespoke autofocus script was implanted in beanshell. This script checked the axial position of a fiducial marker every 10 seconds and corrected any stage drift in 20 nm steps by controlling the piezo drive that the objective lens was mounted on. 100,000 frames were acquired with an exposure time of 30 ms. 96,742 localisations were recorded from the cell presented in figure 6.7.

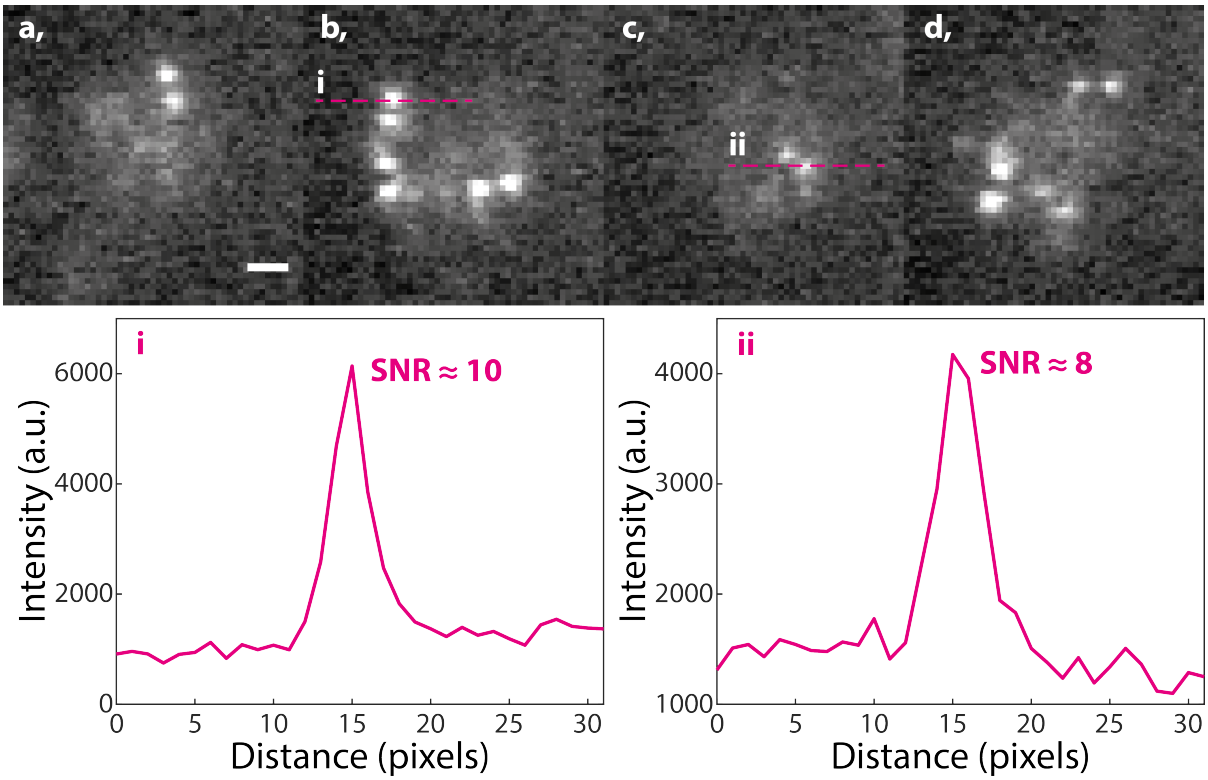

Fig. 6.6 Example DHPSFs for PA-PAINT imaging of WGA-(PA-JF549) at the apical surface of Jurkat T cells. Localisations can be seen spanning the entire depth of focus of the DHPSF. (a-d) Representative 30 ms exposure acquisitions of the outer membrane of Jurkat T cells labelled with WGA-(PA-JF549) via PAINT and imaged with continuous HILO illumination with 561 nm and 405 nm lasers. Two line profiles of typical DHPSF lobes are shown with corresponding SNR. Signal and noise are defined as the intensity above background and the variation in background, respectively.

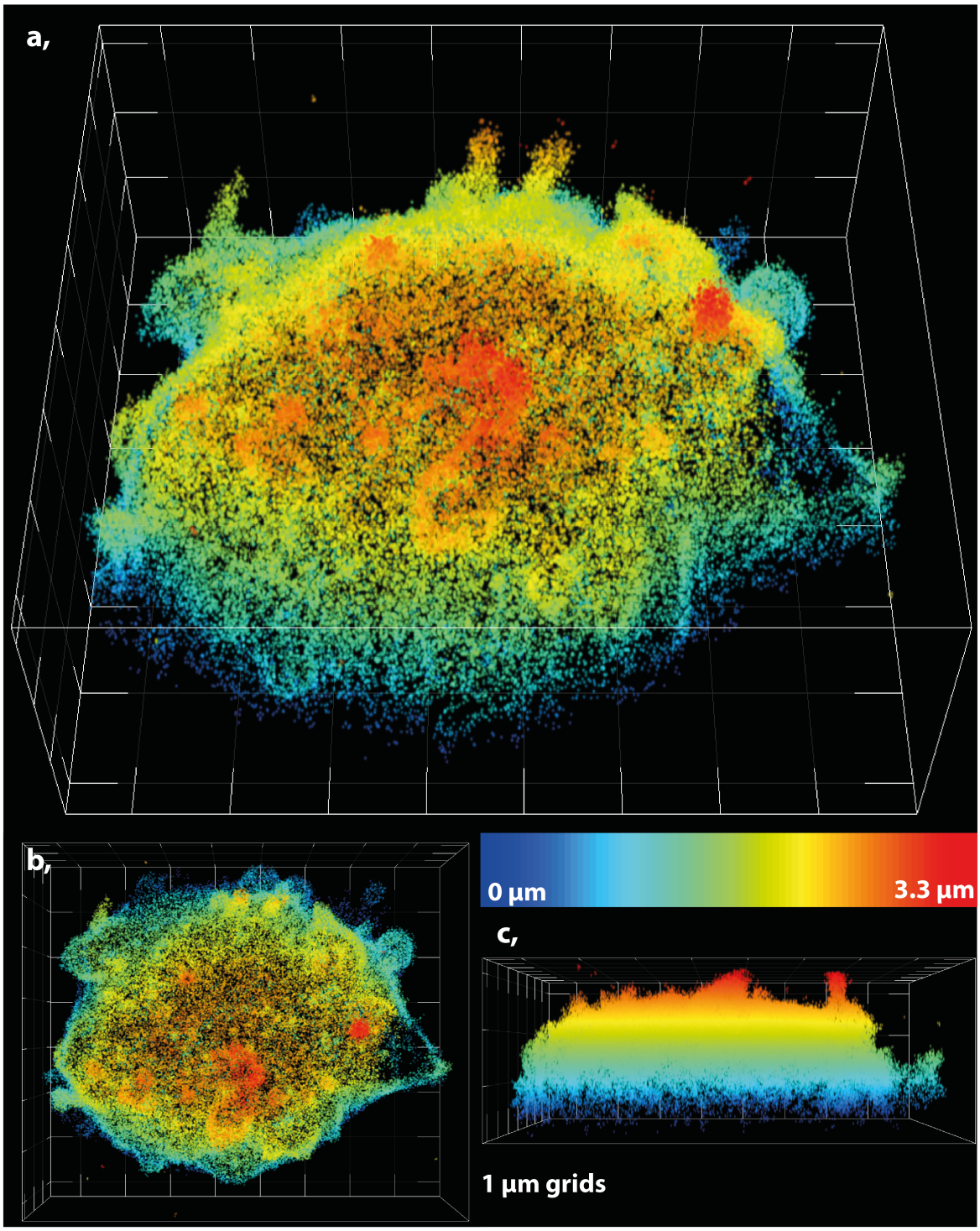

Fig. 6.7 PA-PAINT imaging the apical membrane surface of primary T cells with the DHPSF. (a) A ∼3.3 μm thick section imaged at the apical surface of a primary T cell labelled WGA-(PA-JF549). (n=96,742) (b&c) top-down and side-on views of the cell presented in (a). All localisations are coloured axially across a 3.3 μm thick section and are rendered with 40 *nm* FWHM laterally and 60 nm axially, representing the measured localisation for the DHPSF. Ticks and grid lines are 1 μm.

Membrane nanostructure is clearly visible with pseudopodia observed with a $\sim$300 nm diameter and a range of lengths. The observed thickness of the outer membrane was $\sim$200 nm. Although the plasma membrane is expected to be just a few nanometers thick [276], WGA binds to glycoprotein sugars that can be >100 nm long [277] resulting in an increased thickness being observed. A small fraction of WGA localisations were observed within the cell volume as WGA is capable of permeating the outer membrane. This fraction was significantly higher in stressed/unhealthy cells (determined by increased autofluorescence), perhaps indicating the presence of holes in the membrane after fixation. Example line profiles of a 300 nm axial section of the outer membrane are presented in figure 6.8.

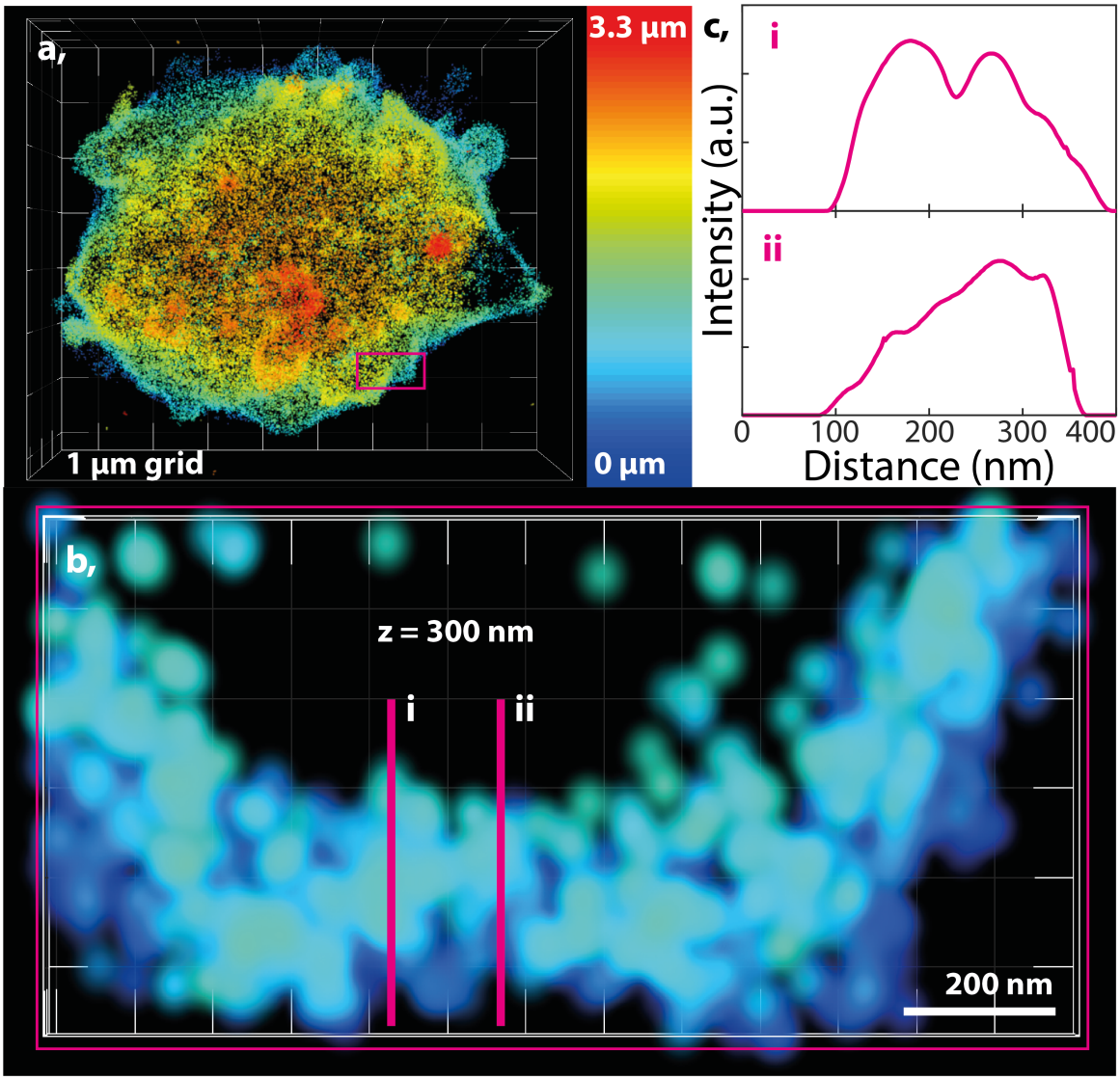

Fig. 6.8 Membrane thickness by PA-PAINT imaging with the DHPSF. (a) A ∼3.3 μm thick section imaged at the apical surface of a primary T cell labelled WGA-(PA-JF549). (n=96,742) (b) 300 nm axial section of membrane highlighted in (a). (c) Line profiles across the membrane as shown in (b). All localisations are coloured axially across a 3.3 μm thick section and are rendered with 40 nm FWHM laterally and 60 nm axially, representing the measured localisation for the DHPSF. Ticks and grid lines are 1 μm in (a) and 100 nm in (b).

6.4.1 Whole T-Cell Membrane Imaging with High Density

The topology of the outer membrane of whole Jurkat T cells that were fixed in suspension was determined by imaging WGA tagged with PA-JF549 in a PA-PAINT mode. Jurkat cells were suspended in agarose with fiducial markers as described in figure 6.3. Similarly to the data presented in chapter 5, entire cell volumes were imaged in multiple focal planes separated axially by $\sim$3 μm. Typically Jurkat cells required 3-4 image planes to cover their volume. Each sequential focal plane shared at least one fiducial marker so that the localisation data taken from neighbouring planes could be aligned after drift correction. 200,000 frames were recorded from each image plane with a 30 ms exposure time, corresponding to a total acquisition time of 6 hours and 40 minutes to image four planes. 1,399,455 localisations were recorded across the entire cell presented in figure 6.9 at a rate of $\sim$60 localisations per second.

Nanoscale features were observed across the entire surface of fixed Jurkat cells with some cells exhibiting large scale protrusions, as seen in figure 6.9. The presence of this nanostructure gives the appearance of changes in surface localisation density in 2D representations of the 3D data. Dynamic videos of the cell data presented in figure 6.9 are included in the digital appendix of this thesis, along with additional reconstructions. A 300 nm thick section at the centre of the cell is presented in figure 6.10 with highlighted regions of nanostructure. In this case pseudopodia appeared mostly hollow (figure 6.10b) and are seen with length >2 μm. There is a small amount of intracellular WGA localisations, most likely corresponding to internal membrane labelled by WGA molecules that have passed through the outer membrane. The same effect was seen in a previous study using PAINT labelling of fluorescently tagged WGA [82].

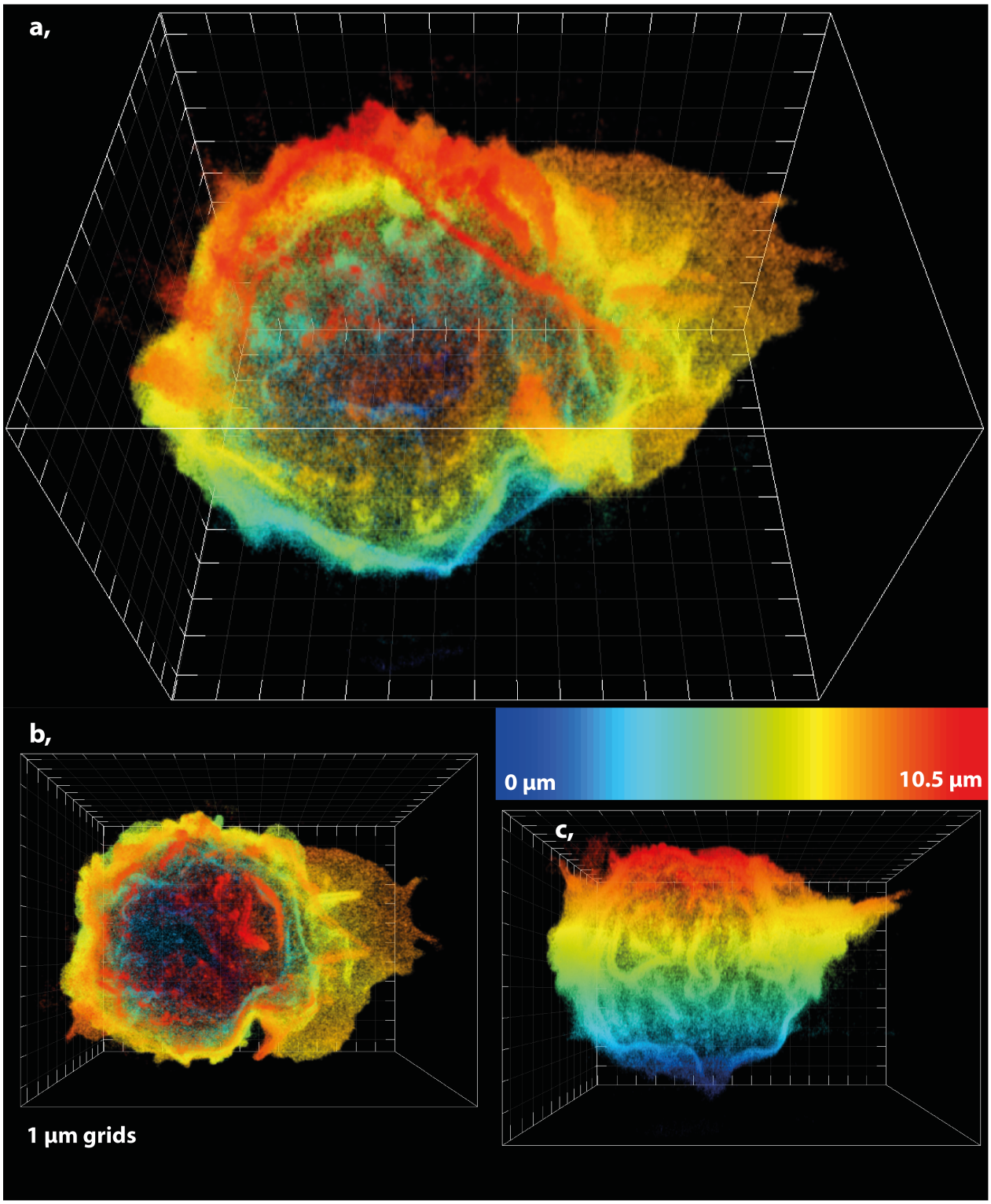

Fig. 6.9 Whole-cell PA-PAINT imaging of the outer membrane surface of Jurkat T cells, fixed in solution, with the DHPSF. (a) WGA-(PA-JF549) localisations from a $\sim$10.5 μm axial volume spanning an entire Jurkat T cell (1.4×10^6 localisations). (b&c) Top-down and side-on views of the cell presented in (a). All localisations are coloured axially across the $\sim$10.5 μm thick axial volume of the cell. Localisations are rendered with 40 nm FWHM laterally and 60 nm FWHM axially, representing the localisation precision of the DHPSF. Ticks and gridlines are spaced 1μm apart.

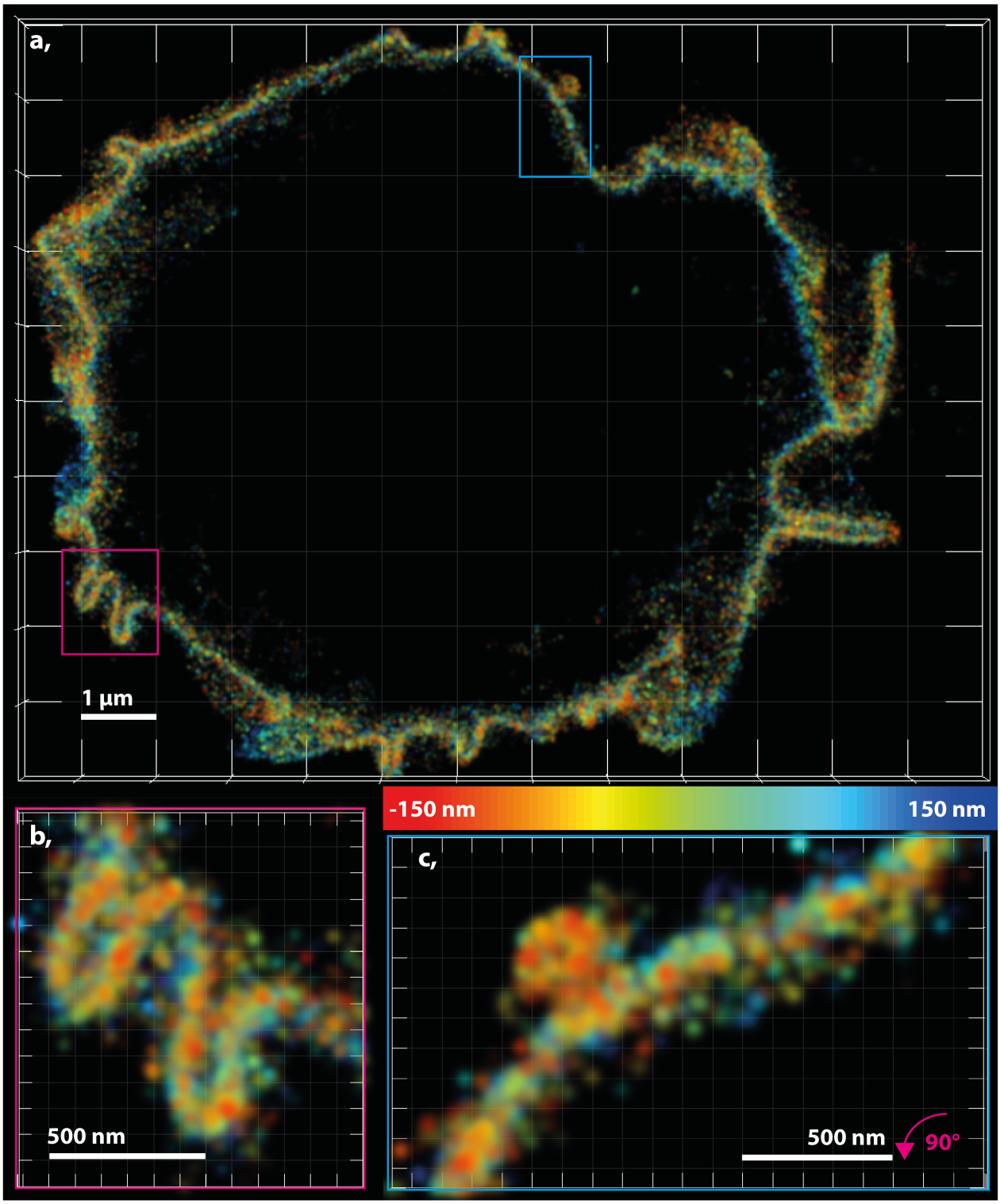

Fig. 6.10 A 300 nm thick section of the outer membrane surface of Jurkat T cells, fixed in solution, with the DHPSF. (a) WGA-(PA-JF549) localisations from a 300 nm axial section from the centre of the entire Jurkat T cell presented in figure 6.9 (70,361 localisations. (b&c) Highlighted regions from (a) that include membrane nanostructure. Localisations are rendered with 40 nm FWHM laterally and 60 nm FWHM axially, representing the localisation precision of the DHPSF. Ticks and gridlines are spaced 1μm apart in (a) and 100 nm apart in (b&c).

6.4.2 Imaging the Morphology of Jurkat T Cells Contacting PLL-Coated Surfaces

The outer membrane of Jurkat T cells contracting PLL-coated coverslips was imaged with the same PA-PAINT methodology and fiducial markers set up as previously described. In this case, Jurkat T cells were fixed after 10 minutes contacting a PLL-coated coverslip. Agarose beads coated with fluorescence nanodiamonds were then added to the sample and immobilised in an agarose gel. This experiment continues the work presented in chapter 5, observing morphological changes exhibited by T cells upon adhesion coated surfaces, but with high density sampling of the position of the outer membrane.

Typically Jurkat cells required 3-4 image planes to cover their volume. Each sequential focal plane shared at least one fiducial marker so that the localisation data taken from neighbouring planes could be aligned after drift correction. 200,000 frames were recorded from each image plane with a 30 ms exposure time, corresponding to a total acquisition time of 6 hours and 40 minutes to image four planes. 955,748 localisations were recorded across the entire cell presented in figure 6.11 at a rate of $\sim$40 localisations per second. Large-scale membrane reorganisation was observed targeted towards the PLL-coated surface. Less nanoscale structure was observed away from the surface compared to Jurkat cells that were fixed in solution. This could indicate that the cells are perturbed from their resting state even when imaging away from the contact between cell and PLL-coated surface. A thin layer of membrane is observed to spread out across the surface, extending beyond the radius of the cell volume. This data supports recent publications suggesting that contact with PLL-coated surface can perturb the resting state of T cells [150, 151]. Dynamic videos of the cell data presented in figure 6.11 are included in the digital appendix of this thesis, along with additional reconstructions.

Fig. 6.11 Figure on following page. Whole-cell PA-PAINT imaging of the outer membrane surface of Jurkat T cells fixed after 10 minutes contacting a PLL-coated surface. (a) WGA-(PA-JF549) localisations from a $\sim$12 μm axial volume spanning an entire Jurkat T cell (1×10^6 localisations). (b&c) Top-down and side-on views of the bottom 4 μm of the cell presented in (a). (d) Highlighted region from (b) showing large scale membrane reorganisation targeted towards the PLL-coated surface. Localisations are coloured axially across the $\sim$12 μm thick axial volume of the cell in (a-c) and over a 4 μm axial depth in (c). Localisations are rendered with 40 nm FWHM laterally and 60 nm FWHM axially, representing the localisation precision of the DHPSF. Ticks and gridlines are spaced 1μm apart.

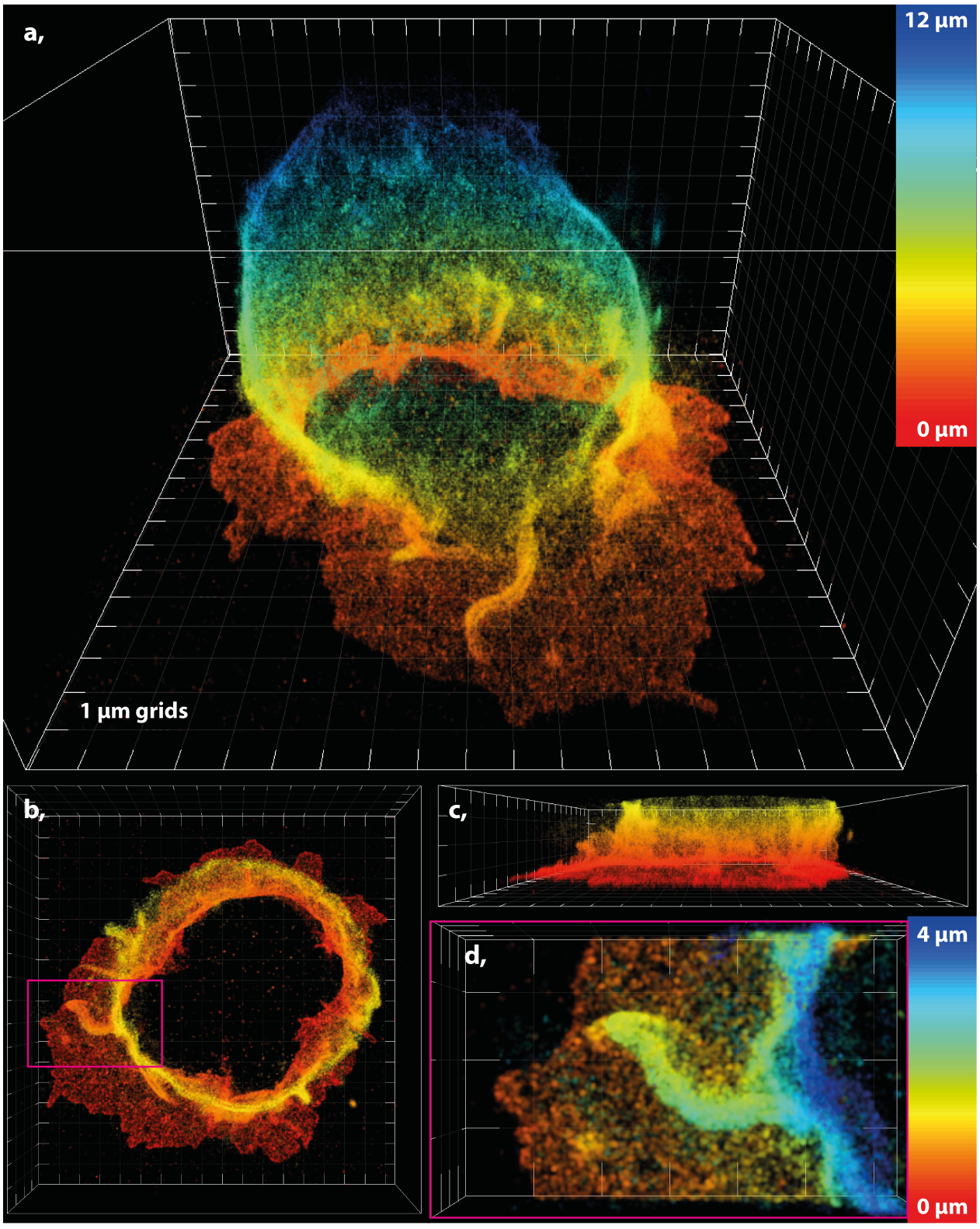

Fig. 6.11 Figure caption on previous page.

6.5 Multiplexed Imaging of the TCR and Outer T-Cell Membrane

Multi-target imaging can be achieved by labelling with multiple types of fluorophore that can be imaged simultaneously or sequentially, depending on the geometry of the microscope platform. This has been previously demonstrated for the DHPSF by the Moerner group [104, 105]. However, multi-colour imaging requires the correction of chromatic aberrations for datasets to be aligned and increased spectral filtering is required to prevent cross-channel fluorescence being detected. The protocol presented in figures 6.6-6.11 for labelling the outer membrane of T cells does not require cell labelling prior to imaging as the fluorescent probes are present in the imaging buffer, which can be added or replaced during image acquisition. As a result, it is compatible with sequential multi-target imaging of the TCR and the outer membrane by employing the same fluorophore for both targets. This eliminates the need for chromatic aberration correction and does not increase background signal as the fluorophores are not present within the sample together. Therefore, the position of the TCR can be imaged in a PALM mode for labelled cells, before WGA-(PA-JF549) is added to the imaging buffer for PA-PAINT imaging, creating two 3D-SMLM datasets.

As the WGA binds irreversibly to sugars in the membrane, it must be imaged last so that the two populations can be separated. Typically the position of the TCR was imaged on the apical surface of multiple cells with fiducial markers present within the image. The position of the stage was recorded so that the same cells could be found later. After all cells were imaged to completion and no more fluorescent events were observed, WGA-(PA-JF549) was added to the imaging buffer and allowed to equilibrate for at least 30 minutes. The three cells were then imaged under the same imaging conditions to localise the position of the outer membrane. The position of the fiducial markers was used to align to two datasets to create multi-target 3D-SMLM datasets of the top $\sim$4 μm of T cells fixed in solution.

The TCR on the outer membrane of Jurkat and primary cells was labelled with anti-CD3 fabs fused to PA-JF549 and cells were suspended in 1% agarose gel with fluorescent nanodiamonds fiducial markers immobilised away from the coverslip surface, bound the surface of 50 μm agarose beads, as described in figure 6.3. Constant 561 nm and 405 nm illumination was incident in a HILO geometry and the sample was imaged in a PALM mode. Typically >30,000 frames were acquired for each cell with an exposure time of 30 ms, until no more fluorescence events were seen. After all cells were imaged, WGA-(PA-JF549) was added to the imaging buffer and allowed to equilibrate for at least 30 minutes. The position of

the outer membrane was then imaged for all cells in turn in a PA-PAINT mode with the same 561 nm and 405 nm HILO illumination. During these acquisitions the position of the focal plane was maintained an autofocus script in beanshell controlling a piezo drive mounted under the objective lens. 100,000 frames were acquired for each cell with an exposure time of 30 ms. For each cell, both datasets were filtered for repeat localisations of the same fluorophore in space (500 nm) and time (1 second) and were corrected for stage drift and aligned with the position of the fiducial marker.

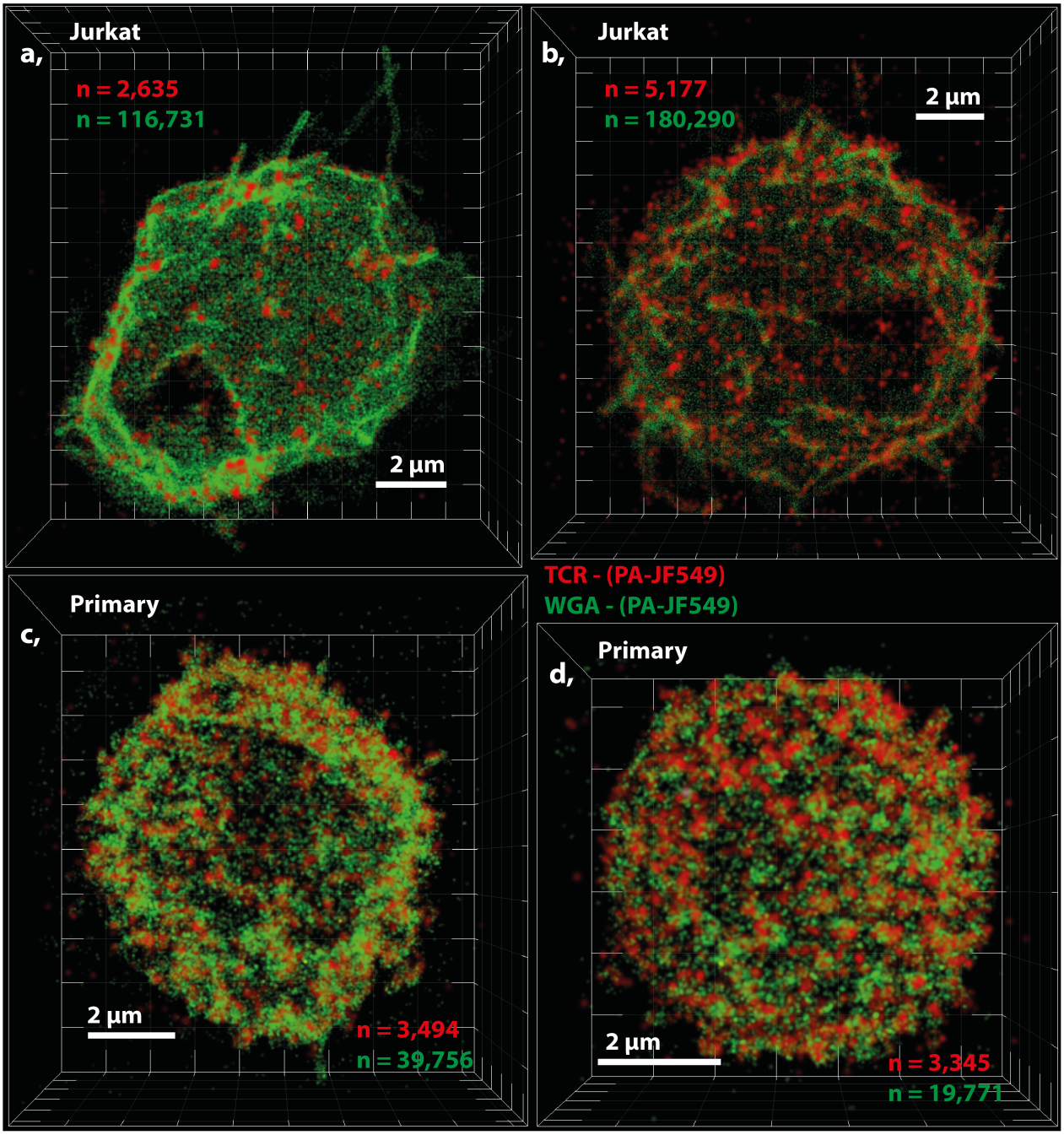

Fig. 6.12 Multi-colour imaging of the TCR (red) and outer membrane (green) in Jurkat and primary T cells. Both targets were labelled with PA-JF549 and were imaged sequentially. (a&b) The position of the TCR relative to the apical membrane surface of two representative Jurkat T cells that were fixed in solution, with corresponding localisation numbers. (c&d) The position of the TCR relative to the apical membrane surface of two representative primary T cells that were fixed in solution, with corresponding localisation numbers. WGA Localisations are rendered with 40 nm FWHM laterally and 60 nm FWHM axially, representing the localisation precision of the DHPSF. TCR localisations are rendered with 100 nm FWHM for visibility. Ticks and gridlines are spaced 1μm apart.

These datasets allow for relation between membrane nanostructure and protein distribution to be investigated. A recent study determined that ∼90% of TCRs were located at the tips of membrane protrusions in primary T cells fixed in suspension by variable-angle TIRF [201]. Such a distribution should be visible by eye but was not observed in any T cells imaged by our methodology. For both Jurkat and primary cells the distribution of the TCR was not obviously correlated to membrane nanostructure. A small fraction of pseudopodia are observed without any TCR localisations in their vicinity (figure 6.12). Primary T cells appeared to be roughly half the diameter of Jurkat T cells but expressed a similar number of TCR localisations after filtering for repeat localisations of the same fluorescence event. 3,400±800 TCR localisations were recorded from primary T cells (5 cells) and 3,300±1,300 TCR localisations were recorded from Jurkat T cells (4 cells). The primary T cells used in this experiment were measured to express ∼13,000 copies of the TCR (measured by FACs in the Davis group). As the primary cells were smaller than Jurkat T cells (a radius of ∼4 μm) a greater fraction of the cell could be simultaneously imaged. Combining this with the activation efficiency of PA-JF549 results in an estimation of 5,850 possible localisations of the TCR from a single field of view with the DHPSF. This localisation efficiency (0.58±0.14) matches well with that observed for Jurkat T cells (0.49±0.19 assuming a copy number of 30,000). The reduction in imaging efficiency compared to that described in chapter 5 could be in part due to dissociation of the anti-CD3 fabs during labelling, washing and fixation as well as the localisation efficiency of the DHPSF for PA-JF549. A higher density of pseudopodia was also seen on the outer membrane of primary cells compared to Jurkat cells, but this was not quantified.

These dataset facilitate quantitative analysis of the distribution of the TCR at the outer surface of primary and Jurkat T cells. The clustering state of the TCR remains a contested topic, with multiple publications attempting to quantify its distribution by 2D imaging methods in recent years [268, 121, 278]. The large depth of field of the DHPSF make it capable of imaging a significant fraction of T-cell membrane surfaces, enabling quantification of the TCR on non-flat surfaces that may represent more physiological conditions. The next section of this chapter describes the work done in quantifying the clustering state of the TCR in primary and Jurkat T cells.

6.6 Quantification of Clustering of the TCR

In order to extract clustering information from the datasets, a code employing Ripley's K analysis on 3D-SMLM data was written in MATLAB (code available in appendix. As described in chapter 1, Ripley's K analysis compares the number of localisations within a radius, r, of each localisation. This is compared to a model distribution using the general equation:

$$L(r) - r = \sqrt{\frac{N(r)r^2}{M(r)}} - r \tag{6.1}$$

Where $N(r)$ is the mean number of localisations within a radius r from each localisation and $M(r)$ is the mean number of localisations within a radius r from a complete spatial randomness (CSR) model distribution. If the measured distribution is randomly distributed, $N(r) = M(r)$ and equation 6.1 becomes: $L(r) - r = \sqrt{r^2} - r = 0$. For clustered distributions $L(r) - r > 0$ and $L(r) - r < 0$ for anti-clustered distributions.

In many 2D studies employing Ripley's K analysis [145, 118], CSR model distributions are defined by the geometry of the system. For example, when considering flat a circular area at the coverslip surface the model distribution is given by the measured localisation density, ρ, and the area being considered. Therefore, $M(r) = \rho\pi r^2$ and thus:

$$L(r) - r = \sqrt{\frac{N(r)}{\rho\pi}} - r \tag{6.2}$$

However, when imaging away from the coverslip the geometry of the system is not necessarily prior knowledge and the model CSR distribution may not fit the recorded data, leading to artefacts in Ripley's K analysis. In order to accommodate non-standard 3D geometries, the written analysis code requires the input of model distributions of point data in order to calculate $M(r)$.

6.6.1 Benchmarking Ripley's K Analysis in 3D

The performance of the analysis was tested on against model data sets representing 3D-SMLM localisation data of a membrane-associated protein on the top surface of a spherical cell. CSR 'unclustered' distributions were simulated by placing points at random on the top $\sim$2 μm of a sphere with 4.5 μm radius. In all simulated cases, all points were displaced by a distance sampled from a normal distribution with width equal to the worst case localisation precision expected from the DHPSF (30 nm laterally and 60 nm axially). Clustered distributions were simulated in the same way but with the addition of randomly placed groups of localisations to represent clusters. These clusters contained a defined number of points that were placed with uniform random probability within a set radius of the centre position in order to represent cluster size with a flat profile. 5,000 points were simulated to represent typical datasets for TCR imaging with PA-JF549. 20 clusters of 100 nm diameter, each containing 20 points (corresponding to 8% of points), were incorporated into the CSR distributions to represent 'clustered' distributions. An example distribution is plotted in figure 6.13a.

Ten simulations of clustered and unclustered distributions containing 5,000 points were passed to the written algorithm as $N(r)$ and $M(r)$ respectively to calculate $L(r)$. The mean and standard deviation of $L(r)$ was plot as $L(r)-r$. The mean and standard deviation of $L(r)$ was plotted for ten simulations with unclustered distributions as both $N(r)$ and $M(r)$ (figure 6.13b). An increase in $L(r)-r$ was seen for the clustered distribution compared to the unclustered distribution, indicating that the additional clusters were identified by the analysis. $L(r)-r$ for the clustered distribution peaked at $\sim$130 nm corresponding to a combination of cluster size (100 nm) and simulated localisation uncertainty (30 nm laterally and 60 nm axially). This result indicates that Ripley's K analysis is capable of identifying low-levels of clustering (<10% of molecules) in model 3D-SMLM datasets.

The algorithm was then tested on data with a range of clustering values. The effect of the total number of points on perceived clustering was investigated by simulating distributions with 20 clusters, each with 20 points and a diameter of 100 nm with at different number of overall points, changing the fraction of points within a cluster. Values ranging from 4% of points in clusters (10,000 points) to 40% of points in clusters (1,000) were chosen with ten repeats for each used to define a mean and standard deviation of $L(r)-r$ (figure 6.14). Distributions with a larger fraction of points within clusters (lower total number of points for the same number of clusters) reported greater clustering. Only the 4% clustered case could not be identified as significantly clustered.

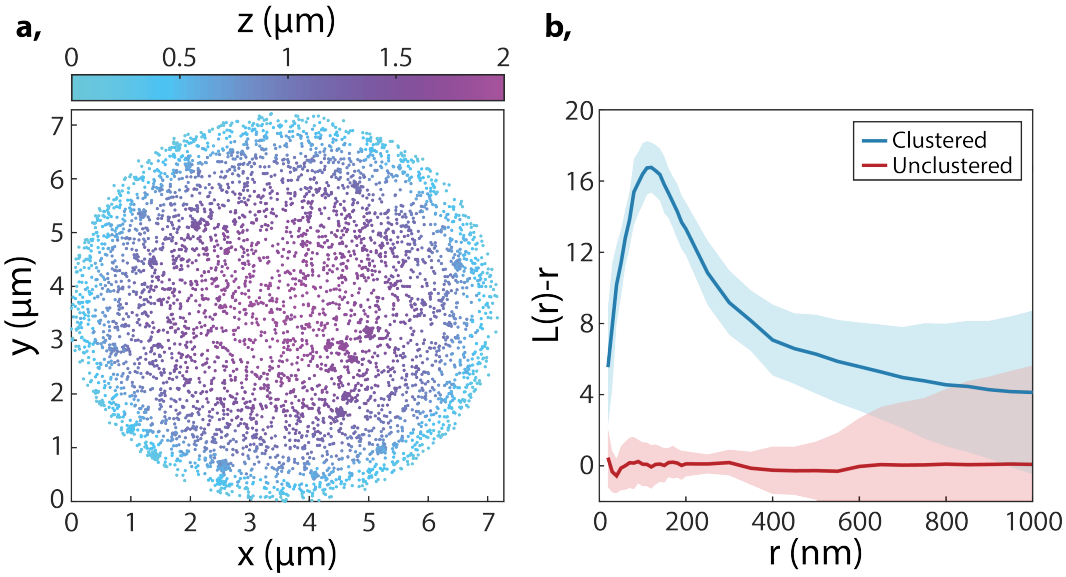

Fig. 6.13 Simulated clustered distribution and corresponding Ripley's K analysis. (a) A model distribution was simulated with 5,000 points on the top surface of a 4.5 μm radius sphere, containing 20 clusters of 100 nm diameter and 20 points. (b) Mean and standard deviation of Ripley's K analysis for 10 repeats of the clustered distribution shown in (a). $L(r) - r$ of a CSR distribution is also plot ('Unclustered').

The effect of the number of clusters on perceived clustering was investigated by simulating distributions with different numbers of clusters, each containing 20 points and with a radius of 100 nm. In this case, the total number of points was kept constant at 5,000. Values ranging from one cluster (0.4% of points in clusters) to 100 clusters (40% of points in clusters) were chosen with ten repeats for each used to define a mean and standard deviation of $L(r) - r$ (figure 6.14b&c). As before, distributions with a larger fraction of points within clusters (more clusters for the same number of total points) reported greater clustering. However, in this case clustering could be identified with just 2% of points in clusters. This indicates that factors other than the fraction of points in clusters have some effect on the ability to identify clustering.

The effect of the number of points in each cluster on perceived clustering was investigated by simulating distributions with 20 clusters of 100 nm diameter with different number of points per cluster (all clusters within a simulation had an equal number of points per cluster). The total number of points was kept constant, varying the fraction of points within a cluster. Values ranging from 2 points per cluster (0.8% of points in clusters) to 100 points per cluster (40% of points in clusters) were chosen with ten repeats for each used to define a mean a standard deviation $L(r) - r$ (figure 6.14d&e). Unsurprisingly, distributions with a larger

fraction of points within clusters reported greater clustering. In this case clustering was marginally above noise for 4% of points in clusters (10 points per cluster). However, a cluster size of 10 would likely be identified if a larger fraction of points occupied clusters.

The analysis presented in figure 6.14a indicates that the fraction of points in clusters is a key parameter for identifying clustering within a distribution. In all cases a clustered fraction of $\sim$8% allowed for clustering to be identified. However, the difference in $L(r) - r$ for each of the three cases investigated at the same clustering fraction hint that the number of points per cluster and density of clusters can also have a significant effect on analysis. Ripley's K typically reports a length scale that clustering occurs on, although this appears to be a convolution of the true cluster size and uncertainty in positional measurement. In any case, Ripley's K analysis provides a robust metric to identify clustering but does not provide a complete description of the type of clustering present. Therefore it will be suitable for addressing the relative clustering state of the TCR at the surface of T cells.

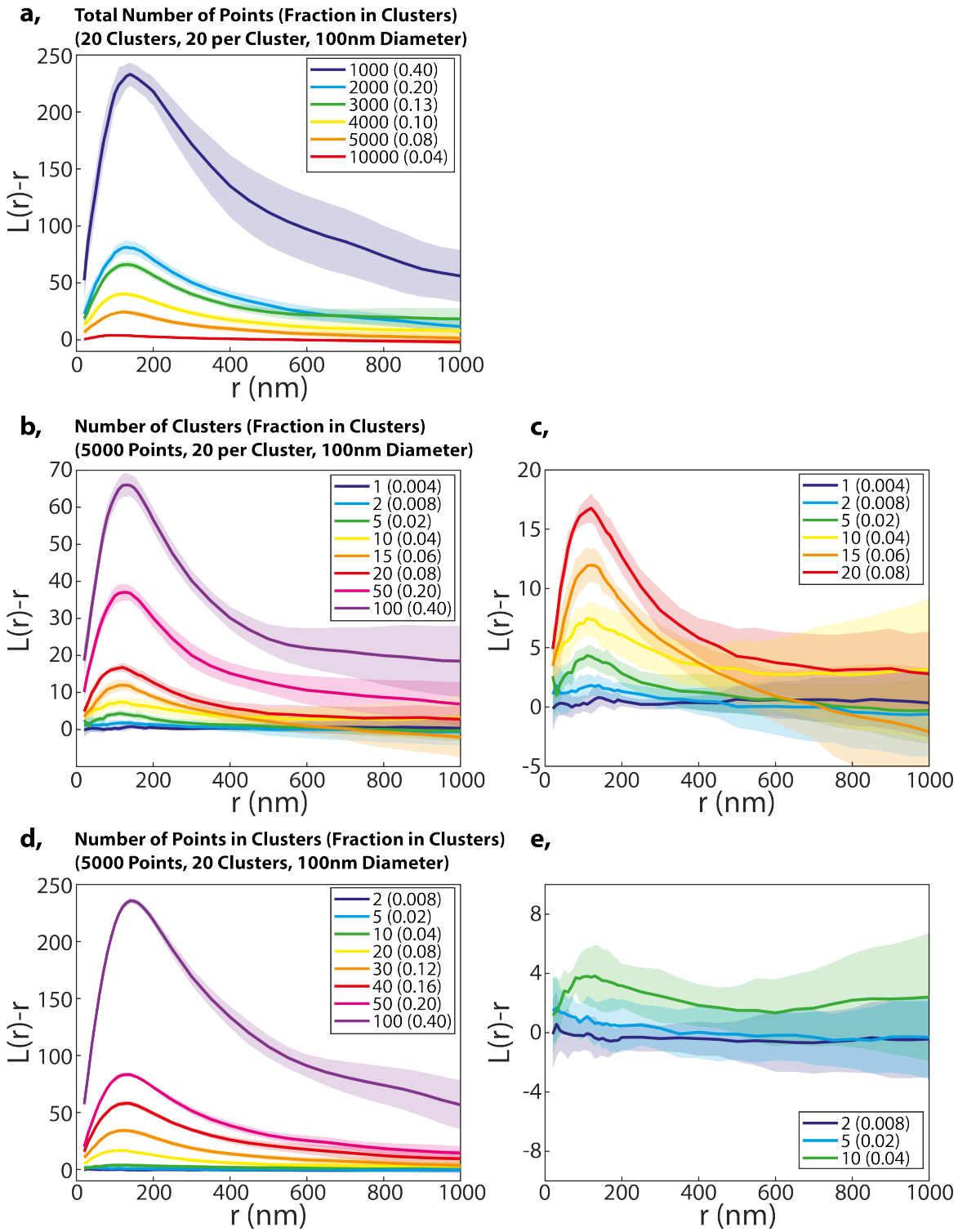

Fig. 6.14 Ripley's K analysis on a range simulated clustering values. (a) $L(r) - r$ for a range of total number of points for simulated distributions with 20 clusters, each with 20 points and a diameter of 100 nm with fraction of points in clusters noted. (b) $L(r) - r$ for a range of total number of clusters for simulated distributions with 5,000 points, each cluster has 20 points and a diameter of 100 nm. The fraction of points in clusters is noted. (c) Zoom in of (b), highlighting lower clustering values. (d) $L(r) - r$ for a range of number of points within individual clusters for simulated distributions with 5,000 points including 20 clusters with a diameter of 100 nm. The fraction of points in clusters is noted. (e) Zoom in for (d), highlighting lower clustering values.

The analysis was tested against a dataset with clustering parameters based on a previous study of the distribution of the TCR by PALM imaging conducted by Pageon *et. al.* (For CD3ζ on the basal surface of Jurkat T cells on PLL-coated coverslips: 84±9 nm cluster diameter was approximated to 100 nm, ∼70% of molecules in clusters, ∼20 molecules per cluster and ∼20 clusters per μm^2) [278]. In order to maintain the observed cluster density (∼70% of molecules in clusters and ∼20 μm^{-2}), ∼28,500 localisations were required on the simulated surface area (∼50 μm^2), which is significantly more than were recorded for the TCR by PA-JF549. 10 instances of model datasets were created and a 4×4 μm^2 area was analysed to reduce computing costs (figure 6.15a&b). These distributions were then subsampled to produce datasets containing 5,000 points for comparison with our recorded TCR datasets (figure 6.15c&d). Clustering could be identified in both distributions, indicating that 3D-SMLM is compatible with Ripley's K analysis for protein distributions expected on the surface of T cells. Both the complete and sub-sampled distributions exhibit the same form of $L(r) - r$, with both peaking at 120 nm. The form of the $L(r) - r$ distribution remained constant when subsampling the model distribution to 1,000 points, which is below the minimum number of TCR localisation recorded from any cell in the later analysis (2,573). The error bars between clustered and unclustered distributions started to overlap at all r values for subsampled distributions with fewer than 300 points, which is an order of magnitude fewer points than recorded from a comparable area on the T cells.

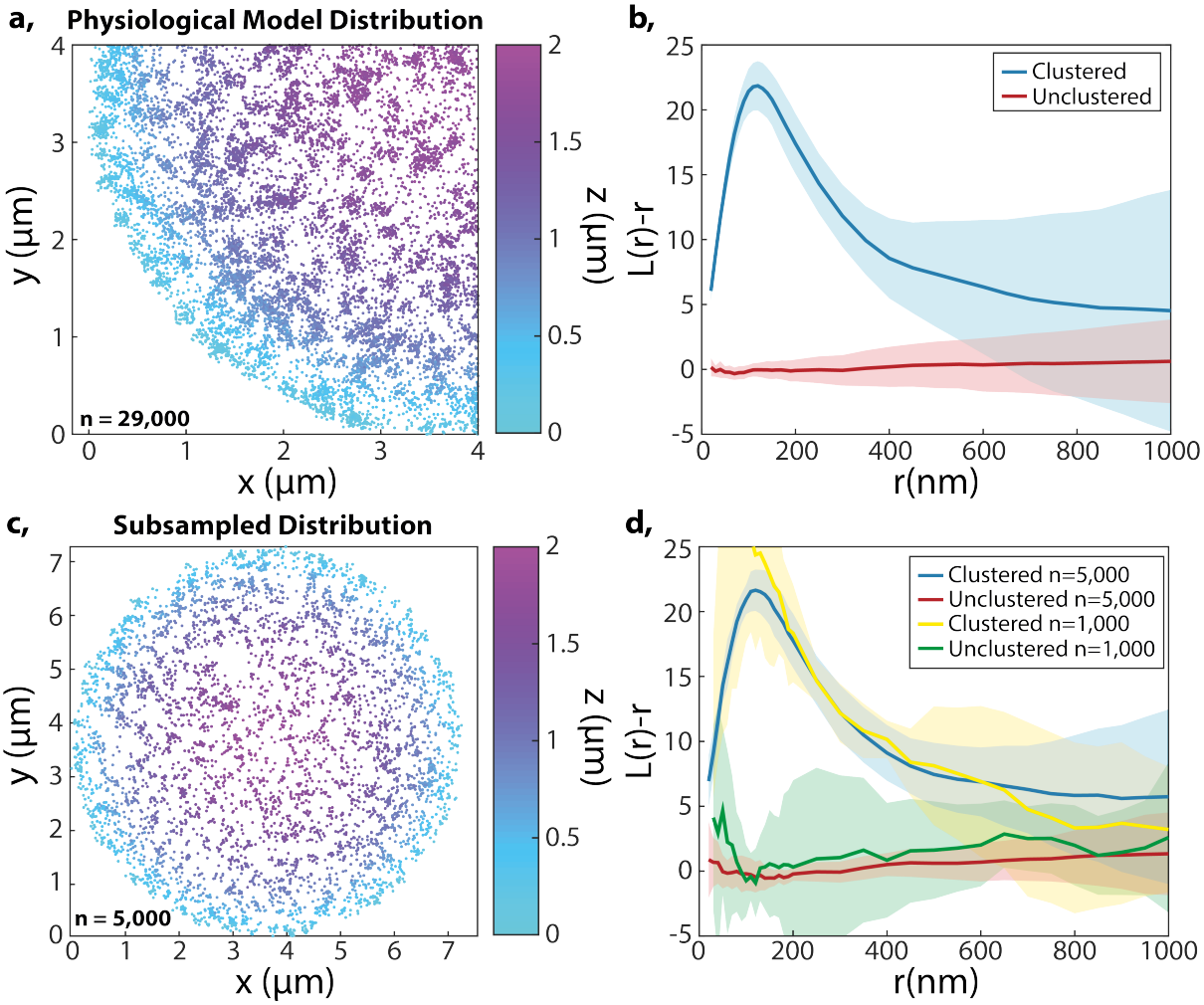

Fig. 6.15 Simulated clustered distribution with experimentally determined parameters for the TCR and corresponding Ripley's K analysis. (a) A model distribution was simulated following previous measurements of the TCR [278]. (a) Example model distribution with a density of 20 clusters per μm^2 and each cluster containing 20 molecules with a 100 nm diameter. 70% of molecules are cluster-associated. (b) Mean and standard deviation of Ripley's K analysis for 10 repeats of the clustered distribution shown in (a). $L(r) - r$ of the corresponding unclustered distribution is also plot. (c) Subsampled model distribution from (a). 5,000 points were randomly chosen and analysed. (d) Mean and standard deviation of Ripley's K analysis for 10 repeats of the subsampled clustered distribution shown in (a) and a subsampled distribution with 1,000 points. $L(r) - r$ of the corresponding (subsampled) unclustered distribution is also plot.

6.6.2 Comparing Model Distributions for Ripley's K Analysis

In order to fairly compare SMLM distributions by Ripley's K analysis the geometry of the 'unclustered' model distribution must match that of the sample. This is especially true for membrane-bound distributions on non-flat surfaces. Model distributions that do not accurately follow the shape of the surface will miscalculate the surface area and thus the density of points will not match if the same numbers of points are simulated and the $L(r) - r$ curve will be affected.

In order to probe the effect of mis-matched distribution geometries 'unclustered' CSR distributions were compared between a flat surface and a flat surface with 500 nm long and 300 nm diameter hollow cylinders representing typical membrane pseudopodia at a density of one 'pseudopodia' per μm^2 (figure 6.16a). 10 simulations were conducted to obtain the mean and standard deviation of $L(r) - r$ in the case of matched surface density of points (100 points per μm^2, determined from TCR-(PA-JF549) datasets) between unclustered models and matched total number of points (3,000 points on a 30 μm^2 area for the flat surface) between unclustered models. These were compared to the $L(r) - r$ of a distribution matching the geometry of the initial simulation (figure 6.16b&c). The two approximated distributions (with no 'pseudopodia' and surface density or total number of points matched to the initial distribution) did not correctly report an unclustered distribution at the size ranges that typical clustering should be observed ($\sim$100 nm). Instead, matching the surface density of points caused the analysis to report clustering at all length scales (0.02-1 μm). Matching the total number of points had the opposite effect, causing the analysis to report anti-clustering from 0.02 μm to $\sim$0.5 μm, above which error bars overlap with the true distribution. Only comparison with a distribution that matched the geometry of the system of interest faithfully reported an unclustered distribution with $L(r) - r$ close to zero. This analysis indicates that, when investigating non-flat or complicated geometries, knowing the underlying geometry of the sample is crucial for accurate identification of clustering. This is especially true for T cells as they are known to exhibit significant 3D membrane structure at comparable length scales to reported TCR clustering clustering [201]. Indeed, in the data presented in figures 6.7-6.12, pseudopodia and other nanostructure is observed at length scales below 1 μm. This is not the case when imaging the basal surface of T cells sat onto adherent coated surfaces (*e.g.* PLL and OKt3), in which case the geometry is flat (see figure 6.11). In these cases, the surface itself may cause membrane-protein clustering [150, 151].

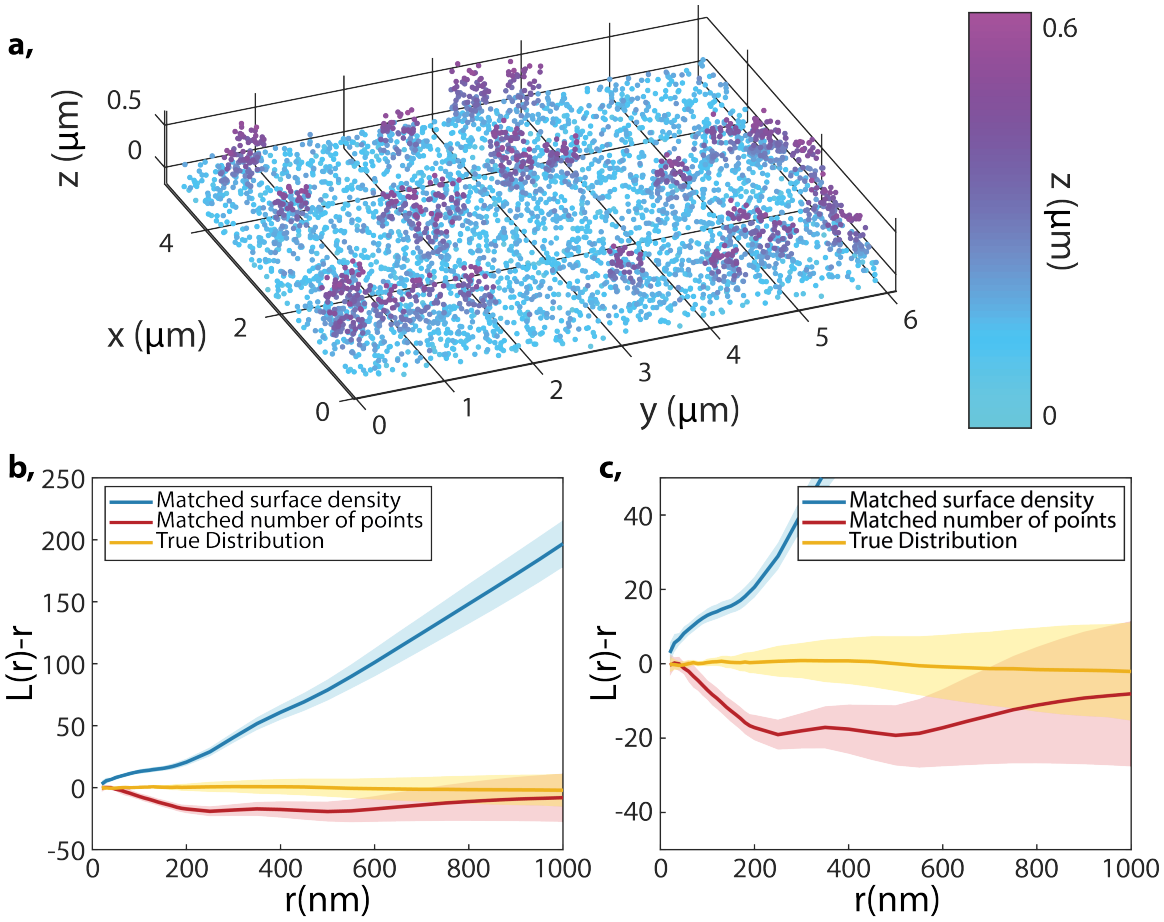

Fig. 6.16 Comparing simulated unclustered distributions with axial structure to flat-surface approximations. (a) Representative distribution of unclustered points distributed onto a surface with one pseudopodia per μm^2 and 100 points per μm^2. Pseudopodia are represented as 500 nm long and 300 nm wide hollow cylinders. (b) Mean and standard deviation of $L(r) - r$ plotted for 10 simulated repeats with comparison to a flat model distributions with equal surface density of points (blue) and equal total number of points (red). These were compared to the mean and standard deviation of 10 repeats of $L(r) - r$ of the same distribution compared to a model distribution with correct geometry (yellow). (c) Zoom in for (b), highlighting lower clustering values.

6.6.3 Quantification of the TCR Clustering State on PLL-Coated Surfaces

In order to test the capability of the DHPSF in combination with PA-JF549 labelling as a tool to probe the clustering state of membrane proteins, previous Ripley's K measurements of the Jurkat T cells fixed on PLL-coated coverslips were repeated. Jurkat T cells labelled with anti-CD3 fabs fused to PA-JF549 and allowed to drop onto PLL-coated coverslips and were fixed after 10 minutes. The TCR was then imaged on the DHPSF instrument as described before to create localisation datasets of the position of the TCR. Localisations were filtered in space (500 nm) and time (1 second) to remove repeat localisations of the same fluorophore. Rectangular areas contacting the PLL-coated coverslip were cropped out of the localisation data (figure 6.17a) and compared to ten CSR distributions of the same size and number of points on a plane to calculate $L(r) - r$. The mean and standard deviation between five cells was plot and the simulated CSR distributions were used to create an unclustered control (figure 6.17b).

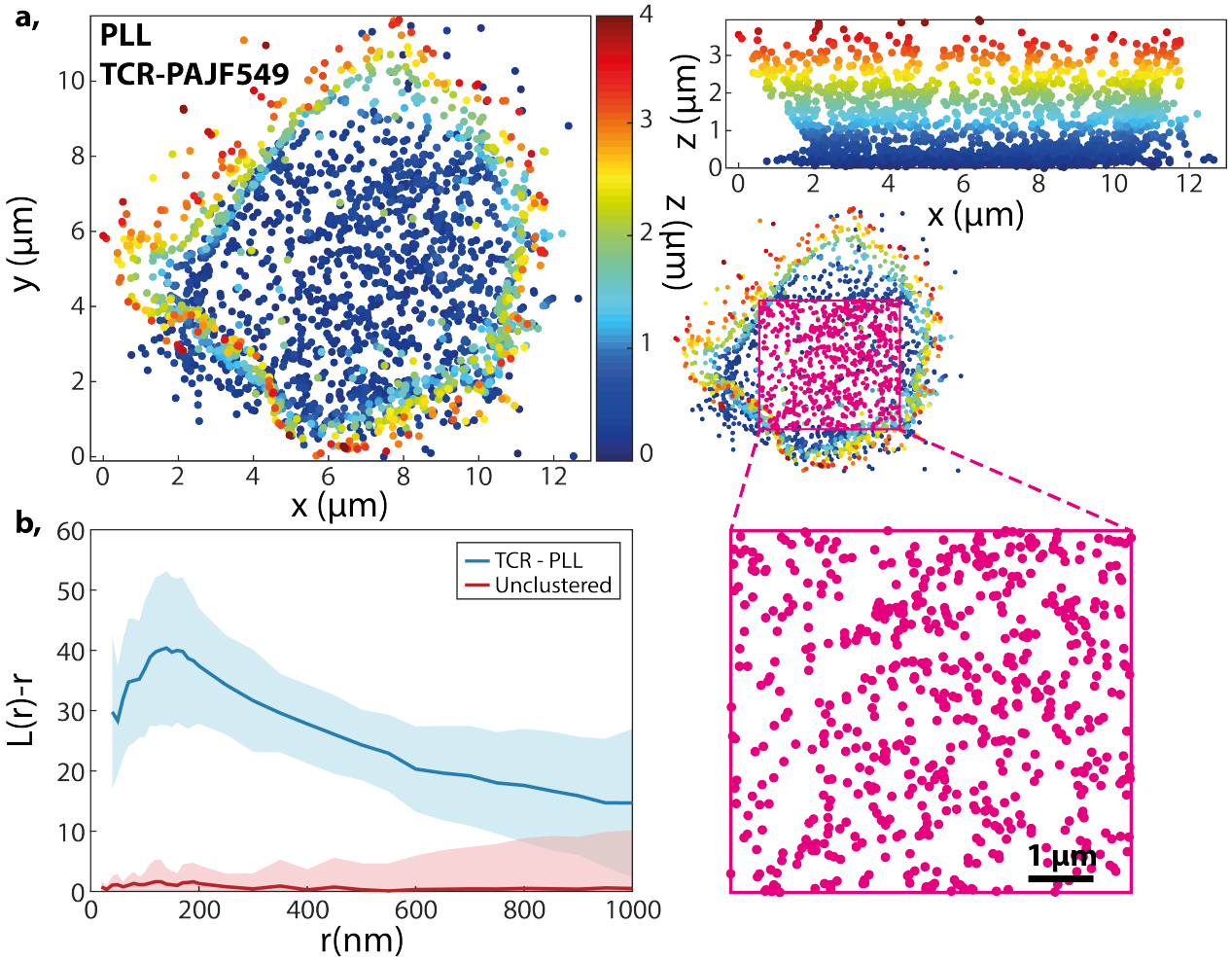

Fig. 6.17 TCR clustering in Jurkat T cells at PLL-coated surfaces. (a) Representative localisation data of the TCR on the bottom ∼4 μm of fixed Jurkat T cells contacting PLL-coated surfaces for 10 min. Localisations are rendered with ∼200 nm diameter for visibility. Top-down (left) and side-on (right) views are shown. A region corresponding to an area of the T-cell outer membrane that is contacting the PLL-coated surface was cropped out for Ripley's K analysis (magenta region, bottom right). (b) Mean and standard deviation of $L(r) - r$ for TCR molecules contacting PLL-coated surfaces (4 cells).

These results repeat the findings of a previous study investigating the clustering state of the TCR on coated surfaces by Pageon *et. al.* [278]. In this previous study, Jurkat T cells expressing CD3ζ fused to the fluorescent protein PSCFP2 were imaged in a 2D-PALM mode via TIRF illumination. In this study, many more localisations were recorded compared to the data presented in figure 6.17, likely due to a lack of filtering for repeat localisation of the same fluorophore. None the less, the computed $L(r)-r$ distributions for the TCR (both via labelling of the CD3 co-receptor) match well (for a direct comparison of the two $L(r)-r$ distributions see appendix A). Both distributions peak at an $L(r)-r$ of $\sim$40. This peak occurs at $\sim$100 nm in the previous study and $\sim$150 nm in our data, likely due to the increased localisation uncertainty of the DHPSF compared to 2D SMLM and the presence of an additional localisation error (x, y and z compared to just x and y). This analysis demonstrates that the DHPSF is capable of identifying clustering in real-cell imaging, providing an appropriate CSR model can be produced.

6.6.4 Quantification of the TCR Clustering State away from Coated Surfaces

In order to implement Ripley's K analysis for membrane-bound proteins away from the coverslip the geometry of the surface must be known. As shown in figure 6.16, nanostructure of similar size-order to the expected clustering must be accounted for in order to achieve reliable clustering identification. This makes approximations of overall cell shape, like those shown in chapter 5 figure 5.7, unsuitable for creating CSR distributions. Therefore, it is imperative that the position of the outer membrane is identified with suitable precision to resolve membrane nanostructure. As shown in chapter 5, this can be achieved in T cells with single-colour imaging by STORM labelling as each fluorophore is localised multiple times, increasing the recorded localisation density. However, this fluorescence intermittency is prone to create clustering artefacts, making it less suitable for stoichiometry analysis. Another solution is duel-labelling of the protein of interest and the outer membrane of the cell. This allows for the position of the membrane to be directly determined, creating an unbiased view of cell morphology that is independent of the expression and labelling density of the protein of interest. As shown in figure 6.12, this can be achieved with sequential imaging of the protein of interest, in a PALM mode via a photoactivatable fluorophore, and the outer membrane, in a PA-PAINT mode via fluorescently labelled WGA.

The WGA datasets serve as an 'unclustered' control distribution for Ripley's K analysis, sharing the same topology as the TCR dataset. However, a fraction of the control localisations are observed within the cell volume as WGA can pass through the membrane and label intracellular membranes and sugars [82]. This fraction varies between cells but was always small compared to the outer-membrane-bound localisations for healthy T cells. As demonstrated in figure 6.16, the model distribution must closely match the geometry of the target distribution and thus internal WGA localisations should not be considered. In order to separate the membrane-bound and internal populations, WGA datasets were filtered by proximity to TCR localisations. A threshold was based on the density of localisations in the TCR dataset so that the membrane was fully represented, without holes, in low-density datasets. As no ordering is expected to be present in the TCR dataset at $\sim$1 μm, $L(1\mu\text{m}) - 1\mu\text{m}$ should go to zero for appropriate-geometry distributions. It was found that a threshold of at least three TCR localisations occurring within a distance defined by five times the modal nearest neighbour distance in the corresponding TCR dataset resulted in a unpatchy WGA distributions and a lack of perceived clustering at $\sim$1 μm for all cells. After proximity filtering, WGA distributions were randomly subsampled to match the number of localisations observed in the corresponding TCR datasets for use as a model distribution. For each cell, the mean of 10 instances of these model distributions were used to define $M(r)$ when calculating $L(r) - r$. The mean and standard deviation of 10 instances of subsampled WGA distributions defining $N(r)$ and $M(r)$ were used define an unclustered control.

The clustering state of the TCR was investigated on the surface of Jurkat T cells by sequential imaging of the TCR and the outer membrane in the presence of fiducial markers, as previously described in section 6.5. The TCR was labelled with anti-CD3 fabs tagged with PA-JF549 before fixation in solution, representing the resting state of the T cell. After the position of the TCR was imaged in a PALM mode, the outer membrane of the cells was labelled with WGA and imaged in a PA-PAINT mode, both with HILO activation and excitation illumination. The two datasets were aligned by their position relative to a single fiducial marker present in both acquisitions. The mean and standard deviation of $L(r) - r$ between three cells was plotted for the TCR and WGA (figure 6.18b).

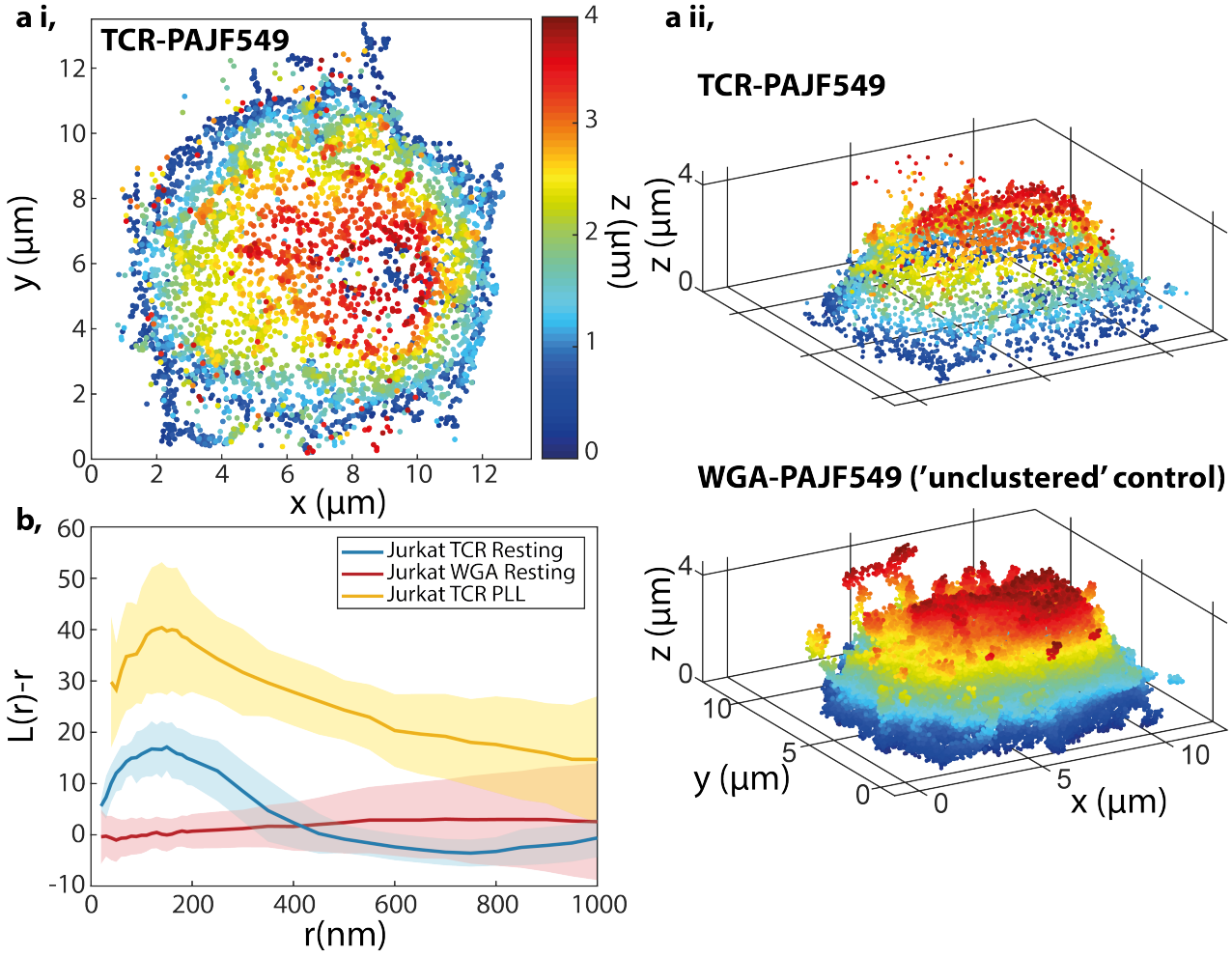

Fig. 6.18 TCR clustering in Jurkat T cells away from coated surfaces. (ai) Representative TCR localisation data on the apical surface of Jurkat T cells fab-labelled with PA-JF549 and fixed in suspension. Localisations are coloured axially across the depth of focus of the DHPSF. (aii) TCR and membrane-bound WGA localisations of the cell presented in (ai).The WGA distribution was sub-sampled to provide an unclustered control for Ripley's K analysis. (b) Mean and standard deviation of $L(r) - r$ for TCR and WGA molecules on the surface of Jurkat T cells (n=3).

The results presented in figure 6.18 indicate that the TCR is less clustered on the membrane of Jurkat T cells when fixed in solution, in a resting state, (blue curve) compared to when fixed contacting PLL-coated surfaces (yellow curve). This is unsurprising as PLL has been shown to perturb the resting dynamics of the TCR [151] and can lead to immunological activation [150]. The distribution of the TCR on resting Jurkat T cells was significantly clustered between 100 nm and 300 nm compared to WGA on the outer membrane (red curve). Both PLL and resting $L(r) - r$ curves peak at $\sim$100 nm, likely corresponding to the limit of detection due to the localisation precision of the DHPSF in three dimensions. This analysis represents a case in which 3D imaging is essential as flat surfaces can have a perturbative effect on the resting state of protein distributions. When imaging away from surface, the intrinsic 3D nature of the outer membrane is not well captured by 2D-projections but is required for direct comparisons of model distributions.

6.6.5 Quantification of the TCR Clustering State in Primary T Cells

The clustering state of the TCR on the surface of primary T cells fixed in suspension was investigated by sequential imaging of the TCR and outer membrane in the presence of fiducial markers (figure 6.19a). Primary T cells were isolated from healthy donors via a CD4+ T-Cell isolation kit, before being labelled with anti-CD3 fabs tagged with PA-JF549 and fixed in solution by Dr Mafalda Santos in the Weatherall Institute of Molecular Medicine in Oxford. The cells were then put on ice and transported to the Department of Chemistry in Cambridge for imaging. The position of the TCR was imaged in a PALM mode before the position of the outer membrane was imaged in a PA-PAINT mode with HILO activation and excitation geometry. The two datasets were aligned by their relative position to a fiducial marker present in both acquisitions. The mean and standard deviation of $L(r) - r$ between three resting cells was plotted for the TCR and WGA (figure 6.19b). Another batch of primary T cells were incubated with anti-TCR$\alpha\beta$ and secondary antibodies during CD3-fab labelling in an attempt to promote TCR clustering. These cells were imaged with the same protocol and the mean and standard deviation of $L(r) - r$ between three antibody-stimulated cells was plotted for the TCR and WGA (figure 6.19c).

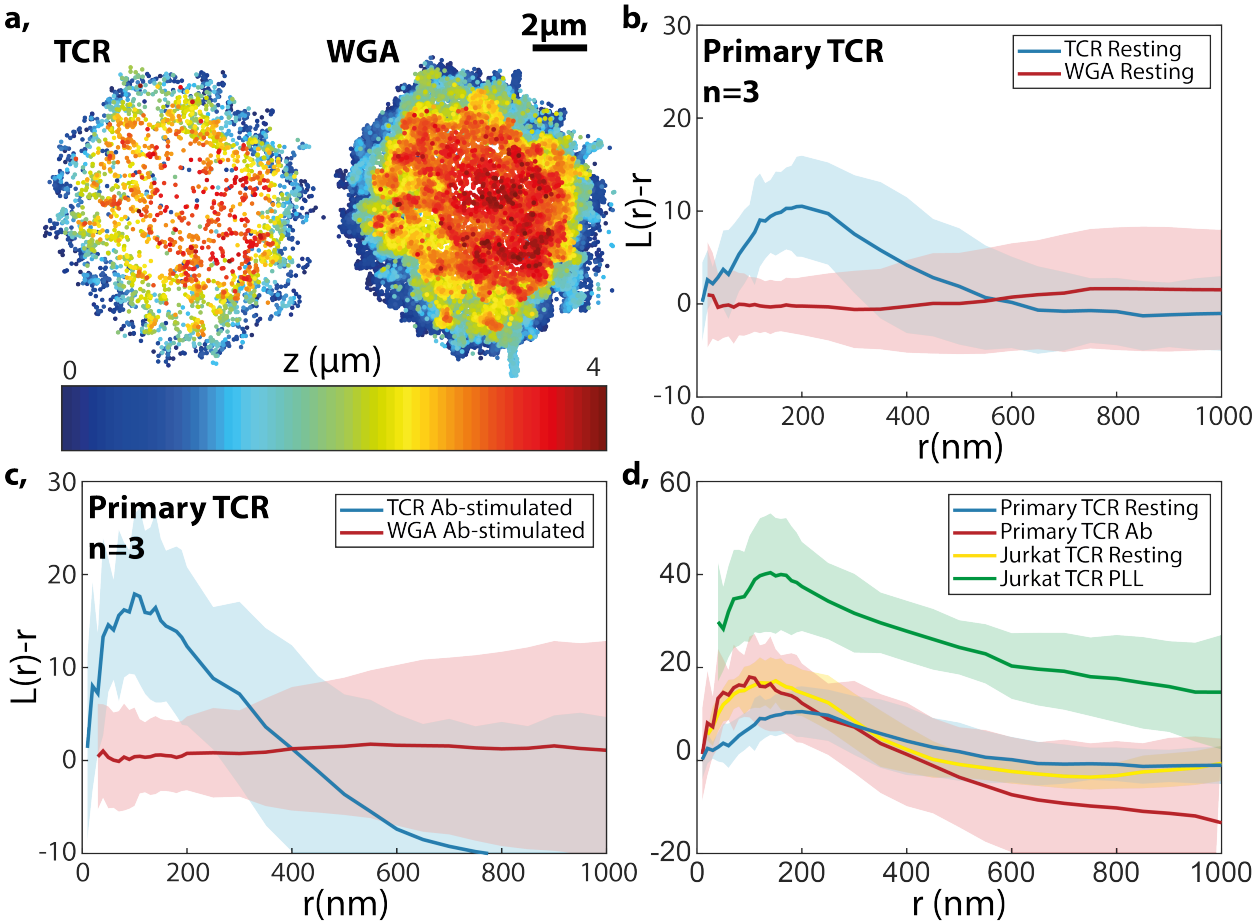

Fig. 6.19 TCR clustering on resting and antibody-stimulated primary T cells. (a) Representative TCR and WGA localisation data on the apical surface of Primary T cells fixed in suspension. Localisations are coloured axially across the depth of focus of the DHPSF. (b) Mean and standard deviation of $L(r) - r$ for TCR and WGA molecules on the surface of resting Jurkat T cells (n=3). (c) Mean and standard deviation of $L(r) - r$ for TCR and WGA molecules on the surface of Jurkat T cells incubated with anti-TCR$\alpha\beta$ antibodies (n=3). (d) Comparison of $L(r) - r$ for TCR molecules on the surface of Jurkat T cells (resting and at PLL-coated surfaces) and primary T cells (resting and antibody-stimulated).

These results suggest that the clustering state of the TCR is not significantly different between Jurkat and primary T cells. The mean peak of $L(r)-r$ is at $\sim$10 in primary cells, which is lower than observed for Jurkat cells ($\sim$17), although the error limits overlap. Stimulation by primary and secondary antibodies did not have a dramatic effect on the $L(r)-r$ distribution in primary cells. In stimulated cells a larger $L(r)-r$ peak of $\sim$18 was observed but this change was not significant. For stimulated cells, $L(r)-r$ peaked at a lower distance ($\sim$100 nm compared to $\sim$190 nm for resting primary cells). This is likely within error but could indicate an increase in low-order clustering caused by the antibodies. Longer incubation with the antibodies may result in larger clusters being formed but it seems that the current protocol does not lead to large clusters formation. Figure 6.19 shows the $L(r)-r$ curves for the TCR in Jurkat cells, at PLL-coated surfaces and in a resting state, and primary cells in a resting state and stimulated by antibodies. Although the n numbers are small, this analysis indicates that the resting state of the TCR is not significantly different between the three conditions fixed in solution, with all three exhibiting a low level of clustering observed between 100-300 nm that is less than previously reported at PLL-coated surfaces [278]. The distribution of the TCR on the outer membrane of resting Jurkat and primary T cells did not appear significantly different.

It is possible to estimate the typical number and size of clusters present in the datasets by adding simulated clusters to the WGA distributions and comparing the resulting $L(r)-r$ curves. A single WGA dataset from a resting primary cell was used to create simulated cluster distributions. For each repeat, this distribution was randomly subsampled to match the number of TCR localisations recorded for the same cell (4,580). A number of points were chosen at random to act as the centre of clusters. Around these points a number of additional points were added with a random distribution within a radius of 50 nm to simulate clusters. The final distribution was then randomly subsampled back to the original number of points (4,580) and compared to another subsampled instance of the overall WGA distribution without additional clusters. The mean of 10 repeats of $L(r)-r$ was plot for a range distributions with the $L(r)-r$ distribution of TCR in primary cells overlaid for comparison (figure 6.20. The effect of the number of points per cluster on $L(r)-r$ was investigated by simulating 10 clusters with a number of points ranging from 2-50 molecules per cluster (figure 6.20c). The effect of the number of cluster added on $L(r)-r$ was investigated by simulating a range of clusters from 1-50, each with 10 points (figure 6.20d).

As shown in figure 6.14, the composition of the clustering distribution can have a significant effect on the form of the observed $L(r)-r$ curve for the same geometry, however, in all cases increased clustering was observed as a larger fraction of the total points were

included in clusters. The same trend was seen when simulating additional clusters in WGA data when changing both the number of clusters and the number of points per cluster (figure 6.20c&d). Simulating 10 additional clusters containing between ∼10 and 20 points matched well to the $L(r) - r$ distribution for the TCR in Jurkat and primary T cells. This corresponds to clustering of ∼3-7% of TCR molecules. Simulating additional clusters with 10 points per cluster matched the $L(r) - r$ distribution for the TCR in Jurkat and primary cells when ∼5-30 clusters were added. This corresponds to clustering of ∼3-10% of TCR molecules. Although these data are not sufficient to draw accurate conclusions on the size and number of TCR clusters present on resting T cells, a rough estimate for the fraction of clustered molecules that would result in the same $L(r) - r$ distribution on the same geometry can be made to be ∼0.03-0.10. This value is significantly less than predicted by a previous study that determined that a fraction of ∼0.70 of TCR molecules are clustered by PALM imaging of PSCFP-2 fluorescent protein at PLL-coated surface [278]. This could in part be explained by the reduced fluorescence intermittency and clustering of PA-JF549 compared to PSCFP-2 [69, 279] and as repeat localisation of the same fluorescence event are filtered out of our datasets prior to Ripley's K analysis.

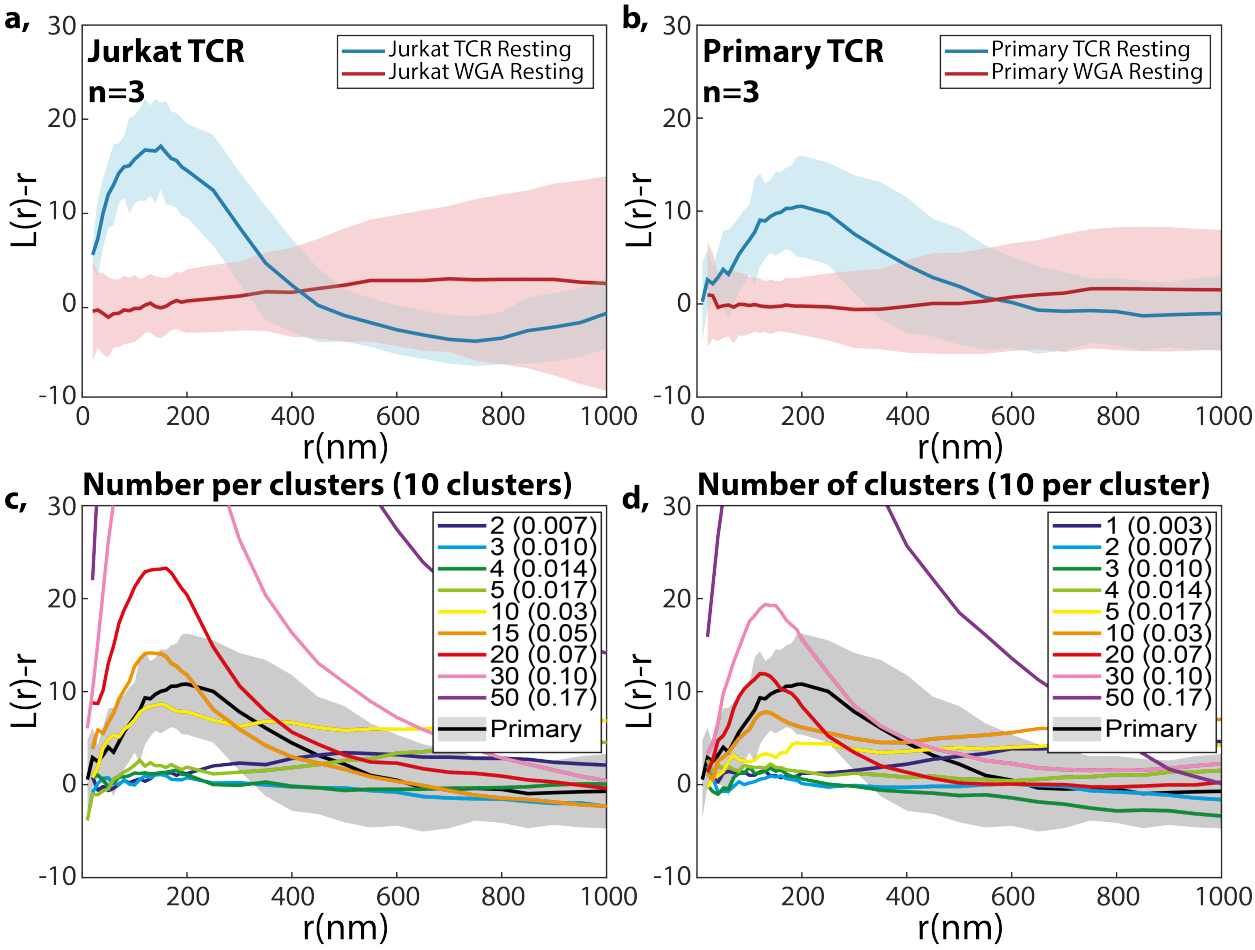

Fig. 6.20 Estimation of TCR clustering parameters by simulation of clustering in WGA data. (a) Mean and standard deviation of $L(r) - r$ for TCR and WGA molecules on the surface of resting Jurkat T cells. (b) Mean and standard deviation of $L(r) - r$ for TCR and WGA molecules on the surface of resting primary T cells. (c) $L(r) - r$ curves for WGA distributions from resting primary cells with 10 additional clusters randomly placed on the outer membrane with varying number of molecules per cluster. The $L(r) - r$ distribution of TCR on resting primary T cells is overlaid in black. (d) $L(r) - r$ curves for WGA distributions from resting primary cells with additional clusters containing 10 points randomly placed on the outer membrane with varying number of added clusters. The $L(r) - r$ distribution of TCR on resting primary T cells is overlaid in black.

6.7 Discussion

The DHPSF allows for direct observation of a significant fraction of biological samples to be imaged in a single focal plane. We have shown 3D-SMLM imaging of membrane-bound targets in Jurkat and primary T cells by fab labelling and imaging in a PALM mode. The DHPSF reports localisation of approximately 50% of the expected number of localisations of the TCR. As shown in figure 6.15, Ripley's K analysis should be capable of quantifying the clustering state of a protein even in subsampled distributions. Therefore the DHPSF is expected to be compatible with direct observation and quantification of the distribution of membrane-bound proteins on T cells. We have also shown high-density imaging of the outer membrane of Jurkat and primary T cells by PA-PAINT imaging of WGA tagged with a photoactivatable fluorophore. The combination of these two methodologies allow for the spatial distribution of important proteins involved with immunological activation of T cells to be directly imaged in the resting state.

6.7.1 PAINT Imaging with the DHPSF

The DHPSF is compatible with high-density large-volume imaging in a PAINT mode, as demonstrated by WGA PAINT labelling of the outer membrane of whole Jurkat T cells. Approximately one million localisations were recorded across whole-cell volumes. To our knowledge this is the first example of PAINT imaging with the DHPSF. This was achieved without complicated excitation-confinement techniques, with HILO illumination. This was facilitated by the use of a photoactivatable fluorophore in a new methodology referred to as PA-PAINT. Compared to PAINT imaging, PA-PAINT has the advantages of reducing background fluorescence and providing the ability to control the localisation rate with the power density of the 405 nm activation illumination. The reduction in background fluorescence occurs as, when using HILO illumination or other excitation-confinement techniques, fluorophores outside of the depth of focus are unlikely to be fluorescently active. This reduces the need for ultra-thin excitation confinement in order to employ 3D SMLM techniques, significantly reducing experimental complexity. The activation efficiency of the chosen photoactivatable fluorophore is not important as PAINT labelling provides a theoretically infinite number of fluorescent events the target distribution.

PA-PAINT provides an elegant solution for background reduction and control of localisation rate for implementations of PAINT labelling in which a fluorophore is bound

to the labelling probe. The SNR of DNA-PAINT [39] imaging was also improved with the introduction of photoactivatable fluorophores for PA-DNA-PAINT imaging in neuronal cells. PA-PAINT as a general methodology enables PAINT labelling strategies to be employed for 3D-SMLM techniques without the need for additional excitation-confinement techniques. This allows for standard sample geometries to be imaged in 3D with high SNR and experimentally-feasible localisation rates.

6.7.2 High-Density Whole-Cell Imaging of Jurkat Morphology

The whole-cell membrane imaging presented in figures 6.9 and 6.11 are examples of imaging facilitated by PA-PAINT. In this imaging, significant differences in morphology were observed between Jurkat T cells that were fixed in a resting state in suspension compared to those fixed after contacting PLL-coated coverslip surface. Resting Jurkat cells displayed an increased number of small pseudopodia compared to regions of the membrane away from the surface in Jurkat cell contacting PLL surfaces. Large-scale spreading of the membrane was observed at the contact between Jurkat cells and the PLL-coated surface. This could be attributed to the charge interaction between the PLL and membrane acting to pull the cell towards the surface. A similar spreading out was observed in Jurkat T cells at activating-coated surface in chapter 5 as well as in literature [171]. These data are consistent with recent publications that report that PLL-coated surfaces perturb the resting state of T cells [150, 151]. We believe that that is the first example of high-density DHPSF imaging of whole eukaryotic cells, achieving image quality that is in-line with the current state of 3D-SMLM [82, 146].

Dynamic 3D rendering of the datasets presented in figures 6.9 and 6.11 are presented in the digital appendix of this thesis. In collaboration with Imagination, a creative agency specialising in virtual reality (VR), we are developing a stand-alone program to visualise 3D-SMLM datasets in VR titled 'Project LUME'. Project LUME allows the user to explore datasets intuitively in an truly 3D environment. Examples of this are also attached in the digital appendix of this thesis. Project LUME will be freely distributed upon completion as a tool for any groups outputting 3D-SMLM datasets.

6.7.3 Multi-Target Imaging with the DHPSF

Sequential DHPSF imaging of the TCR and outer membrane in Jurkat and primary T cells was presented. The same fluorophore was used to label both targets, eliminating aberration caused by the differing emission spectra of different fluorophores. However, there is not reason that the DHPSF cannot be used for multi-target imaging employing multiple fluorophores, as previously demonstrated by the Moerner group [105].

Two-colour SMLM datasets of the position of the TCR and outer membrane were aligned by their position relative to fiducial markers that were present in both sequential acquisitions, creating a map of the TCR relative to membrane structure over a $\sim$4 μm section of Jurkat and primary T cells. The high localisation density of the membrane dataset was able to resolve membrane nanostructure such as pseudopodia, that was not obvious from the TCR dataset alone. Pseudopodia were mostly observed with co-localised TCR molecules, although some pseudopodia were observed without TCR localisations. This suggests that the presence of the TCR is not necessary for pseudopodia to occur.

As shown in chapter 5, it is possible to fit mesh surfaces to 3D localisation datasets. The high-density of WGA localisations should allow for fitted meshes to resolve nanostructure and act as super-resolved volumetric representation of the cell volume. In this case, it would be possible to quantitatively describe and identify membrane nanostructure, separating pseudopodia from the cell body. Unfortunately, current methodologies developed for fitting volumes to point location datasets (*e.g.* LIDAR mapping of real-world spaces) struggle to fit the outer membrane due to erroneous localisations that are present in the datasets. In these cases the fitted meshes either contain a large amount of noise, over fitting to sparse points outside the cell volume, or do not resolve membrane nanostructure but provide an approximation of the overall cell shape. Work continues towards robust and accurate mesh fitting to 3D-SMLM datasets, although a method that is compatible with batch processing of multiple cells has not yet been accomplished.

6.7.4 Quantification of Clustering in 3D by Ripley's K Analysis

Ripley's K analysis was implemented for analysis of 3D-SMLM datasets in MATLAB. The input of these functions were datasets containing the x, y and z coordinates of the distribution of interest and an 'unlclustered' distribution of the same geometry. The relative density of the number of localisations within a sphere or radius r from each point was then compared

between the two distributions to create a plot of $L(r) - r$. Simulated clustered and unclustered distributions on the apical surface of a sphere with a range of clustering parameters were used to verify the analysis. The fraction of points within clusters was identified as a key metric for cluster identification, although other factors such as the number of clusters and number of points per cluster were observed to affect the ability of Ripley's K analysis to identify clustering. Simulated distributions with as low as 4% of clustered points could be identified as significantly different from unclustered distributions.

The analysis was tested on a model distribution of the TCR on the surface of T cells using clustering parameters determined by a previous 2D study of TCR clustering at PLL-coated surfaces in Jurkat T cells [278]. In this case, Ripley's K analysis was able to identify clustering from randomly subsampled datasets with as low as 500 points across a $\sim$50 μm^2 area surface, corresponding to an approximately six-fold lower density than observed in recorded TCR datasets. Thus Ripley's K analysis was verified to be a suitable tool for identifying clustering in 3D, even low-expression targets such as the TCR.

It was determined that the geometry of the distribution of interest can have a significant effect on the ability to identify clustering by Ripley's K analysis, as the number of neighbours within a set distance of a point is closely related to the geometry. A mismatch in geometry between input distributions can lead to perceived clustering or anticlustering of CSR distributions and thus the unclustered control distribution used for comparison should follow the same underlying geometry as the distribution of interest. This consideration is especially important for imaging away from the coverslip where the intrinsic 3D nature of biological samples makes it unlikely that flat geometries are present. At the coverslip, the presence of ruffles in the membrane can lead to misidentification of clustering states. This effect can be reduced by adhering the outer membrane of cell samples to the coverslip to create an artificial flat surface, however, this may affect the behaviour of surface proteins [150, 151]. Even in fixed cells contacting PLL-coated surfaces, distortion of the outer membrane was observed as the bottom of cells was flattened out by the charge attraction to the surface.

The ability of the DHPSF to image above the coverslip surface without significant spherical aberration (see chapter 3) allows for the distribution of membrane-bound proteins to be studied under more physiological conditions, away from interactions with coated-surfaces. Membrane nanostructure was typically observed to be on the order of 500 nm, which is comparable to the depth of focus of other commonly-used 3D-SMLM techniques ($\sim$500 nm for Astigmatism and Biplane). As a result, these techniques would not be capable of representing the apical surface of T cells in a single image plane, requiring focal-

plane scanning methodologies to faithfully reconstruct the morphology of the T-cell outer membrane. Due to the increased depth of focus of the DHPSF compared to these techniques, a significant fraction of the T-cell outer membrane could be captured by a single image plane, reducing experimental complexity. By implementing duel-labelling of the TCR and the outer membrane the geometry of outer membrane could be determined independently to the position of the TCR. This reduces biases in model-distribution geometry that may be caused by potential preferential distribution of the TCR relative to certain regions of the membrane and decouples the localisation density of the TCR from the geometry of unclustered distributions for comparison in Ripley's K analysis.

6.7.5 Quantification of the Clustering State of the TCR in Jurkat and Primary T Cells

The clustering state of membrane-bound TCRs was quantified at the apical surface of Jurkat and primary T cells by Ripley's K analysis of dual-labelling 3D-SMLM datasets of the position of the TCR relative to WGA bound to the outer membrane. The position of the TCR was input to the written analysis as the distribution of interest. The position of WGA was randomly subsampled to match the localisation density and input as an unclustered control. WGA data is expected to be unclustered as WGA binds to N-Acetylglucosamine residues that are highly abundant across T-cell membrane proteins. A study of the carbohydrate pattern on Vero kidney epithelial cells labelled by WGA and imaged by dSTORM in 2D observed that WGA bound to the outer membrane in nanoscale regions that were obviously visible by eye [280]. However, no such regions were observed in any recorded WGA dataset and uniform membrane labelling by WGA was reported but not quantified by another study employing WGA for high-density imaging of membrane surfaces by 3D-SMLM [82]. The clustering state of WGA is expected to remain constant between Jurkat and the primary T cells as they exhibit a similar distribution of membrane-protein expression, allowing for a direct comparison between Jurkat and primary T-cell samples. Once mesh fitting to WGA datasets is achieved, it will be possible to simulate a true CSR distribution with geometry matched to the T-cell outer membrane. This will facilitate an unbiased unclustered model distribution for use in Ripley's K analysis, decoupling the $L(r) - r$ of the TCR from potential clustering that may be present in the distribution of WGA.

The performance of the methodology and analysis was verified by imaging the TCR at the coverslip surface of Jurkat T cells contacting PLL-coated surfaces, repeating a previous study

employing Ripley's K analysis of 2D PALM imaging of the TCR [278]. The results of this study were reproduced, with significant clustering of the TCR observed and corresponding $L(r) - r$ curves closely matching (see appendix A).

A significant increase in TCR clustering was observed between TCR at PLL-coated surfaces and on cells fixed in suspension. A low but significant level of clustering was observed in T cells fixed in suspension. It has been theorised that PLL can compress pockets between PLL-coated surfaces and the outer T-cell membrane caused by membrane nanostructure [151], artificially clustering nearby molecules as the membrane is pulled into close contact with the surface. Additionally, PLL-coated surfaces have been shown to have an activating effect on T cells by immobilisation of the TCR [150], which is known to result in membrane-protein redistribution towards clustering [218, 206, 216]. Our results support the notion that PLL-coated surfaces can cause a redistribution of T-cell membrane proteins from the resting state. Imaging T cells away from coated surfaces may provide more physiological conditions for the study of mechanisms relating to immune-response triggering. Although this is not always possible, the DHPSF represents a suitable tool for imaging and tracking applications in non-flat geometries.

Primary T cells fixed in suspension were observed to exhibit a comparable level of TCR clustering to Jurkat T cells fixed in suspension. This suggests that the distribution of TCR on the surface of Jurkat cells is a good representation of that in primary cells. In both cases, the $L(r) - r$ of the TCR was significantly different to WGA, indicating increased clustering. Incubation with primary and secondary TCR antibodies during fab-(PA-JF549) labelling did not have a significant effect on perceived clustering of the TCR. This is not entirely surprising as there is no evidence in literature to suggest that large-scale clusters would be created. It has been shown that the phosphorylation of 1-2 TCR molecules can initiate immunological triggering in T cells [258], suggesting that it is possible for early-stage immunological activation to occur without the formation of large TCR clusters. It is possible that longer incubation times would lead to large-scale clustering, although when this was attempted T cells became stressed or did not survive, increasing intrinsic background fluorescence when imaging to unmanageable levels.

Ideally, additional T-cell membrane proteins would be imaged with the same methodology to provide additional controls and more information on the overall protein distribution of the outer T-cell membrane. Monomeric proteins such as CD2 could provide a useful unclustered control sample. Unfortunately, the necessity of a HaloTag to increase the activation efficiency of PA-JF549 limits the available antibodies and fabs that can be used. Currently, we only have

access to anti-CD3 fabs fused to a HaloTag, however, the Davis group is working to produce additional HaloTag-fabs to label CD2 and CD45. It would also be extremely useful to image a known clustered control to calibrate the performance of the methodology. Clathrin-coated pits on the outer membrane could serve as a clustered control that is compatible with WGA membrane imaging, providing they can be labelled by a HaloTag.

6.7.6 Advantages and Disadvantages of the Methodology and Future Plans

The imaging methodology presented in this chapter is the able to record the distribution of membrane proteins, away from unphysiological coated surfaces, relative to membrane nanostructure. Employing a photoactivatable organic dye (PA-JF549) over current photoactivatable fluorescent proteins provides high SNR PALM imaging of a significant fraction of labelled proteins (estimated to be $\sim$90% [69]). This should facilitate robust stoichiometry measurements of cluster size, however, the activation efficiency of PA-JF549 is known to be sensitive to its environment. In order to determine the activation efficiency under the experimental conditions presented, a target of known stoichiometry should be imaged under the same conditions. However, this also requires a HaloTag to be present for a fair comparison to be made. We are currently searching for a suitable target of known stoichiometry to calibrate the detection efficiency of the methodology in order to facilitate absolute stoichiometric measurements. A potential candidate is the nuclear pore complex, which is comprised of eight identical subunits [281].

PALM imaging is advantageous for the study of clustering and stoichiometry compared to STORM as it is less prone to over-counting artefacts caused by repeated florescence events from each fluorophore. In STORM imaging, each fluorophore exhibits multiple fluorescence events before photobleaching as it switches between emissive and nonemissive states. The number of events depends on the imaging conditions and follows a normal distribution that can span an order of magnitude [41]. In low-stoichiometry samples, it is impossible to decouple the number of targets present within the localisation precision from the blinking kinetics of the fluorophore as the variation in events is comparable to the number of molecules. Although photoactivatable fluorophores can display fluorescence intermittency, significantly fewer fluorescence events are observed compared to STORM imaging (a mean of 2.8 events are observed from individual mEos fluorescent proteins [65] and a mean of 1.4 events are observed for PA-JF549 [69]). A recent study employing dSTORM imaging of AlexaFluor647

estimated that the TCR was clustered at the surface of naïve lymph node-resident T cells with approximately 10 TCRs per cluster [121]. The average number of events per antibody was measured to be $\sim$20, however, in some cases individual antibodies were observed to exhibit >100 fluorescent events. Although $\sim$50% of the number of expected TCR localisations were observed by our methodology, individual clusters of $\sim$10 proteins should be able to be identified by the DHPSF providing a sufficient fraction of the overall distribution is clustered. However, the analysis presented in figure 6.20 estimates that $\sim$10% of TCRs are clustered, making this unlikely to be distinguishable above the background unclustered population.

Quantification of the outer-membrane morphology should allow for robust analysis of the spatial distribution of membrane-bound protein. Such analysis may provide information on the functional role of the membrane nanostructure for T-cell immune-response triggering. Mesh fitting of WGA datasets in order to represent cell volumes is the current focus of this project. As previously mentioned, a recent study determined that $\sim$90% of membrane-bound TCR molecules were associated with membrane nanostructure in primary T cells [201]. In this study, primary T cells were labelled with anti TCR$\alpha\beta$ antibodies tagged with Alexa647 and fixed in suspension. After fixation, the outer membrane was fluorescently stained at bulk concentration. The position of the outer membrane was determined with diffraction-limited imaging laterally and sub-diffraction precision axially by variable-angle TIRF. The TCR was then imaged by 2D in two axial planes by TIRF illumination.This methodology allows for the position of the TCR to be inferred relative to membrane nanostructure but may lead to biases towards detection of fluorophores closer to the coverslip. In contrast the methodology presented for duel-imaging of the TCR and outer membrane in this chapter directly measures both the position of the TCR and membrane nanostructure in 3D under the same imaging conditions. This allows for unbiased measurement of the relative density of TCR molecules associated with membrane nanostructure and the cell body. We have not yet been able to automate nanostructure identification to quantify the relative density between the two populations. By eye, the TCR appears homogeneously distributed across the outer membrane, with no obvious preferential association with nanostructure in Jurkat and primary T cells. Accurate mesh fitting to WGA datasets should allow for regions of nanostructure to be identified by local curvature of the fitted mesh. If this is realised, the relative density of TCR localisations could be directly quantified between the two regions using the fitted mesh as a measure of membrane area.

The key drawback of the presented labelling methodology is the requirement of a HaloTag to increase the activation efficiency of PA-JF549. In high expression targets or PAINT labelling the activation efficiency of the fluorophore is less important. However, for low-

expression targets such as the TCR, high detection efficiency is necessary to properly represent the population.

Another issue with the methodology is low throughput caused by a reduced field of view from HILO illumination and extended acquisition times for PA-PAINT. This is exacerbated by the increased size of the DHPSF compared to other imaging PSFs as a lower localisation density is required for isolated PSFs to occur. Due to the excellent brightness of PA-JF549 compared to other photoactivatable fluorophores, the photon-splitting nature of the DHPSF and the reduced collection efficiency of water-immersion objective lenses compared to oil-immersion objective lenses was not a limiting factor. Experiments were optimised to provide maximum SNR by tuning the excitation power density so that PA-JF549 molecules were typically emissive for one frame after activation. A mean and standard deviation of 2,900$\pm$700 photons were detected from each PA-JF549 molecule from the imaging conditions presented in this chapter, corresponding to an expected localisation precision of $\sim$10-12 nm laterally and $\sim$20-27 nm laterally (see chapter 2). However, for initial WGA PAINT imaging without a photoactivatable fluorophore, the increased depth of focus of the DHPSF compared to 2D imaging caused a significant increase in detected background, making traditional PAINT labelling impractical.

A novel method to improve the SNR of PAINT imaging with the use of a photoactivatable fluorophore and HILO excitation was demonstrated. For the applications demonstrated in this chapter, the activation efficiency of the fluorophore was not important as the activation illumination power density could be increased to tune the localisation rate to optimal levels. Therefore, no HaloTag was required to increase activation efficiency of PA-JF549 and standard NHS ester labelling of WGA was sufficient. The improvement in SNR was not quantified as in order to achieve low enough background signal for DHPSF imaging by traditional PAINT less than one localisation per second was observed, making high-density imaging unfeasible. PA-PAINT allowed for >30 localisations per second to be recorded from a single T cell with minimal background signal. In fact, the factor limiting localisation rate was overlapping PSFs rather than SNR.

6.8 Concluding Remarks

The work presented in this chapter represents the first implementation of the DHPSF for high-density imaging and quantification of the spatial distribution of proteins in eukaryotic cells. We have developed a methodology capable of localising a significant fraction of the total number of T-cell membrane proteins relative to 3D membrane nanostructure in a single focal plane. Fiducial markers immobilised on the surface of agarose beads facilitate multi-target imaging away from the coverslip with extended acquisition times by continuous drift correction and the alignment of multiple datasets, without the need for the focal plane to be moved.

This methodology allows for quantification of the clustering state of T-cell membrane proteins on non-flat surfaces, away from the influence of unphysiological coated surfaces. The datasets produced are compatible with quantification of the relationship between the spatial distribution of the membrane-bound proteins and membrane nanostructure, once membrane nanostructure identification can be automated.

Further imaging of T-cell membrane-bound targets is planned once additional antibodies including HaloTags are completed. This will provide a more complete description of the resting-state surface distribution of T cells.

6.9 Methodology

Preparation of WGA-(PA-JF549)

WGA (L9640, sigma) was labelled with PA-JF549-NHS ester (6149, Tocris). 100 μM PA-JF549-NHS ester was added to 26 μM WGA in filtered (0.22 μm Millex-GP syringe filter unit, Millipore) phosphate-buffered saline (PBS) (molecular mass 150–300 kDa; P4832, Sigma) was supplemented with 0.1 M sodium bicarbonate (Sigma). The solution was reacted at room temperature for 2 hours in darkness. Labelled WGA was then separated using a Bio-Spin P-6 gel column (Bio-Rad).

Preparation of TCR Fab-(PA-JF549)

UCHT-1 (anti CD3) – HaloTag fab at was diluted to 40 μM in filtered PBS before incubation with 200 μM Halo ligand-(PA-JF549) (gift from Marco di Antonio) for 1 hour in room temperature and in darkness. Labelled fab was then separated using a Bio-Spin P-6 gel column (Bio-Rad).

Sample Preparation with Fiducial Markers Immobilised above the Coverslip

100 μL of 50 μm diameter agarose beads (20349, ThermoFisher) were incubated with poly-L-lysine (molecular mass 150–300 kDa; P4832, Sigma) in a 1:1 ratio for 10 minutes. The beads were centrifuged at 1500$\times g$ for 1 min) and washed three times with filtered PBS. The beads were then incubated with fluorescent nanodiamonds (798134, Sigma) in a 1:1 ratio for 10 minutes at room temperature. The labelled beads were then washed three times with PBS via centrifugation and were resuspended in 100 μL of PBS.

Coverslips (22$\times$22 mm borosilicate, thickness No. 1, VWR) were heated to 37°C. 3 μL of labelled agarose beads and 25 μL of labelled cells were added and allowed to equilibrate. 50 μL a 1% solution of pre-warmed agarose in filtered PBS was added to the coverslip and allowed to settle for 10 minutes. The sample was then cooled to room temperature before 50 μL of filtered PBS was added on top of the set agarose.

Imaging the TCR in Jurkat and Primary T Cells

$\sim 10^6$ T cells were labelled with 200 nM of the labelled TCR-(PA-JF549) fabS on ice for 25 minutes. Cells were then washed three times in filtered PBS (involving centrifugation). Labelled T cells were fixed in 4% paraformaldehyde (Sigma) and 0.2% glutaraldehyde (Sigma) for 60 minutes at room temperature. The fixed cells were washed three times in filtered PBS and suspended in filtered PBS. This was conducted in Cambridge for Jurkat T cells and Oxford, by Dr Mafalda Santos, for primary T cells. Fixed primary T cells were transported to Cambridge on ice and imaged over the next 1-2 days. Immediately prior to imaging, cells were then added to samples with fiducial markers as described above.

The sample was imaged with a 1.27 NA 60x water-immersion objective lens (Plan Apo VC 60x, Nikon). A quadband dichroic and longpasss and bandpass filters were used to separate the emission signal (Di01-R405/488/561/ 635-25x36, and BLP02-561R-25 and FF01-580/14-25, respectively, Semrock) before the detector. Fixed T cells were imaged for until no more fluorescence events were observed, typically >30,000 frames with continuous 561 nm (at a power density of $\sim$5 kW/cm^2, measured before the objective lens) and 405 nm HILO excitation and a 30 ms exposure. DHPSF fitting was conducted with easy-DHPSF [210] in MATLAB. After reconstruction, a rolling-mean of the fiducial marker's position over 50 frames was used to correct for drift in x, y and z.

Imaging WGA on the Out Membrane by PA-PAINT

The sample was prepared as above with or without labelling the TCR. If the TCR was labelled, WGA imaging was conducted after TCR imaging as described above. 50 μm of a 1:500 dilution of WGA-(PA-JF54) in filtered PBS was added on top of the T-cell sample contained within agarose with immobilised fiducial markers. The sample was left to equilibrate for at least 30 minutes. The sample was then imaged with a 1.27 NA 60x water-immersion objective lens (Plan Apo VC 60x, Nikon). A quadband dichroic and longpasss and bandpass filters were used to separate the emission signal (Di01-R405/488/561/ 635-25x36, and BLP02-561R-25 and FF01-580/14-25, respectively, Semrock) before the detector. 100,000 frames with continuous 561 nm (at a power density of $\sim$5 kW/cm^2, measured before the objective lens) and 405 nm HILO excitation and a 30 ms exposure were recorded for duel-labelling experiments. The axial position of the focal plane was maintained relative to a fiducial marker via a piezo motor controlled by an auto-focus script written by Dr Aleks Ponjavic

in beanshell. DHPSF fitting was conducted with easy-DHPSF [210] in MATLAB. After reconstruction, a rolling-mean of the fiducial marker's position over 50 frames was used to correct for drift in x, y and z and align the dataset to the corresponding TCR dataset for duel-labelling experiments.

Whole-Cell Membrane Imaging by PA-PAINT

$\sim 10^6$ Jurkat T cells were fixed in 4% paraformaldehyde and 0.2% glutaraldehyde for 60 minutes at room temperature. The fixed cells were washed three times in filtered PBS and suspended in filtered PBS. The unlabelled cells prepared as described above, with fluorescent nanodiamonds immobilised above the surface.

The sample was then imaged with a 1.27 NA 60x water-immersion objective lens (Plan Apo VC 60x, Nikon). A quadband dichroic and longpasss and bandpass filters were used to separate the emission signal (Di01-R405/488/561/ 635-25x36, and BLP02-561R-25 and FF01-580/14-25, respectively, Semrock) before the detector. Continuous 561 nm (at a power density of $\sim$5 kW/cm^2, measured before the objective lens) and 405 nm HILO excitation was incident on the sample. The focal plane was axially scanned through the sample in 3–3.5 μm steps via the piezo-mounted objective, with each position containing at least one fiducial marker. 200,000 frames were acquired at 30 ms exposure at each position before moving to the next position. The axial position of the focal plane was maintained relative to fiducial markers via a piezo motor controlled by an auto-focus script written by Dr Aleks Ponjavic in beanshell. DHPSF fitting was conducted with easy-DHPSF [210] in MATLAB. After reconstruction, a rolling-mean of the fiducial marker's position over 50 frames was used to correct for drift in x, y and z. The resulting localisations were aligned across the whole cell by their position relative to fiducial markers that were present in sequential focal planes.

Chapter 7

Conclusion

7.1 Thesis Summary

This thesis has described the development and characterisation of a microscopy platform implementing 3D localisation microscopy with a double-helix point spread function (DHPSF) for application in mammalian cell samples. In chapter 2, the stability of the instrument was measured under experimentally relevant conditions and compatible illumination geometries and labelling methods were developed. Chapter 3 describes the quantification of aberration caused by Fourier-plane misalignment and spherical aberration present when imaging away from the coverslip surface, and the development of methods to reduce these effects facilitate large-volume imaging with the DHPSF.

After optimisation the platform was applied to imaging large eukaryotic cell volumes. This demonstrated, for the first time, the application of both single-particle tracking (SPT) and super-resolution imaging modalities to non-flat geometries and to traditionally technically demanding areas of biological samples. A number of different biological questions were addressed and presented in chapters 4-6.

In chapter 4 2D diffusion analysis methods were extended for use with 3D SPT. Tracking of targets at the apical membrane of T cells and within the nucleus of embryonic stem cells demonstrated the capability of the DHPSF for tracking applications [147]. This was the first application of the DHPSF for SPT in mammalian cells.

In chapter 5 a range of super-resolution imaging and quantification applications are presented. These applications include whole-cell membrane-protein quantification in T

cells, cytoplasmic-protein imaging in HeLa and HEK cells and imaging synaptic proteins in mouse-brain slices. These studies were facilitated by the extended depth of field of the DHPSF compared to typical 3D single-molecule localisation microscopy (SMLM) methods.

Finally, chapter 6 describes quantification of the organisation of the T-cell receptor (TCR) on the outer membrane of Jurkat and primary T cells. The extended depth of focus of the DHPSF enabled clustering analysis to be conducted in a physiologically relevant environment, away from flat coated-surfaces. Duel-labelling of the TCR and the outer membrane allowed for the effect of surface morphology to be separated from perceived clustering by Ripley's K analysis. This analysis showed that the TCR is less clustered in the resting state than previously reported [52, 278, 121].

7.2 Concluding Discussion

This work represents a number of key steps in the development of the DHPSF as a technique. Previously, the DHPSF had only been used to investigate volumes directly adjacent to coverslip surfaces in biological samples [101, 100, 106, 103, 105, 104]. Although the effect of spherical aberration had been investigated by Ghosh and Preza [168], its influence had not been mitigated for biological imaging, limiting the potential applications of the DHPSF. By applying the findings of Hell *et. al.* (1993) on the effect of refractive index mismatch between objective lens immersion liquid and sample media on spherical aberration [172, 173], a simple solution to reduce spherical aberration in the DHPSF was identified. A water-immersion objective lens was employed to reduce this refractive index mismatch, and thus spherical aberration, facilitating imaging deep into biological samples with the DHPSF for the first time.

Single-Particle Tracking

The first application of the DHPSF to SPT in mammalian cells was demonstrated [147]. Imaging away from the surface allowed membrane proteins to be tracked as they diffuse over the complex topography of the apical membrane surface of T cells, which often exceeds the depth of field of common 3D-SMLM techniques such as Biplane and Astigmatism ($\sim$500 nm). Nuclear proteins are notoriously difficult targets for SPT due to their fast 3D diffusion, often resulting in the protein of interest leaving the depth of field before

sufficiently long track lengths can be recorded. 2D-SPT studies in the nucleus have been able to quantify residence time of binding events [154, 177] but have struggled to accurately measure diffusion coefficients. I have demonstrated that the DHPSF is capable of recording extended trajectories that are compatible with MSD analysis for typical nuclear-protein diffusion coefficients. The comparable depth of field of Multifocus Microscopy (MFM) has also been shown to facilitate nuclear-protein tracking in mammalian cells [93]. Compared to Astigmatism and Biplane methods, the large depth of field of the DHPSF and MFM represent some of the most well-suited solutions for 3D-SPT away from coverslip surfaces, sacrificing imaging density or field of view, respectively.

Single-Molecule Localisation Microscopy

In this work I have presented the first example of whole-cell imaging in mammalian cell samples with the DHPSF [147]. Previous DHPSF publications relied on single image planes, without stitching together neighbouring planes. The increased depth of field of the DHPSF compared to Astigmatism and Biplane reduced the number of planes required to cover an entire cell volume by approximately 8-fold. Recently, whole-cell 3D-SMLM has been demonstrated with a 4Pi single-molecule switching nanoscopy (W-4PiSMSN) methodology across a range of cell samples [146]. Since the work presented in chapter 5, multiple DHPSF image planes have been recorded with light sheet illumination to image large volumes ($\sim$6 μm) in HeLa cells [108].

I have also presented the first implementation of the DHPSF for 3D-SMLM in tissue samples by imaging the synaptic protein PSD95 in mouse brain slices. Imaging in tissue samples can be preferable as they represent a more physiological environment than cultured cells. Now that the DHPSF has been shown to be compatible, it can be considered for a wider range of biological studies in which the increased depth of field may be beneficial.

A novel variant of PAINT labelling employing photoactivatable (PA) fluorophores was also presented in the form of PA-PAINT. PA-PAINT reduces background signal that arises from excited unbound fluorophores, significantly increasing the achievable localisation rate. As a result, PAINT methodologies become compatible with large-volume imaging techniques such as the DHPSF without the need for complicated excitation geometry confinement. This methodology would also be compatible with DNA-PAINT labelling, increasing single-to-noise ratio (SNR) and acquisition speed similarly to FRET-PAINT methodologies [72, 71]. PA-PAINT facilitated high-density whole-cell imaging of the outer membrane of Jurkat T

cells, bringing the DHPSF closer to some of the most sophisticated large-volume 3D-SMLM publications [82, 146].

The diverse applications presented in this thesis (SPT of membrane-bound, cytoplasmic and nuclear proteins as well as membrane-protein quantification in T cells, cytoplasmic-protein imaging in HeLa and HEK cells and imaging synaptic proteins in mouse-brain tissue) demonstrate the ubiquity of the DHPSF when combined with a water-immersion objective lens to investigate biological samples.

Quantification of Resting Clustering State of the T-Cell Receptor

In this work, the T-cell receptor (TCR) was determined to be less clustered than previously thought in resting Jurkat and primary T cells, which has implications for the mechanism behind immune-response triggering. Previous studies claimed that the TCR existed in a clustered state in resting T cells [121, 268, 278] and was located preferentially at the tips of membrane protrusions [201]. In the analysis presented in chapter 6, which used duel labelling of the TCR and the outer membrane to distinguish the effect of surface morphology from perceived clustering, the TCR was found to be less clustered than previously reported. The DHPSF analysis is supported by a recent study published by Rossboth *et. al.* (2018), which employed a range of super-resolution techniques to determine that the TCR is randomly distributed on the plasma membrane of resting $CD4^+$ T cells [282]. Together these studies challenge the accepted paradigm of the resting T cell and have lead to the hypothesis that the random distribution of the TCR on the surface of help T cells would increase the likelihood of antigen recognition by maximising TCR-MHC on rates [282].

The methodology developed in chapter 6 was applied to the TCR but is equally compatible with investigating the clustering state of other T-cell membrane proteins. In fact, the methodology is applicable to cell types with an abundance of N-Acetylglucosamine present on the outer membrane to bind wheat-germ agglutinin (WGA). This work demonstrates that the underlying geometry of the distribution must be taken into account in order to provide accurate clustering metrics. A general approach to measure both the morphology of the outer membrane and the protein distribution across a significant portion of the cell without chromatic aberration is outlined, providing a platform to investigate protein distributions across a range of biological samples.

7.3 Future Perspectives

DHPSF Perspectives

While improvements in optical resolution are limited by current fluorescent probes and labelling methodologies, the development of improved cluster analysis and data fitting routines are areas where the DHPSF method could be progressed. As discussed in chapter 6, quantification of clustering analysis could be improved with the implementation of true complete spatial randomness (CSR) distributions that follow the morphology of the system. Such a distribution should follow the morphology of the system in order to be able achieve unbiased clustering metrics. Currently WGA localisations are considered as an unclustered control but CSR models could potentially be generated by mesh fitting to WGA localisation datasets.

Additionally, descriptive cluster analysis could be employed to better quantify the size and stoichiometry of nanoclusters that are present in certain membrane-protein distributions. The 3D Bayesian cluster analysis approach demonstrated by Griffie *et. al.* [127] should be compatible with the current methodology by considering WGA datasets as data specific unclustered models. This approached would also be improved by the creation of CSR model distributions from WGA datasets.

Another area with room for improvement is in fitting of raw DHPSF datasets. Currently, the only freely available fitting tool is easy-DHPSF [137]. Easy-DHPSF is slow compared to 2D fitting routines and does not include batch processing. User-defined thresholds are also required which can introduce bias between datasets. As discussed in chapter 2, new fitting methods outperformed easy-DHPSF at the 2016 Single-Molecule Localization Microscopy Symposium but have yet to be published or distributed.

Finally, the DHPSF method, like other super-resolution technologies, is limited by the availability of suitable fluorophores and labelling methods. Brighter and more photo-stable fluorophores allow for longer tracks to be recorded in SPT experiments and more robust statistical methods to be implemented. For PALM, developing photoactivatable fluorophores with high and reliable activation efficiency will allow for more accurate stoichiometry studies to be conducted. PA-JF549 has been demonstrated to achieve an activation efficiency of 90% [69] but is highly sensitive to its environment, limiting its application to targets that can be labelled with a HaloTag. Photoactivatable fluorophores that are insensitive to their

environment would expand the breadth of stoichiometry applications that could be probed by the DHPSF. For (d)STORM, recent developments in fluorophores that display inherent blinking behaviour, such as HMSiR [283], reduces the need for specific and typically toxic buffer solutions, facilitating live-cell STORM imaging [284]. Although these fluorophores have not yet been applied with the DHPSF, they could provide elegant solutions for tracking slow-evolving processes, such as the development of the immunological synapse in T cells, in 3D.

Biological Perspectives

A number of interesting problems in T-cell biology remain, such as the distribution of membrane-bound proteins on the surface of resting T cells or how the clustering state of the TCR evolves during activation. The DHPSF platform could be used to determine the observed clustering state of a range of T-cell membrane proteins. Initially, imaging of controls, including known monomers (*e.g.* CD2 [285]) and dimers (*e.g.* CD28 [199]) controls would enable quantification of the performance of analysis methods, isolating the perceived clustering caused by the photophysics of the fluorophore. Then, HaloTag antibodies for membrane-bound proteins, such as CD45, L-selectin and Linker for Activation of T cells (LAT), could be investigated to provide a more complete description of the surface of resting T cells.

The methodology could be used to track the evolution of the clustering state of the TCR (and other proteins) during T-cell activation by fixing T cells at different time points during activation. This could be achieved by activating T cells in solution with activating antibodies such as OKT3 or by contacting activating-coated surfaces. A comparison between these two cases could provide information on the importance of an immunological synapse for T-cell signalling.

Extending the methodology using photoactivatable DNA-PAINT (PA-DNA-PAINT) would facilitate the investigation of the distribution of many different targets in the same sample by Exchange-PAINT [162]. This would allow for direct comparison between the distributions of multiple membrane proteins on single cells. T cells have been shown to be highly sensitive to their environment and activation state, therefore more-complete maps of protein distribution across individual cells would provide insight into the origin of their heterogeneity.

Other biological applications include investigating the distribution of K-ras relative to the outer membrane of HeLa cells. Membrane-associated K-ras plays a key role in regulating cell proliferation and differentiation by acting as a switch for growth factors in the environment. An increase in the membrane-bound fraction of K-ras may indicate increased proliferation, as exhibited by cancerous cells. This hypothesis could be tested by quantification of the fraction of membrane-bound K-ras by sequentially imaging the outer membrane with WGA and the distribution of labelled K-ras in wildtype and cancerous-mutant cells.

Final Remarks

Looking forward more generally, the DHPSF will undoubtedly be applied to an increasing number of biological studies as it becomes more widely adopted. The work in this thesis supports its broad applicability and demonstrates some of the advantages afforded by the large depth of field. Currently the main factors limiting its adoption are the relative complexity of the additional optics compared to Astigmatic 3D-SMLM methods and slow data fitting. Once commercial solutions for the implementation of the DHPSF transformation are perfected and fitting routines are improved, the technique could become as common as Astigmatic and Biplane 3D SMLM.

Bibliography

[1] Richard Phillips Feynman. There's plenty of room at the bottom. *Engineering and Science*, 1960.

[2] E. Abbe. Beiträge zur Theorie des Mikroskops und der mikroskopischen Wahrnehmung. *Archiv für Mikroskopische Anatomie*, 9(1):413–418, dec 1873.

[3] Joseph W Goodman. *Introduction to Fourier optics*. Roberts and Company Publishers, 2005.

[4] Anish V Abraham, Sripad Ram, Jerry Chao, E S Ward, and Raimund J Ober. Quantitative study of single molecule location estimation techniques. *Optics express*, 17(26):23352–73, dec 2009.

[5] Andrés Santos and Ian T Young. Model-based resolution: applying the theory in quantitative microscopy. *Applied Optics*, 39(17):2948, jun 2000.

[6] Rayleigh. XXXI. Investigations in optics, with special reference to the spectroscope. *The London, Edinburgh, and Dublin Philosophical Magazine and Journal of Science*, 8(49):261–274, oct 1879.

[7] G. G. Stokes. On the Change of Refrangibility of Light. *Philosophical Transactions of the Royal Society of London*, 142(0):463–562, jan 1852.

[8] Jeff W Lichtman and José-Angel Conchello. Fluorescence microscopy. *Nature methods*, 2(12):910–9, dec 2005.

[9] Steven F Lee and Mark a Osborne. Brightening, blinking, bluing and bleaching in the life of a quantum dot: friend or foe? *Chemphyschem : a European journal of chemical physics and physical chemistry*, 10(13):2174–91, sep 2009.

[10] Chi-Cheng Fu, Hsu-Yang Lee, Kowa Chen, Tsong-Shin Lim, Hsiao-Yun Wu, Po-Keng Lin, Pei-Kuen Wei, Pei-Hsi Tsao, Huan-Cheng Chang, and Wunshain Fann. Characterization and application of single fluorescent nanodiamonds as cellular biomarkers. *Proceedings of the National Academy of Sciences*, 104(3):727–732, jan 2007.

[11] Elana M S Stennett, Monika a Ciuba, and Marcia Levitus. Photophysical processes in single molecule organic fluorescent probes. *Chemical Society reviews*, 43(4):1057–75, feb 2014.

[12] Charles A Janeway Jr, Paul Travers, Mark Walport, and Mark J Shlomchik. The structure of a typical antibody molecule. 2001.

[13] David P Bishop, Nerida Cole, Tracy Zhang, Philip A Doble, and Dominic J Hare. A guide to integrating immunohistochemistry and chemical imaging. *Chemical Society Reviews*, 47(11):3770–3787, 2018.

[14] Georgyi V Los, Lance P Encell, Mark G. McDougall, Danette D Hartzell, Natasha Karassina, Chad Zimprich, Monika G. Wood, Randy Learish, Rachel Friedman Ohana, Marjeta Urh, Dan Simpson, Jacqui Mendez, Kris Zimmerman, Paul Otto, Gediminas Vidugiris, Ji Zhu, Aldis Darzins, Dieter H Klaubert, Robert F Bulleit, and Keith V Wood. HaloTag: A Novel Protein Labeling Technology for Cell Imaging and Protein Analysis. *ACS Chemical Biology*, 3(6):373–382, jun 2008.

[15] Antje Keppler, Susanne Gendreizig, Thomas Gronemeyer, Horst Pick, Horst Vogel, and Kai Johnsson. A general method for the covalent labeling of fusion proteins with small molecules in vivo. *Nature Biotechnology*, 21(1):86–89, jan 2003.

[16] Britta Barlag, Oliver Beutel, Dennis Janning, Frederik Czarniak, Christian P Richter, Carina Kommnick, Vera Göser, Rainer Kurre, Florian Fabiani, Marc Erhardt, et al. Single molecule super-resolution imaging of proteins in living salmonella enterica using self-labelling enzymes. *Scientific reports*, 6:31601, 2016.

[17] Mark A Hink, Remko A Griep, Jan Willem Borst, Arie van Hoek, Michel HM Eppink, Arjen Schots, and Antonie JWG Visser. Structural dynamics of green fluorescent protein fused with a single chain fv protein. *Journal of Biological Chemistry*, 2000.

[18] Bo Huang, Mark Bates, and Xiaowei Zhuang. Super-resolution fluorescence microscopy. *Annual review of biochemistry*, 78:993–1016, jan 2009.

[19] Kyu Young Han, Katrin I Willig, Eva Rittweger, Fedor Jelezko, Christian Eggeling, and Stefan W Hell. Three-dimensional stimulated emission depletion microscopy of nitrogen-vacancy centers in diamond using continuous-wave light. *Nano letters*, 9(9):3323–9, sep 2009.

[20] Ke Xu, Hazen P Babcock, and Xiaowei Zhuang. Dual-objective STORM reveals three-dimensional filament organization in the actin cytoskeleton. *Nature methods*, 9(2):185–8, feb 2012.

[21] Stefan W. Hell and Jan Wichmann. Breaking the diffraction resolution limit by stimulated emission: stimulated-emission-depletion fluorescence microscopy. *Optics Letters*, 19(11):780, jun 1994.

[22] Thomas A. Klar and Stefan W. Hell. Subdiffraction resolution in far-field fluorescence microscopy. *Optics Letters*, 24(14):954, jul 1999.

[23] Giuseppe Vicidomini, Paolo Bianchini, and Alberto Diaspro. STED super-resolved microscopy. *Nature Methods*, 15(3):173–182, jan 2018.

[24] Stefan W Hell. Fluorescence nanoscopy: Breaking the diffraction barrier by the RESOLFT concept. *NanoBiotechnology*, 1(3):296–297, sep 2005.

[25] Joshua C Vaughan and Xiaowei Zhuang. New fluorescent probes for super-resolution imaging. *Nature biotechnology*, 29(10):880, 2011.

[26] V Westphal, M a Lauterbach, a Di Nicola, and S W Hell. Dynamic far-field fluorescence nanoscopy. *New Journal of Physics*, 9(12):435–435, dec 2007.

[27] Volker Westphal, Silvio O Rizzoli, Marcel A Lauterbach, Dirk Kamin, Reinhard Jahn, and Stefan W Hell. Video-Rate Far-Field Optical Nanoscopy Dissects Synaptic Vesicle Movement. *Science*, 320(5873):246–249, apr 2008.

[28] M G L Gustafsson. Surpassing the lateral resolution limit by a factor of two using structured illumination microscopy. *Journal of Microscopy*, 198(January):82–87, 2000.

[29] M. G. L. Gustafsson. Nonlinear structured-illumination microscopy: Wide-field fluorescence imaging with theoretically unlimited resolution. *Proceedings of the National Academy of Sciences*, 102(37):13081–13086, sep 2005.

[30] Eric Betzig, George H Patterson, Rachid Sougrat, O Wolf Lindwasser, Scott Olenych, Juan S Bonifacino, Michael W Davidson, Jennifer Lippincott-schwartz, and Harald F Hess. Imaging Intracellular Fluorescent Proteins at Nanometer Resolution. *Science*, 313(September):1642–1646, 2006.

[31] Samuel T Hess, Thanu P K Girirajan, and Michael D Mason. Ultra-high resolution imaging by fluorescence photoactivation localization microscopy. *Biophysical journal*, 91(11):4258–72, dec 2006.

[32] Michael J Rust, Mark Bates, and Xiaowei Zhuang. Sub-diffraction-limit imaging by stochastic optical reconstruction microscopy (STORM). *Nature methods*, 3(10):793–5, oct 2006.

[33] Seamus J Holden, Stephan Uphoff, and Achillefs N Kapanidis. DAOSTORM: an algorithm for high- density super-resolution microscopy. *Nature methods*, 8(4):279–80, apr 2011.

[34] Sean a McKinney, Christopher S Murphy, Kristin L Hazelwood, Michael W Davidson, and Loren L Looger. A bright and photostable photoconvertible fluorescent protein. *Nature methods*, 6(2):131–3, feb 2009.

[35] Colin Echeverría Aitken, R Andrew Marshall, and Joseph D Puglisi. An oxygen scavenging system for improvement of dye stability in single-molecule fluorescence experiments. *Biophysical journal*, 94(5):1826–35, mar 2008.

[36] Ivan Rasnik, Sean a McKinney, and Taekjip Ha. Nonblinking and long-lasting single-molecule fluorescence imaging. *Nature methods*, 3(11):891–3, nov 2006.

[37] Mike Heilemann, Sebastian van de Linde, Anindita Mukherjee, and Markus Sauer. Super-resolution imaging with small organic fluorophores. *Angewandte Chemie (International ed. in English)*, 48(37):6903–8, jan 2009.

[38] Alexey Sharonov and Robin M Hochstrasser. Wide-field subdiffraction imaging by accumulated binding of diffusing probes. *Proceedings of the National Academy of Sciences*, 103(50):18911–18916, dec 2006.

[39] Ralf Jungmann, Christian Steinhauer, Max Scheible, Anton Kuzyk, Philip Tinnefeld, and Friedrich C. Simmel. Single-Molecule Kinetics and Super-Resolution Microscopy by Fluorescence Imaging of Transient Binding on DNA Origami. *Nano Letters*, 10(11):4756–4761, nov 2010.

[40] Mark Bates, Bo Huang, Graham T Dempsey, and Xiaowei Zhuang. Multicolor super-resolution imaging with photo-switchable fluorescent probes. *Science (New York, N.Y.)*, 317(5845):1749–53, 2007.

[41] Mike Heilemann, Sebastian Van De Linde, Mark Schüttpelz, Robert Kasper, Britta Seefeldt, Anindita Mukherjee, Philip Tinnefeld, and Markus Sauer. Subdiffraction-resolution fluorescence imaging with conventional fluorescent probes. *Angewandte Chemie - International Edition*, 47(33):6172–6176, 2008.

[42] Nicholas A. Frost, Hari Shroff, Huihui Kong, Eric Betzig, and Thomas A. Blanpied. Single-Molecule Discrimination of Discrete Perisynaptic and Distributed Sites of Actin Filament Assembly within Dendritic Spines. *Neuron*, 67(1):86–99, jul 2010.

[43] Stephan Uphoff and David J Sherratt. Single-molecule analysis of bacterial dna repair and mutagenesis. *Annual review of biophysics*, 46:411–432, 2017.

[44] Steven F Lee, Michael A Thompson, Monica A Schwartz, Lucy Shapiro, and WE Moerner. Super-resolution imaging of the nucleoid-associated protein hu in caulobacter crescentus. *Biophysical journal*, 100(7):L31–L33, 2011.

[45] Jerod L Ptacin, Steven F Lee, Ethan C Garner, Esteban Toro, Michael Eckart, Luis R Comolli, WE Moerner, and Lucy Shapiro. A spindle-like apparatus guides bacterial chromosome segregation. *Nature cell biology*, 12(8):791, 2010.

[46] Boerries Brandenburg, Lily Y Lee, Melike Lakadamyali, Michael J Rust, Xiaowei Zhuang, and James M Hogle. Imaging poliovirus entry in live cells. *PLoS biology*, 5(7):e183, 2007.

[47] Adish Dani, Bo Huang, Joseph Bergan, Catherine Dulac, and Xiaowei Zhuang. Superresolution imaging of chemical synapses in the brain. *Neuron*, 68(5):843–856, 2010.

[48] Anna Löschberger, Sebastian van de Linde, Marie-Christine Dabauvalle, Bernd Rieger, Mike Heilemann, Georg Krohne, and Markus Sauer. Super-resolution imaging visualizes the eightfold symmetry of gp210 proteins around the nuclear pore complex and resolves the central channel with nanometer resolution. *J Cell Sci*, 125(3):570–575, 2012.

[49] Min Wu, Bo Huang, Morven Graham, Andrea Raimondi, John E Heuser, Xiaowei Zhuang, and Pietro De Camilli. Coupling between clathrin-dependent endocytic budding and F-BAR-dependent tubulation in a cell-free system. *Nature cell biology*, 12(9):902–8, sep 2010.

[50] Kuo Chinkei and Robin M Hochstrasser. Super-resolution Microscopy of Lipid Bilayer Phases. *J. Am. Chem. Soc.*, 133(13):4664–4667, 2012.

[51] Marie N. Bongiovanni, Julien Godet, Mathew H. Horrocks, Laura Tosatto, Alexander R. Carr, David C. Wirthensohn, Rohan T. Ranasinghe, Ji-Eun Lee, Aleks Ponjavic, Joelle V. Fritz, Christopher M. Dobson, David Klenerman, and Steven F. Lee. Multi-dimensional super-resolution imaging enables surface hydrophobicity mapping. *Nature Communications*, 7:13544, dec 2016.

[52] Björn F Lillemeier, Manuel A Mörtelmaier, Martin B Forstner, Johannes B Huppa, Jay T Groves, and Mark M Davis. Tcr and lat are expressed on separate protein islands on t cell membranes and concatenate during activation. *Nature immunology*, 11(1):90, 2010.

[53] Malte Renz, Brian R Daniels, György Vámosi, Irwin M Arias, and Jennifer Lippincott-Schwartz. Plasticity of the asialoglycoprotein receptor deciphered by ensemble fret imaging and single-molecule counting palm imaging. *Proceedings of the National Academy of Sciences*, page 201211753, 2012.

[54] Marco Scarselli, Paolo Annibale, and Aleksandra Radenovic. Cell type-specific β2-adrenergic receptor clusters identified using photoactivated localization microscopy are not lipid raft related, but depend on actin cytoskeleton integrity. *Journal of Biological Chemistry*, 287(20):16768–16780, 2012.

[55] David Lando, Ulrike Endesfelder, Harald Berger, Lakxmi Subramanian, Paul D Dunne, James McColl, David Klenerman, Antony M Carr, Markus Sauer, Robin C Allshire, et al. Quantitative single-molecule microscopy reveals that cenp-acnp1 deposition occurs during g2 in fission yeast. *Open biology*, 2(7):120078, 2012.

[56] D Axelrod, Thomas P Burghardt, and N L Thompson. Total Internal Reflection Fluorescence. *Annual Review of Biophysics and Bioengineering*, 13(1):247–268, jun 1984.

[57] Alexa L Mattheyses, Sanford M Simon, and Joshua Z Rappoport. Imaging with total internal reflection fluorescence microscopy for the cell biologist. *Journal of Cell Science*, 123(21):3621–3628, nov 2010.

[58] Makio Tokunaga, Naoko Imamoto, and Kumiko Sakata-Sogawa. Highly inclined thin illumination enables clear single-molecule imaging in cells. *Nature Methods*, 5(2):159–161, feb 2008.

[59] Catherine A. Konopka and Sebastian Y. Bednarek. Variable-angle epifluorescence microscopy: a new way to look at protein dynamics in the plant cell cortex. *The Plant Journal*, 53(1):186–196, jan 2008.

[60] Ying S. Hu, Maxwell Zimmerley, Yu Li, Robin Watters, and Hu Cang. Single-Molecule Super-Resolution Light-Sheet Microscopy. *ChemPhysChem*, 15(4):577–586, mar 2014.

[61] Jörg Gerhard Ritter, Roman Veith, Andreas Veenendaal, Jan Peter Siebrasse, and Ulrich Kubitscheck. Light Sheet Microscopy for Single Molecule Tracking in Living Tissue. *PLoS ONE*, 5(7):e11639, jul 2010.

[62] G. H. Patterson. A Photoactivatable GFP for Selective Photolabeling of Proteins and Cells. *Science*, 297(5588):1873–1877, sep 2002.

[63] J. Wiedenmann, S. Ivanchenko, F. Oswald, F. Schmitt, C. Rocker, A. Salih, K.-D. Spindler, and G. U. Nienhaus. EosFP, a fluorescent marker protein with UV-inducible green-to-red fluorescence conversion. *Proceedings of the National Academy of Sciences*, 101(45):15905–15910, nov 2004.

[64] Konstantin A. Lukyanov, Dmitry M. Chudakov, Sergey Lukyanov, and Vladislav V. Verkhusha. Photoactivatable fluorescent proteins. *Nature Reviews Molecular Cell Biology*, 6(11):885–890, nov 2005.

[65] Nela Durisic, Lara Laparra-Cuervo, Ángel Sandoval-Álvarez, Joseph Steven Borbely, and Melike Lakadamyali. Single-molecule evaluation of fluorescent protein photoactivation efficiency using an in vivo nanotemplate. *Nature Methods*, 11(2):156–162, jan 2014.

[66] Mingshu Zhang, Hao Chang, Yongdeng Zhang, Junwei Yu, Lijie Wu, Wei Ji, Juanjuan Chen, Bei Liu, Jingze Lu, Yingfang Liu, Junlong Zhang, Pingyong Xu, and Tao Xu. Rational design of true monomeric and bright photoactivatable fluorescent proteins. *Nature Methods*, 9(7):727–729, jul 2012.

[67] P. Annibale, M. Scarselli, A. Kodiyan, and A. Radenovic. Photoactivatable Fluorescent Protein mEos2 Displays Repeated Photoactivation after a Long-Lived Dark State in the Red Photoconverted Form. *The Journal of Physical Chemistry Letters*, 1(9):1506–1510, may 2010.

[68] Vladimir N. Belov, Gyuzel Yu Mitronova, Mariano L. Bossi, Vadim P. Boyarskiy, Elke Hebisch, Claudia Geisler, Kirill Kolmakov, Christian A. Wurm, Katrin I. Willig, and Stefan W. Hell. Masked Rhodamine Dyes of Five Principal Colors Revealed by Photolysis of a 2-Diazo-1-Indanone Caging Group: Synthesis, Photophysics, and Light Microscopy Applications. *Chemistry - A European Journal*, 20(41):13162–13173, oct 2014.

[69] Jonathan B. Grimm, Brian P. English, Heejun Choi, Anand K. Muthusamy, Brian P. Mehl, Peng Dong, Timothy A. Brown, Jennifer Lippincott-Schwartz, Zhe Liu, Timothée Lionnet, and Luke D. Lavis. Bright photoactivatable fluorophores for single-molecule imaging. *Nature Methods*, 13(12):985–988, 2016.

[70] Sebastian van de Linde, Ivan Krstić, Thomas Prisner, Sören Doose, Mike Heilemann, and Markus Sauer. Photoinduced formation of reversible dye radicals and their impact on super-resolution imaging. *Photochem. Photobiol. Sci.*, 10(4):499–506, 2011.

[71] Alexander Auer, Maximilian T. Strauss, Thomas Schlichthaerle, and Ralf Jungmann. Fast, Background-Free DNA-PAINT Imaging Using FRET-Based Probes. *Nano Letters*, 17(10):6428–6434, oct 2017.

[72] Jongjin Lee, Sangjun Park, Wooyoung Kang, and Sungchul Hohng. Accelerated super-resolution imaging with FRET-PAINT. *Molecular Brain*, 10(1):63, dec 2017.

[73] T Dertinger, R Colyer, G Iyer, S Weiss, and J Enderlein. Fast, background-free, 3D super-resolution optical fluctuation imaging (SOFI). *Proceedings of the National Academy of Sciences*, 106(52):22287–22292, dec 2009.

[74] Eran A. Mukamel, Hazen Babcock, and Xiaowei Zhuang. Statistical deconvolution for superresolution fluorescence microscopy. *Biophysical Journal*, 102(10):2391–2400, 2012.

[75] Susan Cox, Edward Rosten, James Monypenny, Tijana Jovanovic-Talisman, Dylan T Burnette, Jennifer Lippincott-Schwartz, Gareth E Jones, and Rainer Heintzmann. Bayesian localization microscopy reveals nanoscale podosome dynamics. *Nature methods*, 9(2):195, 2012.

[76] Nils Gustafsson, Siân Culley, George Ashdown, Dylan M. Owen, Pedro Matos Pereira, and Ricardo Henriques. Fast live-cell conventional fluorophore nanoscopy with ImageJ through super-resolution radial fluctuations. *Nature Communications*, 7:12471, aug 2016.

[77] C.E. Shannon. Communication in the Presence of Noise. *Proceedings of the IRE*, 37(1):10–21, jan 1949.

[78] Niccolò Banterle, Khanh Huy Bui, Edward A. Lemke, and Martin Beck. Fourier ring correlation as a resolution criterion for super-resolution microscopy. *Journal of Structural Biology*, 183(3):363–367, sep 2013.

[79] Steffen J Sahl, Francisco Balzarotti, Jan Keller-Findeisen, Marcel Leutenegger, Volker Westphal, Alexander Egner, Flavie Lavoie-Cardinal, Andriy Chmyrov, Tim Grotjohann, and Stefan Jakobs. Comment on "Extended-resolution structured illumination imaging of endocytic and cytoskeletal dynamics". *Science*, 352(6285):527.1–527, apr 2016.

[80] Dong Li and Eric Betzig. Response to Comment on "Extended-resolution structured illumination imaging of endocytic and cytoskeletal dynamics". *Science*, 352(6285):527.2–527, apr 2016.

[81] Robert P J Nieuwenhuizen, Keith A. Lidke, Mark Bates, Daniela Leyton Puig, David Grünwald, Sjoerd Stallinga, and Bernd Rieger. Measuring image resolution in optical nanoscopy. *Nature Methods*, 10(6):557–562, jun 2013.

[82] Wesley R Legant, Lin Shao, Jonathan B Grimm, Timothy A Brown, Daniel E Milkie, Brian B Avants, Luke D Lavis, and Eric Betzig. High-density three-dimensional localization microscopy across large volumes. *Nature Methods*, 13(4):359–365, mar 2016.

[83] Alex Von Diezmann, Yoav Shechtman, and W. E. Moerner. Three-Dimensional Localization of Single Molecules for Super-Resolution Imaging and Single-Particle Tracking. *Chemical Reviews*, 117(11):7244–7275, 2017.

[84] Alex Small and Shane Stahlheber. Fluorophore localization algorithms for super-resolution microscopy. *Nature methods*, 11(3):267–79, mar 2014.

[85] Russell E Thompson, Daniel R Larson, and Watt W Webb. Precise nanometer localization analysis for individual fluorescent probes. *Biophysical journal*, 82(5):2775–83, may 2002.

[86] B. Hein, K. I. Willig, and S. W. Hell. Stimulated emission depletion (STED) nanoscopy of a fluorescent protein-labeled organelle inside a living cell. *Proceedings of the National Academy of Sciences*, 105(38):14271–14276, sep 2008.

[87] Thomas a Planchon, Liang Gao, Daniel E Milkie, Michael W Davidson, James A Galbraith, Catherine G Galbraith, and Eric Betzig. Rapid three-dimensional isotropic imaging of living cells using Bessel beam plane illumination. *Nature Methods*, 8(5):417–423, may 2011.

[88] Liang Gao, Lin Shao, Christopher D. Higgins, John S. Poulton, Mark Peifer, Michael W. Davidson, Xufeng Wu, Bob Goldstein, and Eric Betzig. Noninvasive Imaging beyond the Diffraction Limit of 3D Dynamics in Thickly Fluorescent Specimens. *Cell*, 151(6):1370–1385, dec 2012.

[89] B.-C. Chen, W. R. Legant, K. Wang, L. Shao, D. E. Milkie, M. W. Davidson, C. Janetopoulos, X. S. Wu, J. A. Hammer, Z. Liu, B. P. English, Y. Mimori-Kiyosue, D. P. Romero, A. T. Ritter, J. Lippincott-Schwartz, L. Fritz-Laylin, R. D. Mullins, D. M. Mitchell, J. N. Bembenek, A.-C. Reymann, R. Bohme, S. W. Grill, J. T. Wang, G. Seydoux, U. S. Tulu, D. P. Kiehart, and E. Betzig. Lattice light-sheet microscopy: Imaging molecules to embryos at high spatiotemporal resolution. *Science*, 346(6208):1257998–1257998, oct 2014.

[90] Mathew H Horrocks, Matthieu Palayret, David Klenerman, and Steven F Lee. The changing point-spread function: single-molecule-based super-resolution imaging. *Histochemistry and Cell Biology*, 141(6):577–585, jun 2014.

[91] Manuel F Juette, Travis J Gould, Mark D Lessard, Michael J Mlodzianoski, Bhupendra S Nagpure, Brian T Bennett, Samuel T Hess, and Joerg Bewersdorf. Three-dimensional sub–100 nm resolution fluorescence microscopy of thick samples. *Nature Methods*, 5(6):527–529, jun 2008.

[92] Majid Badieirostami, Matthew D Lew, Michael a Thompson, and W E Moerner. Three-dimensional localization precision of the double-helix point spread function versus astigmatism and biplane. *Applied Physics Letters*, 97(16):161103, oct 2010.

[93] Sara Abrahamsson, Jiji Chen, Bassam Hajj, Sjoerd Stallinga, Alexander Y Katsov, Jan Wisniewski, Gaku Mizuguchi, Pierre Soule, Florian Mueller, Claire Dugast Darzacq, Xavier Darzacq, Carl Wu, Cornelia I Bargmann, David A Agard, Maxime Dahan, and Mats G L Gustafsson. Fast multicolor 3D imaging using aberration-corrected multifocus microscopy. *Nature Methods*, 10(1):60–63, dec 2012.

[94] G. Shtengel, J. A. Galbraith, C. G. Galbraith, J. Lippincott-Schwartz, J. M. Gillette, S. Manley, R. Sougrat, C. M. Waterman, P. Kanchanawong, M. W. Davidson, R. D. Fetter, and H. F. Hess. Interferometric fluorescent super-resolution microscopy resolves 3D cellular ultrastructure. *Proceedings of the National Academy of Sciences*, 106(9):3125–3130, mar 2009.

[95] Bo Huang, Wenqin Wang, Mark Bates, and Xiaowei Zhuang. Three-Dimensional Super-Resolution Imaging by Stochastic Optical Reconstruction Microscopy. *Science*, 319(5864):810–813, feb 2008.

[96] Adam Greengard, Yoav Y. Schechner, and Rafael Piestun. Depth from diffracted rotation. *Optics Letters*, 31(2):181, jan 2006.

[97] Sri Rama Prasanna Pavani and Rafael Piestun. High-efficiency rotating point spread functions. *Optics Express*, 16(5):3484, mar 2008.

[98] Sri Rama Prasanna Pavani and Rafael Piestun. Three dimensional tracking of fluorescent microparticles using a photon-limited double-helix response system. *Optics express*, 16(26):22048–22057, 2008.

[99] Sri Rama Prasanna Pavani, Michael A Thompson, Julie S Biteen, Samuel J Lord, Na Liu, Robert J Twieg, Rafael Piestun, and W E Moerner. Three-dimensional, single-molecule fluorescence imaging beyond the diffraction limit by using a double-helix point spread function. *Proceedings of the National Academy of Sciences*, 106(9):2995–2999, mar 2009.

[100] Michael A. Thompson, Matthew D. Lew, Majid Badieirostami, and W. E. Moerner. Localizing and Tracking Single Nanoscale Emitters in Three Dimensions with High Spatiotemporal Resolution Using a Double-Helix Point Spread Function. *Nano Letters*, 10(1):211–218, jan 2010.

[101] Michael a Thompson, Jason M Casolari, Majid Badieirostami, Patrick O Brown, and W E Moerner. Three-dimensional tracking of single mRNA particles in Saccharomyces cerevisiae using a double-helix point spread function. *Proceedings of the National Academy of Sciences of the United States of America*, 107(42):17864–71, oct 2010.

[102] Mikael P Backlund, Ryan Joyner, Karsten Weis, and WE Moerner. Correlations of three-dimensional motion of chromosomal loci in yeast revealed by the double-helix point spread function microscope. *Molecular biology of the cell*, 25(22):3619–3629, 2014.

[103] Ginni Grover, Sean Quirin, Callie Fiedler, and Rafael Piestun. Photon efficient double-helix PSF microscopy with application to 3D photo-activation localization imaging. *Biomedical optics express*, 2(11):3010–20, nov 2011.

[104] Matthew D Lew, Steven F Lee, Jerod L Ptacin, Marissa K Lee, and Robert J Twieg. Three-dimensional superresolution colocalization of intracellular protein superstructures and the cell surface in live Caulobacter crescentus. *PNAS*, 108(46):1102–1110, 2011.

[105] Andreas Gahlmann, Jerod L. Ptacin, Ginni Grover, Sean Quirin, Alexander R. S. von Diezmann, Marissa K. Lee, Mikael P. Backlund, Lucy Shapiro, Rafael Piestun, and W. E. Moerner. Quantitative Multicolor Subdiffraction Imaging of Bacterial Protein Ultrastructures in Three Dimensions. *Nano Letters*, 13(3):987–993, mar 2013.

[106] Hsiao-lu D. Lee, Steffen J. Sahl, Matthew D. Lew, and W. E. Moerner. The double-helix microscope super-resolves extended biological structures by localizing single blinking molecules in three dimensions with nanoscale precision. *Applied Physics Letters*, 100(15):153701, 2012.

[107] Jie Yu, Bo Cao, Heng Li, Bin Yu, Danni Chen, and Hanben Niu. Improved localization accuracy in double-helix point spread function super-resolution fluorescence microscopy using selective-plane illumination. *Proc. SPIE*, sep 2014.

[108] Anna-Karin Gustavsson, Petar N. Petrov, Maurice Y. Lee, Yoav Shechtman, and W. E. Moerner. 3D single-molecule super-resolution microscopy with a tilted light sheet. *Nature Communications*, 9(1):123, dec 2018.

[109] Matthew D Lew, Steven F Lee, Majid Badieirostami, and W E Moerner. Corkscrew point spread function for far-field three-dimensional nanoscale localization of pointlike objects. *Optics Letters*, 36(2):202, jan 2011.

[110] Shu Jia, Joshua C. Vaughan, and Xiaowei Zhuang. Isotropic three-dimensional super-resolution imaging with a self-bending point spread function. *Nature Photonics*, 8(4):302–306, mar 2014.

[111] David Baddeley, Mark B. Cannell, and Christian Soeller. Three-dimensional sub-100 nm super-resolution imaging of biological samples using a phase ramp in the objective pupil. *Nano Research*, 4(6):589–598, jun 2011.

[112] Yoav Shechtman, Steffen J. Sahl, Adam S. Backer, and W. E. Moerner. Optimal Point Spread Function Design for 3D Imaging. *Physical Review Letters*, 113(13):133902, sep 2014.

[113] Yoav Shechtman, Lucien E Weiss, Adam S Backer, Steffen J Sahl, and W E Moerner. Precise Three-Dimensional Scan-Free Multiple-Particle Tracking over Large Axial Ranges with Tetrapod Point Spread Functions. *Nano letters*, may 2015.

[114] S.-H. Lee, J. Y. Shin, A. Lee, and C. Bustamante. Counting single photoactivatable fluorescent molecules by photoactivated localization microscopy (PALM). *Proceedings of the National Academy of Sciences*, 109(43):17436–17441, oct 2012.

[115] A. Shivanandan, H. Deschout, M. Scarselli, and A. Radenovic. Challenges in quantitative single molecule localization microscopy. *FEBS Letters*, 588(19):3595–3602, oct 2014.

[116] H. Deschout, A. Shivanandan, P. Annibale, M. Scarselli, and A. Radenovic. Progress in quantitative single-molecule localization microscopy. *Histochemistry and Cell Biology*, 142(1):5–17, jul 2014.

[117] Prabuddha Sengupta, Tijana Jovanovic-Talisman, Dunja Skoko, Malte Renz, Sarah L. Veatch, and Jennifer Lippincott-Schwartz. Probing protein heterogeneity in the plasma membrane using PALM and pair correlation analysis. *Nature Methods*, 8(11):969–975, nov 2011.

[118] Dylan M. Owen, David J. Williamson, Astrid Magenau, and Katharina Gaus. Sub-resolution lipid domains exist in the plasma membrane and regulate protein diffusion and distribution. *Nature Communications*, 3(1):1256, jan 2012.

[119] Travis J. Gould, Samuel T. Hess, and Joerg Bewersdorf. Optical Nanoscopy: From Acquisition to Analysis. *Annual Review of Biomedical Engineering*, 14(1):231–254, aug 2012.

[120] Peter J. Diggle. On Parameter Estimation and Goodness-of-Fit Testing for Spatial Point Patterns. *Biometrics*, 35(1):87, mar 1979.

[121] Ying S Hu, Hu Cang, and Björn F Lillemeier. Superresolution imaging reveals nanometer- and micrometer-scale spatial distributions of T-cell receptors in lymph nodes. *Proceedings of the National Academy of Sciences*, 113(26):7201–7206, jun 2016.

[122] Matthew J. Broadhead, Mathew H. Horrocks, Fei Zhu, Leila Muresan, Ruth Benavides-Piccione, Javier DeFelipe, David Fricker, Maksym V. Kopanitsa, Rory R. Duncan, David Klenerman, Noboru H. Komiyama, Steven F. Lee, and Seth G N Grant. PSD95 nanoclusters are postsynaptic building blocks in hippocampus circuits. *Scientific Reports*, 6(1):24626, jul 2016.

[123] Martin Ester, Hans-Peter Kriegel, Jorg Sander, and Xiaowei Xu. A Density-Based Algorithm for Discovering Clusters in Large Spatial Databases with Noise. *AAAI-Press*, pages 226–231, mar 1996.

[124] Florian Levet, Eric Hosy, Adel Kechkar, Corey Butler, Anne Beghin, Daniel Choquet, and Jean-Baptiste Sibarita. SR-Tesseler: a method to segment and quantify localization-based super-resolution microscopy data. *Nature Methods*, 12(11):1065–1071, nov 2015.

[125] Leonid Andronov, Igor Orlov, Yves Lutz, Jean-Luc Vonesch, and Bruno P. Klaholz. ClusterViSu, a method for clustering of protein complexes by Voronoi tessellation in super-resolution microscopy. *Scientific Reports*, 6(1):24084, jul 2016.

[126] Patrick Rubin-Delanchy, Garth L. Burn, Juliette Griffié, David J. Williamson, Nicholas A. Heard, Andrew P. Cope, and Dylan M. Owen. Bayesian cluster identification in single-molecule localization microscopy data. *Nature Methods*, 12(11):1072–1076, nov 2015.

[127] Juliette Griffié, Leigh Shlomovich, David J. Williamson, Michael Shannon, Jesse Aaron, Satya Khuon, Garth L. Burn, Lies Boelen, Ruby Peters, Andrew P. Cope, Edward A. K. Cohen, Patrick Rubin-Delanchy, and Dylan M. Owen. 3D Bayesian cluster analysis of super-resolution data reveals LAT recruitment to the T cell synapse. *Scientific Reports*, 7(1):4077, dec 2017.

[128] Ralf Jungmann, Maier S. Avendaño, Mingjie Dai, Johannes B. Woehrstein, Sarit S. Agasti, Zachary Feiger, Avital Rodal, and Peng Yin. Quantitative super-resolution imaging with qPAINT. *Nature Methods*, 13(5):439–442, 2016.

[129] Maxime Dahan. Diffusion Dynamics of Glycine Receptors Revealed by Single-Quantum Dot Tracking. *Science*, 302(5644):442–445, oct 2003.

[130] A Yildiz. Myosin V Walks Hand-Over-Hand: Single Fluorophore Imaging with 1.5-nm Localization. *Science*, 300(5628):2061–2065, jun 2003.

[131] Carlas S. Smith, Stephan Preibisch, Aviva Joseph, Sara Abrahamsson, Bernd Rieger, Eugene Myers, Robert H. Singer, and David Grunwald. Nuclear accessibility of β-actin mRNA is measured by 3D single-molecule real-time tracking. *The Journal of Cell Biology*, 209(4):609–619, may 2015.

[132] Suliana Manley, Jennifer M Gillette, George H Patterson, Hari Shroff, Harald F Hess, Eric Betzig, and Jennifer Lippincott-Schwartz. High-density mapping of single-molecule trajectories with photoactivated localization microscopy. *Nature Methods*, 5(2):155–157, feb 2008.

[133] Gregory Giannone, Eric Hosy, Florian Levet, Audrey Constals, Katrin Schulze, Alexander I. Sobolevsky, Michael P. Rosconi, Eric Gouaux, Robert Tampe, Daniel Choquet, and Laurent Cognet. Dynamic superresolution imaging of endogenous proteins on living cells at ultra-high density. *Biophysical Journal*, 99(4):1303–1310, 2010.

[134] M.J. Saxton. Single-particle tracking: the distribution of diffusion coefficients. *Biophysical Journal*, 72(4):1744–1753, apr 1997.

[135] Laura Weimann, Kristina A. Ganzinger, James McColl, Kate L. Irvine, Simon J. Davis, Nicholas J. Gay, Clare E. Bryant, and David Klenerman. A Quantitative Comparison of Single-Dye Tracking Analysis Tools Using Monte Carlo Simulations. *PLoS ONE*, 8(5):e64287, may 2013.

[136] Alex Herbert. Single Molecule Light Microscopy ImageJ Plugins.

[137] Matthew D. Lew*, Alexander R. S. von Diezmann*, and W. E. Moerner. Easy-DHPSF open-source software for three-dimensional localization of single molecules with precision beyond the optical diffraction limit. *Protocol Exchange*, feb 2013.

[138] Daniel Sage, Hagai Kirshner, Thomas Pengo, Nico Stuurman, Junhong Min, Suliana Manley, and Michael Unser. Quantitative evaluation of software packages for single-molecule localization microscopy. *Nature methods*, (August 2014):1–12, jun 2015.

[139] Mark a Osborne. Small things bright and beautiful: Single molecule fluorescence detection. In *Davis, AG and Thompson, JMT (eds) ADVANCES IN NANOENGINEERING: ELECTRONICS, MATERIALS AND ASSEMBLY*, pages 283–312. Imperial College Pres, London, 2007.

[140] Jonathan B Grimm, Brian P English, Jiji Chen, Joel P Slaughter, Zhengjian Zhang, Andrey Revyakin, Ronak Patel, John J Macklin, Davide Normanno, Robert H Singer, Timothée Lionnet, and Luke D Lavis. A general method to improve fluorophores for live-cell and single-molecule microscopy. *Nature Methods*, 12(3):244–250, jan 2015.

[141] Fan Long, Shaoqun Zeng, and Zhen-li Huang. Localization-based super-resolution microscopy with an sCMOS camera part II: experimental methodology for comparing sCMOS with EMCCD cameras. *Optics Express*, 20(16):17741–59, jul 2012.

[142] Saumya Saurabh, Suvrajit Maji, and Marcel P. Bruchez. Evaluation of sCMOS cameras for detection and localization of single Cy5 molecules. *Optics Express*, 20(7):7338, mar 2012.

[143] R c Benson, R a Meyer, M e Zaruma, and G m McKhan. Cellular Autofluorescence - Is It Due To Flavins? *The Journal of Histochemistry and Cytochemsitry*, 27(1):44–48, 1979.

[144] Yasushi Sako, S Minoghchi, and Toshio Yanagida. Single-molecule imaging of EGFR signalling on the surface of living cells. *Nature cell biology*, 2(March):168–172, 2000.

[145] Dylan M. Owen, Carles Rentero, Jérémie Rossy, Astrid Magenau, David Williamson, Macarena Rodriguez, and Katharina Gaus. PALM imaging and cluster analysis of protein heterogeneity at the cell surface. *Journal of Biophotonics*, 3(7):446–454, feb 2010.

[146] Fang Huang, George Sirinakis, Edward S. Allgeyer, Lena K. Schroeder, Whitney C. Duim, Emil B. Kromann, Thomy Phan, Felix E. Rivera-Molina, Jordan R. Myers, Irnov Irnov, Mark Lessard, Yongdeng Zhang, Mary Ann Handel, Christine Jacobs-Wagner, C. Patrick Lusk, James E. Rothman, Derek Toomre, Martin J. Booth, and Joerg Bewersdorf. Ultra-High Resolution 3D Imaging of Whole Cells. *Cell*, 166(4):1028–1040, aug 2016.

[147] Alexander R. Carr, Aleks Ponjavic, Srinjan Basu, James McColl, Ana Mafalda Santos, Simon Davis, Ernest D. Laue, David Klenerman, and Steven F. Lee. Three-Dimensional Super-Resolution in Eukaryotic Cells Using the Double-Helix Point Spread Function. *Biophysical Journal*, 112(7):1444–1454, 2017.

[148] Stephen A. Lee, Aleks Ponjavic, Chanrith Siv, Steven F. Lee, and Julie S. Biteen. Nanoscopic Cellular Imaging: Confinement Broadens Understanding. *ACS Nano*, 10(9):8143–8153, sep 2016.

[149] Jeremy Adler, Andrew I Shevchuk, Pavel Novak, Yuri E Korchev, and Ingela Parmryd. Plasma membrane topography and interpretation of single-particle tracks. *Nature Methods*, 7(3):170–171, mar 2010.

[150] Ana Mafalda Santos, Aleks Ponjavic, Marco Fritzsche, Ricardo A Fernandes, Jorge Bernardino de la Serna, Martin J Wilcock, Falk Schneider, Iztok Urbančič, James McColl, Consuelo Anzilotti, Kristina A Ganzinger, Meike Aßmann, David Depoil, Richard J Cornall, Michael L Dustin, David Klenerman, Simon J Davis, Christian Eggeling, and Steven F Lee. Capturing resting T cells: the perils of PLL. *Nature Immunology*, 19(3):203–205, mar 2018.

[151] Aleks Ponjavic, James McColl, Alexander R. Carr, Ana Mafalda Santos, Klara Kulenkampff, Anna Lippert, Simon Davis, David Klenerman, and Steven F. Lee. Single-molecule light-sheet imaging of suspended T cells (accepted). *Biophysical Journal*, 112, 2018.

[152] A H Voie, D H Burns, and F A Spelman. Orthogonal-plane fluorescence optical sectioning: three-dimensional imaging of macroscopic biological specimens. *Journal of microscopy*, 170(Pt 3):229–36, jun 1993.

[153] Remi Galland, Gianluca Grenci, Ajay Aravind, Virgile Viasnoff, Vincent Studer, and Jean-Baptiste Sibarita. 3D high- and super-resolution imaging using single-objective SPIM. *Nature methods*, (August 2014), may 2015.

[154] J. Christof M. Gebhardt, David M. Suter, Rahul Roy, Ziqing W. Zhao, Alec R. Chapman, Srinjan Basu, Tom Maniatis, and X. Sunney Xie. Single-molecule imaging of transcription factor binding to DNA in live mammalian cells. *Nature Methods*, 10(5):421–426, mar 2013.

[155] J Durnin, J H Eberly, and J J Miceli. Comparison of Bessel and Gaussian beams. *Optics Letters*, 13(2):79, feb 1988.

[156] G. A. Siviloglou, J. Broky, A. Dogariu, and D. N. Christodoulides. Observation of accelerating Airy beams. *Physical review letters*, 99(21):213901, nov 2007.

[157] Tsung-li Liu, Srigokul Upadhyayula, Daniel E Milkie, Ved Singh, Kai Wang, Ian A Swinburne, Kishore R Mosaliganti, Zach M Collins, Tom W Hiscock, Jamien Shea, Abraham Q Kohrman, Taylor N Medwig, Daphne Dambournet, Ryan Forster, Brian Cunniff, Yuan Ruan, Hanako Yashiro, Steffen Scholpp, Elliot M Meyerowitz, Dirk Hockemeyer, David G Drubin, Benjamin L Martin, David Q Matus, Minoru Koyama, Sean G Megason, Tom Kirchhausen, and Eric Betzig. Observing the cell in its native state: Imaging subcellular dynamics in multicellular organisms. *Science*, 1392(April), 2018.

[158] C. Eggeling, J. Widengren, R. Rigler, and C. A. M. Seidel. Photobleaching of Fluorescent Dyes under Conditions Used for Single-Molecule Detection: Evidence of Two-Step Photolysis. *Analytical Chemistry*, 70(13):2651–2659, jul 1998.

[159] Christos Karathanasis, Franziska Fricke, Gerhard Hummer, and Mike Heilemann. Molecule Counts in Localization Microscopy with Organic Fluorophores. *ChemPhysChem*, 18(8):942–948, apr 2017.

[160] S. D. Fowler and P Greenspan. Application of Nile red, a fluorescent hydrophobic probe, for the detection of neutral lipid deposits in tissue sections: comparison with oil red O. *Journal of Histochemistry & Cytochemistry*, 33(8):833–836, aug 1985.

[161] Giacomo Diaz, Marta Melis, Barbara Batetta, Fabrizio Angius, and Angela Maria Falchi. Hydrophobic characterization of intracellular lipids in situ by Nile Red red/yellow emission ratio. *Micron*, 39(7):819–824, oct 2008.

[162] Ralf Jungmann, Maier S Avendaño, Johannes B. Woehrstein, Mingjie Dai, William M. Shih, and Peng Yin. Multiplexed 3D cellular super-resolution imaging with DNA-PAINT and Exchange-PAINT. *Nature Methods*, 11(3):313–318, feb 2014.

[163] Anne Beghin, Adel Kechkar, Corey Butler, Florian Levet, Marine Cabillic, Olivier Rossier, Gregory Giannone, Rémi Galland, Daniel Choquet, and Jean-Baptiste Sibarita. Localization-based super-resolution imaging meets high-content screening. *Nature Methods*, 14(12), 2017.

[164] Zhaojun Wang, Yanan Cai, Yansheng Liang, Xing Zhou, Shaohui Yan, Dan Dan, Piero R. Bianco, Ming Lei, and Baoli Yao. Single shot, three-dimensional fluorescence microscopy with a spatially rotating point spread function. *Biomedical Optics Express*, 8(12):5493–5506, 2017.

[165] Arthur Edelstein, Nenad Amodaj, Karl Hoover, Ron Vale, and Nico Stuurman. Computer Control of Microscopes Using μManager. In *Current Protocols in Molecular Biology*, number SUPPL. 92, pages 1–17. John Wiley & Sons, Inc., Hoboken, NJ, USA, oct 2010.

[166] Sohaib Abdul Rehman, Alexander R. Carr, Martin O. Lenz, Steven F. Lee, and Kevin O'Holleran. Maximizing the field of view and accuracy in 3D Single Molecule Localization Microscopy. *Optics Express*, 26(4):4631, feb 2018.

[167] Alex von Diezmann, Maurice Y. Lee, Matthew D. Lew, and W. E. Moerner. Correcting field-dependent aberrations with nanoscale accuracy in three-dimensional single-molecule localization microscopy. *Optica*, 2(11):985, nov 2015.

[168] Sreya Ghosh and Chrysanthe Preza. Characterization of a three-dimensional double-helix point-spread function for fluorescence microscopy in the presence of spherical aberration. *Journal of Biomedical Optics*, 18(3):036010, mar 2013.

[169] Wonshik Choi, Christopher Fang-Yen, Kamran Badizadegan, Seungeun Oh, Niyom Lue, Ramachandra R. Dasari, and Michael S. Feld. Tomographic phase microscopy. *Nature Methods*, 4(9):717–719, sep 2007.

[170] Joris J. J. Dirckx, Liesbeth C. Kuypers, and Willem F. Decraemer. Refractive index of tissue measured with confocal microscopy. *Journal of Biomedical Optics*, 10(4):044014, 2005.

[171] Michael Saitakis, Stéphanie Dogniaux, Christel Goudot, Nathalie Bufi, Sophie Asnacios, Mathieu Maurin, Clotilde Randriamampita, Atef Asnacios, and Claire Hivroz. Different TCR-induced T lymphocyte responses are potentiated by stiffness with variable sensitivity. *eLife*, 6:1–29, jun 2017.

[172] S. Hell, G. Reiner, C. Cremer, and E. H. K. Stelzer. Aberrations in confocal fluorescence microscopy induced by mismatches in refractive index. *Journal of Microscopy*, 169(3):391–405, mar 1993.

[173] H. Jacobsen and S. W. Hell. Effect of the specimen refractive index on the imaging of a confocal fluorescence microscope employing high aperture oil immersion lenses, 1995.

[174] Ryan McGorty, Joerg Schnitzbauer, Wei Zhang, and Bo Huang. Correction of depth-dependent aberrations in 3D single-molecule localization and super-resolution microscopy. *Optics Letters*, 39(2):275, jan 2014.

[175] Martin Booth, Débora Andrade, Daniel Burke, Brian Patton, and Mantas Zurauskas. Aberrations and adaptive optics in super-resolution microscopy. *Microscopy*, 64(4):251–261, aug 2015.

[176] Benjamin C. Coles, Stephen E. D. Webb, Noah Schwartz, Daniel J. Rolfe, Marisa Martin-Fernandez, and Valentina Lo Schiavo. Characterisation of the effects of optical aberrations in single molecule techniques. *Biomedical Optics Express*, 7(5):1755, may 2016.

[177] Ignacio Izeddin, Vincent Récamier, Lana Bosanac, Ibrahim I. Cissé, Lydia Boudarene, Claire Dugast-Darzacq, Florence Proux, Olivier Bénichou, Raphaël Voituriez, Olivier Bensaude, Maxime Dahan, and Xavier Darzacq. Single-molecule tracking in live cells reveals distinct target-search strategies of transcription factors in the nucleus. *eLife*, 3(3):1–27, jun 2014.

[178] G.J. Schütz, H. Schindler, and Th Schmidt. Single-molecule microscopy on model membranes reveals anomalous diffusion. *Biophysical Journal*, 73(2):1073–1080, aug 1997.

[179] Arnauld Sergé, Nicolas Bertaux, Hervé Rigneault, and Didier Marguet. Dynamic multiple-target tracing to probe spatiotemporal cartography of cell membranes. *Nature Methods*, 5(8):687–694, aug 2008.

[180] I.F. Sbalzarini and P. Koumoutsakos. Feature point tracking and trajectory analysis for video imaging in cell biology. *Journal of Structural Biology*, 151(2):182–195, aug 2005.

[181] Khuloud Jaqaman, Dinah Loerke, Marcel Mettlen, Hirotaka Kuwata, Sergio Grinstein, Sandra L. Schmid, and Gaudenz Danuser. Robust single-particle tracking in live-cell time-lapse sequences. *Nature Methods*, 5(8):695–702, aug 2008.

[182] Damien Alcor, Géraldine Gouzer, and Antoine Triller. Single-particle tracking methods for the study of membrane receptors dynamics. *European Journal of Neuroscience*, 30(6):987–997, sep 2009.

[183] Mark Goulian and Sanford M Simon. Tracking Single Proteins within Cells. *Biophysical Journal*, 79(4):2188–2198, oct 2000.

[184] Andreas Bruckbauer, Peter James, Dejian Zhou, Ji Won Yoon, David Excell, Yuri Korchev, Roy Jones, and David Klenerman. Nanopipette Delivery of Individual Molecules to Cellular Compartments for Single-Molecule Fluorescence Tracking. *Biophysical Journal*, 93(9):3120–3131, nov 2007.

[185] L S Barak and W W Webb. Diffusion of low density lipoprotein-receptor complex on human fibroblasts. *The Journal of cell biology*, 95(3):846–52, dec 1982.

[186] M.J. Saxton. Single-particle tracking: models of directed transport. *Biophysical Journal*, 67(5):2110–2119, nov 1994.

[187] Juan A. Varela, Julien P. Dupuis, Laetitia Etchepare, Agnès Espana, Laurent Cognet, and Laurent Groc. Targeting neurotransmitter receptors with nanoparticles in vivo allows single-molecule tracking in acute brain slices. *Nature Communications*, 7:10947, mar 2016.

[188] Michael J. Saxton and Ken Jacobson. SINGLE-PARTICLE TRACKING:Applications to Membrane Dynamics. *Annual Review of Biophysics and Biomolecular Structure*, 26(1):373–399, jun 1997.

[189] A. Sonnleitner, G.J. Schütz, and Thomas Schmidt. Free Brownian Motion of Individual Lipid Molecules in Biomembranes. *Biophysical Journal*, 77(5):2638–2642, nov 1999.

[190] Stefan Wieser, Manuel Moertelmaier, Elke Fuertbauer, Hannes Stockinger, and Gerhard J. Schütz. (Un)Confined Diffusion of CD59 in the Plasma Membrane Determined by High-Resolution Single Molecule Microscopy. *Biophysical Journal*, 92(10):3719–3728, may 2007.

[191] Stefan Wieser, Markus Axmann, and Gerhard J. Schütz. Versatile Analysis of Single-Molecule Tracking Data by Comprehensive Testing against Monte Carlo Simulations. *Biophysical Journal*, 95(12):5988–6001, dec 2008.

[192] J. P. Siebrasse, R. Veith, A. Dobay, H. Leonhardt, B. Daneholt, and U. Kubitscheck. Discontinuous movement of mRNP particles in nucleoplasmic regions devoid of chromatin. *Proceedings of the National Academy of Sciences*, 105(51):20291–20296, dec 2008.

[193] W Zhang, A Aubert, J.M. Gomez de Segura, M Karuppasamy, S Basu, A.S. Murthy, A Diamante, T.A. Drury, J Balmer, J Cramard, A.A. Watson, D Lando, S.F. Lee, M Palayret, S.L. Kloet, A.H. Smits, M.J. Deery, M Vermeulen, B Hendrich, D Klenerman, C Schaffitzel, I Berger, and E.D. Laue. The Nucleosome Remodeling and Deacetylase Complex NuRD Is Built from Preformed Catalytically Active Submodules. *Journal of Molecular Biology*, 428(14):2931–2942, jul 2016.

[194] Xavier Michalet and Andrew J. Berglund. Optimal diffusion coefficient estimation in single-particle tracking. *Physical Review E*, 85(6):061916, jun 2012.

[195] Carlo Manzo and Maria F. Garcia-Parajo. A review of progress in single particle tracking: from methods to biophysical insights. *Reports on Progress in Physics*, 78(12):124601, dec 2015.

[196] Thierry Savin and Patrick S. Doyle. Static and Dynamic Errors in Particle Tracking Microrheology. *Biophysical Journal*, 88(1):623–638, jan 2005.

[197] Andrew J. Berglund. Statistics of camera-based single-particle tracking. *Physical Review E*, 82(1):011917, jul 2010.

[198] Zachary B. Katz, Lucie Novotná, Amy Blount, and Björn F. Lillemeier. A cycle of Zap70 kinase activation and release from the TCR amplifies and disperses antigenic stimuli. *Nature Immunology*, 18(1):86–95, nov 2016.

[199] J. R. James, S. S. White, R. W. Clarke, A. M. Johansen, P. D. Dunne, D. L. Sleep, W. J. Fitzgerald, S. J. Davis, and D. Klenerman. Single-molecule level analysis of the subunit composition of the T cell receptor on live T cells. *Proceedings of the National Academy of Sciences*, 104(45):17662–17667, nov 2007.

[200] Jean-Louis Mege, Christian Capo, Anne-Marie Benoliel, Collette Foa, Rémy Galindo, and Pierre Bongrand. Quantification of cell surface roughness; a method for studying cell mechanical and adhesive properties. *Journal of Theoretical Biology*, 119(2):147–160, mar 1986.

[201] Yunmin Jung, Inbal Riven, Sara W Feigelson, Elena Kartvelishvily, Kazuo Tohya, Masayuki Miyasaka, Ronen Alon, and Gilad Haran. Three-dimensional localization of T-cell receptors in relation to microvilli using a combination of superresolution microscopies. *Proceedings of the National Academy of Sciences of the United States of America*, 113(40):E5916–E5924, 2016.

[202] Joanne Sloan-Lancaster, John Presley, Jan Ellenberg, Tetsuo Yamazaki, Jennifer Lippincott-Schwartz, and Lawrence E. Samelson. ZAP-70 Association with T Cell Receptor ζ (TCRζ): Fluorescence Imaging of Dynamic Changes upon Cellular Stimulation. *The Journal of Cell Biology*, 143(3):613–624, nov 1998.

[203] De-Min Zhu, Michael L Dustin, Christopher W Cairo, and David E Golan. Analysis of Two-Dimensional Dissociation Constant of Laterally Mobile Cell Adhesion Molecules. *Biophysical Journal*, 92(3):1022–1034, feb 2007.

[204] Peter Jönsson, Jennifer H. Southcombe, Ana Mafalda Santos, Jiandong Huo, Ricardo A. Fernandes, James McColl, Melissa Lever, Edward J. Evans, Alexander Hudson, Veronica T. Chang, Tomáš Hanke, Andrew Godkin, Paul D. Dunne, Mathew H. Horrocks, Matthieu Palayret, Gavin R. Screaton, Jan Petersen, Jamie Rossjohn, Lars Fugger, Omer Dushek, Xiao-Ning Xu, Simon J. Davis, and David Klenerman. Remarkably low affinity of CD4/peptide-major histocompatibility complex class II protein interactions. *Proceedings of the National Academy of Sciences*, 113(20):5682–5687, may 2016.

[205] Aoife O'Shaughnessy and Brian Hendrich. CHD4 in the DNA-damage response and cell cycle progression: not so NuRDy now. *Biochemical Society Transactions*, 41(3):777–782, jun 2013.

[206] P.Anton van der Merwe, Simon J. Davis, Andrey S. Shaw, and Michael L. Dustin. Cytoskeletal polarization and redistribution of cell-surface molecules during T cell antigen recognition. *Seminars in Immunology*, 12(1):5–21, feb 2000.

[207] Michael Speidel, Alexandr Jonáš, and Ernst-Ludwig Florin. Three-dimensional tracking of fluorescent nanoparticles with subnanometer precision by use of off-focus imaging. *Optics Letters*, 28(2):69, 2003.

[208] B Hajj, J Wisniewski, M El Beheiry, J J Chen, A Revyakin, C Wu, and M Dahan. Whole-cell, multicolor superresolution imaging using volumetric multifocus microscopy. *Proceedings of the National Academy of Sciences of the United States of America*, 111(49):17480–17485, 2014.

[209] Thomas J. Etheridge, Rémi L. Boulineau, Alex Herbert, Adam T. Watson, Yasukazu Daigaku, Jem Tucker, Sophie George, Peter Jönsson, Matthieu Palayret, David Lando, Ernest Laue, Mark A. Osborne, David Klenerman, Steven F. Lee, and Antony M.

Carr. Quantification of DNA-associated proteins inside eukaryotic cells using single-molecule localization microscopy. *Nucleic Acids Research*, 42(19):e146–e146, oct 2014.

[210] Matthew D Lew, Alexander von Diezmann, and W E Moerner. Easy-DHPSF open-source software for three-dimensional localization of single molecules with precision beyond the optical diffraction limit. *Protocol Exchange*, pages 1–29, 2015.

[211] Zeev Pancer and Max D Cooper. The evolution of adaptive immunity. *Annual review of immunology*, 24:497–518, jan 2006.

[212] Simon J Davis and P Anton van der Merwe. Lck and the nature of the T cell receptor trigger. *Trends in immunology*, 32(1):1–5, jan 2011.

[213] David N. Garboczi, Partho Ghosh, Ursula Utz, Qing R. Fan, William E. Biddison, and Don C. Wiley. Structure of the complex between human T-cell receptor, viral peptide and HLA-A2. *Nature*, 384(6605):134–141, nov 1996.

[214] Tadashi Yokosuka, Kumiko Sakata-Sogawa, Wakana Kobayashi, Michio Hiroshima, Akiko Hashimoto-Tane, Makio Tokunaga, Michael L Dustin, and Takashi Saito. Newly generated T cell receptor microclusters initiate and sustain T cell activation by recruitment of Zap70 and SLP-76. *Nature immunology*, 6(12):1253–62, dec 2005.

[215] John R James and Ronald D Vale. Biophysical mechanism of T-cell receptor triggering in a reconstituted system. *Nature*, 487(7405):64–9, jul 2012.

[216] Yair Razvag, Yair Neve-Oz, Julia Sajman, Meital Reches, and Eilon Sherman. Nanoscale kinetic segregation of TCR and CD45 in engaged microvilli facilitates early T cell activation. *Nature Communications*, 9(1):732, dec 2018.

[217] Geoff P O'Donoghue, Rafal M Pielak, Alexander a Smoligovets, Jenny J Lin, and Jay T Groves. Direct single molecule measurement of TCR triggering by agonist pMHC in living primary T cells. *eLife*, 2:e00778, jan 2013.

[218] Alice C N Brown, Stephane Oddos, Ian M. Dobbie, Juha-Matti Alakoskela, Richard M. Parton, Philipp Eissmann, Mark A A Neil, Christopher Dunsby, Paul M W French, Ilan Davis, and Daniel M. Davis. Remodelling of Cortical Actin Where Lytic Granules Dock at Natural Killer Cell Immune Synapses Revealed by Super-Resolution Microscopy. *PLoS Biology*, 9(9):e1001152, sep 2011.

[219] P. Anton van der Merwe and Omer Dushek. Mechanisms for T cell receptor triggering. *Nature Reviews Immunology*, 11(1):47–55, jan 2010.

[220] Michael Kazhdan, Matthew Bolitho, and Hugues Hoppe. Poisson Surface Reconstruction. *Proceedings of the Symposium on Geometry Processing*, pages 61–70, jun 2006.

[221] Michael Kazhdan and Hugues Hoppe. Screened poisson surface reconstruction. *ACM Transactions on Graphics*, 32(3):1–13, 2013.

[222] Francesca Finetti, Anna Onnis, and Cosima T. Baldari. Regulation of Vesicular Traffic at the T Cell Immune Synapse: Lessons from the Primary Cilium. *Traffic*, 16(3):241–249, mar 2015.

[223] Kaushik Choudhuri, Jaime Llodrá, Eric W Roth, Jones Tsai, Susana Gordo, Kai W Wucherpfennig, Lance C Kam, David L Stokes, and Michael L Dustin. Polarized release of T-cell-receptor-enriched microvesicles at the immunological synapse. *Nature*, 507(7490):118–123, feb 2014.

[224] Colin R. F. Monks, Benjamin a Freiberg, Hannah Kupfer, Noah Sciaky, and Abraham Kupfer. Three-dimensional segregation of supramolecular activation clusters in T cells. *Nature*, 395(6697):82–86, sep 1998.

[225] a Grakoui. The Immunological Synapse: A Molecular Machine Controlling T Cell Activation. *Science*, 285(5425):221–227, jul 1999.

[226] Simon J Davis and P Anton van der Merwe. The kinetic-segregation model: TCR triggering and beyond. *Nature immunology*, 7(8):803–9, aug 2006.

[227] Veronica T. Chang, Ricardo A. Fernandes, Kristina A. Ganzinger, Steven F. Lee, Christian Siebold, James McColl, Peter Jönsson, Matthieu Palayret, Karl Harlos, Charlotte H. Coles, E. Yvonne Jones, Yuan Lui, Elizabeth Huang, Robert J C Gilbert, David Klenerman, A. Radu Aricescu, and Simon J. Davis. Initiation of T cell signaling by CD45 segregation at 'close contacts'. *Nature Immunology*, 17(5):574–582, mar 2016.

[228] Olivier Leupin, Rossana Zaru, Thierry Laroche, Sabina Müller, and Salvatore Valitutti. Exclusion of CD45 from the T-cell receptor signaling area in antigen-stimulated T lymphocytes. *Current Biology*, 10(5):277–280, mar 2000.

[229] Catherine B. Carbone, Nadja Kern, Ricardo A. Fernandes, Enfu Hui, Xiaolei Su, K. Christopher Garcia, and Ronald D. Vale. In vitro reconstitution of T cell receptor-mediated segregation of the CD45 phosphatase. *Proceedings of the National Academy of Sciences*, 114(44):E9338–E9345, oct 2017.

[230] Yuliya Pylayeva-Gupta, Elda Grabocka, and Dafna Bar-Sagi. RAS oncogenes: weaving a tumorigenic web. *Nature Reviews Cancer*, 11(11):761–774, nov 2011.

[231] Ian A Prior, Paul D Lewis, and Carla Mattos. A comprehensive survey of ras mutations in cancer. *Cancer research*, 72(10):2457–2467, 2012.

[232] Fuquan Zhang and Jit Kong Cheong. The renewed battle against RAS-mutant cancers. *Cellular and Molecular Life Sciences*, 73(9):1845–1858, may 2016.

[233] Daniel Abankwa, Alemayehu A. Gorfe, and John F. Hancock. Ras nanoclusters: Molecular structure and assembly. *Seminars in Cell & Developmental Biology*, 18(5):599–607, oct 2007.

[234] Serena Muratcioglu, Tanmay S. Chavan, Benjamin C. Freed, Hyunbum Jang, Lyuba Khavrutskii, R. Natasha Freed, Marzena A. Dyba, Karen Stefanisko, Sergey G. Tarasov, Attila Gursoy, Ozlem Keskin, Nadya I. Tarasova, Vadim Gaponenko, and Ruth Nussinov. GTP-Dependent K-Ras Dimerization. *Structure*, 23(7):1325–1335, jul 2015.

[235] C. Barcelo, N. Paco, A. J. Beckett, B. Alvarez-Moya, E. Garrido, M. Gelabert, F. Tebar, M. Jaumot, I. Prior, and N. Agell. Oncogenic K-ras segregates at spatially distinct plasma membrane signaling platforms according to its phosphorylation status. *Journal of Cell Science*, 126(20):4553–4559, oct 2013.

[236] Alexander Varshavsky. The Ubiquitin System, Autophagy, and Regulated Protein Degradation. *Annual Review of Biochemistry*, 86(1):123–128, jun 2017.

[237] Ivan Dikic. Proteasomal and Autophagic Degradation Systems. *Annual Review of Biochemistry*, 86(1):193–224, jun 2017.

[238] Cezary Wójcik and George N. DeMartino. Intracellular localization of proteasomes. *The International Journal of Biochemistry & Cell Biology*, 35(5):579–589, may 2003.

[239] Paul Brooks, Graciela Fuertes, Rachael Z MURRAY, BOSE Suchira, Erwin Knecht, Martin C RECHSTEINER, Klavs B HENDIL, Keiji Tanaka, Julian Dyson, and A Jennifer Rivett. Subcellular localization of proteasomes and their regulatory complexes in mammalian cells. *Biochemical Journal*, 346(1):155–161, 2000.

[240] D. Li, L. Shao, B.-C. Chen, X. Zhang, M. Zhang, B. Moses, D. E. Milkie, J. R. Beach, J. A. Hammer, M. Pasham, T. Kirchhausen, M. A. Baird, M. W. Davidson, P. Xu, and E. Betzig. Extended-resolution structured illumination imaging of endocytic and cytoskeletal dynamics. *Science*, 349(6251):aab3500–aab3500, aug 2015.

[241] Florian Schueder, Juanita Lara-Gutiérrez, Brian J. Beliveau, Sinem K. Saka, Hiroshi M. Sasaki, Johannes B. Woehrstein, Maximilian T. Strauss, Heinrich Grabmayr, Peng Yin, and Ralf Jungmann. Multiplexed 3D super-resolution imaging of whole cells using spinning disk confocal microscopy and DNA-PAINT. *Nature Communications*, 8(1):2090, dec 2017.

[242] Tom Vettenburg, Heather I C Dalgarno, Jonathan Nylk, Clara Coll-Lladó, David E K Ferrier, Tomáš Čižmár, Frank J Gunn-Moore, and Kishan Dholakia. Light-sheet microscopy using an Airy beam. *Nature Methods*, 11(5):541–544, apr 2014.

[243] Steven F. Lee, Quentin Vérolet, and Alexandre Fürstenberg. Improved Super-Resolution Microscopy with Oxazine Fluorophores in Heavy Water. *Angewandte Chemie International Edition*, 52(34):8948–8951, aug 2013.

[244] Kathrin Klehs, Christoph Spahn, Ulrike Endesfelder, Steven F. Lee, Alexandre Fürstenberg, and Mike Heilemann. Increasing the Brightness of Cyanine Fluorophores for Single-Molecule and Superresolution Imaging. *ChemPhysChem*, 15(4):637–641, mar 2014.

[245] James E Darnell, Harvey F Lodish, David Baltimore, et al. *Molecular cell biology*, volume 2. Scientific American Books New York, 1990.

[246] Jonathan DG Jones and Jeffery L Dangl. The plant immune system. *Nature*, 444(7117):323, 2006.

[247] Ruslan Medzhitov. Recognition of microorganisms and activation of the immune response. *Nature*, 449(7164):819, 2007.

[248] Polly Matzinger. The danger model: a renewed sense of self. *Science*, 296(5566):301–305, 2002.

[249] Gregory Beck and Gail S Habicht. Immunity and the invertebrates. *Scientific American*, 275(5):60–66, 1996.

[250] Andrew JT George, Jaroslav Stark, and Cliburn Chan. Understanding specificity and sensitivity of t-cell recognition. *Trends in immunology*, 26(12):653–659, 2005.

[251] Wolfgang WA Schamel and Balbino Alarcón. Organization of the resting tcr in nanoscale oligomers. *Immunological reviews*, 251(1):13–20, 2013.

[252] STEFAN C Meuer, Kathleen A Fitzgerald, Rebecca E Hussey, James C Hodgdon, Stuart F Schlossman, and Ellis L Reinherz. Clonotypic structures involved in antigen-specific human t cell function. relationship to the t3 molecular complex. *Journal of Experimental Medicine*, 157(2):705–719, 1983.

[253] Clare L Abram and Clifford A Lowell. The expanding role for itam-based signaling pathways in immune cells. *Sci. STKE*, 2007(377):re2–re2, 2007.

[254] Arthur Weiss and Dan R Littman. Signal transduction by lymphocyte antigen receptors. *Cell*, 76(2):263–274, 1994.

[255] Gerald P Morris and Paul M Allen. How the tcr balances sensitivity and specificity for the recognition of self and pathogens. *Nature immunology*, 13(2):121, 2012.

[256] Yuri Sykulev, Michael Joo, Irina Vturina, Theodore J Tsomides, and Herman N Eisen. Evidence that a single peptide–mhc complex on a target cell can elicit a cytolytic t cell response. *Immunity*, 4(6):565–571, 1996.

[257] Clifford V Harding and Emil R Unanue. Quantitation of antigen-presenting cell mhc class ii/peptide complexes necessary for t-cell stimulation. *Nature*, 346(6284):574, 1990.

[258] Boryana N Manz, Bryan L Jackson, Rebecca S Petit, Michael L Dustin, and Jay Groves. T-cell triggering thresholds are modulated by the number of antigen within individual T-cell receptor clusters. *Proceedings of the National Academy of Sciences of the United States of America*, 108(22):9089–94, may 2011.

[259] R Schwinzer, RA Franklin, J Domenico, H Renz, and EW Gelfand. Monoclonal antibodies directed to different epitopes in the cd3-tcr complex induce different states of competence in resting human t cells. *The Journal of Immunology*, 148(5):1322–1328, 1992.

[260] Rajat Varma, Gabriele Campi, Tadashi Yokosuka, Takashi Saito, and Michael L Dustin. T cell receptor-proximal signals are sustained in peripheral microclusters and terminated in the central supramolecular activation cluster. *Immunity*, 25(1):117–127, 2006.

[261] Ejaz Ahmad, Gulam Rabbani, Nida Zaidi, Mohammad Azam Khan, Atiyatul Qadeer, Mohd Ishtikhar, Saurabh Singh, and Rizwan Hasan Khan. Revisiting ligand-induced conformational changes in proteins: essence, advancements, implications and future challenges. *Journal of Biomolecular Structure and Dynamics*, 31(6):630–648, 2013.

[262] Travis Beddoe, Zhenjun Chen, Craig S Clements, Lauren K Ely, Simon R Bushell, Julian P Vivian, Lars Kjer-Nielsen, Siew Siew Pang, Michelle A Dunstone, Yu Chih Liu, et al. Antigen ligation triggers a conformational change within the constant domain of the $\alpha\beta$ t cell receptor. *Immunity*, 30(6):777–788, 2009.

[263] Zhengyu Ma, Paul A Janmey, and Terri H Finkel. The receptor deformation model of tcr triggering. *The FASEB Journal*, 22(4):1002–1008, 2008.

[264] Simon J Davis and P Anton van der Merwe. The structure and ligand interactions of cd2: implications for t-cell function. *Immunology today*, 17(4):177–187, 1996.

[265] MN McCall, DM Shotton, and AN Barclay. Expression of soluble isoforms of rat cd45. analysis by electron microscopy and use in epitope mapping of anti-cd45r monoclonal antibodies. *Immunology*, 76(2):310, 1992.

[266] Bozidar Purtic, Lisa A Pitcher, Nicolai SC van Oers, and Christoph Wülfing. T cell receptor (tcr) clustering in the immunological synapse integrates tcr and costimulatory signaling in selected t cells. *Proceedings of the National Academy of Sciences*, 102(8):2904–2909, 2005.

[267] Michael L Dustin. Cell adhesion molecules and actin cytoskeleton at immune synapses and kinapses. *Current opinion in cell biology*, 19(5):529–533, 2007.

[268] Ivan a Yudushkin and Ronald D Vale. Imaging T-cell receptor activation reveals accumulation of tyrosine-phosphorylated CD3 in the endosomal compartment. *Proceedings of the National Academy of Sciences*, 107(51):22128–22133, dec 2010.

[269] Michael L Dustin and Jay T Groves. Receptor signaling clusters in the immune synapse. *Annual review of biophysics*, 41:543–56, jan 2012.

[270] Florian Baumgart, Andreas M Arnold, Konrad Leskovar, Kaj Staszek, Martin Fölser, Julian Weghuber, Hannes Stockinger, and Gerhard J Schütz. Varying label density allows artifact-free analysis of membrane-protein nanoclusters. *Nature methods*, 13(8):661, 2016.

[271] P. T. Sage, L. M. Varghese, R. Martinelli, T. E. Sciuto, M. Kamei, A. M. Dvorak, T. A. Springer, A. H. Sharpe, and C. V. Carman. Antigen Recognition Is Facilitated by Invadosome-like Protrusions Formed by Memory/Effector T Cells. *The Journal of Immunology*, 188(8):3686–3699, apr 2012.

[272] Robert D Turner, Alexander F Hurd, Ashley Cadby, Jamie K Hobbs, and Simon J Foster. Cell wall elongation mode in Gram-negative bacteria is determined by peptidoglycan architecture. *Nature communications*, 4:1496, jan 2013.

[273] Bruno H. Zimm and Stephen D. Levene. Problems and prospects in the theory of gel electrophoresis of dna. *Quarterly Reviews of Biophysics*, 25(2):171–204, 1992.

[274] Christian Kleusch, Nils Hersch, Bernd Hoffmann, Rudolf Merkel, and Agnes Csiszár. Fluorescent lipids: Functional parts of fusogenic liposomes and tools for cell membrane labeling and visualization. *Molecules*, 17(1):1055–1073, 2012.

[275] Marcia G. Honig and Richard I. Hume. Dil and dio: versatile fluorescent dyes for neuronal labelling and pathway tracing. *Trends in Neurosciences*, 12(9):333 – 341, 1989.

[276] John F Nagle and Stephanie Tristram-Nagle. Structure of lipid bilayers. *Biochimica et Biophysica Acta (BBA)-Reviews on Biomembranes*, 1469(3):159–195, 2000.

[277] Henry S Slayter and John F Codington. Size and configuration of glycoprotein fragments cleaved from tumor cells by proteolysis. *Journal of Biological Chemistry*, 248(10):3405–3410, 1973.

[278] Sophie Pageon, André Cohnen, Carola Benzing, Yijun Gao, D Michael, Katie Tungatt, Garry Dolton, Andrew K Sewell, David A Price, Oreste Acuto, Robert G Parton, J Justin Gooding, Jérémie Rossy, Jamie Rossjohn, and Katharina Gaus. Functional role of T-cell receptor nanoclusters in signal initiation and antigen discrimination. *Proceedings of the National Academy of Sciences*, 113(44):E6905–E6905, nov 2016.

[279] S. Wang, J. R. Moffitt, G. T. Dempsey, X. S. Xie, and X. Zhuang. Characterization and development of photoactivatable fluorescent proteins for single-molecule-based superresolution imaging. *Proceedings of the National Academy of Sciences*, 111(23):8452–8457, jun 2014.

[280] Junling Chen, Jing Gao, Jiazhen Wu, Min Zhang, Mingjun Cai, Haijiao Xu, Junguang Jiang, Zhiyuan Tian, and Hongda Wang. Revealing the carbohydrate pattern on a cell surface by super-resolution imaging. *Nanoscale*, 7(8):3373–3380, 2015.

[281] G. Kabachinski and T. U. Schwartz. The nuclear pore complex - structure and function at a glance. *Journal of Cell Science*, 128(3):423–429, feb 2015.

[282] Benedikt Rossboth, Andreas M Arnold, Haisen Ta, René Platzer, Florian Kellner, Johannes B Huppa, Mario Brameshuber, Florian Baumgart, and Gerhard J Schütz. Tcrs are randomly distributed on the plasma membrane of resting antigen-experienced t cells. *Nature Immunology*, page 1, 2018.

[283] Shin-nosuke Uno, Mako Kamiya, Toshitada Yoshihara, Ko Sugawara, Kohki Okabe, Mehmet C Tarhan, Hiroyuki Fujita, Takashi Funatsu, Yasushi Okada, Seiji Tobita, et al. A spontaneously blinking fluorophore based on intramolecular spirocyclization for live-cell super-resolution imaging. *Nature chemistry*, 6(8):681, 2014.

[284] Patrick J Macdonald, Susan Gayda, Richard A Haack, Qiaoqiao Ruan, Richard J Himmelsbach, and Sergey Y Tetin. Rhodamine-derived fluorescent dye with inherent blinking behavior for super-resolution imaging. *Analytical chemistry*, 2018.

[285] John R. James, James McColl, Marta I. Oliveira, Paul D. Dunne, Elizabeth Huang, Andreas Jansson, Patric Nilsson, David L. Sleep, C. M. Goncalves, Sara H. Morgan, James H. Felce, Robert Mahen, Ricardo A. Fernandes, Alexandre M. Carmo, David Klenerman, and Simon J. Davis. The T Cell Receptor Triggering Apparatus Is Composed of Monovalent or Monomeric Proteins. *Journal of Biological Chemistry*, 286(37):31993–32001, sep 2011.

Appendix A

Supplementary Figures

A.1 Comparison of Ripley's K Analysis

Comparison of $L(r) - r$ curves for the TCR fixed at the surface of Jurkat T cells fixed after contacting a Poly-L-Lysine (PLL) coated coverslip surface.

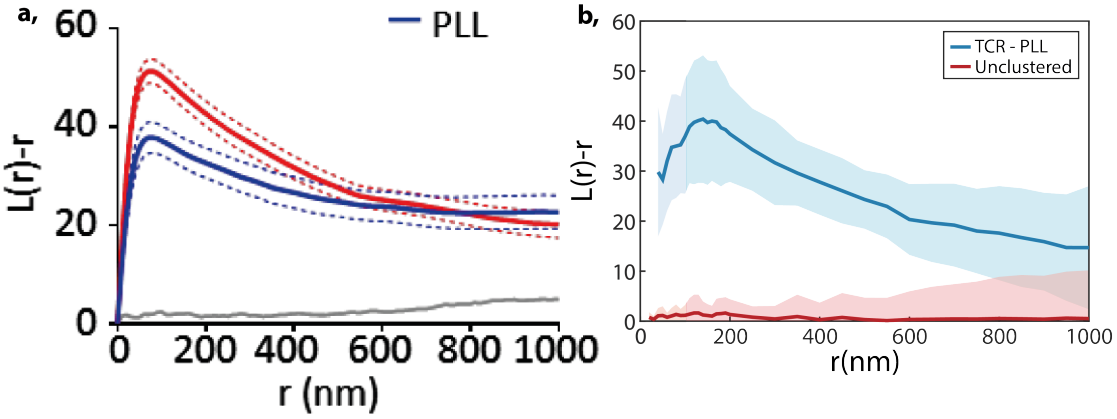

Fig. A.1 Ripley's K analysis for the TCR compared to previously published data. (a) $L(r) - r$ curve for the TCR at PLL-coated coverslips recorded with 2D-SMLM (blue), adapted from Pageon *et. al.* [278]. Errors are given by the standard error of the mean. (b) $L(r) - r$ curve for the TCR at PLL-coated coverslips recorded with 3D-SMLM via the DHPSF. Errors are given by standard deviation.

Appendix B

MATLAB Code

B.1 3D MSD and JD Analysis

Main

Main Tracking Code:

```
%------------------------Parameters-----------------------%
minloc=4;     %minimum number of localisations needed in a track
q=6;          %dimension factor  (2* number of dimensions)
npop=2;       %number of populations for JD analysis (up to 3)
dt=0.02;     %Camera exposure in s
nbins=50;     %number of bins in histgram
nbinsJD=50;   %number of bins for JD analysis
maxdist=5*266*(4/3);  %estimate for maximum distance moved by particle (nm)
skip=3;       %number of frames that can be skipped
fitn=4;       %number of msd points to be fit in analysis
%-------create test positions and find tracks-------%
intensity=500; %intensity in photons for calibrated error
numloc=10; %number of localisations per simulated track
numpar=5000;
%   poslist=f_randomwalk(0.1,dt,numpar,numloc,intensity);
%   poslist=[poslist;f_randomwalk(0.7,dt,numpar,numloc,intensity)];
```

```
%   poslist=[poslist;f_randomwalk(2,dt,numpar,numloc,intensity)];
%   poslist=sortrows(poslist,4);
%   poslist=f_randomwalkfixed(0,dt,numloc,xyprec,zprec);
%   track=f_gettracks(poslist,maxdist,minloc,skip);
% %fill missing localisations in tracks with average positions
[filledtrack,strack]=f_fillTracks(track,skip,16);
% % %calculate JDs
 [JD,JDall,JDav]=f_jumpDist(strack,nbinsJD,10,1);
% %JD analysis
 D_JD=f_JDfitting(JDall,dt,q,npop,nbinsJD);
% %Average JD analysis
D_JDav=f_JDfitting(JDav,dt,q,npop,nbinsJD);
%calculate MSD curves (or single points if not enough points (<7) )
msd=f_3dmsd(filledtrack);
%plot msd curves and calculate Diffusion constants (n>3 for curve fitting)
[Dmsd,sigma,D_msd,Dmsdtot,msddata,msdfit]=f_3dDmsd(msd,dt,q,0,0);
remember output msdfit must be divided by q for D
to plot fit use: plot(1:6,((q*D_msd*dt)*(1:6)+msdfit.p2))
[Dmsd,sigma,D,Dmsdtot,msddata,msdfit,unfilmsddata,unfilmsdfit,Dmsdrej,R]=f_3dDmsdN(ms
%fixed sample. it only fits the first 3 points on the msd.
%fit D and sigma to histogram and analyse
[Dmean,Derr]=f_3dDhist(Dmsd,nbins);
[Dmeanrej,Derrej]=f_3dDhist(Dmsdrej,nbins);
[Dmean1,Derr1]=f_3dDhist(Dmsdtot,nbins);       %include unfiltered D too
[Precision,PrecisionErr]=f_3dDhist(sigma,nbins-5);
```

Functions

```
function [msdtrack, trac]= f_fillTracks(trac,skip,minloc)
%fill in missing frames with average position
%input tracks from 3D tracking program in the format
%[x,y,z,t] where t is the frame number, not the actual time
%remove tracks that have gaps longer than user defined skip
clear temptrac
k=1;
```

```
for i=1:size(trac,2)
    flag=1;
    %check if blinking
    if(size(trac{i},1)/(max(trac{i}(:,4))-min(trac{i}(:,4))+1)<1)
        location=1;
        for j=2:size(trac{i},1)
            %if the difference in time steps is larger than user defined or
            %less than 1, dont take track
            if trac{i}(j,4)-trac{i}(j-1,4)>skip || trac{i}(j,4)-trac{i}(j-1,4)<1
                flag=0;
                if j-location > minloc
                    temptrac{k}=trac{i}(location:j-1,:);
                    k=k+1;
                end
                location=j;
            end
        end
    end
    if flag
    temptrac{k}=trac{i};
    k=k+1;
    end
end
trac=temptrac;
clear temptrac
for i=1:size(trac,2)
%add in missing frames with average of position between localisations
%check if binking occurs
if(size(trac{i},1)/(max(trac{i}(:,4))-min(trac{i}(:,4))+1)<1)
    %initiate msdtrack with only time column
    msdtrack{i}=zeros(max(trac{i}(:,4))-min(trac{i}(:,4))+1,4);
    msdtrack{i}(:,4)=min(trac{i}(:,4)):max(trac{i}(:,4));
    for j=1:size(trac{i},1)
        %fill known positions into msdtrack
        msdtrack{i}(find(msdtrack{i}(:,4)==trac{i}(j,4)),:)=trac{i}(j,1:4);
    end
```

```
    %find empty rows and fill with average positions
    for j=1:size(msdtrack{i},1)
        if msdtrack{i}(j,1)==0
            %get number of empty rows
            nempty=find(msdtrack{i}((j+1):size(msdtrack{i},1),1)~=0,1);
            %calculate difference between previous and future steps
            %and divide by number of missing steps
            dx=(msdtrack{i}(j+nempty,1)-msdtrack{i}(j-1,1))/(nempty+1);
            dy=(msdtrack{i}(j+nempty,2)-msdtrack{i}(j-1,2))/(nempty+1);
            dz=(msdtrack{i}(j+nempty,3)-msdtrack{i}(j-1,3))/(nempty+1);
            %fill in missing rows
            for k=1:nempty
                msdtrack{i}(j+k-1,1)=msdtrack{i}(j-1,1)+(k*dx);
                msdtrack{i}(j+k-1,2)=msdtrack{i}(j-1,2)+(k*dy);
                msdtrack{i}(j+k-1,3)=msdtrack{i}(j-1,3)+(k*dz);
            end
        end
    end
else
    msdtrack{i}=trac{i};
end
end
end


function [D_JD] = f_JDfitting(JDall, dt, q, npop,nbinsJD)
%fit Jump distance analysis (JDall, dt, number of populations)
if nargin<3
    npop=1;
end
%set guess parameters depending on number of populations fit
switch npop
    case 1
        prompt={'Guess 1 population D (um^2/s):'};
        title='Parameter Guessing';
        def(1)={'0.1'};
        answer=inputdlg(prompt,title,1,def);
```

```
        if isempty(answer)
           error('User cancelled the program')
        end
        param_guess(1) = str2num(answer{1});
        param_guess(2)= 1;
        param_guess(1) = 0.1;
    case 2
        prompt={'Guess population 1 D (um^2/s):','Population 1 fraction:',...
            'Population 2 D (um^2/s)','Population 2 fraction'};
        title='Parameter Guessing';
        def(1)={'0.1'};
        def(2)={'0.7'};
        def(3)={'0.02'};
        def(4)={'0.3'};
        answer=inputdlg(prompt,title,1,def);
        if isempty(answer)
           error('User cancelled the program')
        end
        param_guess(1) = str2num(answer{1});
        param_guess(2) = str2num(answer{2});
        param_guess(3) = str2num(answer{3});
        param_guess(4) = str2num(answer{4});
    otherwise
        prompt={'Guess population 1 D (um^2/s):','Population 1 fraction:',...
            'Population 2 D (um^2/s)','Population 2 fraction',...
            'Population 3 D (um^2/s)','Population 3 fraction'};
        title='Parameter Guessing';
        def(1)={'0.1'};
        def(2)={'0.7'};
        def(3)={'0.02'};
        def(4)={'0.2'};
        def(5)={'0.002'};
        def(6)={'0.1'};
        answer=inputdlg(prompt,title,1,def);
        if isempty(answer)
           error('User cancelled the program')
```

```
        end
        param_guess(1) = str2num(answer{1});
        param_guess(2) = str2num(answer{2});
        param_guess(3) = str2num(answer{3});
        param_guess(4) = str2num(answer{4});
        param_guess(5) = str2num(answer{5});
        param_guess(6) = str2num(answer{6});
end
clear D
if q==4
%analyse 1 popluation
D{1}=f_JDfitpop1(JDall,dt,q,param_guess,nbinsJD);
%analyse 2 populations
if npop>1
    D{2}=f_JDfitpop2(JDall,dt,q,param_guess,nbinsJD);
end
%analyse 3 populations
if npop>2
    D{3}=f_JDfitpop3(JDall,dt,q,param_guess,nbinsJD);
end
end
if q==6
% analyse 1 popluation
D{1}=f_3DJDfitpop1(JDall,dt,q,param_guess,nbinsJD);
%analyse 2 populations
if npop>1
    D{2}=f_3DJDfitpop2(JDall,dt,q,param_guess,nbinsJD);
end
% analyse 3 populations
if npop>2
    D{3}=f_3DJDfitpop3(JDall,dt,q,param_guess,nbinsJD);
end
end
D_JD=D;
end
```

```
function [Dout] = f_JDfitpop1(JDall,dt,q,param_guess,nbinsJD)
if q==6
     disp('This is not the right JD for 3D');
end
JD=JDall/1000;  %convert to um
x=sort(JD)';     %sort list of jump distances
y = 1:1:length(x);
y = y/max(y);
%define tolerance of fit
opt = optimset ('TolX',1e-10,'TolFun',1e-10,'MaxFunEvals',2000);
%Fit x to prob function of JD (laura paper)
Dfit=lsqnonlin(@(D) D(2)*(1-exp(-x.^2/(q*D(1)*dt)))-y,[param_guess(1),1],[0,0.9],[4
%Plot fit onto data
G=Dfit(2)*(1-exp(-x.^2/(q*Dfit(1)*dt)));
figure();subplot(3,1,2);plot(x,y)
hold all;
plot(x,G);
xlabel('Jump Distance (um)')
ylabel('Frequency')
%Fit analysis
residual=y-G;
SAM=y-mean(y);        %square about mean
SSE=sum(residual.^2);
SST=sum(SAM.^2);
R2=1-(SSE/SST);       %R^2
shift=residual(length(G));
%Plot residual
subplot(3,1,3);plot(x,residual)
hold on;
plot(x,zeros(length(x),1)')
ylabel('Residual')
xlabel('Jump Distance [um]')
subplot(3,1,2);
legend('JD hist data',strcat('Fit (R^2=',num2str(R2,3),')'),'Location','southeast')
%plot normal hist
JDbin=(max(JD)-min(JD))/nbinsJD;
```

```
JDhistbins=min(JD):JDbin:max(JD)-JDbin;
JDhist=hist(JD,JDhistbins)
JDx=min(JD):0.001:max(JD);
JDG=Dfit(2)*(1-exp(-JDx.^2/(q*Dfit(1)*dt)));
JDG=diff(JDG)*length(JD)*length(JDx)/nbinsJD;
subplot(3,1,1)
bar(JDhistbins,JDhist,'FaceColor',[0.95 0.95 0.95],'EdgeColor','k');
hold on;
plot(JDx(1:end-1),JDG);
ylabel('Frequency');
xlabel('Jump Distance [um]');
legend('JD hist data',strcat('Fit (R^2=',num2str(R2,3),')'));
title(strcat('Jump Distance: D=',num2str((Dfit(1)),3),' um^2/s'));
Dout=Dfit(1);
end


function [Dout] = f_3DJDfitpop3(JDall,dt,q,param_guess,nbinsJD)
if q~=6
    disp('This is not the right JD, this is for 3D');
end
JD=JDall/1000;  %convert to um
x=sort(JD)';     %sort list of jump distances
y = 1:1:length(x);
y = y/max(y);
%define tolerance of fit
opt = optimset ('TolX',1e-10,'TolFun',1e-10,'MaxFunEvals',2000);
%Fit x to prob function of JD (laura paper)
Dfit=lsqnonlin(@(D) D(2)*(((8*pi*D(1)*dt)/(4*pi*D(1)*dt)^(3/2))*...
    ((sqrt(pi*D(1)*dt)*erf(x./sqrt(4*D(1)*dt)))-...
    (x.*exp(-x.^2/(4*D(1)*dt)))))+...
    ...
    D(4)*(((8*pi*D(3)*dt)/(4*pi*D(3)*dt)^(3/2))*...
    ((sqrt(pi*D(3)*dt)*erf(x./sqrt(4*D(3)*dt)))-...
    (x.*exp(-x.^2/(4*D(3)*dt)))))+...
    ...
    D(6)*(((8*pi*D(5)*dt)/(4*pi*D(5)*dt)^(3/2))*...
```

```
    ((sqrt(pi*D(5)*dt)*erf(x./sqrt(4*D(5)*dt)))-...
    (x.*exp(-x.^2/(4*D(5)*dt))))...
    ...
    -y,[param_guess],[0,0,0,0,0,0],[4,1,0.6,1,0.8,1],opt);
%Plot fit onto data
G1=Dfit(2)*(((8*pi*Dfit(1)*dt)/(4*pi*Dfit(1)*dt)^(3/2))*...
    ((sqrt(pi*Dfit(1)*dt)*erf(x./sqrt(4*Dfit(1)*dt)))-...
    (x.*exp(-x.^2/(4*Dfit(1)*dt)))));
G2=Dfit(4)*(((8*pi*Dfit(3)*dt)/(4*pi*Dfit(3)*dt)^(3/2))*...
    ((sqrt(pi*Dfit(3)*dt)*erf(x./sqrt(4*Dfit(3)*dt)))-...
    (x.*exp(-x.^2/(4*Dfit(3)*dt)))));
G3=Dfit(6)*(((8*pi*Dfit(5)*dt)/(4*pi*Dfit(5)*dt)^(3/2))*...
    ((sqrt(pi*Dfit(5)*dt)*erf(x./sqrt(4*Dfit(5)*dt)))-...
    (x.*exp(-x.^2/(4*Dfit(5)*dt)))));
G=G1+G2+G3;
%normalise fractions
f1 = Dfit(2)/(Dfit(2)+Dfit(4)+Dfit(6));
f2 = Dfit(4)/(Dfit(2)+Dfit(4)+Dfit(6));
f3 = Dfit(6)/(Dfit(2)+Dfit(4)+Dfit(6));
Dfit(2)=f1;
Dfit(4)=f2;
Dfit(6)=f3;
figure();subplot(3,1,2);plot(x,y)
hold all;
plot(x,G);
plot(x,G1);
plot(x,G2);
plot(x,G3);
xlabel('Jump Distance (um)')
ylabel('Frequency')
hold off;
%Fit analysis
residual=y-G;
SAM=y-mean(y);        %square about mean
SSE=sum(residual.^2);
SST=sum(SAM.^2);
```

```
R2=1-(SSE/SST);       %R^2
%shift=residual(length(G));
%Plot residual
subplot(3,1,3);plot(x,residual)
hold on;
plot(x,zeros(length(x),1)')
ylabel('Residual')
xlabel('Jump Distance [um]')
subplot(3,1,2);
legend('JD hist data',strcat('Total Fit (R^2=',num2str(R2,3),')'),...
    'Population 1','Population 2','Population 3','Location','southeast');
%plot normal hist
JDbin=(max(JD)-min(JD))/nbinsJD;
JDhistbins=min(JD):JDbin:max(JD)-JDbin;
JDhist=hist(JD,JDhistbins);
JDx=min(JD):0.001:max(JD);
JDG1=Dfit(2)*(((8*pi*Dfit(1)*dt)/(4*pi*Dfit(1)*dt)^(3/2))*...
    ((sqrt(pi*Dfit(1)*dt)*erf(JDx./sqrt(4*Dfit(1)*dt)))-...
    (JDx.*exp(-JDx.^2/(4*Dfit(1)*dt)))));
JDG2=Dfit(4)*(((8*pi*Dfit(3)*dt)/(4*pi*Dfit(3)*dt)^(3/2))*...
    ((sqrt(pi*Dfit(3)*dt)*erf(JDx./sqrt(4*Dfit(3)*dt)))-...
    (JDx.*exp(-JDx.^2/(4*Dfit(3)*dt)))));
JDG3=Dfit(6)*(((8*pi*Dfit(5)*dt)/(4*pi*Dfit(5)*dt)^(3/2))*...
    ((sqrt(pi*Dfit(5)*dt)*erf(JDx./sqrt(4*Dfit(5)*dt)))-...
    (JDx.*exp(-JDx.^2/(4*Dfit(5)*dt)))));
JDG1=diff(JDG1)*length(JD)*length(JDx)/nbinsJD;
JDG2=diff(JDG2)*length(JD)*length(JDx)/nbinsJD;
JDG3=diff(JDG3)*length(JD)*length(JDx)/nbinsJD;
JDG=JDG1+JDG2+JDG3;
subplot(3,1,1)
bar(JDhistbins,JDhist,'FaceColor',[0.95 0.95 0.95],'EdgeColor','k');
hold on;
plot(JDx(1:end-1),JDG);
plot(JDx(1:end-1),JDG1);
plot(JDx(1:end-1),JDG2);
plot(JDx(1:end-1),JDG3);
```

```
ylabel('Frequency');
xlabel('Jump Distance [um]');
legend('JD hist data',strcat('Total Fit (R^2=',num2str(R2,3),')'),...
    'Population 1','Population 2','Population 3');
title(strcat('Jump Distance: D1=',num2str((Dfit(1)),3),...
    ' um^2/s, f1=',num2str((Dfit(2)),2),', D2=',num2str((Dfit(3)),2),...
    'um^2/s, f2=',num2str((Dfit(4)),2),', D3=',num2str((Dfit(5)),2),...
    'um^2/s'));
Dout=Dfit;
end


function msd = f_3dmsd(track)
%calculate MSD curves
%using method defined by Qian et al and Saxton (see laura's paper for refs)
clear msd
%loop over all tracks
for i=1:size(track,2)
%use floor fuction to calcualte number of time steps analysed
%no more than 1/4 of track length
l=size(track{i},1);
if l>7
    %analyse all n
    for n= 1:min([floor(size(track{i},1)/4),6])
        %calculate msd for n*dt
    msdsum=0;
    for j=1:(l-n)
        msdsum=msdsum + (...  %x^2 + y^2 +z^2
            ((track{i}(j+n,1)-track{i}(j,1))*(track{i}(j+n,1)-track{i}(j,1)))...
            +...
            ((track{i}(j+n,2)-track{i}(j,2))*(track{i}(j+n,2)-track{i}(j,2)))...
            +...
            ((track{i}(j+n,3)-track{i}(j,3))*(track{i}(j+n,3)-track{i}(j,3)))...
            );
    end
    msd{i}(n)= (1/(l-n)) * msdsum * 10^-6;   % & convert to um^2 (from nm^2)
    end
```

```
else
    %analyse just n=1 if there are not enough points in track
    %(no curve fitting needed)
    n=1;
        %calculate msd for n*dt
    msdsum=0;
    for j=1:(l-n)
        msdsum=msdsum + (...  %x^2 + y^2 +z^2
            ((track{i}(j+n,1)-track{i}(j,1))*(track{i}(j+n,1)-track{i}(j,1)))...
            +...
            ((track{i}(j+n,2)-track{i}(j,2))*(track{i}(j+n,2)-track{i}(j,2)))...
            +...
            ((track{i}(j+n,3)-track{i}(j,3))*(track{i}(j+n,3)-track{i}(j,3)))...
            );
    end
    msd{i}(n)= (1/(l-n)) * msdsum * 10^-6;   % & convert to um^2 (from nm^2)
end
end
end


function [Dout,sigmaout,Dfil,Dtot,msddata,msdfit,unfilmsddata,unfilmsdfit,Drej,R] = f
%calculate Diffusion constant in um^2/s from msd curves
%  MSD= 4* D * ndt   +   4 * sigma^2
%test if good fit to straight line (indication of free diffusion)
%Inputs: (msds, exposure time, diffusion coefficient, include all D[1/0], plot fits[1
%include all D = 1 to analyse all calcualted msds, even those without
%enough points to plot a curve
%plotfit = 1 to plot fits during running
%-------------------------------------------------------------------------
%if no arguments assume fuction not wanted
if nargin < 6
  plotfit =0;
end
if nargin < 5
  allD =0.5;
end
```

```
k=1; %initialise counter of D
g=1; %initialise precision counter
w=1; %initialise filtered msd counter
u=1;
t=1;
r=1;
clear filteredmsd
clear rejectedmsd
rmin=0.85;   %miniumum accepted r square value
%calculate mean msd curve
for i=1:size(msd,2)
    maxn(i)=size(msd{i},2);
end
maxn=max(maxn);
%group MSDs from same ndt
clear groupmsd
for i=1:maxn
    groupmsd{i}=0;
end
for i=1:size(msd,2)
    for j=1:size(msd{i},2)
        groupmsd{j}=[groupmsd{j};msd{i}(j)];
    end
end
for i=1:size(groupmsd,2)
    groupmsd{i}=groupmsd{i}(2:size(groupmsd{i},1),:);
end
%calculate mean for each ndt
for i=1:size(groupmsd,2)
meanmsd(i)=mean(groupmsd{i});
semmsd(i)=std(groupmsd{i})/sqrt(length(groupmsd{i})); %Calculate SEM
end
%linear fit to mean msd curve
[meanfit,meanfiterr]=fit( ((1:fitn)'*dt),(meanmsd(1:fitn))','poly1');
%plot overall MSD curve
figure
```

```
   plot(((0:size(meanmsd,2)+1))*dt,...
       ((meanfit.p1)*(((0:size(meanmsd,2)+1))*dt))+meanfit.p2,'r')
   hold on
   errorbar((((1:size(meanmsd,2)))*dt),(meanmsd),(semmsd),'bo')
   title(strcat('Unfiltered MSD Curve D=',num2str((meanfit.p1/q),3),' um^2/s'));
   xlabel('Time (s)');
   ylabel('MSD (um^2)');
   legend(strcat('Fit r^2 = ',num2str(meanfiterr.rsquare,3)),...
       'All Data (with SEM)','Location','northwest');
%loop over msds
for i=1:size(msd,2)
%check size (minimum for fitting? n>=3?)
if size(msd{i},2)>=4
%fit straight line (convert n into times too)
[msdfit,fiterr]=fit( (((1:size(msd{i},2))')*dt),(msd{i})','poly1');
%calculate D from gradient (m = q * D)
D = msdfit.p1 / q;
%calculate sigma from offset (convert to nm from um)
sigma = sqrt(abs(msdfit.p2) / q) * 1000;    %take positive intercept
%If fit accepted add to output
if fiterr.rsquare > rmin && D > 0
    Dout(k)=D;
    k=k+1;
    sigmaout(g)=sigma;
    g=g+1;
    filteredmsd{w}=msd{i};
    w=w+1;
else
    rejectedmsd{t}=msd{i};
    t=t+1;
    Drej(r)=D;
    r=r+1;
end
Dtot(u)=D;
R(u)=fiterr.rsquare;
u=u+1;
```

```
%include option to plot curves and fits
%************************make this nicer please**********
if plotfit~=0
   plot(msdfit,(((1:size(msd{i},2)))*dt),(msd{i}))
   hold off
   title('MSD Curve');
   xlabel('Time (s)');
   ylabel('MSD (um^2)');
   legend('Data',strcat('r^2 = ',num2str(fiterr.rsquare,3)),'Location','northwest')
   pause(1);
end
else
%include option to include single point msds
%this needs more testing...
if allD~=0
    D = ( mean(msd{i}) - (4*dt*dt) )/(q * dt);
    Dout(k)=D;
    k=k+1;
end
end
%close msd loop
end
%re-analyse overall msd using only fits that were accepted
for i=1:size(filteredmsd,2)
    maxn(i)=size(filteredmsd{i},2);
end
maxn=max(maxn);
%group MSDs from same ndt
clear groupmsd
for i=1:maxn
    groupmsd{i}=0;
end
for i=1:size(filteredmsd,2)
    for j=1:size(filteredmsd{i},2)
        groupmsd{j}=[groupmsd{j};filteredmsd{i}(j)];
    end
```

```
end
for i=1:size(groupmsd,2)
    groupmsd{i}=groupmsd{i}(2:size(groupmsd{i},1),:);
end
%calculate mean for each ndt
for i=1:size(groupmsd,2)
filmeanmsd(i)=mean(groupmsd{i});
filsemmsd(i)=std(groupmsd{i})/sqrt(length(groupmsd{i}));  %Calculate SEM
end
%linear fit to mean msd curve
[filfit,filfiterr]=fit( ((1:fitn)'*dt),filmeanmsd(1:fitn)','poly1');
%plot filtered MSD curve
figure
   plot(((0:size(filmeanmsd,2)+1))*dt,...
       ((filfit.p1)*(((0:size(filmeanmsd,2)+1))*dt))+filfit.p2,'r')
   hold on
   errorbar((((1:size(filmeanmsd,2)))*dt),(filmeanmsd),(filsemmsd),'bo')
   title(strcat('Filtered MSD Curve D=',num2str((filfit.p1/q),3),' um^2/s'));
   xlabel('Time (s)');
   ylabel('MSD (um^2)');
   legend(strcat('Fit r^2 = ',num2str(filfiterr.rsquare,3)),...
       'Filtered Data (with SEM)','Location','northwest');
%re-analyse overall msd using only fits that were rejected
if  exist('rejectedmsd')
for i=1:size(rejectedmsd,2)
    maxn(i)=size(rejectedmsd{i},2);
end
maxn=max(maxn);
%group MSDs from same ndt
clear groupmsd
for i=1:maxn
    groupmsd{i}=0;
end
for i=1:size(rejectedmsd,2)
    for j=1:size(rejectedmsd{i},2)
        groupmsd{j}=[groupmsd{j};rejectedmsd{i}(j)];
```

```
    end
end
for i=1:size(groupmsd,2)
    groupmsd{i}=groupmsd{i}(2:size(groupmsd{i},1),:);
end
%calculate mean for each ndt
for i=1:size(groupmsd,2)
rejmeanmsd(i)=mean(groupmsd{i});
rejsemmsd(i)=std(groupmsd{i})/sqrt(length(groupmsd{i}));  %Calculate SEM
end
%linear fit to mean msd curve
[rejfit,rejfiterr]=fit( ((1:fitn)'*dt),rejmeanmsd(1:fitn)','poly1');
%plot rejected MSD curve
figure
   plot(((0:size(rejmeanmsd,2)+1))*dt,...
       ((rejfit.p1)*(((0:size(rejmeanmsd,2)+1))*dt))+rejfit.p2,'r')
   hold on
   errorbar((((1:size(rejmeanmsd,2)))*dt),(rejmeanmsd),(rejsemmsd),'bo')
   title(strcat('Rejected MSD Curve D=',num2str((rejfit.p1/q),3),' um^2/s'));
   xlabel('Time (s)');
   ylabel('MSD (um^2)');
   legend(strcat('Fit r^2 = ',num2str(rejfiterr.rsquare,3)),...
       'Filtered Data (with SEM)','Location','northwest');
else
   Drej=0;
end
Dall=meanfit.p1/q;
Dfil=filfit.p1/q;
msddata=[(((1:size(filmeanmsd,2)))*dt);filmeanmsd;filsemmsd];
unfilmsddata=[(((1:size(meanmsd,2)))*dt);meanmsd;semmsd];
msdfit=filfit;
unfilmsdfit=meanfit;
end


function [Diff,Derr] = f_3dDhist(D,nbins)
%Fit Hisogram and calculate overall diffusion constant
```

```
%create histogram
dbin=(max(D)-min(D))/nbins;
dhistbins=min(D):dbin:max(D)-dbin;
dhist=hist(D,dhistbins);
%plot just histogram
figure
bar(dhistbins,dhist);
title(strcat('Histogram of D calculated by MSD n = ',num2str(size(D,2))));
xlabel('D (um^2/s)');
ylabel('Counts');
pause(1);
%D by mean
Dpos=D(D(:)>0);
Diff=mean(Dpos);
Derr=std(Dpos);
%Calculate D by fitting a single gaussian
try
dgauss=fit(dhistbins',dhist','gauss1');
Diff=dgauss.b1;                 %middle of gaussian
Derr=confint(dgauss);
Derr=dgauss.b1-Derr(1,2);
%plot histgram with fit gaussian
plot(dgauss,dhistbins,dhist);
grid on;
xlabel('D (um^2/s)');
ylabel('Counts');
pause(1);
catch
    plot(dhistbins,dhist);
    legend(':,(');
    Diff=0;
    Derr=0;
end
end
```

B.2 Simulating Trajectories

```
function [poslist] = f_randomwalk(D,dt,n,nt,intensity)
%Simulate random walk of particles in 3D
%n = 1000;     %number of paritcles is xn*yn*zy
%D = 1;     %diffusion constant
%dt = 30E-3;
%calculate localisation precision useing fit curves from agave
%y=Ae^(-intensity/t)+c
xynoise=(25.3*exp(-intensity/967))+8.5;
znoise=(59.1*exp(-intensity/977))+18;
poslist=[0,0,0,1];
x = rand(n,1)*100;      %initate points in x,y&z
y = rand(n,1)*100;
z = rand(n,1)*100;
for i = 1:nt   %time loop
    x = x+randn(n,1)*sqrt(2*D*dt); %move each particle
    y = y+randn(n,1)*sqrt(2*D*dt); %by a distribution centred
    z = z+randn(n,1)*sqrt(2*D*dt); %at the rmsd
    %plot diffusions
    %plot3(x(:),y(:),z(:),'ro')
    %pause(0.1)
    t(1:(n))=i;
    poslist=[poslist;(x(:)*1000),(y(:)*1000),(z(:)*1000),t(:)];
end
poslist=poslist(2:size(poslist,1),:);
%Add localisation precision
poslist(:,1:2)=poslist(:,1:2)+normrnd(0,xynoise,length(poslist),2);
poslist(:,3)=poslist(:,3)+normrnd(0,znoise,length(poslist),1);
end
```

B.3 3D Ripley's K Analysis

```
function [Lr,r] = f_Ripley(dat,modeldat)
```

```
r=[10:10:190,200:50:1000];
%get N(r)
[Nr,Nstd]=f_Nr(dat,r);
%simulate CRS on sphere based on data
% csrdat=f_createCSR(dat);
% [Mr,Mstd]=f_Nr(csrdat,r);
%get model distribution from wga M(r)
[Mr,Mstd]=f_Mr(dat,modeldat,r,1);
Lr=sqrt((Nr.*(r.^2))./(Mr));
end


function [Nr, Nstd] = f_Nr(dat,Rrange)
n=size(dat,1);
h = waitbar(0, 'Getting N(r)...');
k=0;
%loop over r
for r=Rrange
    k=k+1;
    waitbar(k/length(Rrange), h, 'Getting N(r)...');
    %loop over localisations
    for i=1:n
        x=ones(n,1)*dat(i,1:3); %posisiton of first localisation
        x=(dat(:,1:3) - x).^2;
        x=sqrt(sum(x')'); %cartesian distance to localisations in range
        N(i,k)=sum(x<r)-1; %-1 to account for localisation to itself
    end
end
close(h)
h = waitbar(1, 'Calculating other things');
Nr=mean(N);
Nstd=std(N);
close(h)
end


function [Mr, Mstd] = f_Mr(dat,modeldat,Rrange,nrep)
%get ideal distribution from sampling wga data with same density of
```

```
%localsiation data
h = waitbar(0, 'Getting M(r)...');
%Rrange=100:500:15000;
n=size(dat,1);
%nrep=3;
for rep=1:nrep
%sample model data without replacement
%random sampling
samp=modeldat(randperm(size(modeldat,1),n),:);
%sequential sampling
% nstart=randi([1 (size(modeldat,1)-n+1)],1,1);
% samp=modeldat(nstart:nstart+n-1,:);
waitbar((rep-1)/nrep, h, 'Getting M(r)...');
k=0;
%loop over r
for r=Rrange
    k=k+1;

    %loop over localisations
    for i=1:n
        x=ones(n,1)*samp(i,1:3); %posisiton of first localisation
        x=(samp(:,1:3) - x).^2;
        x=sqrt(sum(x')'); %cartesian distance to localisations in range
        M(i,k)=sum(x<r)-1; %-1 to account for localisation to itself
    end
end
M=mean(M);
if rep==1
    Mr=M;
else
    Mr=[Mr;M];
end
end
close(h)
h = waitbar(1, 'Calculating other things');
if nrep>1
```

```
    Mstd=std(Mr);
else
    Mstd=zeros(size(Mr));
end
Mr=mean(Mr,1);
close(h)
end


function [Lr, Lstd] = f_Lr(dat,modeldat,Rrange)
%get ideal distribution from sampling wga data with same density of
%localsiation data
h = waitbar(0, 'Getting L(r)...');
%Rrange=100:500:15000;
n=size(dat,1);
nrep=3;
for rep=1:nrep
%sample model data without replacement
samp=modeldat(randperm(size(modeldat,1),n),:);
waitbar((rep-1)/nrep, h, 'Getting L(r)...');
k=0;
%loop over r
for r=Rrange
    k=k+1;
    %loop over localisations
    for i=1:n
        x=ones(n,1)*samp(i,1:3); %posisiton of first localisation
        x=(samp(:,1:3) - x).^2;
        x=sqrt(sum(x')'); %cartesian distance to localisations in range
        L(i,k)=sum(x<r)-1; %-1 to account for localisation to itself
    end
end
L=mean(L);
if rep==1
    Lr=L;
else
    Lr=[Lr;L];
```

```
end
end
close(h)
h = waitbar(1, 'Calculating other things');
if nrep>1
Lstd=std(Lr);
end
Lr=mean(Lr);
close(h)
end


function [out] = f_simClusters(points,clusters,clusterR,clusterN)
r = 8000;
x0 = 8700;
y0 = -3500;
z0 = 4800;
% points = 3000;
% clusters = 20; %Number of clusters
% clusterR = 20; %radius of cluster
% clusterN = 10; %points in cluster
points = points - (clusters * clusterN);
theta = rand(points,1)*2*pi;
phi = acos(1-0.4*rand(points,1));
xs = (sin(phi)*r).*cos(theta)-x0;
ys = (sin(phi)*r).*sin(theta)-y0;
zs = cos(phi)*r-z0;
% % rem = find(zs<-2000);
% % xs(rem)=[];
% % ys(rem)=[];
% % zs(rem)=[];
%Generate random points for clusters
theta = rand(clusters,1)*2*pi;
phi = acos(1-0.4*rand(clusters,1));
xc = (sin(phi)*r).*cos(theta)-x0;
yc = (sin(phi)*r).*sin(theta)-y0;
zc = cos(phi)*r-z0;
```

```
for i = 1:clusters
    xes = xc(i)+rand(clusterN,1)*2*clusterR-clusterR;
    yes = yc(i)+rand(clusterN,1)*2*clusterR-clusterR;
    zes = zc(i)+rand(clusterN,1)*2*clusterR-clusterR;
    xs = [xs;xes];
    ys = [ys;yes];
    zs = [zs;zes];
end
%Add precision
xs = xs+randn(length(xs),1)*30; %Std = 50
ys = ys+randn(length(ys),1)*30; %Std = 50
zs = zs+randn(length(zs),1)*60; %Std = 50
out=[xs,ys,zs];
out(:,1)=out(:,1)-min(out(:,1));
out(:,2)=out(:,2)-min(out(:,2));
out(:,3)=out(:,3)-min(out(:,3));
% dlmwrite(['simTest3.3d'],[xs ys zs ones(length(xs),1) (1:length(xs))'],'delimiter',
%plot3(xs,ys,zs,'.')
% plot(theta,phi,'.')


function datclust = f_addClusters(dat,nclust,npclust,rclust)
ntot=size(dat,1);
if ntot<nclust*npclust
    disp('too many clusters, data unchanged')
    datclust=dat;
else
%remove localisations to incorporate cluster
datclust=dat(randperm(ntot,ntot-(nclust*npclust)+nclust),:);
for i=1:nclust
    cen=datclust(randperm(ntot-(nclust*npclust),1),1:3);
    clust = [cen(1)+rand(npclust-1,1)*2*rclust-rclust,...
        cen(2)+rand(npclust-1,1)*2*rclust-rclust,...
        cen(3)+rand(npclust-1,1)*2*rclust-rclust];
    datclust=[datclust(:,1:3);clust];
end
end
```

```
end


function out = f_simFingersPlane(den,denfin,radius1,height1,xyprec,zprec)
%Function simulating localisation data on two finger-like structures on a
%flat membrane surface with known localisation precision in xy &z.
%output is [x,y,z] positions of localistion data
if nargin ~=6
    error('Just put the right arguments in please')
end
% den=1000; %density of points per um^2
% xyprec=0;
% zprec=0;
%if standard plane is too small then dynamically change size
planex=5000; %dimensions of plane in nm
planey=6000;
%calculate number of localisations needed
nplane = round(den * (planex/1000)*(planey/1000)); %number of points on plane
nfinger = floor(((planex/1000)*(planey/1000))*denfin) * round(den * (height1/1000)
ntot=nplane+nfinger;
nfin=round(den * (height1/1000) * 2 * pi * (radius1/1000)); %number of each finger
%initialise localisation
localisations=zeros(ntot,3);
%place points on flat plane
localisations(1:nplane,1)=(planex*rand(nplane,1));
localisations(1:nplane,2)=(planey*rand(nplane,1));
localisations(1:nplane,3)=1000; %add 1um postive z position
for f=1:floor(((planex/1000)*(planey/1000))*denfin)
    cen2x=randperm(planex,1);
    cen2y=randperm(planey,1);
%cut out circle and move localisations up by height1
localisations(((localisations(1:nplane,1)-cen2x).^2 +...
(localisations(1:nplane,2)-cen2y).^2 < radius1^2),3)=...
localisations(((localisations(1:nplane,1)-cen2x).^2 +...
(localisations(1:nplane,2)-cen2y).^2 < radius1^2),3)+height1;
%place points on walls of cylinder
theta=2*pi*rand(nfin,1);
```

```
[localisations(nplane+((f-1)*nfin)+1:nplane+(f*nfin),1),...
    localisations(nplane+((f-1)*nfin)+1:nplane+(f*nfin),2)] =...
    sph2cart(theta,0,radius1);
%move xy to correct position
localisations(nplane+((f-1)*nfin)+1:nplane+(f*nfin),1)=...
    localisations(nplane+((f-1)*nfin)+1:nplane+(f*nfin),1)+cen2x;
localisations(nplane+((f-1)*nfin)+1:nplane+(f*nfin),2)=...
    localisations(nplane+((f-1)*nfin)+1:nplane+(f*nfin),2)+cen2y;
localisations(nplane+((f-1)*nfin)+1:nplane+(f*nfin),3)=height1*rand(nfin,1)+1000;

end
%kick localisations by precision in xy and z
localisations(:,1)=localisations(:,1)+normrnd(0,xyprec,ntot,1);
localisations(:,2)=localisations(:,2)+normrnd(0,xyprec,ntot,1);
localisations(:,3)=localisations(:,3)+normrnd(0,zprec,ntot,1);
out=localisations;
end
```